SERDP

FINAL REPORT

Drinking Water Treatment Residuals as Material for In Situ Capping of Metal Contaminated Sediments

Jean-Claude Bonzongo
Nancy Denslow
Kevin Kroll
Hajime Kurita Oyamada
Jingru Wei
Yulin Zheng
Lang Zhou
University of Florida

Jean-Francois Gaillard
Tiancheng Chen
Roman Gavrilla
Samuel Wallace
Northwestern University

August 2023

SERDP Project ER18-1428

DISTRIBUTION STATEMENT A
This document has been cleared for public release.

This report was prepared under contract to the Department of Defense Strategic Environmental Research and Development Program (SERDP). The publication of this report does not indicate endorsement by the Department of Defense, nor should the contents be construed as reflecting the official policy or position of the Department of Defense. Reference herein to any specific commercial product, process, or service by trade name, trademark, manufacturer, or otherwise, does not necessarily constitute or imply its endorsement, recommendation, or favoring by the Department of Defense.

REPORT DOCUMENTATION PAGE

Form Approved
OMB No. 0704-0188

The public reporting burden for this collection of information is estimated to average 1 hour per response, including the time for reviewing instructions, searching existing data sources, gathering and maintaining the data needed, and completing and reviewing the collection of information. Send comments regarding this burden estimate or any other aspect of this collection of information, including suggestions for reducing the burden, to Department of Defense, Washington Headquarters Services, Directorate for Information Operations and Reports (0704-0188), 1215 Jefferson Davis Highway, Suite 1204, Arlington, VA 22202-4302. Respondents should be aware that notwithstanding any other provision of law, no person shall be subject to any penalty for failing to comply with a collection of information if it does not display a currently valid OMB control number.
PLEASE DO NOT RETURN YOUR FORM TO THE ABOVE ADDRESS.

1. REPORT DATE *(DD-MM-YYYY)*	**2. REPORT TYPE**	**3. DATES COVERED** *(From - To)*
23/08/2023	SERDP Final Report	8/3/2018 - 8/3/2023

4. TITLE AND SUBTITLE

Drinking Water Treatment Residuals as Material for In situ Capping of Metal Contaminated Sediments

5a. CONTRACT NUMBER
18-C-0039

5b. GRANT NUMBER

5c. PROGRAM ELEMENT NUMBER

6. AUTHOR(S)

Jean-Claude Bonzongo, Nancy Denslow, Kevin Kroll, Hajime Kurita Oyamada, Jingru Wei, Yulin Zheng and Lang Zhou
University of Florida

Jean-Francois Gaillard, Tiancheng Chen, Roman Gavrilla and Samuel Wallace
Northwestern University

5d. PROJECT NUMBER
ER18-1428

5e. TASK NUMBER

5f. WORK UNIT NUMBER

7. PERFORMING ORGANIZATION NAME(S) AND ADDRESS(ES)
University of Florida
Environmental Engineering Sciences
PO BOx 116450
Gainesville, FL 32611-6450

8. PERFORMING ORGANIZATION REPORT NUMBER
ER18-1428

9. SPONSORING/MONITORING AGENCY NAME(S) AND ADDRESS(ES)
Office of the Deputy Assistant Secretary of Defense (Energy Resilience & Optimization)
3500 Defense Pentagon, RM 5C646
Washington, DC 20301-3500

10. SPONSOR/MONITOR'S ACRONYM(S)
SERDP

11. SPONSOR/MONITOR'S REPORT NUMBER(S)
ER18-1428

12. DISTRIBUTION/AVAILABILITY STATEMENT

DISTRIBUTION STATEMENT A. Approved for public release: distribution unlimited.

13. SUPPLEMENTARY NOTES

14. ABSTRACT

This research was developed with the aim of adding value to a readily available waste material, DWTR, by exploring the mechanisms through which different types of metals can be immobilized on this highly heterogeneous sorbent in response to changing key water/sediment of DWTR as capping material for metal-contaminated sediments. It was hypothesized: first, that metal cations would form highly stable surface complexes with DWTR through a combination of different sorption mechanisms; and second, that if used as an in situ capping substrate, DWTR would significantly reduce metal effluxes from contaminated sediments towards the water column decreasing therefore their bioavailability and toxicity.

The specific objectives of this study were as follows:
(i) To determine the physicochemical and toxicity characteristics of a wide variety of DWTR and develop a screening approach for identifying DWTR suitable for introduction into US aquatic systems.
(ii) To conduct laboratory studies to assess the efficacy of DWTR in immobilizing metals from aqueous solutions and controlling the release of metals from contaminated sediments into the overlying water, with a focus on how these processes are affected by changes in key water parameters.
(iii) To investigate the effects of extreme environmental changes on the ability of DWTR to sorb and immobilize metals when used as in-situ capping material for contaminated sediments.

15. SUBJECT TERMS

Installation Restoration, Sediments Remediation and Management, Sediment Remediation, Drinking Water Treatment Residuals, In-situ Capping, Metal Contaminated Sediments

16. SECURITY CLASSIFICATION OF:			**17. LIMITATION OF ABSTRACT**	**18. NUMBER OF PAGES**	**19a. NAME OF RESPONSIBLE PERSON**
a. REPORT	**b. ABSTRACT**	**c. THIS PAGE**			Jean-Claude Bonzongo
UNCLASS	UNCLASS	UNCLASS	UNCLASS	145	**19b. TELEPHONE NUMBER** *(Include area code)* 352-392-7604

TABLE OF CONTENT

List of figures……..05
List of tables……...15
List of acronyms……..…17
Executive summary…….....19
1. Background…….……..23
2. Research objectives…….…...24
2.1 Collection and characterization of DWTR samples…….....24
2.2 Metal Sorption by DWTR in batch reactors…….....25
2.3 Ability of DWTR to immobilize metals in flow through columns…….…….....25
2.4 Metal sorption by DWTR in simulated hydrodynamic systems: Gust chamber studies.…….…25
3. Materials and methods…….....26
3.1. Collection of DWTR samples…….…….....26
3.2. Screening approach and identification of suitable DWTR……...…….....28
3.2.1. Toxicity characteristics leaching procedure (TCLP)…….……..28
3.2.2. Elutriate studies…….....28
3.2.3. Metal concentrations and sediment quality guidelines (SQG)…….…....28
3.2.4. Ecotoxicity studies…….…...31
3.2.5. Developed screening method……..……..32
3.3. Solid phase analysis and characterization…….....33
3.3.1. Thermogravimetric analysis coupled to mass spectrometry (TGA-MS)…….…….33
3.3.2. Specific surface area (SSA)…….…….33
3.3.3. Carbon, hydrogen, nitrogen, and sulfur (CHNS) elemental analysis……..….....33
3.3.4. X-Ray Fluorescence (XRF)……..34
3.3.5. X-Ray Diffraction (XRD)……..34
3.3.6. X-Ray Absorption Spectroscopy (XAS)…….....34
3.4. Sorption studies……..35
3.4.1. Sorption kinetics……...35
3.4.2. Sorption isotherms…….....35
3.4.3. Fixed bed flow-through column studies…….....36
3.5. Sediment capping: Effect on sediment resuspension and fate of metals……....37
3.5.1. Metals released from contaminated sediments over time in the absence and presence of a capping substrate under a fixed hydrodynamic critical shear stress (τ=0.05 Pa)……...38
3.5.2. Metals released from contaminated sediments over time in response to increasing hydrodynamic shear stress…….....39
3.5.3. Effects of sediment capping on vertical profiles of dissolved metal concentrations in pore waters using diffusive gradient in thin films (DGT) samplers……..……....40
3.5.4. Effect of DWTR on metal toxicity to water column organisms……..……...41
4. Results and discussion ……..…….....41
4.1 Metal content, toxicity characteristics, and screening results…….....41
4.1.1. Determination of the hazardous characteristics of DWTR using the toxicity characteristics leaching procedure (TCLP) ……. 42
4.1.2. Selection of ideal DWTR samples based on total concentrations of regulated metals and marine sediment quality guidelines……...42
4.1.3. Saltwater elutriation results: Metals leached from the selected DWTR samples with synthetic saltwater (35‰ salinity) prepared using Instant Ocean®……..…...46
4.1.4. Metal content of DWTR and sediment quality guidelines for freshwater sediments……46

4.1.5. Freshwater elutriation results: metals leached from the selected DWTR samples with synthetic freshwater (USEPA, 2002).....47
4.1.6. Ecotoxicity studies using marine benthic organisms.....49
4.1.7. Ecotoxicity studies using freshwater benthic organisms.....50
4.2. Characterization of DWTR.....56
4.2.1. Thermogravimetric mass spectrometry results.....56
4.2.2. Specific surface area and microporosity.....58
4.2.3. Elemental analysis.....59
4.2.4. X-Ray Fluorescence.....60
4.2.5. X-Ray Diffraction.....62
4.2.6. X-ray Absorption Spectroscopy.....64
4.3 Copper (Cu) and lead (Pb) sorption to DWTRs.....70
4.3.1 Microscopic and Spectroscopic characterization of the association of metals with DWTRs.....70
4.3.2 SEM-EDS results.....70
4.3.3 X-Ray Absorption Spectroscopy.....76
4.3.4 Conclusions for SEM-EDS and XAS analysis of Cu and Pb sorption.....85
4.4. Batch sorption studies 86
4.4.1. A predictive approach for the determination of the ability of DWTR to sorb metals based on their bond-forming properties.....86
4.4.2.Sorption isotherm studies.....88
4.4.3. Batch sorption studies of mercury (Hg) by 6 different DWTR samples.....98
4.5. Fixed bed flow-through column studies.....106
4.6. Using DWTR as a cap layer at the interface of metal-contaminated sediments and overlying water: Effects on metal fluxes and vertical concentration profiles in pore waters.....110
4.6.1. DWTR cap and particles resuspension from sediment as a function of increasing hydrodynamic shear stress.....112
4.6.2. Gust chamber studies of metals release from non-capped and capped sediment as a function of changing hydrodynamic shear stress (τ).....117
4.6.3. Effect of capping with DWTR on vertical profiles of dissolved metals in sediment pore and overlying waters using DGT samplers.....126
4.6.4. Toxicity of water overlying uncapped and capped sandy sediments on FHM juveniles.

5. Technology transition 127

5.1. Batch to batch variability of DWTR substrates from either a single or multiple sources and potential effects on their short- and long-term metal immobilization performances.....127
5.2. Parametric sensitivity analysis linking key compositional characteristics to DWTRs for potential applications.....128
5.3. Cost and availability of DWTR from various sources to support commercial scale sediment capping projects.....128
5.4. Short Course / Community meeting.....129
5.5. High quality video summary.....130
5.6. Publication list.....130

6. Future research avenues 131

7. Cited references 132

8. Appendix….......140

LIST OF FIGURES

Figures……..……Pages

Figure 1. Flow diagram of the drinking water treatment process showing the coagulation step which produces the waste substrates (DWTR) used in this study (Adapted from USEPA, 1996, 2011)…….....**24**

Figure 2. Research technical approach showing the four main tasks of the project, designed to meet the specific objectives of the research program…….....**25**

Figure 3. Geographical distribution of the DWTP from which the DWTR samples were obtained. The description of the different samples is given in Table 1…….……..…**26**

Figure 4. **(A).** Picture of example DWTR containers received. **(B)** and **(C)**. Example dewatered DWTR samples……...……..…..**26**

Figure 5. Conceptual sketch of the concentration ranges of contaminants delineated by sediment quality guidelines (SQGs) and the potential for observing adverse effects *(Adapted from MacDonald et al., 1996)*…….....……**30**

Figure 6: Flow chart showing the four steps of the developed screening method to determine the suitability of DWTR for use as fill materials, or as sediment capping substrate in this specific case…….……...…**33**

Figure 7: Schematic diagram of fixed bed column sorption system showing from left to right the metal containing influent solution followed by a peristaltic pump, the acrylic column packed with quartz sand (top & bottom) and DWTR (center); and a fraction collector (*Adapted from Huang et al., 2022*)……...….**36**

Figure 8. Gust Chamber setup A): laptop for parameter setting; B) central controller; C) gust chamber cores; D) pump; E) carboy for containing water; F) turbidimeter for effluent water's turbidity monitor……...…….....….**37**

Figure 9. Schematic illustration of metal-contaminated sediment cores used in gust Chambers.……**39**

Figure 10. Experimental setup used to determine the depth profiles of dissolved metal concentrations in pore and overlying waters using metal-contaminated sediment cores equilibrated in gust chambers at a fixed τ of 0.05 Pa for 7 days. Uncapped sediments (left) and substrate capped sediments (right)……...….**40**

Figure 11. Concentrations of elements extracted from 15 drinking water treatment residuals where only elements with available guideline values are presented. The absence of bars corresponds to values below the analytical detection……..…..….**42**

Figure 12. Total metal concentrations in the DWTR samples. The red horizontal lines are the PEL values while the green lines correspond to TEL values. DWTR with red bars for any of the metals should be considered not suitable for introduction to U.S. waters……...…..….**43**

Figure 13. Saltwater elutriation results obtained from the analysis of 4 drinking water treatment residual samples (OR, WY, NC, and a mixture of OR+NC in a 9 to 1 mass ratio). Horizontal dotted lines represent the EPA's ambient water quality criteria for each of the elements…….…..….**45**

Figure 14. Concentrations of total metals WY, OR, and NC DWTR. The red dotted horizontal lines are the consensus-based probable effect concentrations (PEC) and the solid green horizontal lines are the threshold effect concentrations (TEC). Plotted values are averages (n = 3), and bars are

standard deviations. The absence of bars corresponds to metal concentrations are below the analytical detection limit (DL)……..……**46**

Figure 15. Dissolved total metal concentrations in elutriates from OR, WY, NC, and OR+NC samples. Horizontal dashed red lines are shown only for elements with available EPA's ambient water quality criteria……..……**48**

Figure 16. 10-day survival test using the mysid shrimp *Americamysis Bahia*. Results of the test are acceptable because survival rate numbers from the control are ≥ 90%, and no statistically significant difference was observed between the control sediment and any of the DWTR samples……....……**49**

Figure 17. Results of the 28-day growth tests for *N. arenaceodentata*. All DWTR samples passed the chronic toxicity test……..……**49**

Figure 18. The results of *10-day* survival **(a)** and growth **(b)** tests using the midge *Chironomus tentans*. The stars indicate statistically significant differences between the control sediments and DWTR samples……..…**51**

Figure 19. Results of the 65-day life cycle test using the midge *Chironomus tentans*. (a) Survival, (b) adult emergence, (c) egg case production, and (d) number of eggs produced per female……**53**

Figure 20. Results of the *10-day* survival (a) and growth (b) tests using the amphipod *Hyalella azteca*……..…**54**

Figure 21. The results of 28-day survival **(a)** and growth **(b)** tests using *Hyalella azteca*. Asterisks indicate statistically significant differences between the control and treatment samples..**55**

Figure 22. Thermogravimetric results for DWTR samples. Mass of the DWTR, shown as the percentage of the mass relative to the mass at the end of the initial isothermal step, is compared to temperature…….....…**56**

Figure 23. Peak areas as a function of temperature for *m/z* 18 (water, left subplot) and 44 (carbon dioxide, right subplot) from the mass spectra collected from the TGA-MS. Note the difference in y-axis scales for these two subplots: carbon dioxide reaches much larger peak areas (nearly 80,000 $counts\ per\ min$), specifically above 600°C in lime-based DWTRs. The inset in the bottom subplot zooms in to provide detail at lower temperatures and in non-lime based DWTRs…….....……**57**

Figure 24. Peak forests showing the area corresponding to each ion across the temperature range for TGA-MS analysis. Results are shown for $50 < m/z < 150$ during the rising temperature portion of the experiment. Note the differences in the scales for the peak areas recorded……....……**58**

Figure 25. BET surface area results for the six DWTR samples. Calculated surface areas, along with the uncertainties of the fit to the BET model, are displayed in the left subplot. Pore volume distribution for DWTRs as a function of pore diameter are shown in the right subplot. Results were calculated using desorption data with the BJH method……..……**59**

Figure 26. CHNS elemental analysis results for DWTR samples. Subplot A shows the mass fractions of H, S, N, and acid-volatile and non-acid-volatile carbon in terms of the percent mass of the DWTR. Subplot B shows the moles of N and S per kg DWTR……**60**

Figure 27. X-ray fluorescence spectra for drinking water treatment residual samples. Spectra were

collected at 20 keV and 10 μA with no filter and are not normalized. The left subplot shows the full spectrum for each sample; peaks are immediately discernible down to the Al K_α fluorescence line and up to the Fe K_α fluorescence line. The top right subplot focuses on the Mn K_α fluorescence line. MN and TN have distinct, well-defined peaks here. Signals for OR and WY are also slightly elevated, though the fluorescence here overlaps with what is detected for the high Fe K_α peaks. Finally, the bottom right subplot focuses on Cu K_α and Zn K_α emission lines. Peaks here are poorly defined and very low intensity across all DWTR samples……..…….…**61**

Figure 28. Synchrotron-source X-ray diffraction patterns for the drinking water treatment residual samples, along with identified crystalline mineral phases. Peaks for calcite, quartz, albite, microcline, and dolomite were identified using JADE, as were the clay peaks attributable to either illite or smectite. Note that the intensities are not on the same scales; for instance, NC and WY samples show some especially intense diffraction patterns, while the UT sample has weak diffraction patterns, indicating a poorly crystalline sample……..…**62**

Figure 29. Synchrotron-source X-ray diffraction patterns for the other DWTR samples not studied in detail. Data were collected using the same methodology as for the other six samples. The same phases identified in the main DWTR samples are identified in these other samples in varying combinations, which include clay (illite and/or smectite), feldspar (albite and microcline), carbonate minerals (calcite and dolomite), and quartz. Again, not present in these samples are crystalline iron oxides or aluminum oxides……..…**63**

Figure 30. Fe K-edge first-derivative XANES results for DWTRs. On the left, the spectra for the DWTRs and the standards employed in linear combination fitting (LCF) are shown. The merged spectra for the DWTRs are shown with a solid line, while the range in values from each scan is shown with a lighter shaded area. For most samples, the shaded region is too small to be seen (it may be observed near 7140 eV in the TN spectrum). The fit results using the standard spectra are shown with the dotted lines. On the right, the LCF results are shown as a bar chart, and χ^2 goodness- of-fit values are listed at the base of each bar……**64**

Figure 31. Principal components analysis of Fe K-edge first-derivative XANES spectra for drinking water treatment residuals. The left subplot visualizes the principal components. First, the mean first-derivative XANES spectrum calculated from all the DWTR sample spectra is plotted. Principal components are calculated based on the distance of the samples from the mean across each spectrum. The components plotted in the left subplot are therefore added or subtracted from the mean spectrum to approximately recreate the sample spectra. PC1 and PC2 are scaled based on the variance they account for within the Fe K-edge DWTR spectra (85% and 12%, respectively). The right subplot projects the DWTR samples along with selected standards on the first two principal components. Here, most of the variance is driven by the MN sample. This is reflected in the shape of PC1, which shows the shoulder and small oscillations in the first-derivative XANES that distinguished MN from the other samples. In the projection of standards, common ferric (or mixed-valence iron) minerals do not recreate these features. However, several spinel ferrite minerals, including maghemite, manganese ferrite (jacobsite), copper ferrite (cuprospinel), and magnesium ferrite (magnesioferrite) do……..…….……**65**

Figure 32. Target transformations of first-derivative Fe K-edge XANES standard spectra based on principal components calculated from DWTRs. "LBL" (Fakra, 2010) and "NIMS"

(Masashi et al., 2021, Tanifuji et al., 2019) identify databases from which certain spectra were acquired……..……**66**

Figure 33. Mn K-edge first-derivative XANES results for DWTRs. On the left, the linear combination fitting (LCF) results are shown with χ^2 goodness-of-fit values at the bottom of each bar. The right subplot shows the spectra for the DWTR samples, and the standards employed in LCF. As in Figure 5.10, the fit results using the standard spectra are shown with the dotted lines……**68**

Figure 34. Mn K-edge first-derivative XANES results for DWTR-TN over time. Rhodochrosite ($MnCO_3$) and hausmannite (Mn_3O_4) standards are shown for comparison. Initial scans show that the speciation of manganese in the TN sample is dominated by rhodochrosite. The spectrum increasingly matches that of hausmannite over time, suggesting the manganese in TN has become oxidized……**69**

Figure 35. Mn K-edge first-derivative XANES results for DWTR-UT over time. No changes in speciation are apparent……**69**

Figure 36. Sorption results for copper and lead to DWTRs in SEM-EDS reactors. The left subplot shows the removal of copper relative to the initial concentration, while the right subplot shows the same for lead. The loss of the metals in control reactors with no DWTRs is also shown……..……**70**

Figure 37. SEM-EDS data for DWTRs with sorbed copper. Here, the DWTRs with a lime additive (MN, NC, and TN) are shown. On the left are the SEM micrographs, taken with backscatter detectors. On the right are copper EDS data; despite heterogeneity in each of these samples, there is no clear distinction in the distribution of copper…….……**71**

Figure 38. SEM-EDS data for DWTR samples UT and WY with sorbed copper. As in Figure 36, SEM micrographs are on the left and copper EDS data are on the right; as before, copper is broadly distributed……..……**71**

Figure 39. SEM-EDS data for copper sorbed to DWTR-OR. On the top left, the backscatter SEM image of a particle from the sample is shown. EDS data for Fe, C, and Cu are also shown. Since the EDS samples are placed on carbon tape, there is a strong signal for carbon surrounding the particle. However, on the right side of the particle, C is concentrated with Fe; it is also in this location where Cu is most concentrated……**72**

Figure 40. SEM-EDS data for DWTR-MN with sorbed lead. On the left is the micrograph, captured with the backscatter detectors. Areas where EDS spectra were taken are boxed in cyan and magenta and plotted at the bottom of the figure. The center and right subplots show EDS elemental mapping of iron and lead, respectively. Iron shows strong enrichment in two small areas of the sample and lead also seems to slightly concentrate in those areas. The EDS spectra show that the area with higher iron content in cyan also has a stronger Pb signal compared to the other region of the sample…….……**72**

Figure 41. SEM-EDS data for DWTR-NC with sorbed lead. The SEM micrograph is shown on the left, with two areas selected for further EDS analysis shown in the cyan and magenta boxes, which are plotted at the bottom of the figure. Iron and lead elemental maps from EDS are shown in the center and right subplots. Like DWTR-MN, lead seems to concentrate slightly in areas with higher iron content……..……**73**

Figure 42. SEM-EDS data for DWTR-TN with sorbed lead. The SEM micrograph is shown on the left, with boxes around the areas used to generate the EDS spectra shown at the bottom. The center and right subplots show manganese and lead elemental maps from EDS, respectively. Here, a rather strong correlation between manganese and lead is apparent……..……**73**

Figure 43. SEM-EDS data for DWTR-UT with sorbed lead. The SEM micrograph is shown at the top left subplot. Al, Fe, and C elemental maps from EDS are shown, and the bottom subplot shows EDS spectra in cyan, magenta, and yellow corresponding with the same-colored boxes overlaid on the SEM micrograph. Due to high enrichment of S in this sample, elemental mapping by EDS for Pb was not feasible. No strong lead associations are observed by targeting areas rich in carbon (spectrum 1), aluminum (spectrum 2), and iron (spectrum 3) on the DWTR……**74**

Figure 44. SEM-EDS data for DWTR-WY with sorbed lead. The SEM micrograph is plotted at the top left, and EDS elemental maps for Fe, C, and Pb are shown in the top right, center left, and center right subplots, respectively. The bottom plot shows the EDS spectra for the areas boxed in the SEM micrograph. Here, there is no apparent correlation between iron and lead. In areas of DWTR-WY with elevated carbon content, as in Spectra 1 and 2, elevated lead content is also observed……**74**

Figure 45. SEM-EDS data for DWTR-OR with sorbed lead. The SEM micrograph is on the left, and EDS elemental maps for iron and lead are plotted in the center and right subplots. An EDS spectrum for a particularly iron-rich region (Spectrum 1) is contrasted with an area low in iron (Spectrum 2). Here, lead content correlates with iron content……**75**

Figure 46. SEM-EDS data for another particle of DWTR-OR with sorbed lead. The SEM micrograph is shown at the top left, and EDS elemental maps for iron, carbon, and lead are also shown. The bottom subplot shows the EDS spectra for the areas of interest boxed in the SEM micrograph. In contrast with the other OR sample (**Figure 45**), lead does not correlate with iron and instead seems to correlate with carbon content……**75**

Figure 47. Cluster analysis of selected Cu K-edge XAS data. The left subplot clusters based on the EXAFS data for copper sorbed to DWTRs, with standards for copper sorption or copper minerals included. The right subplot clusters the same samples based on their first-derivative XANES data. DWTR samples are identified by their state of origin and their final measured pH……..……**76**

Figure 48. EXAFS fitting results for copper sorbed to DWTRs in MOPS reactors. UT and TN samples are only fit in the first shell; others are fit with both Cu-O and Cu-O-O paths (shown in the red dashed line) or Cu-Al and Cu-O paths (shown in the thin gray line), with parameters shown in Table 7.3. The left subplot shows the EXAFS and fit results in k-space, the center subplot shows the Fourier transform magnitude for each fit and sample, while the right subplot shows the real component of the Fourier transforms of data and fits……..……**78**

Figure 49. EXAFS fitting results for copper sorbed to DWTRs in HEPES reactors. UT and TN samples are only fit in the first shell; others are fit with both Cu-O and Cu-O-O paths (shown in the red dashed line) or Cu- Al and Cu-O paths (shown in the thin gray line). The left subplot shows the EXAFS and fit results in k-space, the center subplot shows the Fourier transform magnitude for each fit and sample, while the right subplot shows the real

component of the Fourier transforms of data and fits……..……**80**

Figure 50. Principal component analysis (PCA) of first-derivative Cu K- edge XANES data for copper sorbed to DWTRs. The left subplot shows the fraction of the variance explained by the principal components. The middle subplot projects the samples onto the two principal components. Finally, the right subplot visualizes the components. The mean of all the spectra is shown in black, and the components are added to or subtracted from the mean……**80**

Figure 51. Target transformations of standard materials at the Cu K edge based on PCA of spectra from copper sorbed to DWTRs. "NIMS" standards are sourced from the Materials Data Repository (Masashi et al., 2021)……**81**

Figure 52. Cu K-edge first-derivative XANES for copper sorbed to DWTR-MN. Selected standards are included for comparison; "NIMS" standards are sourced from the Materials Data Repository (Masashi et al., 2021) ……..……**82**

Figure 53. Linear combination fitting of first-derivative XANES data for copper-DWTR reactors in MOPS buffer. Standards selected for fitting are plotted, along with the data and fit for each DWTR sample. The weight of each standard in the fit is shown in the right subplot……..……**82**

Figure 54. EXAFS for lead sorbed to DWTRs. FEFF fitting results are shown with the dotted lines, and windows for the Fourier transform and the FEFF fit are shown in the plots in k- and R-space, respectively……...……**83**

Figure 55. XANES spectra for lead sorbed to DWTRs. The left subplot shows the non-normalized fluorescence μ(E) for the samples. The right subplot shows normalized data; all samples are plotted to overlap in this subplot. Several lead standards are included at the bottom of the right subplot for comparison……..……**85**

Figure 56. Effect of pH on the zeta potential of the four DWTR samples used in these batch sorption studies. Note the stability of the zeta potential of Al-DWTR-WY with a net surface charge of about zero across the tested range of pH values……..……**88**

Figure 57: Strontium sorption by the four different DWTR samples at pH 8.0. **(a)** Sorption by Al-DWTR-WY. **(b)** Sorption by (Al+Fe)-DWTR-OR. **(c)** Sorption by Fe-DWTR-AR. **(d)** Sorption on Ca-DWTR-NC. The experimental data were best fit by the Langmuir model for the first 3 DWTR samples. For Ca-DWTR-NC, a modified Langmuir was needed to fit the experimental data……..……**89**

Figure 58: Lead sorption isotherms by four different DWTR samples. **(a)** Sorption by Al-DWTR-WY. **(b)** Sorption by (Al+Fe)-DWTR-OR. **(c)** Sorption by Fe-DWTR-AR. **(d)** Sorption by Ca-DWTR-NC. For the first 3 DWTRs, the experimental data were best fitted by the Langmuir model. For Ca-DWTR, the Freundlich model fitted the experimental better……...……**90**

Figure 59: Thallium sorption by the four different DWTR samples. **(a)** Sorption by Al-DWTR-WY. **(b)** Sorption by (Al+Fe)-DWTR-OR. **(c)** Sorption by Fe-DWTR-AR. **(d)** Sorption by Ca-DWTR-NC. Overall, the Langmuir model resulted in the best fit of the experimental data……...**91**

Figure 60. Sorption kinetics of strontium, lead, and thallium by: **(a)** Al-DWTR-WY, **(b)** (Al+Fe)-DWTR-OR, **(c)** Fe-DWTR-AR, and **(d)** Ca-DWTR-NC. Points are experimental data and lines are model predictions. Note the differences in the range of values for sorbed metals on the Y-axes……..……**94**

Figure 61. Pseudo-second order kinetics of strontium (Sr) sorption by DWTR samples. Al-DWTR-WY, Al/Fe-DWTR-OR, Fe-DWTR-AR, and Ca-DWTR-NC……**94**

Figure 62. Pseudo-second order kinetics of lead (Pb) sorption by DWTR samples. Al-DWTR-WY, Al/Fe-DWTR-OR, Fe-DWTR-AR, and Ca-DWTR-NC……....**95**

Figure 63. Pseudo-second order kinetics of thallium (Tl) sorption by DWTR samples. Al-DWTR-WY, Al/Fe-DWTR-OR, Fe-DWTR-AR, and Ca-DWTR-NC……..……..**95**

Figure 64. Intra-particle diffusion model for kinetic sorption of Sr by Al-DWTR-WY, Al/Fe-DWTR-OR, Fe-DWTR-AR, and Ca-DWTR-NC……**97**

Figure 65. Intra-particle diffusion model for kinetic sorption of Pb by Al-DWTR-WY, Al/Fe-DWTR-OR, Fe-DWTR-AR, and Ca-DWTR-NC……**97**

Figure 66. Intra-particle diffusion model for kinetic sorption of Tl by Al-DWTR-WY, Al/Fe-DWTR-OR, Fe-DWTR-AR, and Ca-DWTR-NC……...……**98**

Figure 67. Langmuir sorption model fitting results for DWTR-Hg reactors, presented graphically. The left subplot shows the data in terms of the final concentration of Hg in solution (C_e) against the amount of Hg sorbed per unit mass of the DWTRs (q_e). The center subplot linearizes the model by comparing q_e/C_e with q_e, and the right subplot offers a closer look at the data following the boundaries established by the dotted gray line on the center subplot……..……**99**

Figure 68. Comparisons of Langmuir sorption model findings against DWTR characteristics. The left subplot compares the mercury sorption capacity (Q_0) against the thermogravimetric mass loss for DWTRs from 200-430°C, an indicator of the amount of organic matter. The center sub- plot compares Q_0 with the non-acid-volatile carbon content of DWTRs, which will consist of organic matter and, for UT and WY samples, activated carbon. Finally, the right subplot compares the non-acid volatile carbon content of DWTRs with the Langmuir sorption affinity (b)……..……**100**

Figure 69. The relationship between the Langmuir sorption capacity for mercury to DWTR samples (Q_0) and the iron and aluminum content of the DWTRs (Zhou et al., 2021a). Iron (the left subplot) does not show a strong relationship with Q_0. The aluminum content (center subplot) and the combined aluminum and iron contend (right subplot) do correlate well with the calculated sorption capacities, but these factors do not account for the high sorption capacity of the MN sample……..……**100**

Figure 70. Principal component analysis (PCA) of Hg L3-edge XANES spectra for mercury sorbed to DWTR samples. The top left subplot shows the variance among samples accounted for by the principal components. The top right subplot visualizes the components, which are shown as the difference from the mean spectrum. The remaining subplots project the DWTR samples on the first two principal components, showing the impact of the DWTR sample, the buffer used (MES, MOPS, and HEPES for 6, 7, and 8, respectively), the use of lime as an additive, and the maximum mass loading of mercury to the DWTRs……..……**101**

Figure 71. Target transformations of standard spectra based on the PCA of DWTR data. Standards best reconstructed are at the bottom right, while the worst-reconstructed standard spectra are in the top left……..…**102**

Figure 72. Linear combination fitting (LCF) results of Hg L3-edge XANES data. Data were fit from a range of 20 eV below to 70 eV above the edge energy using flattened, normalized XANES from standards of mercury sorbed to kaolinite (Hg-O) and complexed with penicillamine (Hg-S), forcing the sum to equal 1. The bars correspond with the percent weights on the left y-axis, while the X markers give the value of the χ^2 goodness-of-fit metric shown on the right y-axis……..……**103**

Figure 73. Hg L3-edge EXAFS for all spectra collected for mercury sorbed to DWTRs. The K-window for FEFF fitting is shown in the light green at the top of the plot. Spectra are separated and color-coded based on the DWTR sample used; the pattern of the lines corresponds with the buffer used in the reactor, while the opacity of the lines signifies the maximum mass loading of mercury to the DWTRs. FEFF fitting results, which are listed in Table 13 are shown in the thin gray line overlayed on each of the spectra. Finally, at the bottom of the plot, simulated spectra for Hg-O and Hg-S single-scattering paths are shown……**104**

Figure 74. FEFF fitting of α-HgS EXAFS data to extract the S_0^2 value used for the FEFF fits of DWTR samples. Here, an S_0^2 value of 1.00±0.16 is found, so the value is fixed at 1 for all samples……..……**104**

Figure 75. Breakthrough profiles from influents containing Pb, Cd, Cu in columns packed with either a non-reactive (sand referred to as blank) or reactive (i.e., DWTR-OR, DWTR-WY, apatite) substrates, and compared to the breakthrough of bromide used as tracer (blue triangles). Experimental data (points) were fitted by the Yan's model (lines)…….……**107**

Figure 76. Breakthrough profiles from influents containing Pb, Cd, Cu in columns packed with either a non-reactive (sand referred to as blank) or reactive (i.e., DWTR-OR, DWTR-WY, apatite) substrates, and compared to the breakthrough of bromide used as tracer (blue triangles). Experimental data (points) were fitted by the Yan's model (lines)……..……**109**

Figure 77. Resuspension of particles to the overlying waters from sandy metal-contaminated sediments as a function of increasing hydrodynamic shear stress (τ) for sediment cores without (red) and with (green) a DWTR cap layer. The major characteristics of this sediment show the prevalence of sand particles which require very strong disturbance to be suspended in the overlying water. The presence of the cap layer stops the resuspension of sediment particles even at a shear stress of 0.45 Pa. *TSS*: Total suspended solids……..……**110**

Figure 78. **(a)** - Resuspension of particles to the overlying waters from metal-contaminated sediments collected from NAS near Pensacola Florida, plotted as a function of increasing hydrodynamic shear stress (τ) for sediment cores without (control) and with (treatment) a DWTR cap layer. TSS: Total suspended solids. **(b)** – Pictures of filters resulting from the filtration of water samples collected as a function of increasing τ values ranging from 0.01 to 0.45 Pa. This sediment is dominated by fine particles and well resuspended with increasing hydrologic shear stress (red line). However, capping with DWTR reduced the resuspension of metal-contaminated particles across the full range of applied shear stress (green line)……**111**

Figure 79. Concentrations of metals (Cu, Cd, Cr, Pb, and Zn) in the aqueous phase of the gust chambers containing site-sediments without (control) or with a DWTR cap layer and as a function of increasing hydrologic shear stress. In contrast to the metal-spiked sediments, all measured total metal concentrations in water in contact with site-sediments were in the ppb range and the actual values shown on the graph. Note the differences in the range of Y-axis values……...…**113**

Figure 80. Trends of total lead (A), cadmium (B), zinc (Zn), and copper (Cu) concentrations in sediment cores overlying waters as a function of increasing hydrologic shear stress (τ). Red lines represent metal concentrations in water overlying non-capped sediments. The blue lines correspond to metal concentrations in waters overlying sediment cores capped with sand, and the green lines are for metal concentrations in waters overlying sediments capped with an active substrate, either DWTR (WY or OR) or apatite……**114**

Figure 81. Kinetics of metal release from intertidal sediments as a function time at a fixed shear stress of 0.05 Pa over 7 days. Sediments capped with DWTR are represented by green circles (treatment), and the non-capped sediments by red circles……**116**

Figure 82. Kinetics of metal release from the freshwater sandy sediments as a function time at a fixed shear stress of 0.05 Pa over 10 days. Sediments capped with DWTR are represented by green circles (treatment), and the non-capped sediments by red circles. Metal concentrations measured in the aqueous phase of the DWTR-capped sediment core (green circles) ranged from 2.3 to 59 ppb for Cu and Cd, and from 2.1 to 59 ppb and 51 to 1,1196 ppb for Pb and Zn, respectively……...…**117**

Figure 83. DGT depth profiles of lead (Pb), cadmium (Cd), Zinc (Zn), copper (Cu), iron (Fe), and manganese (Mn) in a **non-capped sediment core** after an initial equilibration in a gust chamber for 7 days. After seven days, the DGT sampler was inserted into the sediments and left in place for 24 hours. The determined total dissolved metal concentrations (X-axis) are plotted as a function of depth (Y-axis), including values from the overlying water……**119**

Figure 84. DGT depth profiles of lead (Pb), cadmium (Cd), Zinc (Zn), and copper (Cu) in **sand** capped sediment core after an initial equilibration in a gust chamber for 7 days. After seven days, the DGT sampler was inserted into the sediments and left in place for 24 hours. The determined total dissolved metal concentrations (X-axis) are plotted as a function of depth (Y-axis), including values from the overlying water……**120**

Figure 85. DGT depth profiles of lead (Pb), cadmium (Cd), Zinc (Zn), and copper (Cu) in **apatite** capped sediment core after an initial equilibration in a gust chamber for 7 days. After seven days, the DGT sampler was inserted into the sediments and left in place for 24 hours. The determined total dissolved metal concentrations (X-axis) are plotted as a function of depth (Y-axis), including values from the overlying water……**121**

Figure 86. DGT depth profiles of lead (Pb), cadmium (Cd), Zinc (Zn), and copper (Cu) in **DWTR-OR** capped sediment core after an initial equilibration in a gust chamber for 7 days. After seven days, the DGT sampler was inserted into the sediments and left in place for 24 hours. The determined total dissolved metal concentrations (X-axis) are plotted as a function of depth (Y-axis), including values from the overlying water……**122**

Figure 87. DGT depth profiles of lead (Pb), cadmium (Cd), Zinc (Zn), copper (Cu), iron (Fe), and manganese (Mn) in **DWTR-WY-capped** sediment core after an initial equilibration in a gust chamber for 7 days. After seven days, the DGT sampler was inserted into the sediments and left

in place for 24 hours. The determined total dissolved metal concentrations (X-axis) are plotted as a function of depth (Y-axis), including values from the overlying water……..……**123**

Figure 88. DGT profiles of dissolved concentrations of Cd, Cu, Cr, Pb, and Zn in the pore and overlying waters of non-capped (top panel) and DWTR-OR capped intertidal sediment (bottom panel). DGT samplers were inserted into the sediment after a water-sediment equilibration period of 7 days at a fixed hydrologic shear stress of 0.05 Pa. The DGT samplers were retrieved after a 24h contact period and sectioned every 0.5 cm and processed for metal analysis……..……**125**

Figure 89. Survival of Fathead minnow juveniles in a 96h bioassay using water overlying metal-contaminated sediments in the absence and presence of capping substrates. Sand is used as inert substrate while apatite, DWTR-OR and DWTR-WY are reactive substrates……..……**126**

Figure 90. Total metal concentrations in DWTR samples obtained from Oregon and Wyoming over a period of two years, 2019 and 2020……..……**128**

LIST OF TABLES

Tables…….. Pages

Table 1. Drinking water treatment residual samples collected from water-treatment plants across the United States. Total concentrations of Fe, Al, and Ca are averages from triplicate analyses ±1 standard deviation. From the main chemical additives, these DWTR samples are dominated by a combination of Al and Fe or by either Al or Ca ……..…….…….……**27**

Table 2. Criteria maximum concentrations (CMC) of metals determined in elutriates of DWTR……..……**28**

Table 3. Sediment quality guidelines (SQG) based on total metal concentrations in freshwater and marine sediments. Concentrations are expressed in mg/kg (or ppm)……**31**

Table 4. Total concentrations of Cd, Cu, Pb, Cr and Zn in sediments used in this study, and proportions of operationally defined fractions used to assess the potential of sediments to release metals to pore waters. Using a liquid-solid ratio of 20:1 (*v/m*), F1 is extracted with DI-water and F2 is extracted using a 1.0 M CH_3COONa solution, pH = 8.2. Samples were analyzed by ICP-MS……..……**39**

Table 5. Calculated dilution factors (D) based on leached Cu concentrations and the criterion continuous concentration (CCC) of 3.1 µg/L, and assuming non-detectable dissolved Cu in the water of the targeted site……**44**

Table 6. Thermogravimetric analysis results for DWTR samples, showing the percentage mass loss over specified temperature ranges. Mass loss from (1.) 200-430˚C may be attributed to organic matter decomposition, (2.) 430-600˚C inorganic material decomposition, and (3.) 600-825˚C carbonate mineral decomposition……..……**56**

Table 7. FEFF fitting results for copper sorbed to DWTR samples in MOPS buffer. S_0^2 was fixed at 0.75 for each fit. Scattering paths; their calculated coordination numbers, path distances, σ^2, and ΔE values; and R-factor and reduced-χ^2 goodness-of-fit-metrics are shown……..……**77**

Table 8. DWTR reactor Cu K-edge EXAFS findings for HEPES reactors. S_0^2 was fixed at 0.75, and for samples fit beyond the first shell (MN, NC, OR, and WY), the third scattering path was fixed at a σ^2 value of 0.01. For these reactors, second-shell contributions to EXAFS are modeled separately with Al and O, and the results from both fits are reported here……..……**79**

Table 9. FEFF fitting results for lead sorbed to DWTR samples at low (1 mg Pb/g DWTR) and high (5 mg Pb/g DWTR) mass loading values. For all fits, the amplitude reduction factor S_0^2 was fixed at 0.90, while all other variables were fit……**84**

Table 10. Relevant physicochemical characteristics of the four DWTR used as sorbents in batch sorption studies……**87**

Table 11. Parameters for the fitted Langmuir model (***k*** and $\boldsymbol{Q_0}$) and the modified Langmuir model (*****) using experimental data for sorption of Sr, Pb, and Tl by DWTR samples.……..……**92**

Table 12. Fitted pseudo-second-order kinetic parameters for Sr, Pb, and Tl sorption on DWTRs at pH 8.0 and initial concentrations of 20, 100, and 10 mg/L, respectively……..……**96**

Table 13. Langmuir sorption model fitting results. Maximum sorption capacity (Q_0) and sorption affinity (b) are presented……..…**99**

Table 14. FEFF fitting results for EXAFS of mercury sorbed to DWTR samples. For each fit, $S_0^2$was fixed at 1.0, ΔE_0 was fixed at 0.0, and σ^2 was fixed at 0.006……**105**

Table 15. Dynamic maximum sorption capacities (Q_0) derived from the Yan's model for Apatite, DWTR-OR, and DWTR-WY used as sorbents for Pb, Cd, and Cu……..……**108**

Table 16. Annual production rates of DWTR obtained from 5 DWTP……**128**

ACRONYM LIST

Al+Fe-DWTR: Aluminum and Iron-based Drinking Water Treatment Residuals
Al-DWTR: Aluminum-based Drinking Water Treatment Residuals
APS: Advanced Photon Source
AR: Arkansas
AWQC: Aquatic Life Ambient Water Quality Criteria
AZ: Arizona
BET: Brunauer-Emmett-Teller
Ca: Calcium
Ca-DWTR: Calcium-based Drinking Water Treatment Residuals
CCC: Criterion Continuous Concentration
Cd: Cadmium
CHNS: Carbon, Hydrogen, Nitrogen, and Sulfur
CMC: Criterion Maximum Concentration
Cr: Chromium
Cu: Copper
CWA: Clean Water Act
DGT: Diffusive Gradients in Thin Films
DOC: Dissolved Organic Carbon
DOM: Dissolved Organic Matter
DWTP: Drinking Water Treatment Plants
DWTR: Drinking Water Treatment Residuals
Fe-DWTR: Iron-based Drinking Water Treatment Residuals
FHM: Fathead Minnows
FL: Florida
HEPES: 4-(2-hydroxyethyl)-1-piperazineethanesulfonic acid
ICP-MS: Inductively Coupled Plasma Mass Spectrometry
IL: Illinois
KS: Kansas
LCF: Linear Combination Fitting
LOI: Loss On Ignition
ME: Maine
MN: Minnesota
MOPS: 3-(N-morpholino)-propanesulfonic acid
NC: North Carolina
OR: Oregon
PA: Pennsylvania
Pb: Lead
PCA: Principal Component Analysis
PEC: Probable Effect Concentrations
PEL: Probable Effect Level
SEM-EDS: Scanning Electron Microscopy - Energy Dispersive Spectroscopy
SQGs: Sediment Quality Guidelines
Sr: Strontium
SSA: Specific Surface Area

TCLP: Toxicity Characteristics Leaching Procedure
TEC: Threshold Effect Concentrations
TEL: Threshold Effect Level
TGA-MS: Thermogravimetric Analysis - Mass Spectrometry
Tl: Thallium
TN: Tennessee
TX: Texas
USEPA: United States Environmental Protection Agency
UT: Utah
WQC: Water Quality Criteria
WY: Wyoming
XANES: X-Ray Absorption Near Edge Spectra
XAS: X-Ray Absorption Spectroscopy
XRD: X-Ray Diffraction
XRF: X-Ray Fluorescence
Zn: Zinc

EXECUTIVE SUMMARY

Drinking Water Treatment Residuals as Material for in-situ Capping of Metal Contaminated Sediments

Introduction.

Research into the remediation of both contaminated sediments and soils has been ongoing for decades, leading to the development and testing of various remedial techniques under both laboratory and field conditions. For large-scale field remediation of contaminated sediments, conventional methods include in-place strategies such as in situ capping and relocation actions like landfill disposal and dumping at sea (Akil et al., 2015). While in-place remediation holds significant potential for improvement, the latter practices are simply not sustainable.

In the realm of in-situ remediation using active capping substrates many studies have identified sorbents with high sorption capacities, particularly when targeting metals in contaminated environments. Substrates with large specific surface areas (SSA) containing sulfur (S), nitrogen (N), and oxygen (O) as electron donor atoms are deemed ideal sorbents (Kim et al., 2000; Wang and Chen, 2009). Moreover, the zeta potential, an indicator of particles' surface charge property, provides strong insights into binding mechanisms driven by electrostatic forces (Makavipour and Pashley, 2015; Ghorbel-Abid et al., 2016; Zhang et al., 2016). While such knowledge can inform laboratory production/tailoring of sorbents, manufacturing approaches significantly inflate the cost of the remediation process, making them economically less attractive for large-scale remediation efforts.

Consequently, the remediation of contaminated sediments on a large scale remains one of the most challenging issues in environmental restoration. Cost-effective and efficient remedial approaches that avoid adverse effects on treated systems and human health are urgently needed. Hence, remediation research is progressively shifting towards the use of readily available, abundant, efficient, and cost-effective sorbents. This shift introduces the concept of beneficial use of waste materials, especially when such waste materials demonstrate potential in mitigating the adverse biological impacts caused by contaminated sediments and soils.

In this study, we investigated the efficiency of a heterogeneous and readily available waste material, known as drinking water treatment residuals (DWTR), as an effective sorbent for in situ remediation of metal-contaminated sediments. The US produces millions of tons of DWTR each year (Gibbons and Ganon, 2011) from all the drinking water treatment plants (DWTP) operating nationwide. DWTR's ability to adsorb metal cations, oxyanion-forming elements, and organics has been demonstrated in various environmental applications, ranging from small-scale laboratory to field-scale settings (Ippolito et al., 2011; Castaldi et al., 2015; Punamiya et al., 2015; Xu et al., 2015; Quinones et al., 2016; Silvetti et al., 2015; Soleimanifar et al., 2016; Ocinski et al., 2016; Wang et al., 2016). However, the literature lacks references on the use of DWTR as potential capping material for in-situ treatment of metal-contaminated sediments. Given the peculiar physicochemical characteristics of DWTR, one way to add value to these byproducts of drinking water treatment processes is to capitalize on their high sorption capacities for several pollutants, large specific surface area (SSA), and the presence of electron donor atoms, which are ideal for the sequestration of metal cations

Objectives.

This research was developed with the aim of adding value to a readily available waste material, DWTR, by exploring the mechanisms through which different types of metals can be immobilized on this highly heterogeneous sorbent in response to changing key water/sediment

parameters. Additionally, we sought to investigate the potential limitations associated with the use of DWTR as capping material for metal-contaminated sediments.

We hypothesized: first, that metal cations would form highly stable surface complexes with DWTR through a combination of different sorption mechanisms; and second, that if used as an in-situ capping substrate, DWTR would significantly reduce metal effluxes from contaminated sediments towards the water column decreasing therefore their bioavailability and toxicity.

The specific objectives of this study were as follows:

(i) To determine the physicochemical and toxicity characteristics of a wide variety of DWTR and develop a screening approach for identifying DWTR suitable for introduction into US aquatic systems.

(ii) To conduct laboratory studies to assess the efficacy of DWTR in immobilizing metals from aqueous solutions and controlling the release of metals from contaminated sediments into the overlying water, with a focus on how these processes are affected by changes in key water parameters.

(iii) To investigate the effects of extreme environmental changes on the ability of DWTR to sorb and immobilize metals when used as in-situ capping material for contaminated sediments.

Technical Approach.

Laboratory studies were conducted to comprehensively evaluate the physicochemical and toxicological characteristics of DWTR. Characterization studies included chemical analyses, focusing primarily on the determination of total metal concentrations on (i) acid-digested DWTR, (ii) elutriates from the toxicity characteristics leaching procedure, and (iii) elutriates from DWTR leaching with synthetic fresh or marine waters.

Ecotoxicological bioassays were used to assess the potential toxicity of DWTR to aquatic organisms. For freshwater organisms, a combination of growth, life cycle, and survival bioassays were conducted using the midge fly *Chironomus tentans* and the amphipod *Hyalella azteca*. For marine organisms, only survival bioassays were conducted using the mysid shrimp *Mysidopsis bahia* and the polychaeta *Neanthes arenaceodentata*.

A combination of solid phase analytical techniques (*e.g.,* elemental composition (CHNS), thermogravimetric analysis, synchrotron-based x-ray diffraction and x-ray absorption spectroscopy, as well as electron microscopy) were used to elucidate the importance of the various chemical moieties that control the association of metals with different functional groups present in DWTRs.

Furthermore, the capacity of these substrates to immobilize dissolved metals was investigated through batch and flow-through column studies. Gust chamber studies were also conducted using metal-contaminated sediment cores to assess the efficacy of DWTR in reducing or eliminating the efflux of metals from contaminated sediments to the overlying water. Additionally, 96-hour exposure studies with fathead minnow (FHM) juveniles were conducted to evaluate the potential of DWTR to mitigate metal toxicity to water column organisms.

Lastly, diffusive gradients in thin films (DGT) were employed to probe the effects of capping metal-contaminated sediments with DWTR on metal concentrations in both pore and overlying waters, providing further insights into the remediation efficiency of DWTR as a capping material.

Results and Discussion.

The main findings of this research can be summarized as follows:

- Differences in the chemical composition of both treated waters and additives used in the water treatment processes do lead to highly heterogeneous DWTR, and based on State and Federal regulations, not all these substrates will be adequate for introduction to U.S. waters. Although none of the 15 samples tested in this study failed the toxicity characteristics leaching procedure (TCLP) test (*i.e.,* all were non-hazardous), 6 samples (40%) were found non-adequate based on total metal contents and sediment quality guidelines (SQG). Only 3 of the 9 that were classified as acceptable or questionable based on SQG results were qualified further using elutriation and ecotoxicity studies. The results led to the development of a screening method for selection of potentially safe DWTR for use as capping substrate for metal-contaminated sediments.

- Batch studies on the determination of the ability of DWTR to sequester and immobilize metals from aqueous effluents showed that the affinity of metal cations for these substrates is significantly higher for borderline and type-B metals than for type-A metals. We also investigated the mechanisms of the association of metals with the different geochemical fractions of DWTR. For instance, Hg sorption by DWTR is due primarily to two atoms in the first shell and would be bound to oxygen (O) when attached to an aluminum oxide such as kaolinite, and to sulfur (S) when associated with sulfhydryl groups present in organic matter. Some of the tested DWTR showed well-defined second shell features due to the presence of light elements such as N and O, with potential implications on sorption processes.

- The results of the fixed bed column studies showed that DWTR were able to significantly delay the breakthrough of metals when compared to an inert substrate (sand). Fitting of the experimental data with an adsorption model suggested that adsorption was not the only mechanism of metal immobilization, especially in aqueous solutions containing dissolved organic carbon. Precipitation seemed to play an important role, likely due to the presence of high levels of carbonates in some of the DWTR.

- The use of metal-contaminated sediment cores in laboratory experiments, performed with Gust chambers, where sediments were submitted to increasing hydrologic shear stress levels ranging from zero to 0.4 Pa, showed that sediment capping with DWTR does reduce both sediment erosion and the upward flux of metals from sediments to the overlying water. The reduction of the metals' efflux due to both physical and chemical processes was significant for sediments containing high water-extractable and easily exchangeable metal fractions. Results show that the use of DWTR as a sediment capping layer can reduce the metal contamination of the overlying water by up to 95% as compared to the non-capped sediments.

- Fish exposure studies using waters equilibrated with metal-contaminated sediments in either the absence (control) or presence (treatment) of a cap layer made of either sand or DWTR showed the ability of DWTR to reduce/eliminate toxicity to pelagic organisms.

- The use of passive porewater samplers (DGT) showed that the presence of DWTR as capping layer at the water-sediment interface impacted the vertical profiles of soluble metal concentrations in both the overlying and pore waters by reducing the total dissolved metal concentrations through adsorption and precipitation processes.

Conclusions and Implications for Future Research/Implementation.

This research program consisted of laboratory studies conducted primarily to determine if DWTRs could be used as in-situ capping substrates for metal-contaminated sediments. Based on the results of the screening component of the study, some DWTR can qualify for introduction to U.S. waters. This initial research shows clearly that the use of DWTR for capping metal contaminated sediments is promising. However, because DWTR samples were collected only once for most of the DWTP, and twice from two of the DWTP the variability in DWTR composition remains poorly defined. Therefore, after establishing the criteria for the screening of DWTR, the logical follow up step should be a monitoring program to determine the temporal stability or variability of the physicochemical and ecotoxicological characteristics of DWTR as these parameters would affect the availability of DWTR for field applications. Ideally, a few DWTPs should be selected based on the quality and quantity of DWTR they produce, and then monitored as a function of seasons over periods of months to years.

The advanced characterization of DWTR can be costly and/or time consuming (*e.g.,* use of bioassays and synchrotron radiation sources for detailed solid phase analysis respectively). Given the high variability of the physicochemical characteristics of these waste materials, the ideal approach would be to generate a relatively large dataset by taking advantage of the analytical methods and protocols described in this report. Such data could then be used to develop a predictive tool, and ideally with internet interface, which one can use when routine and easy to determine parameters are known (*e.g.,* total metal concentrations, particle size, types of additives used during water treatment, etc.), to determine the suitability of DWTR for introduction to U.S. waterways.

The Gust chamber studies showed that DWTR can act as both physical barrier and active sorbents for metal contaminants. As a result, DWTR can reduce, and in some cases eliminate, the toxicity of metals to pelagic organisms. However, the use of sediment cores in gust chambers lasted only 1 to 2 weeks. Since it is rather difficult to predict the long-term effects of using DWTR as capping substrates based solely on the results of short-term experiments, long-term studies are needed.

Overall, additional work is needed for the development of a robust approach that reduces the probability of failure when contemplating real world applications.

1. BACKGROUND

Aquatic systems have been exposed to pollution by toxic metals for centuries, primarily as result of widespread anthropogenic activities associated with the exponential growth of human populations. Typically, anthropogenic metal pollution of aquatic systems is linked to activities such as mining, manufacturing industries, municipal wastewaters, and agriculture. Once introduced to aquatic systems, metals are transported as either dissolved species or as an integral part of suspended solids (Meade, 1995), which would then settle through sedimentation, contaminating the sediments. Toxic metals accumulating in the sediments can be bio-accumulated by sediment dwelling organisms, and therefore, enter the food chain, with detrimental effects on both ecosystem functions and living organisms. Accordingly, ongoing research has focused on both pollution prevention (e.g., removal of pollutants from waste streams prior to the release to the environment) and pollution control, which is primarily a remediation task dealing with already contaminated systems. For the latter, which is the focus of this research, two types of technologies have already been adopted for cleaning of metal-contaminated sediments. The first group consists of *in-situ* methods, which are aimed at increasing the stabilization/immobilization of metals on sediment particles. The second group consists of *ex-situ* methods, which seek the separation (or extraction) of metals from contaminated sediments (Peng et al., 2009), or simply the disposal of dredged sediments as hazardous wastes. However, because of its relatively low cost and limited disruption to natural ecological conditions, *in-situ* metal immobilization technologies developed rapidly in the past several decades. One of the most used *in-situ* remediation techniques is the capping of contaminated sediments with layers of clean substrates, with predetermined physicochemical characteristics.

In-situ capping of sediments refers to the placement of a sub-aqueous cap made of clean materials over contaminated sediments that remain in place. Caps are generally composed of granular materials such as clean sediments, upland sand-rich soils, sand, or gravel (USEPA, 2005). A more complex cap may include geosynthetic materials in multiple layers used to attenuate the upward flux of contaminants from sediments to the overlying waters (USEPA, 2005). Specialized materials (e.g., clay minerals, and reactive/adsorptive materials such as activated carbon, zeolite, coke, apatite, organoclay, zero-valent iron) may also be used to boost the chemical isolation capacity or otherwise decrease the thickness of caps compared to sand caps (USEPA, 2005). However, except for sand, most of these substrates are relatively expensive, and in general, sorbent manufacturing approaches do significantly increase the cost of the remediation. Therefore, readily available, potentially efficient, and cost-effective sorbents for immobilization of toxic metals for large scale remediation of contaminated sediments are needed.

In this study, drinking water treatment residuals (DWTR) were evaluated for use as in-situ active capping substrate for metal-contaminated sediments. This choice stems from the well-established ability of DWTR to sorb and immobilize cationic chemicals (Bonzongo and Hovsepyan, 2009; Ippolito et al., 2011; Castaldi et al., 2015; Quiñones et al., 2016; Abo-El-Enein et al., 2017; Zeng et al., 2020; Wang et al., 2021; Quiñones and Bonzongo, 2023). DWTR are by-products in the conventional coagulation-filtration water treatment processes as shown in **Figure 1**, and where aluminum and iron salts (e.g., $Al_2(SO_4)_3 \cdot 14H_2O$, $FeCl_3$, or $Fe_2(SO_4)_3$) are used as coagulants to remove the suspended solids and natural organic matter from the raw water supply (Ippolito et al., 2011). Accordingly, aluminum (Al) and iron (Fe) based DWTR (referred to thereafter as Al-DWTR and Fe-DWTR, respectively) are the most common wastes in drinking water treatment facilities. The other major DWTR type is Ca-DWTR, which is produced in water plants when lime is used for hardness removal, and Ca-DWTR has been used for liming agricultural fields for several decades (Elliott et al., 2002).

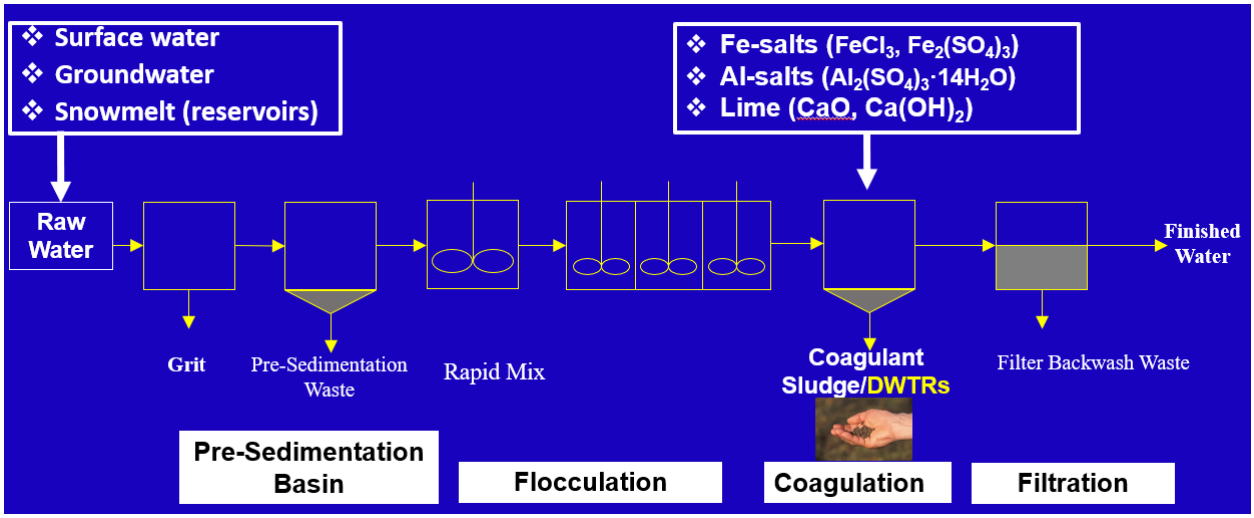


Figure 1. Flow diagram of the drinking water treatment process showing the coagulation step which produces the waste substrates (DWTR) used in this study (Adapted from USEPA, 1996, 2011).

One way to add value to these readily available and abundant byproducts of drinking water treatment processes is to take advantage of their physicochemical reactivity with- and high sorption capacity for inorganic and organic compounds as demonstrated in a wide variety of environmental applications. DWTR have strong sorption capacities for metal cations (Abo-El-Enein et al., 2017; Chiang et al., 2012a; Hovsepyan & Bonzongo, 2009; Quiñones and Bonzongo, 2023), but also for anions such as phosphorus and perchlorate, as well as selenium and arsenic oxyanions (Ippolito et al., 2011; Wang et al., 2013; Castaldi et al., 2014). While a number of studies on the potential use of DWTR in the remediation of contaminated environmental compartments are available in peer reviewed literature (e.g., Codling et al., 2002; Silveira et al., 2006; Sarkar et al., 2007; Fan et al., 2011; Wang et al., 2013; Walkons et al., 2018; Quiñones and Bonzongo, 2023), studies on the use of DWTR as *in-situ* capping materials for metal-contaminated sediments are lacking. Given the diverse physicochemical compositions and additives used in producing DWTRs from various raw waters, it is crucial to establish a set of selection criteria based on existing state and federal regulations. Moreover, it is essential to identify key compositional characteristics that validate the suitability of DWTRs as active substrates for capping of metal-contaminated sediments.

2. RESEARCH OBJECTIVES

This study is subdivided into four main tasks, and the overall approach is summarized in **Figure 2**. Each task was designed to meet specific research objectives as described below.

2.1. Collection and characterization of DWTR samples (Task 1). The introduction of fill materials to U.S. open waters is regulated by the Clean Water Act (CWA), which defines specific criteria to be met prior to use. Based on the anticipated high variability in the chemical composition of DWTRs, samples were requested from 30 different drinking water treatment plants (DWTP) across the U.S., and 15 responded positively. Received DWTR were analyzed for their physicochemical and ecotoxicological characteristics, based on the requirement of the CWA regarding both marine and freshwater systems. We hypothesized that *the variability in sources of*

waters and chemicals used during water treatment would lead to differences in the composition of DWTR, and therefore, to different physiochemical characteristics, making them either compliant or not compliant to the CWA. Therefore, if used as capping materials, the alteration of water chemistry and toxicity to aquatic organisms could be prevented by a screening process that relies on selection based on *CWA* criteria. Laboratory studies focused on the use of metal sediment quality guidelines (SQGs), DWTR elutriation with synthetic fresh and salt waters, and exposure bioassays using freshwater and marine benthic organisms.

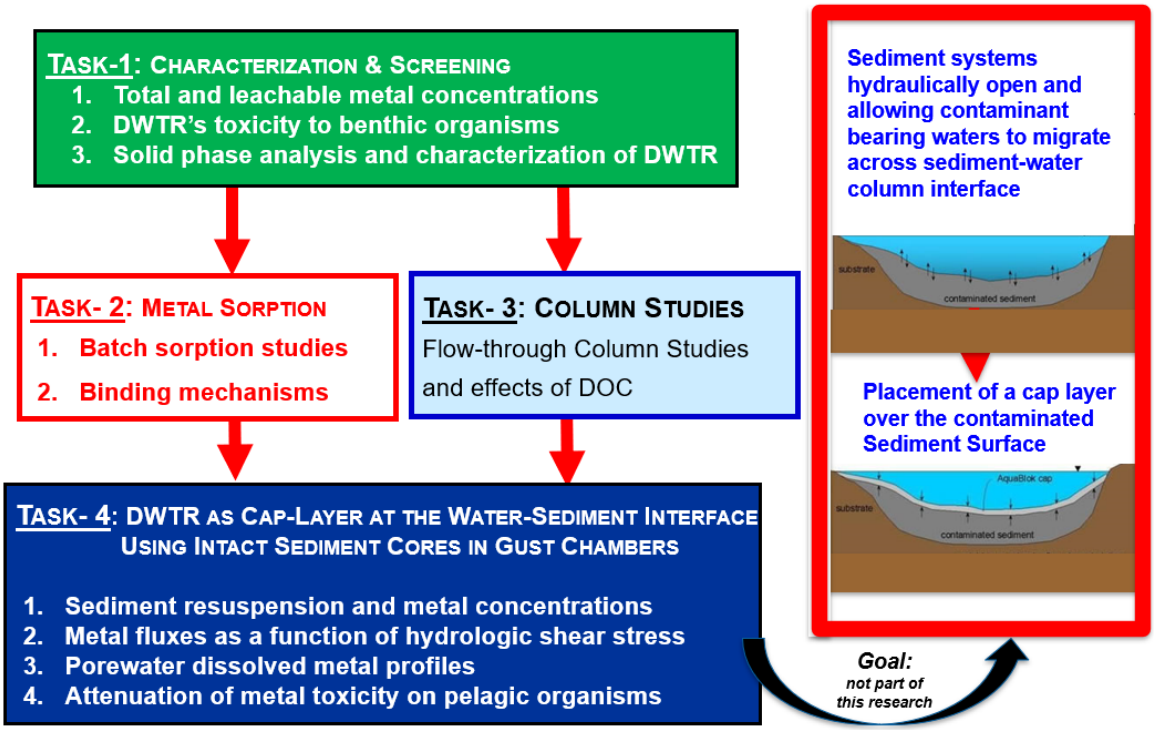


Figure 2. Research technical approach showing the four main tasks of the project, designed to meet the specific objectives of the research program.

2.2. Metal Sorption by DWTR in batch reactors (Task 2). The objective of this task was to determine the capacity of DWTR with different chemical compositions to sorb and immobilize metals. Our goal was to develop an approach that could help identify the appropriate DWTR matrices for specific metals found in contaminated sediments. The hypothesis driving this task is that *"metals would bind to DWTR through a combination of sorption mechanisms dominated by their ability to form ionic and/or covalent bonds, resulting in metal affinities that would differ based on the environmental classification of metals into type-A, type-B, and borderline"*.

2.3. Ability of DWTR to immobilize metals in flow through columns (Task 3). Column studies were used to assess the dynamic sorption capacities of DWTR under laboratory-controlled conditions, and to determine the potential effects of dissolved organic carbon (DOC) on the sequestration of metals by DWTR.

2.4. Metal sorption by DWTR in simulated hydrodynamic systems: Gust chamber studies (Task 4). We used metal-contaminated sediment cores in a hydrodynamic system to control metal exchanges between contaminated sediments and the overlying water. Experiments were conducted to determine the ability of DWTR to reduce or eliminate the upward flux of metals from

contaminated sediments to surface waters in gust chambers where physical disturbances (e.g., bioturbation, effects of boat's propellers, or storms induced water mixing) were simulated. The working hypothesis in this case is that *the capping of metal-contaminated sediments with DWTR would provide protection against the upward flux of metals as well as sediment erosion and resuspension*.

3. MATERIALS AND METHODS

3.1. Collection of DWTR samples

We contacted 30 drinking water treatment plants (DWTP) across the U.S., and 15 responded positively. The geographical distribution of these DWTP is shown in **Figure 3**.

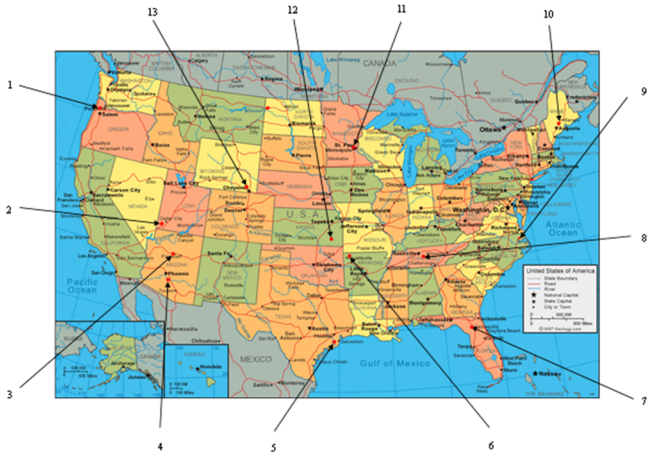


Figure 3. Geographical distribution of the DWTP from which the DWTR samples were obtained. The description of the different samples is given in Table 1.

The DWTR samples were shipped to our laboratory in plastic buckets (**Figure 4A**) and were mostly dewatered solid materials with different colors and physical structures (e.g., **Figures 4B and 4C**), depending on the chemical composition of treated raw waters and the types of chemical additives used during treatment (**Table 1**). A description of main additives, sources of treated waters and the concentrations of Fe, Al, and Ca which are commonly used to classify DWTR into iron (Fe-DWTR), aluminum (Al-DWTR), calcium (Ca-DWTR) based DWTR are presented in **Table 1**. The DWTR samples are identified by the abbreviation of the state from which they came from, and in the case of Arizona (AZ) from which we received 2 samples, they were labeled AZ-1 and AZ-2.



Figure 4. **(A).** Picture of example DWTR containers received. **(B)** and **(C)**. Example dewatered DWTR samples.

DWTR samples ID	Main additives used during water treatment	Source of treated water	Conc. of Fe (g/kg)	Conc. of Al (g/kg)	Conc. of Ca (g/kg)	DWTR classification
AR	$FeSO_4$, alum, polymers	Surface water	94.20 ± 0.54	61.23 ± 0.67	2.43 ± 0.03	(Fe+Al)-DWTR
AZ-1	Aluminum chloro-hydrate	Groundwater	60.84 ± 0.88	81.32 ± 0.64	3.22 ± 0.11	(Al+Fe)-DWTR
AZ-2	Alum, polymer dry A-3320	Groundwater	3.06 ± 0.04	20.65 ± 1.87	13.75 ± 0.20	(Al+Ca)-DWTR
FL	Alum, polymers	Mixed surface/groundwater	3.58 ± 0.03	56.20 ± 1.35	1.09 ± 0.04	Al-DWTR
IL	Lime, alum, cationic polymer	Surface water	1.90 ± 0.00	5.86 ± 0.00	225.45 ± 0.00	Ca-DWTR
KS	Alum, lime, polymers, $KMnO_4$, Cl_2	Surface water	28.72 ± 0.32	25.91 ± 0.37	8.64 ± 0.40	(Fe+Al)-DWTR
ME	Alum, cationic polymer	Surface water	8.69 ± 0.15	37.87 ± 0.63	1.88 ± 0.14	Al-DWTR
MN	Lime, alum, $FeCl_3$	Mixed surface/groundwater	8.50 ± 0.16	4.27 ± 0.01	136.05 ± 4.37	Ca-DWTR
NC	Lime, alum, anionic polymers	Groundwater	8.98 ± 0.06	8.60 ± 0.12	137.94 ± 2.33	Ca-DWTR
OR	Alum, Cl_2, US Poly 7510, NaOH	Surface water	39.88 ± 0.43	46.13 ± 0.70	3.07 ± 0.11	(Al+Fe)-DWTR
PA	Alum, nonionic polymer, NaOCl, NaOH	Surface water	19.96 ± 0.00	30.22 ± 0.00	2.88 ± 0.00	(Al+Fe)-DWTR
TN	Lime, polymers, soda ash, $KMnO_4$, H_2O_2	Surface water	3.45 ± 0.09	3.99 ± 0.07	176.55 ± 5.35	Ca-DWTR
TX	Cationic and anionic polymers, alum	Groundwater	31.44 ± 0.14	43.09 ± 0.58	4.30 ± 0.17	(Al+Fe)-DWTR
UT	Alum, polymers, activated carbon, $KMnO_4$	Surface water	5.55 ± 0.04	147.10± 2.50	24.57 ± 0.76	Al-DWTR
WY	Alum, Nalco7193+, poly alum chloride, sodium fluorosilicate	Mixed surface/groundwater	18.75 ± 0.14	84.57 ± 1.22	7.05 ± 0.24	Al-DWTR

Table 1. Drinking water treatment residual samples collected from water-treatment plants across the United States. Total concentrations of Fe, Al, and Ca are averages from triplicate analyses ±1 standard deviation. From the main chemical additives, these DWTR samples are dominated by a combination of Al and Fe or by either Al or Ca.

3.2. Screening approach and identification of suitable DWTR

3.2.1. Toxicity characteristics leaching procedure (TCLP)*:* This is an approved procedure designed to determine the hazardous characteristics of solid wastes based on the mobility of pollutants present in the substrates (US-EPA, 1992). This test was used to verify if the collected DWTR samples could be classified as either hazardous or nonhazardous materials. To do so, 2 different TCLP fluids were used following the protocol outlined in US-EPA Method 1311 (US-EPA, 1992). *Extraction fluid 1* is an aqueous solution containing approximately 0.1 M CH_3COOH and 0.064 M NaOH, with a final pH of 4.93. *Extraction fluid 2* is a non-buffered acetic acid solution (~0.1 M), with a final pH of 2.88. For each TCLP fluid, metals in DWTR sample were extracted using a fluid to DWTR ratio of 20 mL to 1 g, while control samples contained no DWTR. For these extractions, each DWTR sample was prepared in triplicate. Mixtures were rotated at 30 rpm for 18 h and then filtered (0.45µm), before being acidified with trace metal–grade concentrated HNO_3 to a final acid concentration of 5% (v/v). The acidified filtrates were analyzed for metals with published concentration guidelines (e.g., As, Ba, Cd, Cr, Pb, Hg, Se, and Ag) by ICP-MS as described above for the liquid samples.

3.2.2. Elutriate studies. Elutriate studies were conducted on selected pre-screened DWTR samples, using the procedure outlined in the Green Book (US-EPA, 1991), and based on the concentrations of metals/metalloids shown in **Table 2**.

Metals/Metalloids	Aquatic Life Ambient Water Quality Criteria (AWQC)	
	Freshwater criterion maximum concentration (µg/L)	**Saltwater** criterion maximum concentration (µg/L)
Aluminum (Al)	Site-specific	*N/A
Arsenic (As)	340	69
Cadmium	1.8	33
Chromium (III)	570	N/A
Chromium (VI)	16	1100
Copper (Cu)	Site-specific	4.8
Lead (Pb)	82	140
Mercury (Hg)	1.4	1.8
Nickel (Ni)	470	74
Selenium (Se)	Site-specific	290
Silver (Ag)	3.2	1.9
Zinc (Zn)	120	90

Table 2. Criteria maximum concentrations (CMC) of metals determined in elutriates of DWTR. *N/A: not available

Synthetic fresh or salt water was combined with DWTR at a ratio of one-part residuals per four-parts water at room temperature (22 ± 2°C). The mixture was stirred for 30 min using a magnetic stirrer. In addition to the mechanical mixing, the mix was shaken manually every 10 min, within the above 30 min, to ensure complete mixing. Afterwards, the mixture was allowed to settle for 1 hour. The supernatant was then filtered through a 0.45µm filter to remove solids, and the filtrate analyzed for dissolved metals of interest as summarized in **Table 2,** which also contains the corresponding maximum concentrations for Aquatic Life Ambient Water Quality Criteria (US-EPA,2018). For chromium, only total Cr is reported here because measured concentrations did not

exceed the Criterion Maximum Concentration (CMC) established by the EPA's Ambient Water Quality Criteria (AWQC) (US-EPA, 2018), to justify the determination of trivalent and hexavalent Cr species. For each analyzed metal, results were compared to the CMC established by the Ambient Water Quality Criteria (US-EPA, 2017), corresponding to the concentration at which acute toxic effects are expected.

3.2.3. Metal concentrations and sediment quality guidelines (SQG).

a. Determination of total metal concentrations in solid and liquid samples. Total metal concentrations in each of the DWTR samples and in sediments in the different laboratory experiments were determined following hot acid digestion in which 20 mL of 15.8 M HNO_3 were added to 1 g (dry wt.) of DWTR in an acid precleaned volumetric flask. The mixture reacted first at room temperature until all signs of chemical reactions were gone. The volumetric flasks were then covered with acid-cleaned glass watches and heated at 95 °C for 12 h. After cooling, aliquot volumes of a 30% H_2O_2 solution (up to 5 mL) were added to the digested samples until all signs of chemical reactions were gone. Nanopure® water was then added to the digested samples to a final volume of 200 mL, mixed by stirring, and filtered (0.45µm). Next, samples were analyzed for the total concentrations of selected metals (Ag, Al, As, Ba, Ca, Cd, Cr, Cu, Fe, Hg, Ni, Pb, Se, and Zn) by inductively coupled plasma mass spectrometry (*Element-2 HR-ICP-MS;* Thermo-Fisher Scientific).

In addition to solid samples, total metal concentrations were also determined in liquid samples (i.e., aqueous samples and chemical extracts from DWTR or sediment samples). In this case, small-volume fractions of the acidified liquid samples were diluted with a 0.8 N HNO_3 solution and spiked with rhodium (Rh) and rhenium (Re) at final concentrations of 8 ppb (or 8 µg/L). Like the solid samples described above, liquid samples were also analyzed for total metal concentrations by ICP-MS.

For both solid and liquid samples, quantification of the results was achieved via an external 7-point standard calibration curve prepared using a commercial high-purity ICP-MS standard *(www.highpuritystandards.com).* In addition, the quality control and quality assurance protocol included blanks and a calibration verification solution after every 10 samples. The samples were analyzed at medium resolution, and Re and Rh were used as internal standards to correct for instrumental drift. The limit of detection for the analyzed metals was ~0.1 ppb, and the error on the reported concentrations was <5%. For DWTR and sediment samples, a certified reference material (LKSD-4; National Research Council, Canada) was used, and acceptable results needed to be within 90 to 110% of the reported values for each metal of interest. Acid digestion blanks were also included to account for metal contribution by the different chemicals used.

b. Using sediment quality guidelines and total metal concentrations to identify suitable DWTR. For DWTRs to be considered adequate materials for *in-situ* capping of metal contaminated sediments in U.S. waterways, they need to satisfy specific environmental guidelines. Unfortunately, and in contrast to soils and land application practices, there are no federal nor State DWTR application guidelines for aquatic sediments. However, available sediments quality guidelines (SQGs) can be used as guidelines in assessing the potential adverse effects of metals present in sediments. In the 1990's, research supported by the Florida Department of Environmental Protection resulted in the publication of sediment quality assessment guidelines for Florida's coastal waters (MacDonald, 1994; MacDonald, Carr, Calder, Long, & Ingersoll, 1996). A comprehensive sediment quality assessment guideline for Florida inland waters was reported a few years later (MacDonald et al., 2003). Overall, consensus-based SQG have been developed to help protect sediment-dwelling organisms (MacDonald, Ingersoll, & Berger, 2000).

Two common sediment quality assessment values, the *threshold effect level* (TEL) and the *probable effect level* (PEL), are used for the assessment of metal-contaminated sediments (MacDonald et al., 1996; Smith, MacDonald, Keenleyside, Ingersoll, & Field, 1996). The TEL and PEL values help define three ranges of chemical concentrations as illustrated in **Figure 5** (MacDonald et al., 1996; Smith et al., 1996), delimited by 2 vertical lines. As one moves from left to right in Figure 5, there is first the minimal effect range region (i.e., concentrations below or equal to the TEL), within which adverse biological effects would be rare. Next is the possible effect region, corresponding to contaminant concentrations >TEL but <PEL), and where possible toxicity effects can be observed. Finally, the probable effect region, corresponding to contaminant concentrations above the PEL vertical line, and where adverse biological effects are expected to occur. SQG values used for the protection of sediment-dwelling organisms in freshwater ecosystems have also been grouped into *threshold effect concentrations* (TECs) and *probable effect concentrations* (PECs), which are calculated by determining the geometric mean of relevant SQGs (MacDonald et al., 2000), and used to establish reliable effects-based SQGs for inland waters (MacDonald et al., 2003).

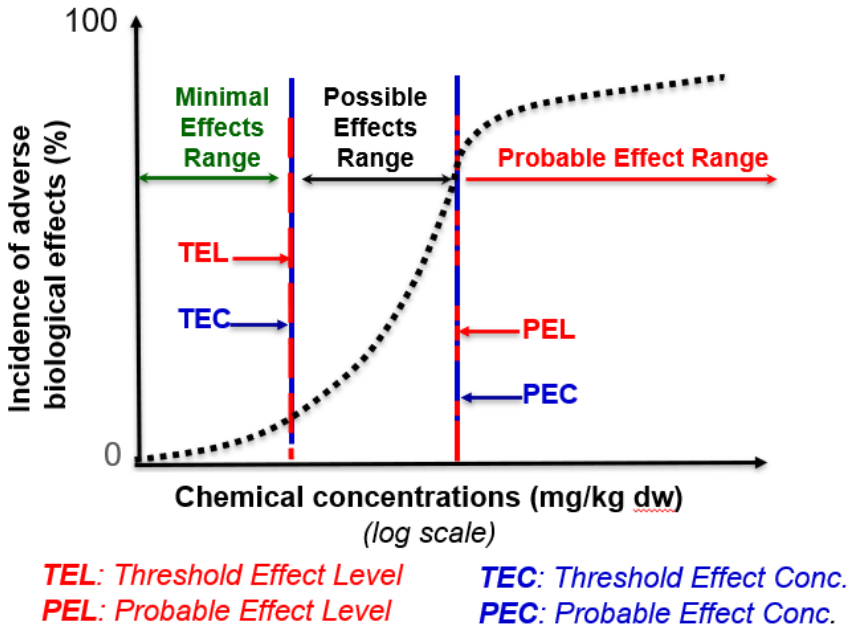


Figure 5. Conceptual sketch of the concentration ranges of contaminants delineated by sediment quality guidelines (SQGs) and the potential for observing adverse effects *(Adapted from MacDonald et al., 1996)*

Using the concept described in Figure 5 and available SQG guidelines for metals in freshwater and marine sediments presented in **Table 3**, DWTR were screened based on their total metal contents. The results are presented and discussed later herein.

Table 3. Sediment quality guidelines (SQG) based on total metal concentrations in freshwater and marine sediments. Concentrations are expressed in mg/kg (or ppm).

	Freshwater sediments				Marine sediments	
Metals	**TEL**	**PEL**	**TEC**	**PEC**	**TEL**	**PEL**
As	5.90	17.0	9.79	33.0	7.24	41.6
Cd	0.59	3.53	0.99	4.98	0.68	4.21
Cr	37.3	90.0	43.4	111	52.3	160
Cu	35.7	197	31.6	149	18.7	108
Pb	35.0	91.3	35.8	128	30.2	112
Hg	0.17	0.49	0.18	1.06	0.13	0.70
Ni	18.0	36.0	22.7	48.6	15.9	42.8
Ag	-	-	-	-	-	1.77
Zn	123	315	121	459	124	271

***TEL**: threshold effect level, **PEL**: probable effect level, **TEC**: threshold effect concentration, **PEC**: probable effect concentration.*

3.2.4. Ecotoxicity studies. To provide a strong basis on which to assess sublethal toxicity and enhance the risk-assessment process, test methods that incorporate a combination of sensitive and ecologically relevant endpoints were used in whole-substrate toxicity assays. Tested substrates included the DWTR samples and control clean sediments, using both marine and freshwater organisms.

a). Marine organisms. Since the use of DWTR as potential capping substrate for metal-contaminated marine sediments in the U.S. would likely fall under the regulation of dredged material for ocean disposal, we used bioassays proposed for the evaluation of dredged materials for discharge to waters in the U.S. The toxicity of DWTR samples on marine benthic organisms was studied using the mysid shrimp *Americamysis Bahia* (previously known as *Mysidopsis bahia*) in short term acute toxicity assays (US-EPA/US-ACE 1991; US-EPA 1994), and the polychaeta *Neanthes arenaceodentata* for chronic exposure (US-EPA/US-ACE 1998; Farrar and Bridges, 2011). In these whole sediment-based bioassays, DWTR was used as sole substrate, not mixed with sediments. Reference sediments used as control substrates were collected from a seasonally flooded area near the Cellon Creek watershed in Alachua County, Florida. Sediments were collected from the top 5 cm, wet sieved (<400 μm) with the relevant method's control synthetic seawater. The following two bioassays were used:

- The 10-day survival test using the mysid shrimp *Mysidopsis bahia*.
- The 28-day survival and growth test using the polychaeta *Neanthes arenaceodentata*.

The Kruskal-Wallis' test (R Core Team, 2017) was used to compare the endpoint results obtained following exposure of the organisms to control sediment and DWTR. A significance threshold of $\alpha=0.05$ was applied.

A full description of experimental procedures and bioassays used has been published in *Environmental Toxicology and Chemistry* (Zhou et al., 2021a).

b). Freshwater organisms. The freshwater sediment bioassays were conducted based on the requirements of U.S. Clean Water Act 404(B)(1). Tested substrates included the DWTR samples and control sediments from Cellon Creek in Alachua County, Florida. For all bioassays, the DWTR samples or control sediments were mixed with water in a volume ratio of 1.75. Briefly, 100 mL of either control sediment or DWTR (corresponding to about 80±3.0 g of solids) were equilibrated with 175 mL of moderately hard reconstituted freshwater or MHR in 300 mL containers as recommended by the Clean Water Act 404(B)(1). The following bioassays were used:

- 10-day survival and growth test using the midge fly *Chironomus tentans* **(**EPA 600/R-99/064, Test Method 100.2).
- Life cycle test using the midge fly *Chironomus tentans* **(**US-EPA 600/R-99/064, Test Method 100.5).
- *10*-day survival and growth test using the amphipod *Hyalella azteca*.
- 28-day survival and growth test using the amphipod *Hyalella azteca*. This bioassay was conducted using US-EPA's Method 100.4 (EPA-600-R-99-064).

Like the results of the bioassays using marine organisms, the Kruskal-Wallis' test was used to compare the endpoint results obtained following exposure of the organisms to control clean sediment and DWTR substrates, and a significance threshold of $\alpha = 0.05$ was applied, with any significant differences further examined via multiple pairwise comparisons with a Tukey's range test procedure.

A full description of the bioassays used has been published in *Environmental Toxicology and Chemistry* (Zhou et al., 2021b).

3.2.5. Developed screening method. To identify DWTR that are suitable for introduction to U.S. waterways, we developed a 4-step screening approach (**Figure 6**). First, the results of the TCLP test were used to eliminate or retain the DWTR based on their classification as hazardous or non-hazardous wastes. This first step uses total concentrations of selected metals compared to guidelines as described earlier. Second, the determined total metal concentrations and sediment quality guidelines (SQG) were used to qualify the DWTR based on available regulations. Third, elutriation studies using synthetic fresh and salt waters were conducted to assess the potential for DWTR to release metals versus the Clean Water Act criteria. Finally, the toxicity of DWTR used as sol substrate on sediment dwelling organisms was determined. Therefore, only the DWTR samples that passed these 4 tests were considered suitable for introduction to U.S. waterways. However, after steps 1 and 2, the screening resulted in a classification of the DWTR samples in to three groups: acceptable (4 samples), questionable (5 samples), and inadequate (6 samples) (see **Table A1**, Appendix A). From the acceptable, only 3 DWTR samples were investigated for toxicity studies due to cost limitations. For physicochemical characterization and metal sorption studies, both acceptable and questionable samples were used.

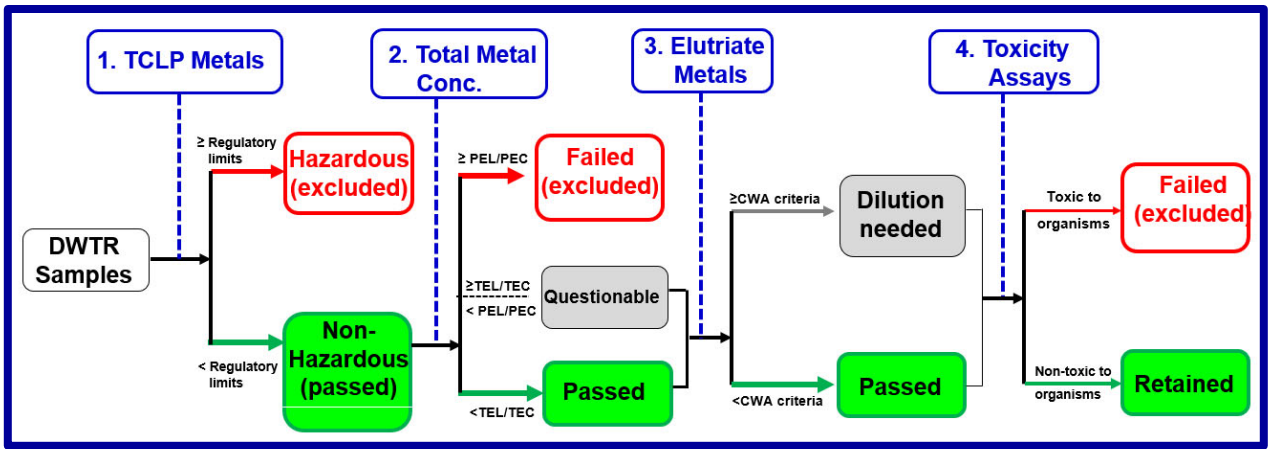


Figure 6: Flow chart showing the four steps of the developed screening method to determine the suitability of DWTR for use as fill materials, or as sediment capping substrate in this specific case.

3.3. Solid phase analysis and characterization.

3.3.1. Thermogravimetric analysis coupled to mass spectrometry (TGA-MS). For these analyses, ~15 mg of powdered DWTR were used. Samples were first dried at 40°C for one day prior to analysis. TGA data were collected using a Netzsch STA 449 F3 Jupiter Simultaneous Thermal Analysis (STA) instrument. Measurements were made under ultra-high purity He, flowing at 211 mL/min. Following a 10-minute isothermal step at 30°C, the temperature was increased at a rate of 10°C/min up to 900°C and held at that temperature in a final isothermal step for 10 minutes. Gases were transferred to an Agilent Technologies 7890A Gas Chromatograph equipped with an Agilent HP-5 column and Agilent 5975 MSD spectrometer. Injections of 250 µL of the gas mixtures were analyzed every minute through the heating and final isothermal steps, and mass spectra were collected from 10-400 m/z. A baseline measurement using an empty alumina crucible under the same operating conditions was collected to correct for the buoyancy effect. Mass spectrometry (MS) data were analyzed using Agilent ChemStation software. For quantification of the major ions at m/z 18 (water) and 44 (carbon dioxide). For the peak forest maps showing the m/z ranging from 50 to 150, raw data were exported. The median count value for each m/z was calculated starting at 5 min after the commencement of the high-temperature isothermal step and ending at the last collected MS data point ~20 min later during the declining temperature step. This median value provided the baseline to estimate the integrated peak area for the high m/z ions.

3.3.2. Specific surface area (SSA). Surface area analysis was conducted on the fine fraction of DWTR samples based on the physisorption of nitrogen using a Micromeritics 3Flex instrument. DWTR samples were first dried at 40°C, then immediately prior to analysis, samples were degassed at 100 and 120°C using a Micromeritics Smart VacPrep. SSA calculations were based on the Brunauer-Emmett-Teller (BET) theory (Brunauer et al., 1938), while pore size distributions were based on the Barrett-Joyner-Halenda (barrett et al., 1951) method with the Halsey t-curve (Hasley, 1948)) as applied to desorption data.

3.3.3. Carbon, hydrogen, nitrogen, and sulfur (CHNS) elemental analysis. The Elementar Vario EL Cube was used for the determination of CHNS. Each DWTR sample was analyzed in

triplicate, and measurements were taken for DWTR samples with and without the addition of phosphoric acid. Acidification allows for the contribution of acid-volatile carbon to be distinguished from non-acid volatile forms of carbon; most often, the acid-volatile carbon is dominated by carbonate minerals, and the non-acid-volatile carbon would primarily be made up of organic matter (Phillips et al., 2011). H, N, S, and total C abundance values were taken from the results of un-acidified samples. The non-acid-volatile C was taken from the acidified samples (corrected based on the change in mass with the addition of acid), and the acid-volatile C abundance was taken to be the difference between C measurements in the two samples.

3.3.4. X-Ray Fluorescence (XRF). For these analyses, the fine fraction of each DWTR sample was analyzed by XRF using a Xenemetrix Ex-Calibur EX-2600 with a Rh X-ray source, operated at 20 keV and 10 μA, and a silicon energy-dispersive detector. Samples were placed on 6 μm Mylar film stretched over plastic cups, and the spectra collected at room temperature under vacuum for 120 s with no filter over the detector.

3.3.5. X-Ray Diffraction (XRD). Synchrotron-based high-resolution powder XRD analyses were conducted at the bending magnet beamline of the Dow-Northwestern-Dupont Collaborative Access Team (DND-CAT), Sector 5 of the Advanced Photon Source at Argonne National Laboratory in Lemont, IL, USA. Fine and ground samples were sieved through a 63 μm 230 mesh. These were subsequently sealed in glass capillaries that were rotated within the monochromatic x-ray beam, which had a wavelength $\lambda = 0.620426$ Å, which translates to an energy of 20 keV. The scan ran from 2θ values of 7.5 to 41.5°. Peak identification was performed using MDI-JADE software (Materials Data, 2020) with the International Centre for Diffraction Data database (Gates-Rector and Blanton, 2019), and additional crystallographic information was collected from the American Mineralogist Crystal Structure Database (Downs and Wallace, 2003).

3.3.6. X-Ray Absorption Spectroscopy (XAS). Fe K-edge standards for this experiment were collected from previous XAS experiments (Xie et al., 2019), the Lawrence Berkeley National Laboratory XAS database (Fraka, 2010), and the National Institute for Materials Sciences Materials Data Repository (MDR) (Tanifuji et al., 2019; Ishii et al., 2021). Mn database standards include spectra from previous studies (Saratovsky et al., 2006), distributed with the Demeter suite for XAFS analysis (Ravel et al., 2005), found on the MDR (Ishii et al., 2021; Tanifuji et al., 2019). For standards without reference foil data included a spectrum from the database was aligned to data collected at the Dow- Northwestern-Dupont Collaborative Access Team (DND-CAT) (either Mn or Fe metal foil or manganese carbonate), and the offset for the alignment was applied to all the spectra from that database. For the interpretation of x-ray absorption near edge spectra (XANES), principal component analysis (PCA) and target transformation performed on the spectral libraries of references (TT) were performed to inform about the selection of the proper set spectra to use. This was followed by performing spectral decompositions based on linear combination fitting (LCF) (Gaillard et al., 2000; Da Silva-Cadoux et al., 2012; Webb and Gaillard, 2015). These techniques were applied to the first-derivative XANES for spectra at both the Mn and Fe K-edge (Xie et al., 2019). Calculations for the LCF were performed using lmfit (Newville et al., 2016), forcing the sum of standards to be equal to 1. Standards were eliminated from the LCF for each sample if (i) the uncertainty for that standard's weight in the fit encompassed 0 or (ii) the omission of that standard from the LCF resulted in an increase of <0.001 in the χ^2 measure for goodness-of-fit.

DWTR data were collected at the bending magnet beamline of Sector 5, the DND-CAT, at the Advanced Photon Source (APS), Argonne National Laboratory, Lemont, IL. Intensities for *I*0, *IT* 1, and *IT* 2 were measured with Oxford ionization chambers at 29.6 cm path lengths, and energy was set using a Si (111) double crystal monochromator. Data collected in fluorescence mode used

two Vortex ME-4 silicon drift detectors. Standard data were supplemented with online databases, including the Materials Data Repository (Ishii et al., 2021; Tanifuji et al., 2019), data included with the Demeter suite (Ravel et al., 2005), and supplemental Mn K-edge data (Manceau et al., 2012). In addition, several standards were collected by previous members of the Laboratory of Metals in Aquatic Systems (lMAS) at DND-CAT. All data were aligned based on a reference foil collected concurrently when applicable; in data without a reference foil, a spectrum from the same dataset was aligned to data collected at DND-CAT (e.g., a separate metal foil scan), and the offset for the alignment was applied to all the spectra from that database.

3.4. Sorption studies

3.4.1. Sorption kinetics. DWTR samples were used comparatively in laboratory studies to determine their sorption capacities for metal ions. The aqueous solutions of selected metal ions were prepared using nitrate salts purchased from Fisher Scientific. For each metal, the aqueous solution was mixed with a DWTR sample in 50 mL metal-free polypropylene (PP) tubes to produce a final mass/volume ratio of 1g DWTR per liter of solution. Blanks consisted of PP tubes with metal solutions but no DWTR. The pH of prepared mixtures was stabilized to desired values using buffers (MOPS for pH<7 or HEPES for pH>7). KNO_3 was used as background electrolyte at a final concentration of 0.01 M. Produced mixtures were shaken using an orbital shaker at a speed of 180 rpm. The sacrifice method was used, and after pre-determined times, the mixtures were removed from the shaker and centrifuged. The supernatant was filtered (0.45μm), acidified with trace metal grade HNO_3. The metal contents in the aqueous was analyzed by ICP-MS, except for mercury (Hg). For the latter, analyses were performed using the total mercury analyzer Milestone DMA-80. Sorption reactors for XAS experiments were prepared at three different Hg concentrations and three different pH values using buffers (MES, MOPS, and HEPES). All the experiments were run in triplicate. Obtained experimental data were fit using commonly used sorption pseudo-first order and pseudo-second order kinetic models.

3.4.2. Sorption isotherms. Acidic (10% HNO_3) solutions of metal ions were prepared using nitrate salts to produce final concentrations of 1000 mg/L. These concentrated solutions were then diluted to prepare solutions with increasing concentrations for use in batch sorption studies. Like for the kinetics studies, 50 mL metal-free PP tubes were used and DWTR were mixed with the metal aqueous solution in a mass to volume ratio of 1g DWTR per liter. The background electrolyte and pH adjustment methods were the same as described for the above kinetic sorption. Sorption studies were conducted at room temperature (around 23±2°C) and the PP tubes then continuously shaken at 180 rpm on the orbital shaker for 72 hours. After the equilibration process, the pH was measured again to make sure it didn't drift away from the pre-shaking adjusted value. The slurries were then centrifuged, and the supernatant filtered (0.45μm) and analyzed for the tested metals by ICP-MS. All the experiments were run in triplicate. Experimental sorption data were fit to Langmuir model using Eq.1(Langmuir, 1918), where C_e is the equilibrium liquid phase concentration (mg/L); q_e is the equilibrium mass of metals sorbed onto DWTR (mg/g); b is the sorption affinity constant, and Q_0 (or Q_{max}) is the maximum sorption capacity (mg/g).

$$q_e = \frac{Q_0.b.C_e}{1+ b.C_e} \qquad \text{Eq. 1}$$

Whenever applicable, the Freundlich model (Eq. 2) was also used to fit experimental data,

$$q_e = k_f \times C_e^{1/n} \qquad \text{Eq. 2}$$

and where C_e is the equilibrium liquid phase concentration (mg/L); q_e is the equilibrium mass of metals sorbed onto DWTR (mg/g) n and k_f are the Freundlich constants, indicating the adsorption capacity and the adsorption intensity, respectively (Freundlich, 1907).

3.4.3. Fixed bed flow-through column studies. Column experiments were conducted to investigate the ability of DWTR to remove metals from flowing water using the experimental setup illustrated in Figure 7. Briefly, acrylic columns (16 mm inside diameter and 50 mm height) were used to hold the sorbent. Meshes with 50µm pores (Spectra/Mesh, Spectrum Laboratories, Inc.) were used at both inlet (bottom) and outlet (top) to seal the columns and to distribute the flow while stabilizing the column content. To pack a DWTR column, half of the column was first wet packed with acid cleaned quartz sand (particle size <1 mm). DWTR was then carefully layered on the top of the packed sand as a thin layer. Next, the rest of the column was filled with sand using the wet-packing method. The same approach was used when another sorbent, apatite in this case, was used for comparison. Columns containing only sand and no sorbent were also prepared to act as controls. Before initiating the sorption study, Nanopure® water was pumped upward through the column using a peristaltic pump for ~12 hours to remove trapped air bubbles and water-soluble impurities. After this step, the Nanopure® water influent was replaced by the metal solution (mixture of Cd, Cu, and Pb, each at a final concentration of 2 mg/L and with or without dissolved organic matter (DOM) added at a final concentration of 1 mg C/L) and pumped through at a flow rate of 0.5 ml/min. Bromide (10 mg/L) was used as tracer to help in the determination of the retardation factor. Column effluent samples were collected with a fraction collector (IS-95 Interval Sampler, Spectrum Chromatography) and the concentrations of metals in effluents collected over time and preset intervals and then processed as described before for metal analysis in liquid samples by ICP-MS.

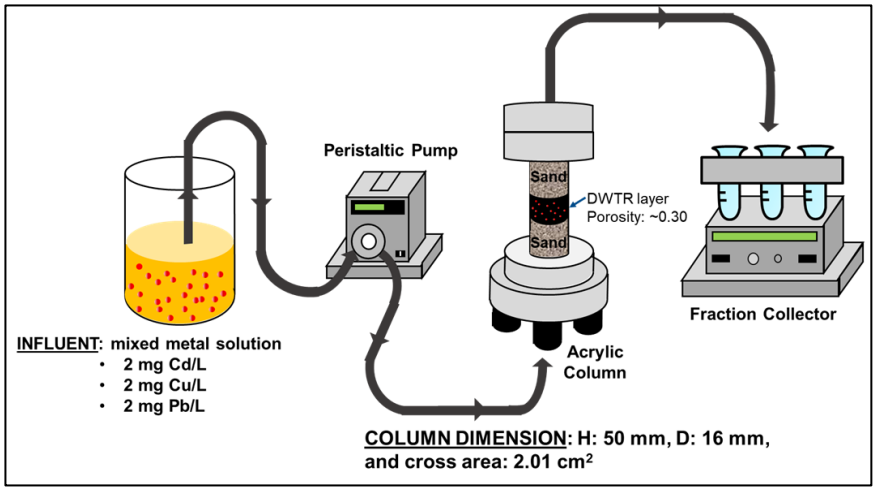


Figure 7: Schematic diagram of fixed bed column sorption system showing from left to right the metal containing influent solution followed by a peristaltic pump, the acrylic column packed with quartz sand (top & bottom) and DWTR (center); and a fraction collector (*Adapted from Huang et al., 2022*).

In general, column experiments seek concentration–time profiles or breakthrough curves with the goal of calculating the maximum solid-phase concentration representing the maximum sorption capacity of the sorbent (Yan et al., 2001). The dynamic sorption performance of tested

substrates (DWTR and apatite) for the removal of metals from aqueous solutions were simulated using a modified version of the Thomas' kinetic model (Thomas, 1948), proposed by Yan et al. (2001), to describe breakthroughs in packed columns. The model assumes multiple rate-limiting steps in the sorption process such as mass transfer at the solid surface and diffusion and can be written as follows:

$$\frac{C_t}{C_0} = 1 - \frac{1}{1 + \left(\frac{C_0 v t}{Q_0 x}\right)^a} \qquad Eq.\,3.$$

where C_0 (mg/L) is the original metal concentrations in the influent, C_t (mg/L) is the metal concentration in the effluent at t (min), a is the Yan model constant, Q_0 (mg/kg) is the amount of metal adsorbed onto the sorbent at equilibrium, x (g) is the dosage mass of sorbent, and v (mL/min) is the flow rate. The value of Q_0 at a given C_t can be predicted from a plot of $\frac{C_t}{C_0}$ against time t, using the non-linear regression.

Therefore, if we assume that adsorption is a major mechanism for the observed metal immobilization in the columns, this equation can be used to model the experimental breakthrough data.

3.5. Sediment capping: Effect on sediment resuspension and fate of metals.

To determine the ability of DWTRs to control the upward flux of metals from contaminated sediments to the overlying water, a 2-core UGEM unit manufactured by Green Eyes, LLC was used (**Figure 8**). This system allowed for parallel runs of non-capped (control) and capped (treatment) sediments.

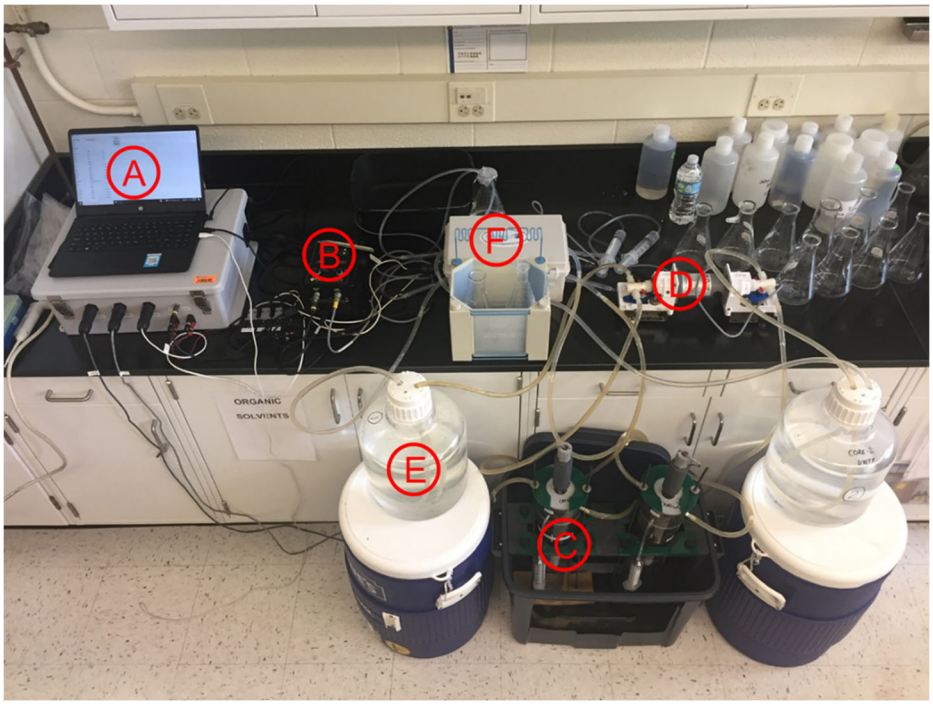


Figure 8. Gust Chamber setup A): laptop for parameter setting; B) central controller; C) gust chamber cores; D) pump; E) carboy for containing water; F) turbidimeter for effluent water's turbidity monitor.

The gust chambers used are made of polycarbonate. To minimize the contamination that could come from metal sources other than the tested sediments, all parts of the setup in contact with water and sediments were first soaked in a diluted acid solution (5% HNO_3) for 24 hours, followed by thorough rinsing with Nanopure® water before use. For a good comparison between control (non-capped) and treated (capped) sediments, and given the high heterogeneity of sediments, metal-contaminated sediment cores used for this task were prepared in the laboratory by equilibrating wet sieved *(<2 mm*) and homogenized sediments with either lab or site water in pre-defined mass-to-volume ratios. After an initial equilibration period of one week, the prepared sediments cores were ready for use in lab experiments.

The original intent of this experimental setup is the determination of erosion rates of soil/sediments exposed to increasing hydrologic shear stress. Therefore, although our goal was the release of metals, we recorded changes in the concentrations of total suspended solids (TSS) as a function of increasing hydrodynamic shear stress as well. However, in this case, the total liquid volume was increased to 20 L (**Figure 8**), to allow for the collection of large water volumes needed for the determination of TSS. To generate a quasi-uniform shear stress on the water-sediment interface, a spinning disk and central suction were combined in the erosion head of the Gust Chamber (Green Eyes, 2015; Xie et al., 2015). The water containing TSS flowed through a turbidimeter, and the turbidity of the effluent was recorded. The process was maintained for about 30 minutes until equilibrium was achieved, meaning that the turbidity observed from the turbidimeter was constant at the applied shear stress. In this study, the emphasis was on the measurement of TSS retained on a filter (0.45 μm) as the use of turbidity is not advised as reliable parameter by the manufacturer. The critical shear stress (τ=0.05 Pa), defined as the lowest shear stress which causes observable sediment erosion (Xie et al., 2015; Work and Schoellhamer, 2018), was determined in this process.

3.5.1. Metals released from contaminated sediments over time in the absence and presence of a capping substrate under a fixed hydrodynamic critical shear stress (τ=0.05 Pa). For each pair of prepared sediment cores, the capping substrate was added to one (cap layer of 24 mm in thickness) and the other served as control (no cap). A total volume of 1.7 L of water (including the overlying water in the core, water in the tubes and in the sampling container (**Figure 9**). The hydrologic disturbance in these cores was initiated through computer-controlled erosion heads equipped with a motor which makes the water in the chamber rotate and then exerts a shear stress across the sediment-water interface. The relevant calibration equations for the rotation speed, shear velocity, shear stresses, and pumping rates are as follows (Gust & Müller, 1997), where v_{15} is the shear velocity (cm/s) at 15°C, n is the disk rotation rate in rotations per minute, τ is the bottom shear stress (Pa) and ρ is the water density (g/cm^3), Q is the pumping rate in mL/min.

$$v_{15} = 0.0318 \cdot n^{0.763} \quad \text{Eq.4}$$

$$\tau = {v_{15}}^2 \cdot \rho \quad \text{Eq.5}$$

$$Q = -28.31 \cdot {v_{15}}^2 + 170.2 \cdot v_{15} - 23.85 \quad \text{Eq.6}$$

Next, the following equation was used to convert the shear velocity at a given temperature T to equivalent v_{15}, and where v_T is the shear velocity at temperature of T (Gust & Müller, 1997).

$$v_{15} = v_T \cdot (1 + 0.006 \cdot (T - 15)) \quad \text{Eq.7}$$

Water samples (5 mL) were collected as a function of time and acidified with trace metal grade HNO_3 at a final concentration of 5% (v/v), then heated for 12 hours at 60°C. After cooling down, the samples were filtered (0.45 µm) and then analyzed for the total metal concentrations by ICP-MS as described earlier.

For these experiments, the hydrologic disturbance was initiated by applying a constant shear stress equivalent to the critical shear stress value ($\tau = 0.05$ Pa), selected after tests aimed at assessing the effect of τ on sediment resuspension, while recirculating the water at a constant rate between the sediment-core overlying water compartment and the sampling container.

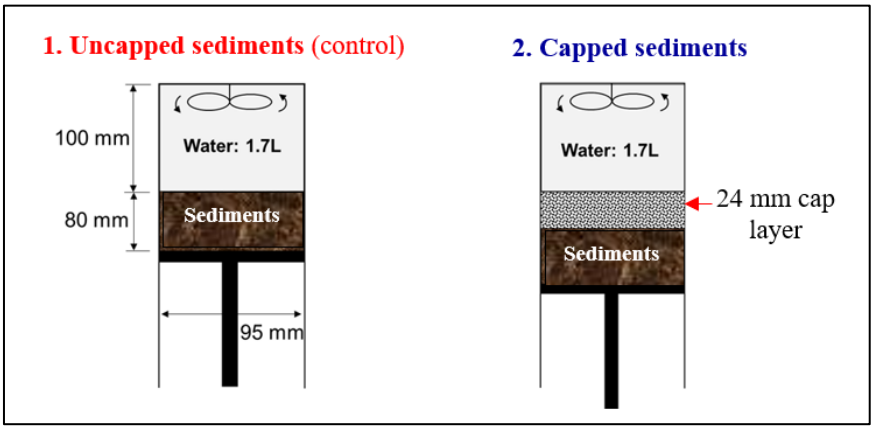


Figure 9. Schematic illustration of metal-contaminated sediment cores used in gust Chambers.

3.5.2. Metals released from contaminated sediments over time in response to increasing hydrodynamic shear stress. Two types of metal-contaminated sediment cores were used in this study: (i) freshwater sediment cores collected from a creek near the University of Florida, and (ii) sediment cores from an intertidal system with oceanic water diluted with freshwater run-off from the land, located at the Naval Air Station in Pensacola, Florida. Total metal concentrations in sediments collected from these sites are given in **Table 4**, in addition to the percentages of the operationally defined mobile fractions.

Table 4. Total concentrations of Cd, Cu, Pb, Cr and Zn in sediments used in this study, and proportions of operationally defined fractions used to assess the potential of sediments to release metals to pore waters. Using a liquid-solid ratio of 20:1 (*v/m*), F1 is extracted with DI-water and F2 is extracted using a 1.0 M CH_3COONa solution, pH = 8.2. Samples were analyzed by ICP-MS.

Sediment types	Parameters	Cu	Zn	Cd	Pb	Cr
Spiked freshwater sandy sediments	Total concentrations (mg/kg)	344 ± 11	492 ± 15	471 ± 4	392 ± 24	-
	% of water-soluble metal fractions (F1)	12.01	71.18	76.80	6.66	-
	% of exchangeable-metal fractions (F2)	10.35	6.78	12.81	32.41	-
Intertidal sediments	Total concentrations (mg/kg)	38 ± 5	90 ± 7	5 ± 0	272 ± 28	264 ± 20
	% of water-soluble metal fractions (F1)	0.89	2.49	1.18	0.79	0.25
	% of exchangeable-metal fractions (F2)	0.69	5.04	13.53	1.98	0.09

For these experiments, the applied shear stress ($\boldsymbol{\tau}$) was varied from 0.05, 0.10, 0.2, 0.3 to 0.4 Pa, and the test time for the application of each shear stress level lasted 12 hours. Water samples

were collected after running the chamber at a given shear stress level and prior to increasing to the next τ value. Collected water samples were processed and analyzed as described above.

3.5.3. Effects of sediment capping on vertical profiles of dissolved metal concentrations in pore waters using diffusive gradient in thin films (DGT) samplers. The flux of metals and other pollutants from contaminated sediments to the overlying water can be measured using passive sampling devices such as the diffusive gradient in thin films (DGT) samplers, which have been widely used over the past two decades (Guan et al., 2016; Harper et al., 1998; Parker et al., 2017; Wu et al., 2015; Zhang et al., 2014; Zhang et al., 1995, 1995; Zhou et al., 2016). DGT technology allows for measurements of solutes present in both pore and overlying waters at different vertical/spatial resolutions. This technology provides an approach for the *in-situ* measurement of the labile forms of metals in waters and sediments (Zhang et al., 1995; Zhang & Davison, 1995).

For metals, DGT samplers are made of a hydrogel binding layer impregnated with Chelex-100 resin where metal ions accumulate. The binding layer is overlaid by a diffusive layer of hydrogel and a filter. Metal ions would diffuse through the filter and the diffusive layer to reach the binding layer. It is the establishment of a constant concentration gradient in the diffusive layer that forms the basis for measuring chemical element concentrations in solution quantitatively. The deployment time can vary from 1 hour to 3 months provided the binding resin is not saturated. DGT based measurements are independent of ionic strength if the range is within 10 mM and 1.0 M. When Chelex-100 is used as the binding resin, the measurement is independent of pH (if its values vary from ~5 to 8.3). The effect of temperature (T) can be predicted from the known T dependence of the diffusion coefficient (Zhang & Davison, 1995).

In this study, DGT samplers were inserted into non-capped and capped sediment cores which have been in the gust chamber for 7 days exposed to a constant shear stress of τ = 0.05 Pa. The DGT samplers were inserted after bringing the shear stress to zero and then left to equilibrate for 24 hours (**Figure 10**).

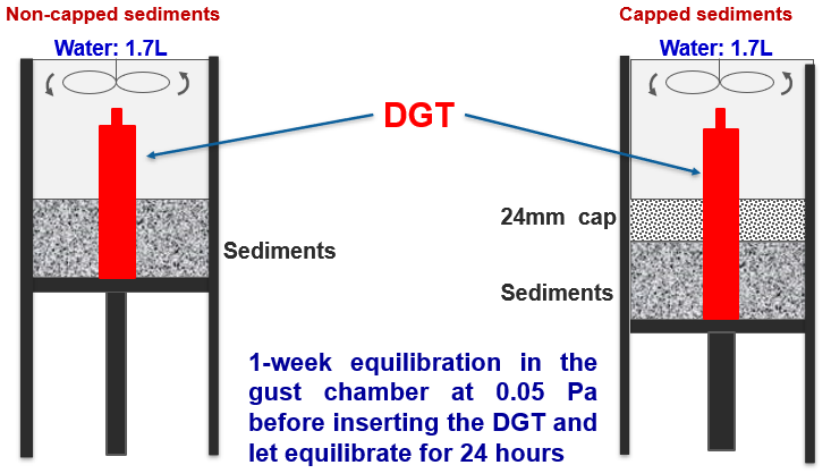


Figure 10. Experimental setup used to determine the depth profiles of dissolved metal concentrations in pore and overlying waters using metal-contaminated sediment cores equilibrated in gust chambers at a fixed τ of 0.05 Pa for 7 days. Uncapped sediments (left) and substrate capped sediments (right).

After the retrieval of the DGT, knowing the surface area (A) of the diffusive layer in contact with the sediment or the overlying water, the flux for a given metal (F) from sediment (or overlying

water) to the DGT probe was calculated using Equation 8, and where M is the accumulated mass and t the deployment time.

$$F = \frac{M}{t \times A} \qquad \text{Eq. 8}$$

The calculated flux can be interpreted as the mean concentration, C_i, at the surface of the probe for the duration of the deployment period and calculated using Eq. 9, and where Δg is the thickness of the diffusive layer (0.094cm) and D is the effective diffusion coefficient in the gel. The D-values in cm^2/s used in this study are: 3.30×10^{-6} for Cu, 3.29×10^{-6} for Cd, $2.73 \times 10^{-6}$for Cr, $3.30 \times 10^{-6}$for Fe, $3.16 \times 10^{-6}$for Mn, 4.34×10^{-6}Pb, and $3.28 \times 10^{-6}$for Zn.

$$C_i = \frac{F \times \Delta g}{D} \qquad \text{Eq. 9}$$

The use of DGT allows insights to the interfacial metal concentrations as well as to the capability of the solid phase to resupply the depleted metal solutes as a function of changing key physicochemical parameters.

3.5.4. Effect of DWTR on metal toxicity to Fathead Minnow (Pimephales promelas) juveniles. 10-day old fathead minnow (FHM) were obtained from Aquatic Biosystems Inc. The water samples used for the exposure studies were from the Gust Chambers where cores of metal-spiked sediments were equilibrated with facility water in either the absence (control) or presence (treatment) of a cap layer made of either sand, apatite, DWTR-OR or DWTR-WY for a period of 7 days under a constant hydrologic shear stress of 0.05 Pa (*see Section 3.5.3*). At the end of the equilibration period and prior to fish exposure studies, water overlying the sediments was withdrawn, filtered (0.45 μm), and the pH adjusted to 7.4.

All fish exposure studies were conducted in sextuplicate with 8 fish per 40 mL beaker. Fifty percent water changes were performed on all beakers each day to provide fresh solutions to the fish. The experiment lasted for 96 hours. The conditions that were tested included: a negative control composed of water from the fish facility, and a positive control composed of 400 μg $CuSO_4 \cdot 5H_2O$/L. Fish were examined daily for mortality, and dead fish were removed from the beakers.

All fish experiments were conducted in strict accordance with protocols approved by the University of Florida IACUC.

4. RESULTS AND DISCUSSION

4.1 Metal content, toxicity characteristics, and screening results.

4.1.1. Determination of the hazardous characteristics of DWTR using the toxicity characteristics leaching procedure (TCLP). Although not used to qualify waste materials for introduction to waterways, the results of TCLP allow for their classification into hazardous and non-hazardous materials. For metals, regulatory guidelines exist for As, Ba, Cd, Cr, Pb, Hg, Se, and Ag. Accordingly, after the extraction of the DWTR samples by two TCLP fluids, the determined total metal concentrations were compared to regulatory guidelines (**Figure 11)**. The results show that concentrations measured in all DWTR samples were far below the regulatory guidelines. Accordingly, based on this test, all tested DWTR would be classified as non-hazardous for disposal in landfills.

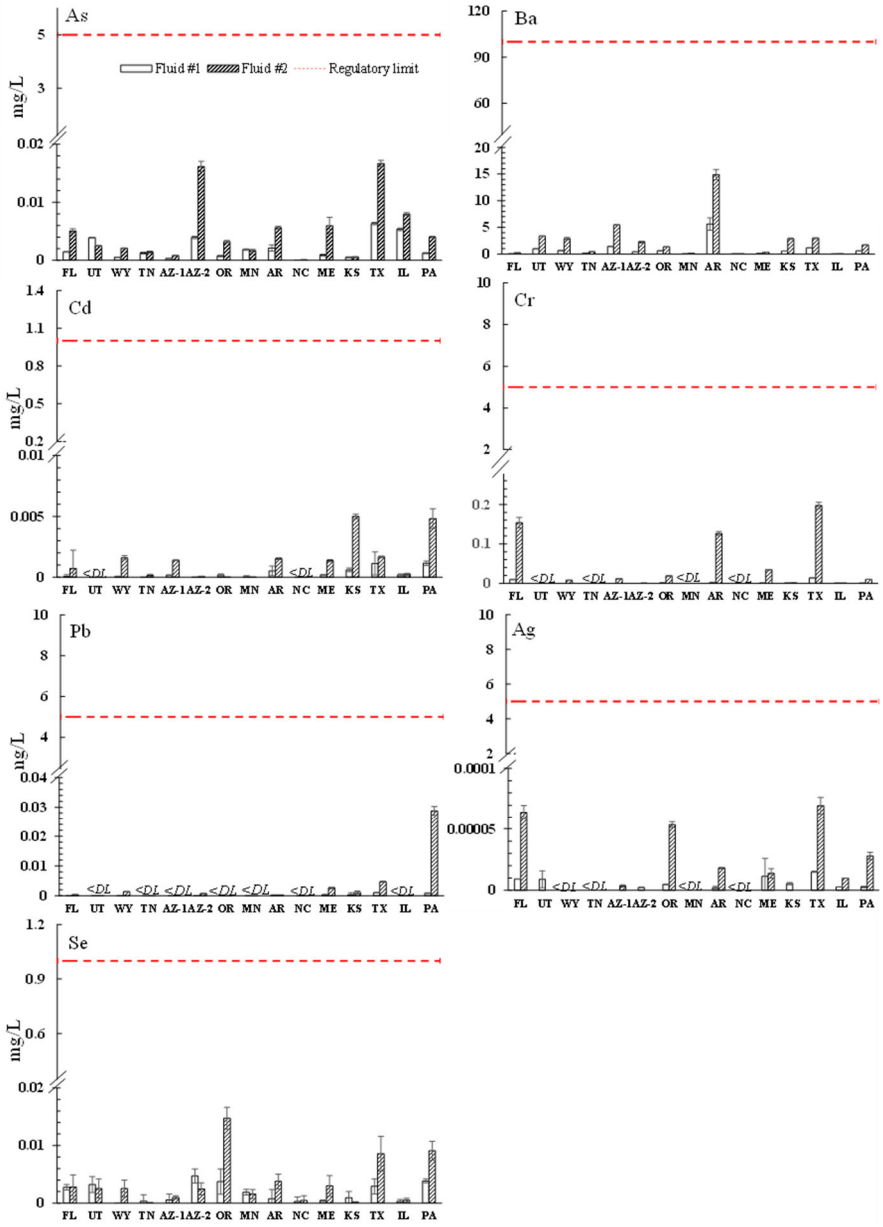
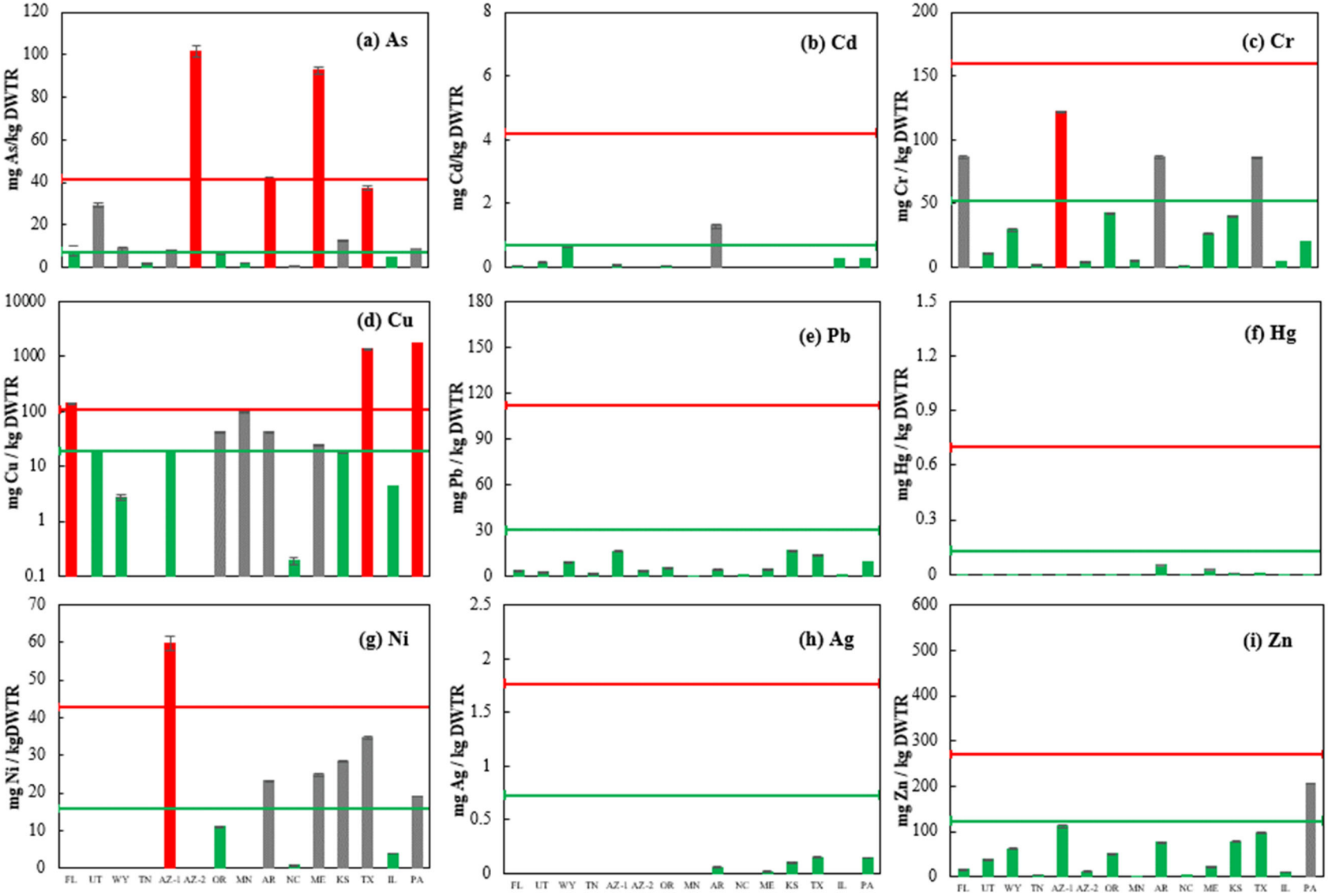


Figure 11. Concentrations of elements extracted from 15 drinking water treatment residuals where only elements with available guideline values are presented. The absence of bars corresponds to values below the analytical detection.

4.1.2. Selection of ideal DWTR samples based on total concentrations of regulated metals and marine sediment quality guidelines. Besides the total concentrations of Al, Ca, and Fe presented earlier in **Table 1**, the DWTR samples were analyzed for the concentrations of As, Cd, Cr, Cu, Pb, Hg, Ni, Ag, and Zn. **Figure 12** gives the concentrations of these elements in comparison to the TEL/TEC (bottom horizontal line) and PEL/PEC (top horizontal line). Based on this approach, DWTR containing chemical elements with concentrations at or exceeding the PEL were assumed to be toxic to marine sediment dwelling organisms and, therefore, not qualified for introduction to United States freshwater and marine systems.

Figure 12. Total metal concentrations in the DWTR samples. The red horizontal lines are the PEL values while the green lines correspond to TEL values. DWTR with red bars for any of the metals should be considered not suitable for introduction to U.S. waters.



A total of 7 samples did not pass this screening method because the total concentrations of arsenic (As) exceeded the PEL in AZ-2, AR, and ME; Cu in FL, TX, and PA; and Ni in AZ-1. The SQG approach systematically excludes substrates based on total metal contents. However, total metal concentrations, although high, may not necessarily translate into adverse biological impacts to exposed organisms because the metals may not be bioavailable. Overall, only 8 DWTR samples out of the tested 15 were deemed acceptable for marine systems (**Figure 12**).

4.1.3. Saltwater elutriation results: Metals leached from the selected DWTR samples with synthetic saltwater (35‰ salinity) prepared using Instant Ocean®. Only 3 of the DWTR samples (OR, WY, NC, and a mixture of OR+NC) that passed the above two screening tests were screened further using the elutriation test. Except for copper (**Figure 13**), the concentrations of all leached metals were below the maximum levels for Aquatic Life Ambient Water Quality Criteria (WQC). For copper, the CMC for acute toxicity is 4.8 μg/L (ppb), and the criterion continuous concentration (CCC) for chronic exposure is 3.1 μg/L. Concentrations measured in the DWTR extracts ranged from about 8 to 15 μg/L, which are about 3.3 to 5 times higher than the CMC and CCC, respectively. Regarding the disposal of dredged materials into waterways, when the concentration (C_e) of a dissolved contaminant in elutriate is greater than the applicable WQC (C_{wq}), a dilution becomes necessary to meet the guidelines. Therefore, compliance with the WQC becomes subject to running an appropriate numerical mixing model with the data from the chemical analysis of elutriate to determine the dilution (D) requirements (USEPA, 1991). For the contaminant of concern, Cu in this case, **Eq. 10** is used, and where: C_e is the concentration of the dissolved contaminant of concern in the standard elutriate in μg/L, C_{wq} is the applicable marine WQC in μg/L; and C_{ds} is the background concentration of the same contaminant at the disposal site in μg/L (USEPA, 1991).

$$D = \frac{(C_e - C_{wq})}{(C_{wq} - C_{ds})} \qquad \textit{Eq. 10}$$

Accordingly, when the leached concentrations of regulated metals exceed the CMC and CCC, the process described above is used and it requires information specific to the site under consideration. For illustration, **Table 5** shows example dilution factors (D) calculated for each of the DWTR based on the criteria for introduction of fill materials to US marine systems using Eq.10, and assuming a negligible or near zero background concentration of Cu at the targeted site.

Table 5. Calculated dilution factors (D) based on leached Cu concentrations and the criterion continuous concentration (CCC) of 3.1 μg/L, and assuming non-detectable dissolved Cu in the water of the targeted site.

DWTR samples	Concentrations of total dissolved Cu in elutriates (μg/L)	Dilution factor (D) based on total dissolved Cu concentrations
DWTR-OR	9.58	2.09
DWTR-WY	8.00	1.58
DWTR-NC	13.21	3.26
DWTR-OR/NC	14.71	3.74

It is worth noting that these elutriate studies give total concentrations of dissolved metals, but no information on the actual chemical speciation of metals. Several key water parameters are known modulators of the toxicity of metals in waters, and total concentrations alone may not be adequate in the derivation of WQC when assessing the adverse effects on aquatic organisms.

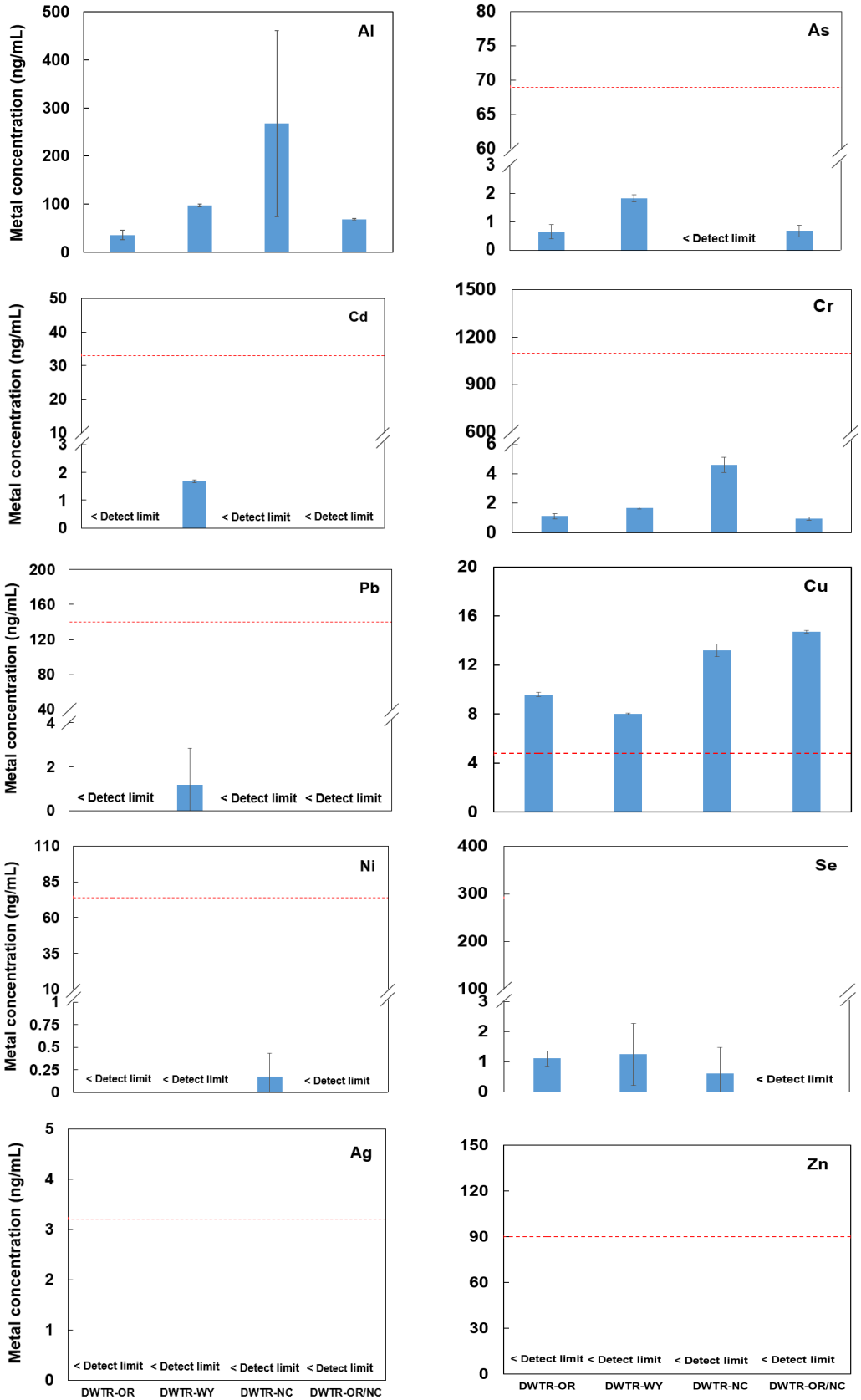


Figure 13. Saltwater elutriation results obtained from the analysis of 4 drinking water treatment residual samples (OR, WY, NC, and a mixture of OR+NC in a 9 to 1 mass ratio). Horizontal dotted lines represent the EPA's ambient water quality criteria for each of the elements.

4.1.4. Metal content of DWTR and sediment quality guidelines for freshwater sediments. **Figure 14** gives the total concentrations of As, Cd, Cr, Cu, Pb, Hg, Ni, and Zn determined in the DWTR samples plotted in comparison with the consensus-based threshold effect concentrations (TEC) and probable effect concentrations (PEC) represented by the horizontal lines.

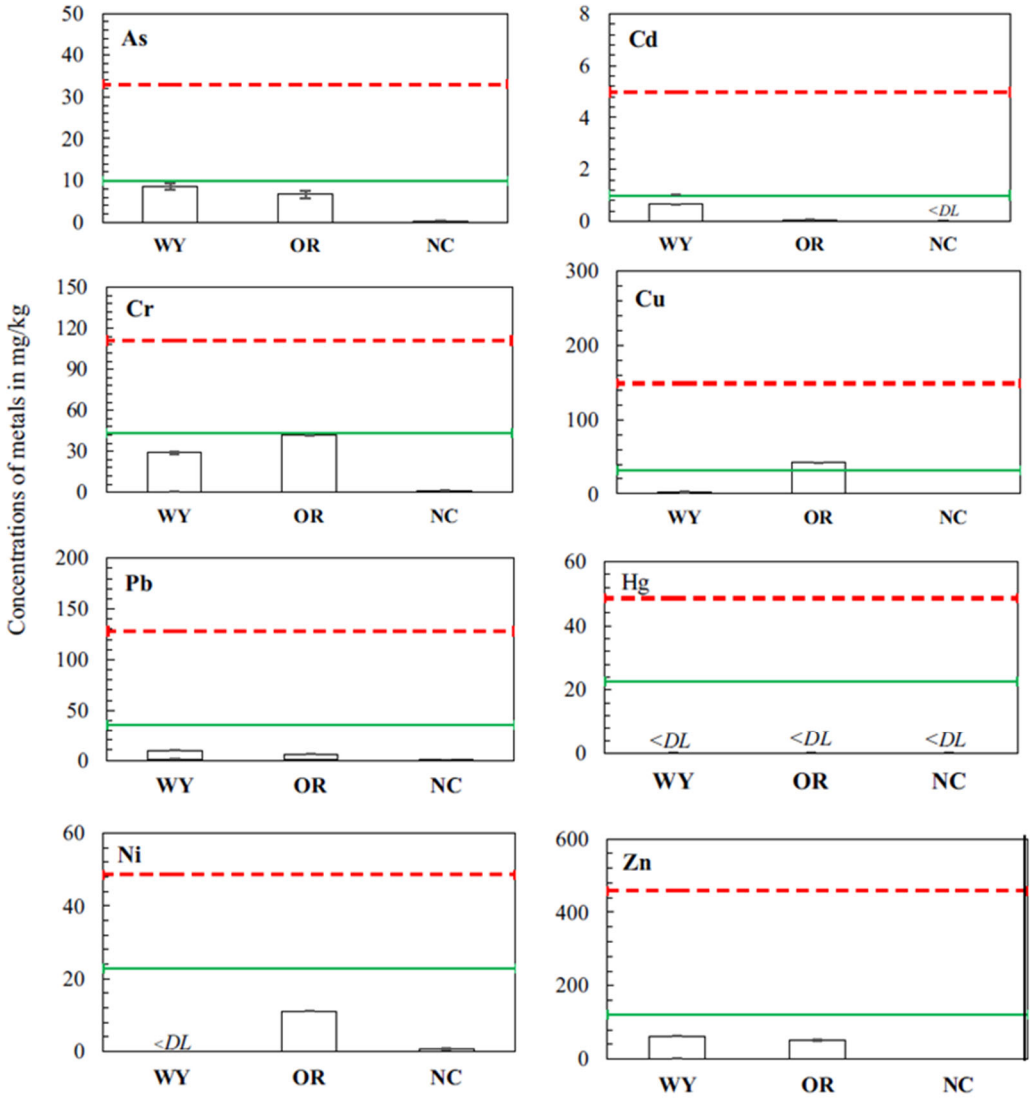


Figure 14. Concentrations of total metals WY, OR, and NC DWTR. The red dotted horizontal lines are the consensus-based probable effect concentrations (PEC) and the solid green horizontal lines are the threshold effect concentrations (TEC). Plotted values are averages (n = 3), and bars are standard deviations. The absence of bars corresponds to metal concentrations are below the analytical detection limit (DL).

Based on this approach, DWTR samples containing any of the above metals at concentrations exceeding the PEC are likely to be toxic to aquatic organisms, while those with metal contents below the TEC would have no noticeable adverse biological impacts. If total metal concentrations fall within the above two endmembers, that is >TEC but <PEC, the samples may or may not induce toxicity. The results show that none of the above-listed metals exceeds the PEC for

the tested DWTR samples. However, Cu exceeded the TEC in the OR sample. Based on this approach, one could hypothesize that DWTR samples such as WY and NC, with total metal concentrations below both the PEC and the TEC, would likely be non-toxic to freshwater benthic organisms. In contrast, exposure to OR, with a total Cu concentration above the TEC, could potentially result in adverse biological effects.

4.1.5. Freshwater elutriation results: metals leached from the selected DWTR samples with synthetic freshwater (USEPA, 2002). Samples of the same DWTR leached with synthetic marine water were used here. The elutriation procedure followed the guidelines established in the Evaluation of Dredged Material Proposed for Ocean Disposal Testing Manual (USEPA, 1991). For each analyzed metal, results were compared to the CMC established by the USEPA's Ambient WQC, corresponding to the concentration at which acute toxic effects are expected. The results are presented in **Figure 15**. Total concentrations of dissolved metals (As, Cd, Cr, Ni, Pb, and Zn) determined in the elutriate solutions were all below the CMC for Aquatic Life Ambient Water Quality Criteria or WQC. However, when compared to the CCC, Pb exceeded the 2.5 µg/L guideline in elutriates obtained from the mixed OR+NC sample, with an average concentration of 5.48 ±1.7 µg/L. Accordingly, one would anticipate Pb to contribute to the toxicity of this sample. For the other detected elements, the WQC is defined based on site-specific water parameters like hardness and dissolved organic carbon (DOC) concentrations for Cu (USEPA 2017); and pH, hardness, and DOC for Al (USEPA 2018). The WQC for protecting freshwater aquatic life from harmful effects are defined as not to exceed 3.1 µg/L in flowing waters and 1.5 µg/L in standing waters, more than once in three years on average. Unfortunately, the lack of DOC data and that of an association of used experimental conditions with a specific freshwater system do not allow for an effective assessment of the potential toxicity of these elements. Nevertheless, the trends of measured concentrations can still be examined in parallel with the recorded toxicity responses of each tested DWTR. It should be noted that these concentrations are total dissolved values and do not allow insight into the chemical speciation of the different elements and their potential for toxicity. Since the ionic strength of the synthetic water used to solubilize these metals is quite similar to that of the solutions used to extract the bioavailable metal fractions from soils (Kim et al., 2015), these measured exchangeable metal fractions could be proxies for the bioavailable metals present in DWTR samples. Based on these results, one could anticipate the toxic responses of exposed organisms to be somewhat high when in contact with the WY sample because of the comparatively higher levels of soluble Cu, Se, Al, and Ni. A similar trend would be expected from exposure to OR+NC because of high Cu and Zn concentrations. In contrast, samples with low extractable metals such as OR should result in rather mild to no toxicity effects to exposed organisms. This hypothetical trend does not overlap with the one outlined above based on total metal contents, and where, following those guidelines, the OR sample would be more toxic than the WY sample based on CMC guidelines.

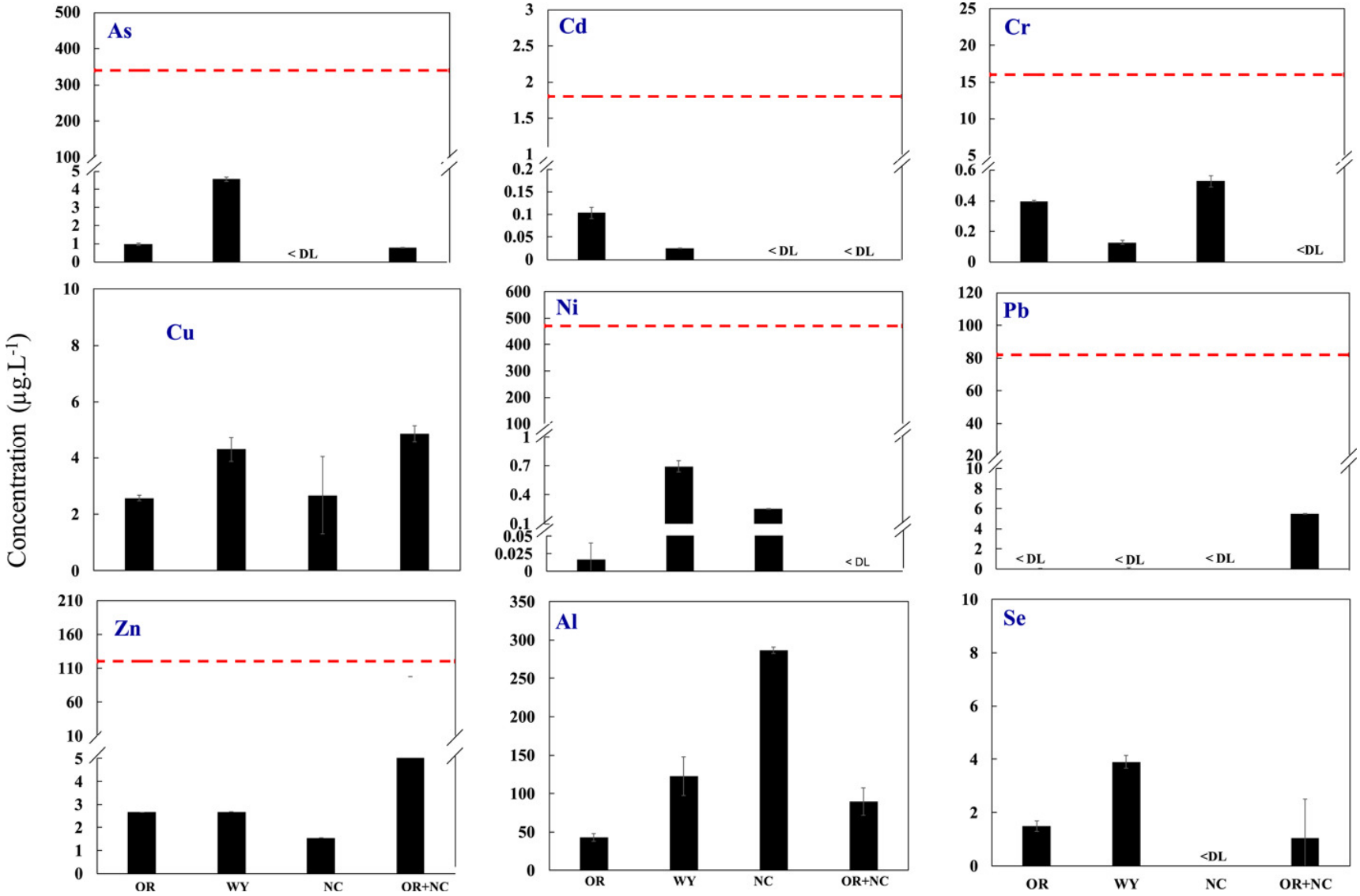


Figure 15. Dissolved total metal concentrations in elutriates from OR, WY, NC, and OR+NC samples. Horizontal dashed red lines are shown only for elements with available EPA's ambient water quality criteria.

4.1.6. Ecotoxicity studies using marine benthic organisms.

*a. 10-day survival test using the marine mysid shrimp **A. bahia***. The results of the survival test are presented in **Figure 16**. The acceptability criterion for this assay was met, in that the mean survival rate in the control exceeded 90%. The tested DWTR samples showed survival responses similar to that of organisms in the control, with no toxicity recorded ($p > 0.05$). Additionally, no statistical differences were observed when all four samples (1 control + 3 DWTR samples) were compared ($p > 0.05$). Overall, the obtained results suggested that it is unlikely that these DWTR would cause acute toxicity to the tested sediment-dwelling organisms.

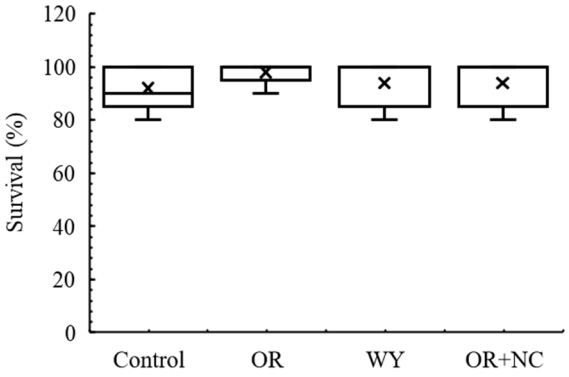


Figure 16. 10-day survival test using the mysid shrimp *Americamysis Bahia*. Results of the test are acceptable because survival rate numbers from the control are ≥ 90%, and no statistically significant difference was observed between the control sediment and any of the DWTR samples.

*b. The 28-day survival and growth tests using the marine species **N. arenaceodentata***. Two endpoints (survival and growth) were measured for these bioassays. For all the tested DWTR, the survival of *N. arenaceodentata* was 100%. In contrast, the growth data varied, but with no significant differences ($p>0.05$) between either the control and any of the tested DWTR or between any two of the tested DWTR were observed (**Figure 17**), and no toxicity.

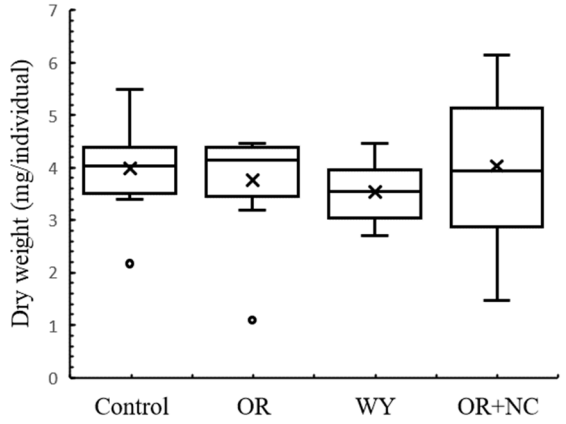


Figure 17. Results of the 28-day growth tests for *N. arenaceodentata*. All DWTR samples passed the chronic toxicity test.

Several studies have tested the toxicity of sediments contaminated with either metals or organic pollutants using *N. arenaceodentata* (Lotufo et al., 2000; Murdoch et al., 1997; Pesch et al., 1995). For instance, in metal-contaminated sediments, toxicity has been linked to the values of molar ratios of acid volatile sulfides (AVS) to simultaneously extracted metals (SEM). For AVS/SEM values <1.0, a very low mortality was observed. In contrast, for values > 1.0 exposures were lethal (Pesch et al., 1995). While AVS/SEM ratios were not measured in this study for adequate comparison, it is obvious that the bioavailability of the contaminants present in the sediments does drive the observed biological responses. The nearly irreversible sorption of contaminants such as phosphorus by DWTR (Miller et al., 2011), suggests that the bioavailability of DWTR-bound chemicals may be very limited, resulting in little to no toxicity to exposed benthic organisms.

4.1.7. Ecotoxicity studies using freshwater benthic organisms.

a. 10-day survival and growth of the midge fly Chironomus tentans. **Figure 18** gives the results of survival (18a) and growth (18b) bioassays using *C. tentans*. This acute toxicity study shows that the OR sample resulted in survival and growth rates that were not significantly different from the control samples. In contrast, both the survival and growth of *C. tentans* were adversely impacted when exposed to WY, as compared to controls. We can note that in the WY sample, the elutriate concentration of Se exceeded the reference values of 3.1 µg/L for flowing waters and 1.5 µg/L for standing waters and could therefore contribute to the observed toxicity. However, the trend of these toxicity results is not fully in line with the observations made based on both the elutriate study and total metal content results. Therefore, the observed biological responses cannot be explained based on metal data only. Looking at the trend of temperatures during the exposure studies, measured values for all treatments were similar, excluding the potential for a significant impact of this parameter. In contrast, the trends of dissolved oxygen (DO) concentrations showed a clear separation between control and treatment samples, with less oxygen in the control chambers. The results are rather counter-intuitive, in that the lowest measured survival and growth rates are recorded in the presence of high DO levels. While the lethal and sublethal effects of low DO levels have been reported for both *C. tentans* and *H. azteca* (Irving et al. 2004), experimental data do also suggest that *Chironomus* larvae and several other aquatic invertebrates can be harmed by high DO levels (Fox and Taylor, 1954 and 1955), but only in exposure conditions lacking solid substrates. In this study, the observed lower DO levels in chambers with control sediments are likely due to higher microbial respiration from the microflora present in the sediments as compared to the treatment chambers containing only DWTRs as substrates. Finally, and unlike the OR and WY samples, the hybrid OR+NC sample gave mixed results by passing the survival test but failing the growth test.
Overall, using the combination of both 10-day survival and growth test results, our findings suggest that only the OR would be an acceptable DWTR substrate for introduction to freshwater systems based on the US WQC, while WY and OR+NC could potentially result in adverse ecological impacts. Although these results seem to imply that total metal concentrations and metals solubilized using synthetic freshwater might not be good predictors of the toxicity of DWTR to *C. tentans*, it is worth noting that this conclusion is based on the statistical significance of the differences observed in measured endpoints between controls and treatments. However, data presented in **Figure 18** show that *C. tentans* does survive (34 and 49 % as compared to controls) and grow (61 to 78.5% as compared to controls) when exposed to either WY or OR+NC. Therefore, a long-term exposure study such as the 65-day life cycle test would be necessary to verify if the test organism could recover from the initial adverse effects of DWTR.

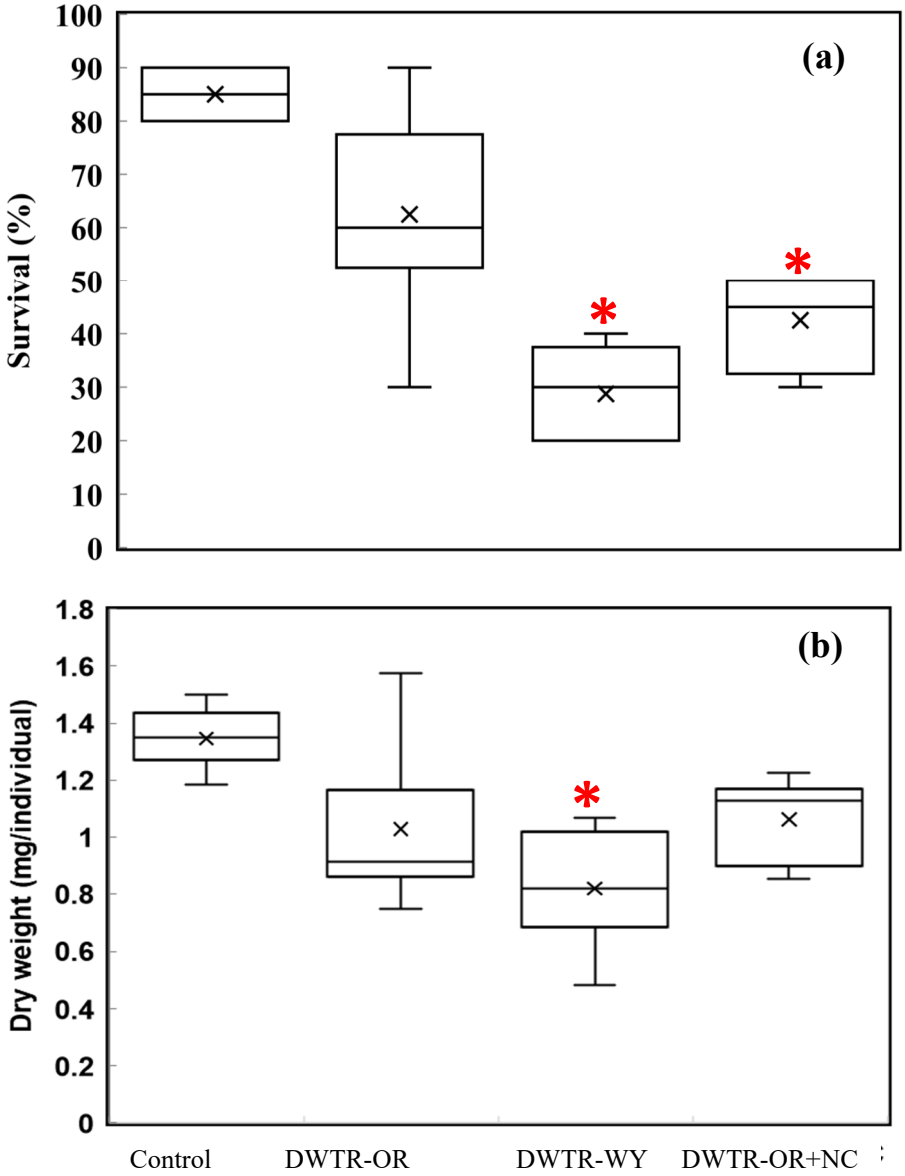


Figure 18. The results of *10-day* survival **(a)** and growth **(b)** tests using the midge *Chironomus tentans*. The stars indicate statistically significant differences between the control sediments and DWTR samples.

b. 65-day life cycle test using the midge fly Chironomus tentans. For this test, the endpoints included survival (%), adult emergence (%), egg case production (%), and the number of eggs produced per female. The results are presented in **Figure 19**. In contrast to the results obtained from the 10-day survival and growth tests discussed above, all tested DWTR samples performed as well as the controls, with average values better than the controls in most cases. Monitored temperature and DO in the aqueous phase during the exposure studies were similar in the controls and each of the different treatments. Trends in pH showed an initial separation between the control (with values

as low as 7.4) and the different treatments (with pH values at or >7.7) during the first week before becoming similar. However, these rather minor differences had no significant effects based on the statistical comparison of the endpoints. Overall, these results contradict those obtained from the short-term exposure assays for WY and OR+NC and suggest that the biological responses of *C. tentans* likely depend on a combination of factors, and not only on metal contents. Comparatively, more weight should be given to the long-term than to the short-term exposure results, as the former offers the possibility to account for recovery following the initial acute toxic effects. Therefore, all tested DWTR samples show no chronic toxicity towards larvae of *C. tentans*, a conclusion that is in line with the fact that total metal concentration is not a good predictor of toxicity.

c. 10-day survival and growth tests using the amphipod Hyalella azteca. Common in North and South America's freshwaters, *H. azteca* is very sensitive to aquatic contaminants while tolerating a wide range of DO concentrations, sediment grain size, and organic matter content (Wang 2004). The results obtained in this study using both survival and growth tests showed that the tested DWTR samples were not toxic, with no significant statistical differences between numbers obtained in the controls and the treatments (**Figure 20**). However, control sediments did perform slightly better than the treatments, and a decreasing trend in average values was observed for growth in the order: controls, OR, WY, and OR+NC. From these decreasing trends, it appears that the growth of test organisms was more affected by the different DWTR samples than their survival rates. Monitored temperatures and DO during the exposure studies were similar, with no statistical differences between the controls and each of the treatments, or between any two treatments.

Based on this short-term assay, the tested DWTR samples would be acceptable for introduction to freshwater systems.

Samples WY and OR+NC failed the survival test when compared to the control (**Figure 21a**). However, all tested DWTR samples passed the growth test (**Figure 21b**), that is, no statistical differences were observed when comparing each of the DWTR samples to the control, or when the different DWTR samples were compared to each other. Given the similarities in temperatures and DO-values recorded during the exposure studies, the observed toxicity response for the WY sample, for example, cannot be explained by considering simply total metal contents and trends of metals leached out in elutriate studies. Measurements of the toxicity of DWTRs, as conducted in this study, consider not only the potential adverse effects of metals but that of any other toxic substances present in the DWTRs.

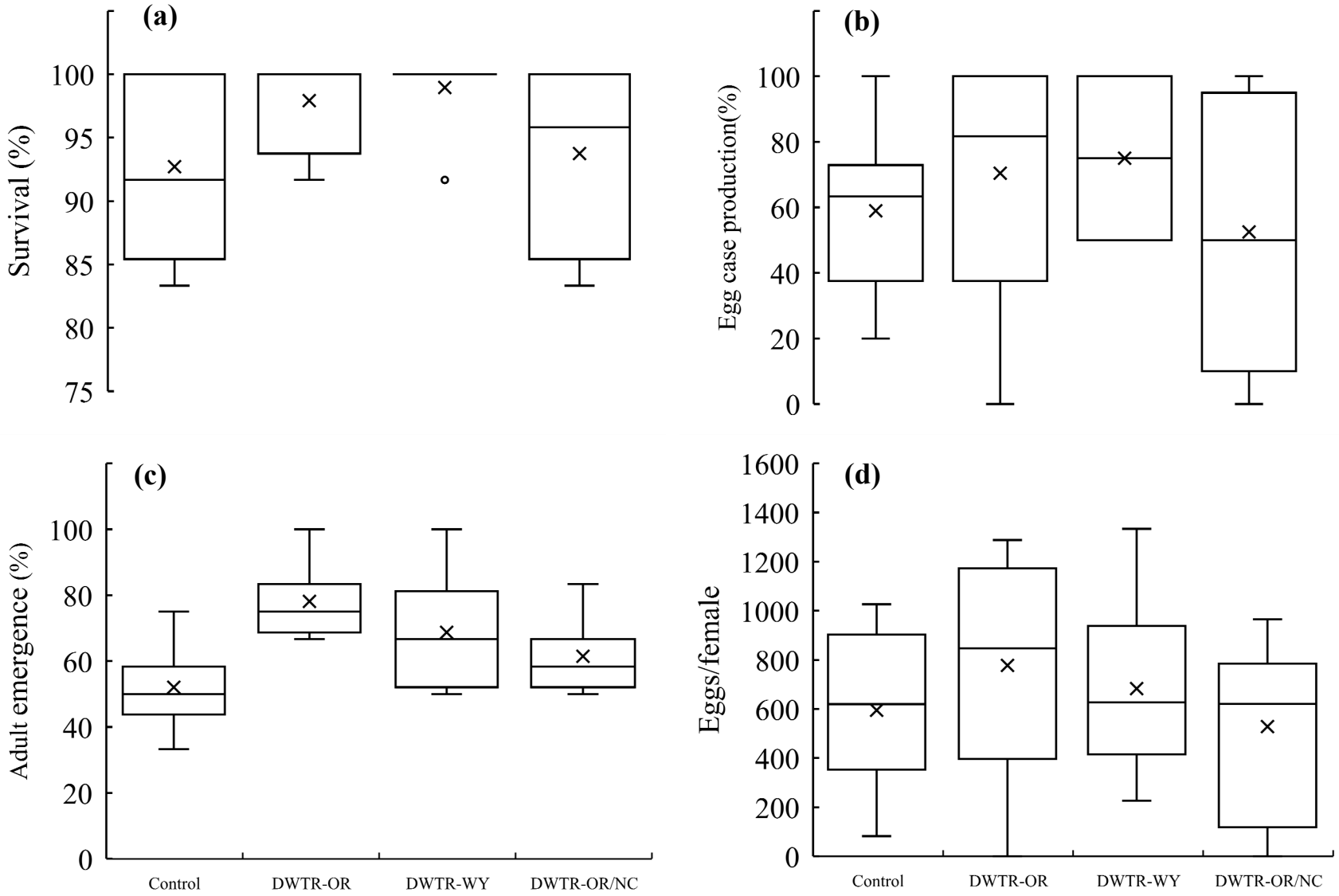


Figure 19. Results of the 65-day life cycle test using the midge *Chironomus tentans*. (a) Survival, (b) adult emergence, (c) egg case production, and (d) number of eggs produced per female.

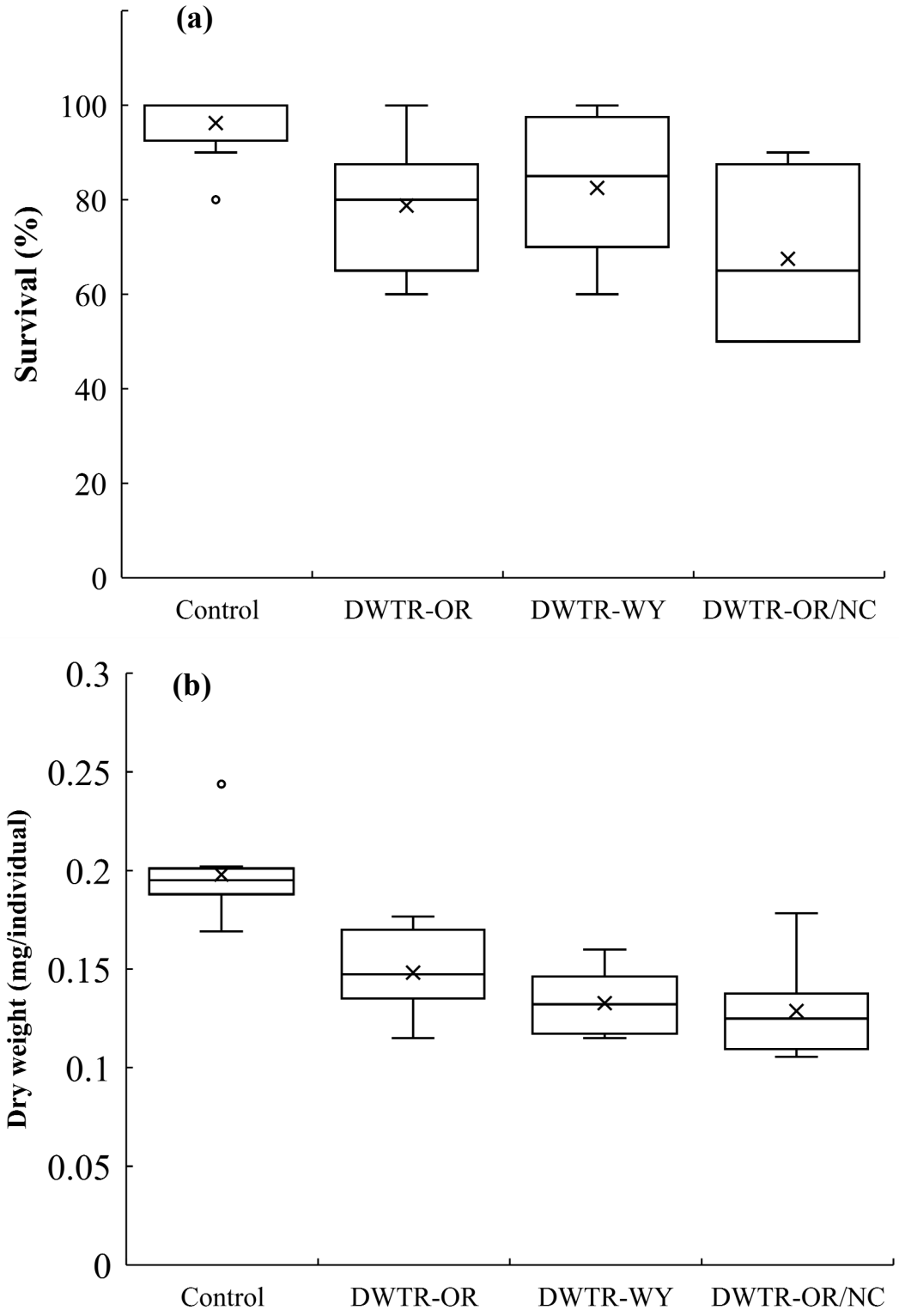


Figure 20. Results of the *10-day* survival (a) and growth (b) tests using the amphipod *Hyalella azteca*.

***d**. 28-day survival and growth tests using the amphipod Hyalella azteca*. In contrast to the acute exposure studies in which the recorded biological responses were statistically similar in both control and treatment chambers, the 28-day assays gave mixed results **(Figure 21**).

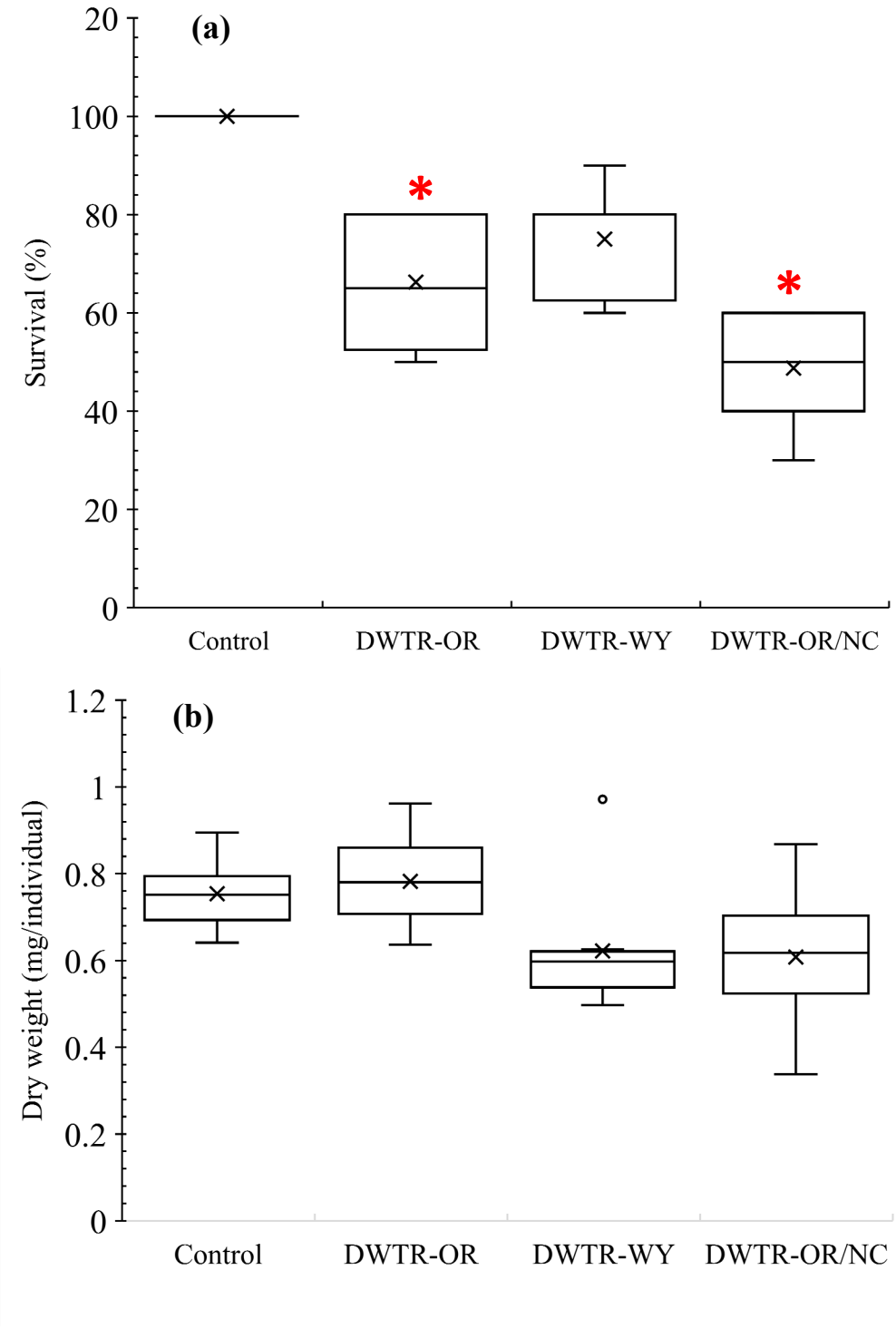


Figure 21. The results of 28-day survival **(a)** and growth **(b)** tests using *Hyalella azteca*. Asterisks indicate statistically significant differences between the control and treatment samples.

4.2. Characterization of DWTR

Six DWTR samples (MN, NC, OR, TN, UT, and WY) were selected for advanced characterization studies. The selection emphasized differences in the additive used, in addition to differences of the chemistries of treated raw waters.

4.2.1. Thermogravimetric mass spectrometry results. Thermogravimetric results are presented in **Figure 22.** These data divide the tested 6 DWTR samples into two groups: those with relatively consistent declines in mass from 100-600˚C, and those which see steep declines in mass above 600˚C. This division corresponds with the use of lime as an additive. Above 600˚C, carbonate minerals decompose, releasing carbon dioxide; the high mass loss in that region is tied to high carbonate mineral content in lime based DWTRs (MN, NC, TN). Mass loss in other regions is broadly indicative of the organic matter and water content of these materials. Below 200˚C, most mass loss will be connected to the dehydration of the materials. Between 200 and 600˚C, several decomposition processes may contribute to mass loss.

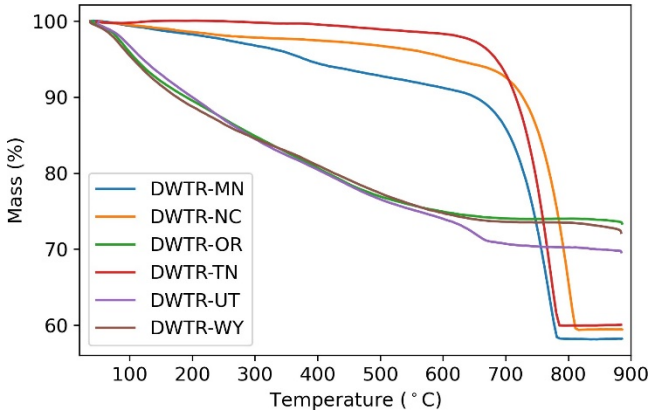


Figure 22. Thermogravimetric results for DWTR samples. Mass of the DWTR, shown as the percentage of the mass relative to the mass at the end of the initial isothermal step, is compared to temperature.

DWTR Samples		Mass loss (%) 200-430˚C	430-600˚C	600-825˚C
Lime-based	NC	1.3	2.0	35.9
	MN	4.4	2.7	33.1
	TN	0.7	1.1	38.4
Non-lime based	OR	10.1	4.5	1.0
	UT	10.8	5.2	3.9
	WY	8.9	5.1	1.4

Table 6 Thermogravimetric analysis results for DWTR samples, showing the percentage mass loss over specified temperature ranges. Mass loss from (1.) 200-430˚C may be attributed to organic matter decomposition, (2.) 430-600˚C inorganic material decomposition, and (3.) 600-825˚C carbonate mineral decomposition.

Mass losses in these regions are presented in **Table 6** DWTRs without lime lose approximately 10% of their mass in the "organic" region for TGA; by comparison, NC and

TN samples lose much less, approximately 1%. MN is intermediate to these extremes, but because magnesium hydroxide decomposes in a similar region, further evidence through mass spectrometry and elemental analysis will be needed to assert that MN has more organic matter than its lime-based peers.

Figure 23 shows the peak areas of two mass-to-charge ratios from the mass spectra of the gases released from the DWTRs as a function of temperature: water (*m/z 18*) and carbon dioxide (*m/z 44*). The steep release of carbon dioxide in lime-based DWTRs (and, to a lesser extent, DWTR-UT) further validate the connection between mass loss above 600˚C and carbonate decomposition.

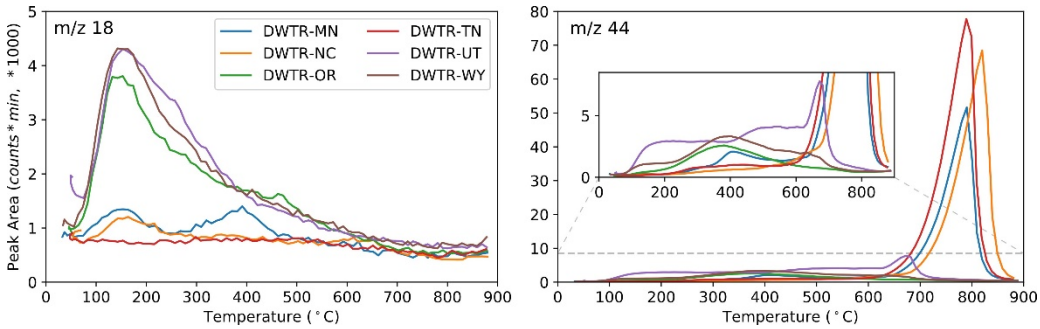


Figure 23. Peak areas as a function of temperature for *m/z* 18 (water, left subplot) and 44 (carbon dioxide, right subplot) from the mass spectra collected from the TGA-MS. Note the difference in y-axis scales for these two subplots: carbon dioxide reaches much larger peak areas (nearly 80,000 *counts per min*), specifically above 600˚C in lime-based DWTRs. The inset in the bottom subplot zooms in to provide detail at lower temperatures and in non-lime based DWTRs.

Assuming all mass loss in that region is due to the release of carbon dioxide, carbon from carbonates will make up less than 0.5% of the mass in OR and WY samples; 1.1% of the UT sample; and range from 9.0% (MN) to 10.5% (TN) in the lime based DWTRs. Provided that all this inorganic carbon is in the form of calcium carbonate, lime based DWTRs are found by Equation 10 to range from 75% (MN) to 87% (TN) calcium carbonate. Particularly at 87% calcium carbonate, these findings align with the order-of-magnitude increase in waste volume at lime softening drinking water treatment plants.

$$CaCO_3 \rightarrow CaO + CO_{2(g)} \qquad \text{Eq. 10}$$

The peak areas in the lower temperature ranges show that the phases contributing to mass loss here are less clear-cut. DWTRs OR, WY, and MN have distinct peaks in the release of carbon dioxide near 400˚C, which would suggest the decomposition of organic matter could be significant near that temperature. However, that carbon dioxide release tails off well above the 430˚C informal threshold between organic matter and inorganic decomposition. The peak for water (m/z 18) near 400˚C in the MN sample also doesn't discount the dehydration of magnesium hydroxide driving some change in mass for that sample, though both the change in mass and the release of carbon dioxide are strong indicators that MN has greater quantities of organic matter than the other lime-based samples. Moreover, UT sees relatively consistent release of carbon dioxide from 100- 600˚C. A better understanding of these processes may be achieved by tracking the release of higher m/z ions attributable to organic matter, though more

precise quantification will demand elemental analysis. The mass spectra as a function of temperature for higher m/z values, ranging from 50 to 150, are shown in **Figure 24.** Lime-based DWTRs MN, NC, and TN show low intensity and low diversity in the peaks here. MN, and to a lesser extent, NC, show some high- temperature release of an ion at m/z 64, which could be attributable to the decomposition of sulfates and the release of SO_2. DWTRs without lime (OR, UT, and WY) show much higher intensity and diversity in their mass spectra at this m/z range. The peak forests here show a clear division between lime- and non-lime-based DWTRs. Lime- based DWTRs (MN, NC, TN) show relatively low peak areas and diversity in this range, while non-lime-based DWTRs (OR, UT, WY) show intense, diverse peaks, particularly between 300-600°C, but also spreading into lower and higher temperature ranges.

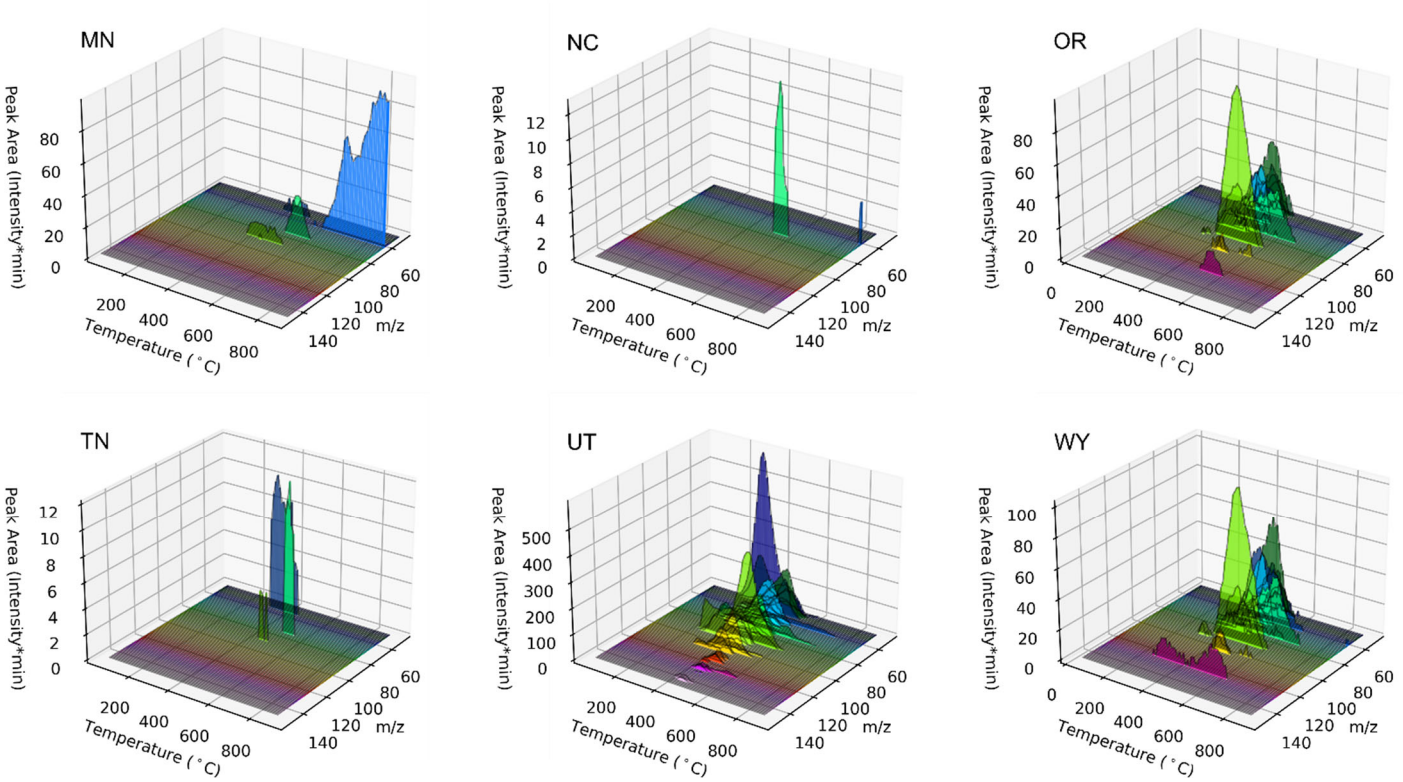


Figure 24. Peak forests showing the area corresponding to each ion across the temperature range for TGA-MS analysis. Results are shown for $50 < m/z < 150$ during the rising temperature portion of the experiment. Note the differences in the scales for the peak areas recorded.

4.2.2. Specific surface area and microporosity. BET surface area results are presented in Figure 5.5 along with pore size distributions. SSA of the samples tested vary between 7.23 to 197.6 m^2/g for TN and UT samples, respectively.

The UT sample shows an especially large pore volume in the micropore region, which drives its large BET surface area and is likely due to the use of activated carbon as an additive. WY also contains activated carbon as an additive, but that limited fraction does not lead to a similarly high surface area or microporosity. Among the lime- based DWTRs, MN and TN both have relatively low calculated surface areas. NC is the exception, using lime as an additive and possessing the second-highest BET surface area among all samples. Except

for the UT sample, microporosity is limited in these DWTRs, which should be accurately characterized as mesoporous.

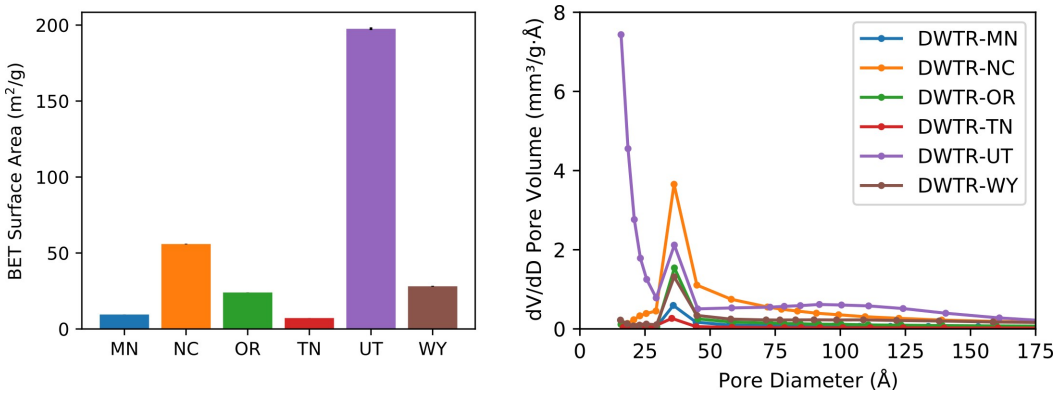


Figure 25. BET surface area results for the six DWTR samples. Calculated surface areas, along with the uncertainties of the fit to the BET model, are displayed in the left subplot. Pore volume distribution for DWTRs as a function of pore diameter are shown in the right subplot. Results were calculated using desorption data with the BJH method.

4.2.3. Elemental analysis. CHNS results are presented in **Figure 26**, with each element plotted as its percentage mass in the DWTR in Subplot A. The lime-based DWTRs have a very high quantity of acid-volatile carbon; the quantities here are well-aligned with those estimated from TGA-MS, with findings through CHNS of 9.34 ±0.09% acid-volatile carbon in MN, 9.58 ±0.05% in NC, and 10.4 ±0.1% in TN (compared with 9.0, 9.8, and 10.5% carbonate carbon, respectively, by TGA-MS). In contrast, the non-lime based DWTRs tend to have very high standard deviations for measurements of inorganic carbon relative to the mean findings. DWTR-WY had an especially large variance in measurements of both acid-volatile and non-acid-volatile C not seen in H, N, or S measurements. This indicates heterogeneity specific to carbon measurements, which may be attributable to some non-uniformity in the distribution of the activated carbon additive for WY.

The non-acid-volatile carbon measurements follow a general pattern where they are least abundant in lime-based DWTRs, more abundant in OR and WY, and most abundant in UT. The non-acid-volatile C is generally attributable to organic carbon (Phillips et al., 2011), but it also will include activated carbon in both the UT and WY samples. These results confirmed what was observed previously by the determination of the specific surface area, *i.e.,* the large fraction of non-acid-volatile C in the UT sample compared to any of the other samples is likely due to a large addition of activated carbon. Within the lime-based DWTRs, MN has nearly double the non-acid-volatile C content (1.86 ±0.09%) compared to the next-highest sample (1.0±0.1% for TN). Subplot B of **Figure 26** shows the molar fraction of N and S in the DWTRs. As before, lime-based DWTRs show significantly lower concentrations of these elements than non-lime-based DWTRs. In the group without lime, some of the effects from before are slightly tempered without the influence of activated carbon. UT, which has the highest non-acid-volatile C fraction, also has the highest quantities of N and S; WY, which clearly had the second-most non-acid-volatile C, is on par with OR in terms of concentration

for N and S. In the lime group, MN has the greatest quantity of N and S combined – a notable finding, considering MN is the only DWTR in this set that does not include a synthetic organic polymer. NC has a disproportionately high concentration of S along with a very low concentration of N. It is also the only DWTR sample to be drawn exclusively from groundwater. Given the occurrence of reducing conditions in aquifers of the region (Degnan et al., 2020), this could be reflective of a small, but still impactful fraction of sulfide minerals pulled up from the aquifer. The CHNS findings for the UT sample along with the division between DWTRs with and without lime highlight the contribution of chemical additives to DWTR composition; however, the MN and NC sample results show that the influence of source water chemistry, particularly on these elements, cannot be discounted.

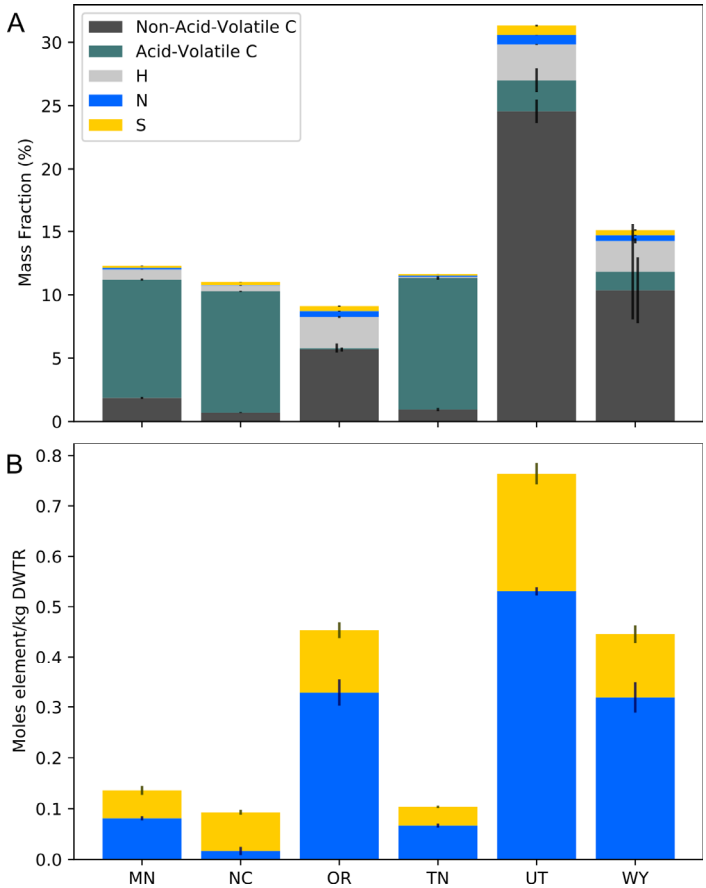


Figure 26. CHNS elemental analysis results for DWTR samples. Subplot A shows the mass fractions of H, S, N, and acid-volatile and non-acid-volatile carbon in terms of the percent mass of the DWTR. Subplot B shows the moles of N and S per kg DWTR.

4.2.4. X-Ray Fluorescence. To detect the presence of dominant elements in DWTR samples, we used XRF. Results are presented in **Figure 27.** Fluorescent yield (ω) increases with increasing atomic number (Bertin, 1975); as such, despite the relatively high expected concentrations of Al from the coagulants, the limited fluorescent yield of x-rays by this element limits the intensity of the peaks. It is also worth emphasizing that direct comparisons of the peak size for different samples only provide limited meaning. Factors, including the thickness of the sample, will impact the intensities of the XRF spectra. However, relative comparisons of elemental abundance are possible. For example, WY has a peak for

iron that is larger than its peak for Ca, while NC has a peak for Ca that is larger than its peak for Fe. Ergo, NC will have a greater ratio of Ca to Fe compared to WY, while WY will have a greater ratio of Fe to Ca compared to NC.

DWTRs that use lime as an additive (NC, MN, TN) are dominated by an intense signal at 3.7 keV corresponding to the Ca K_α fluorescence lines (Bertin, 1975). All DWTRs showed some peak there; of the DWTRs without a lime additive, only UT had its largest peak at the Ca K_α line, though relative to the other elements seen in the UT spectrum, this line was less intense than NC, MN, and TN samples. At lower energies, the distinct peak for Cl in the UT sample implies a relatively high salt content in that DWTR. This is unsurprising, given the desert environment of Utah, but it does highlight the caution needed prior to utilizing these materials for environmental remediation in freshwater environments (Zhou et al., 2021b).

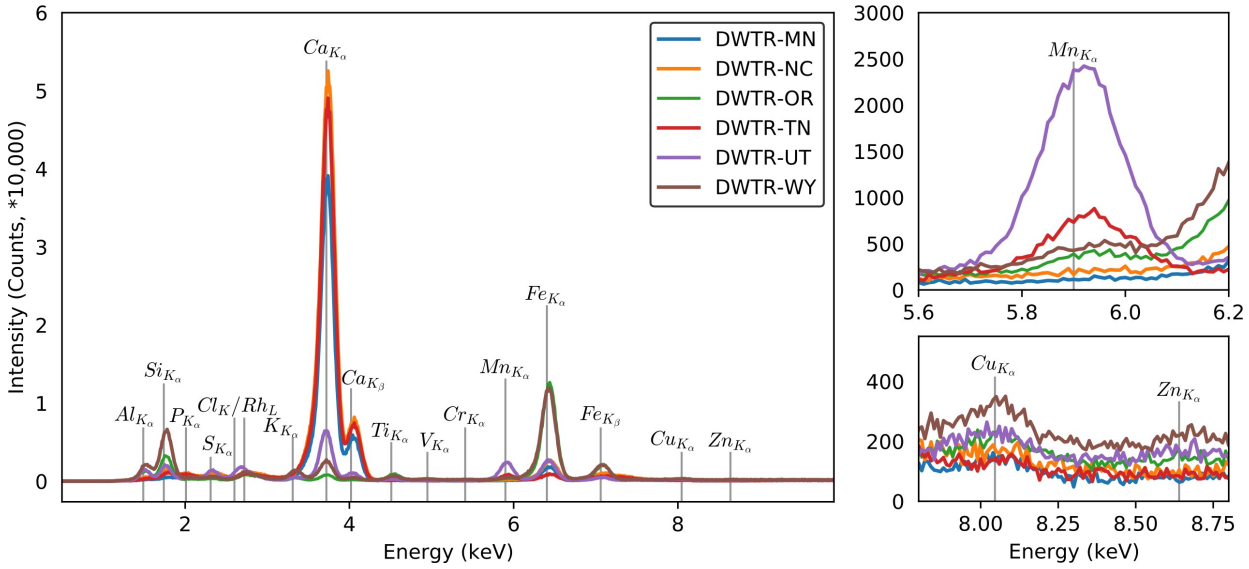


Figure 27. X-ray fluorescence spectra for drinking water treatment residual samples. Spectra were collected at 20 keV and 10 μA with no filter and are not normalized. The left subplot shows the full spectrum for each sample; peaks are immediately discernible down to the Al K_α fluorescence line and up to the Fe K_α fluorescence line. The top right subplot focuses on the Mn K_α fluorescence line. MN and TN have distinct, well-defined peaks here. Signals for OR and WY are also slightly elevated, though the fluorescence here overlaps with what is detected for the high Fe K_α peaks. Finally, the bottom right subplot focuses on Cu K_α and Zn K_α emission lines. Peaks here are poorly defined and very low intensity across all DWTR samples.

Of the elements suitable for XAS analysis at the bending magnet beamline of the Sector 5 of the Advanced Photon Source (APS), only Mn and Fe are present in sufficient quantities to provide a sizable fluorescent signal. Like Ca, all samples show a discernible peak at the Fe K_α line, with WY and OR showing particularly strong fluorescence. On the other hand, UT and TN show the largest signals for Mn. Unsurprisingly, these are the two DWTR samples that include $KMnO_4$ as an additive. OR and WY samples have slightly elevated intensities in the region of the Mn K_α line, but these are strongly influenced by the intense Fe K_α

fluorescence. For other trace elements that may be suitable for XAS analysis, including Cu and Zn, peaks were indistinct and of low intensity. Based on these results, XAS data were collected at the Fe K-edge for all DWTR samples and at the Mn K-edge for UT and TN.

4.2.5. X-Ray Diffraction. In contrast to laboratory-source powder XRD, high-resolution XRD produces a diffraction pattern with especially well-resolved peaks and practically no background signal due to the use of monochromatic X-rays. Hence, it greatly eases mineral identification. The high- resolution XRD patterns for the six DWTR samples are shown in **Figure 28.** Additional high-resolution XRD patterns for DWTRs collected during this study are shown in **Figure 29**.

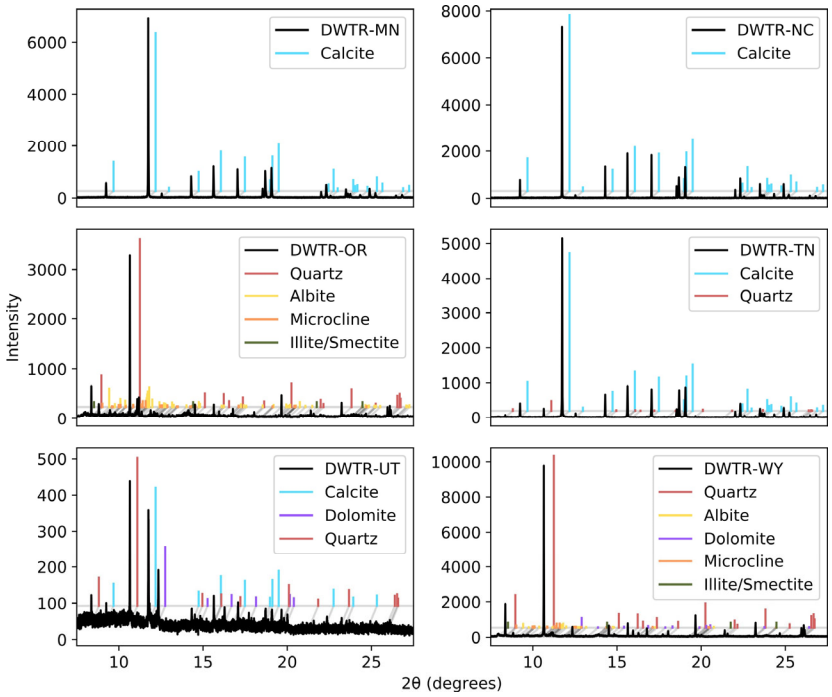


Figure 28. Synchrotron-source X-ray diffraction patterns for the drinking water treatment residual samples, along with identified crystalline mineral phases. Peaks for calcite, quartz, albite, microcline, and dolomite were identified using JADE, as were the clay peaks attributable to either illite or smectite. Note that the intensities are not on the same scales; for instance, NC and WY samples show some especially intense diffraction patterns, while the UT sample has weak diffraction patterns, indicating a poorly crystalline sample.

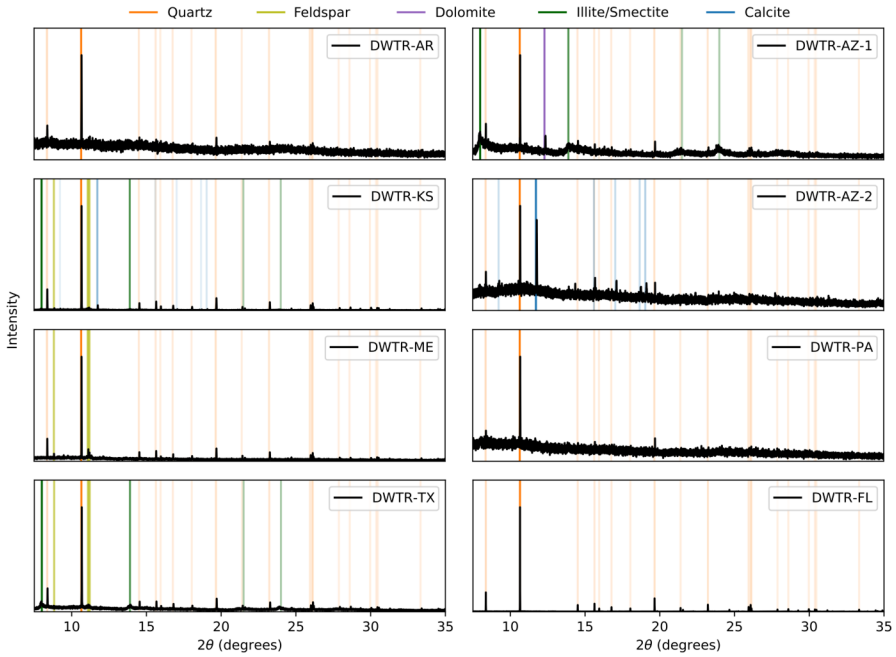


Figure 29. Synchrotron-source X-ray diffraction patterns for the other DWTR samples not studied in detail. Data were collected using the same methodology as for the other six samples. The same phases identified in the main DWTR samples are identified in these other samples in varying combinations, which include clay (illite and/or smectite), feldspar (albite and microcline), carbonate minerals (calcite and dolomite), and quartz. Again, not present in these samples are crystalline iron oxides or aluminum oxides.

Lime-based DWTRs (MN, NC, and TN) showed high-intensity diffraction patterns corresponding to calcite, suggesting an abundance of highly crystalline calcite. Low-intensity peaks for calcite and dolomite were also present in the UT diffraction pattern, whereas in the WY sample, only dolomite was detected. Quartz tends to be ubiquitous in many DWTRs and was identified in the diffraction patterns of TN, UT, OR, and WY. Finally, patterns corresponding to feldspar (albite and microcline) and clay (illite or smectite) were observed in OR and WY samples at low intensities.

Aside from calcite in the lime based DWTRs, all crystalline phases identified correspond to minerals that would originate from the source waters rather than be generated by chemical additives. In fact, each of the identified crystalline phases is commonly found in XRD of sediments (Hardy and Tucker, 1988). Crystalline aluminum and iron hydroxides were not present, and no crystalline manganese minerals can be detected in the UT and TN samples which use $KMnO_4$ as an additive. Aside from calcite, which is ubiquitous in lime based DWTRs, chemical additives applied at DWTPs would generally lead to the formation of amorphous forms. Consequently, a method that probes short range order, such as XAS, is required to assess the amorphous nature of the mineral phases present in DWTRs that can play a significant role in sorption processes. This can be primarily done by looking at the Fe and Mn K-edges.

4.2.6. X-ray Absorption Spectroscopy

a. *Fe K-edge.* First-derivative XANES data at the Fe K-edge and LCF results are presented in **Figure 30** Target transformations based on the first derivative of the spectra performed after principal component analysis are presented in **Figure 31** and **32**. Most of the samples are quite similar with one exception: the spectrum of the MN sample shows very distinct features. There is a pronounced shoulder above 7130 eV and oscillations near 7140 eV. One should note that the MN DWTR is the only one that contains $FeCl_3$ as an additive, which is applied in storage lakes prior to intake for the iron (oxy-)hydroxides. This aligns with previous findings highlighting complex nature of iron minerals in the environment, where ferric iron may be structurally incorporated into clays in significant fractions (Yan et al., 2022), or associated with a wide range of elements beyond what is found in simple iron oxides or oxy-hydroxides (Perret et al., 2000).

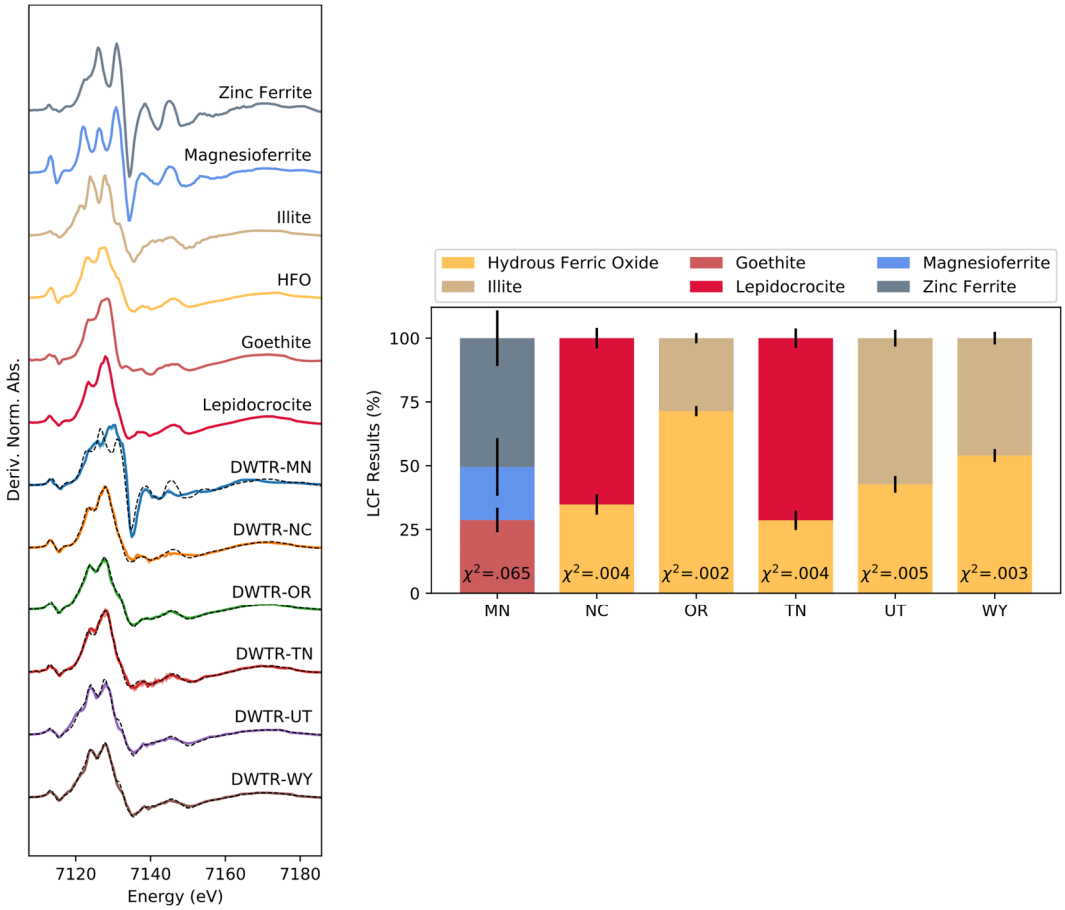


Figure 30. Fe K-edge first-derivative XANES results for DWTRs. On the left, the spectra for the DWTRs and the standards employed in linear combination fitting (LCF) are shown. The merged spectra for the DWTRs are shown with a solid line, while the range in values from each scan is shown with a lighter shaded area. For most samples, the shaded region is too small to be seen (it may be observed near 7140 eV in the TN spectrum). The fit results using the standard spectra are shown with the dotted lines. On the right, the LCF results are shown as a bar chart, and χ^2 goodness- of-fit values are listed at the base of each bar.

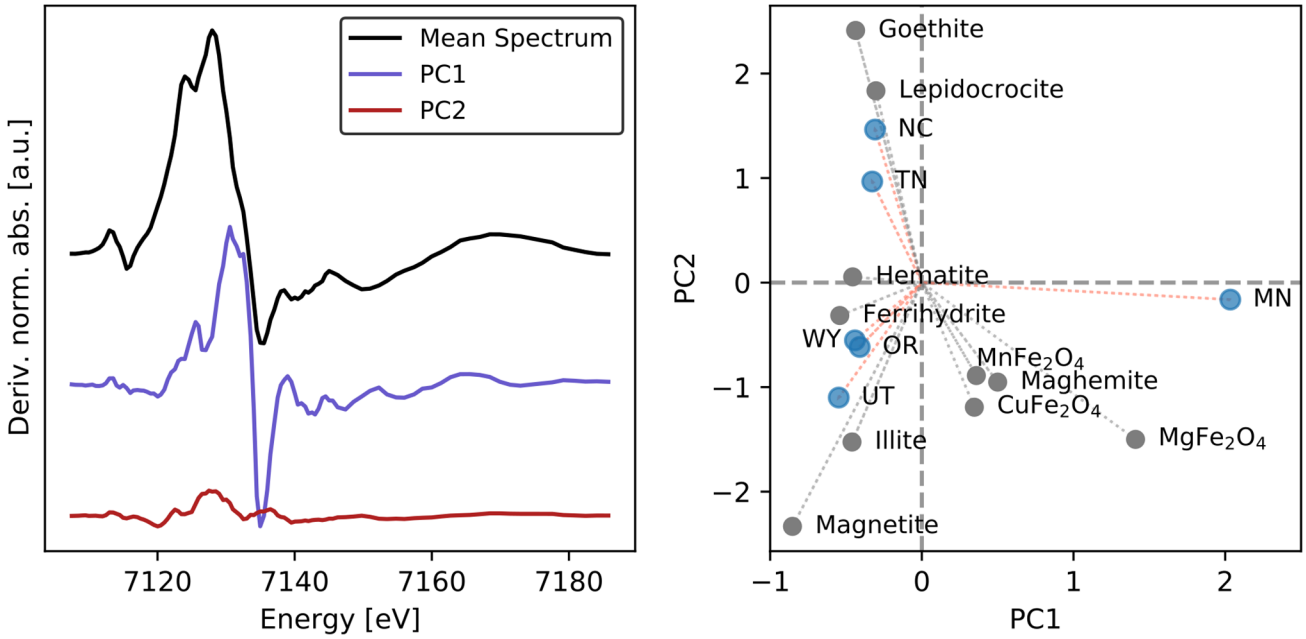


Figure 31. Principal components analysis of Fe K-edge first-derivative XANES spectra for drinking water treatment residuals. The left subplot visualizes the principal components. First, the mean first-derivative XANES spectrum calculated from all the DWTR sample spectra is plotted. Principal components are calculated based on the distance of the samples from the mean across each spectrum. The components plotted in the left subplot are therefore added or subtracted from the mean spectrum to approximately recreate the sample spectra. PC1 and PC2 are scaled based on the variance they account for within the Fe K-edge DWTR spectra (85% and 12%, respectively). The right subplot projects the DWTR samples along with selected standards on the first two principal components. Here, most of the variance is driven by the MN sample. This is reflected in the shape of PC1, which shows the shoulder and small oscillations in the first-derivative XANES that distinguished MN from the other samples. In the projection of standards, common ferric (or mixed-valence iron) minerals do not recreate these features. However, several spinel ferrite minerals, including maghemite, manganese ferrite (jacobsite), copper fer- rite (cuprospinel), and magnesium ferrite (magnesioferrite) do.

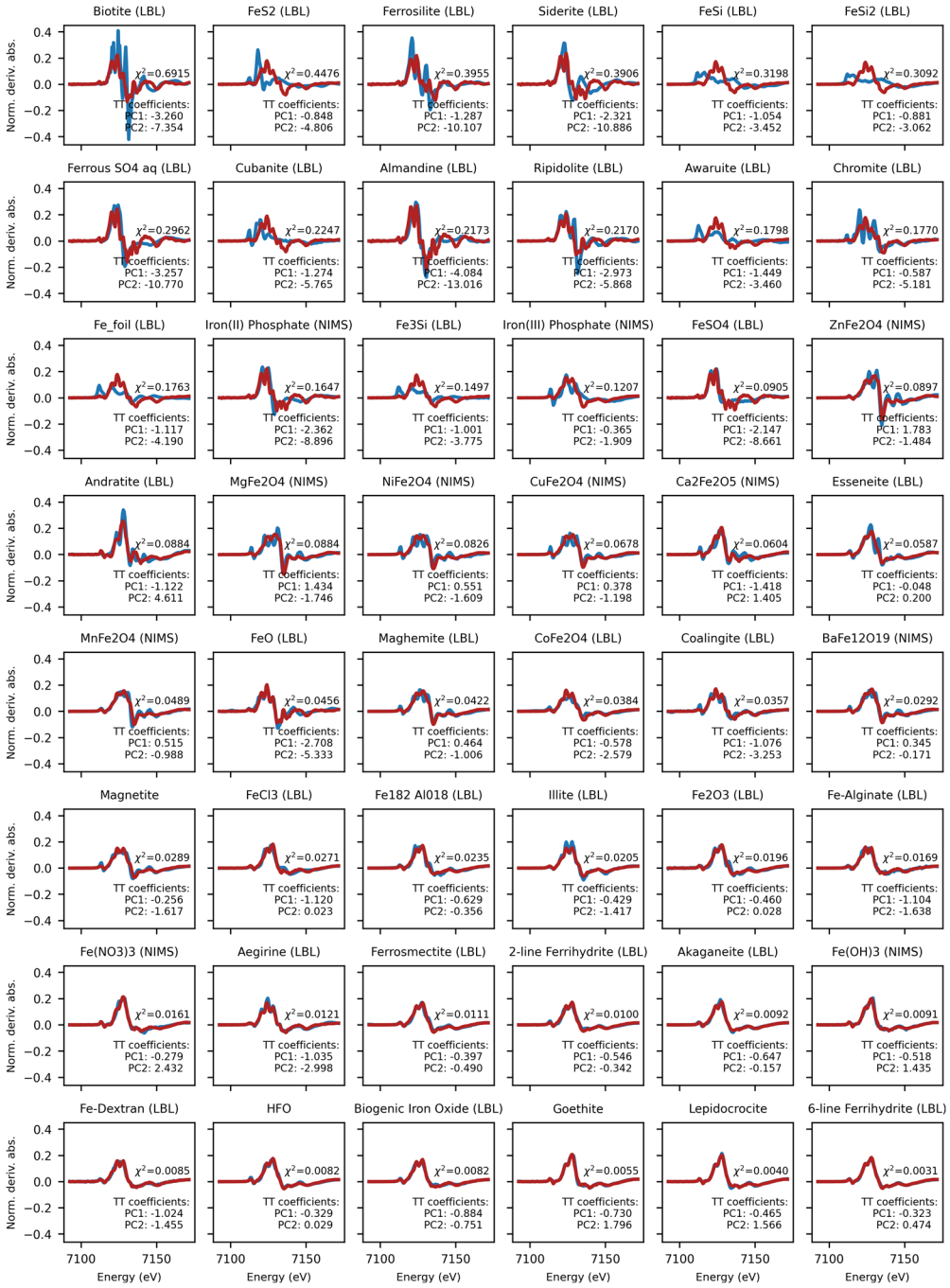


Figure 32. Target transformations of first-derivative Fe K-edge XANES standard spectra based on principal components calculated from DWTRs. "LBL" (Fakra, 2010) and "NIMS" (Masashi et al., 2021, Tanifuji et al., 2019) identify databases from which certain spectra were acquired.

NC and TN spectra are best reconstructed with HFO and lepidocrocite. For both samples, lepidocrocite accounts for the majority of the fit. Unlike the non-lime based DWTRs, there is no spectroscopic evidence of iron associated with clays in these materials. Finally, the MN sample is reconstructed using goethite, zinc ferrite and magnesioferrite

(Masashi et al., 2021, Tanifuji et al., 2019). The χ^2 value for this fit is much higher than in the other samples, indicating the imperfect nature of this result. However, the magnesio- and zinc ferrite standards are able to account for the unusual features seen in the MN sample, including the shoulder and the oscillations. These features are not specific to magnesio- ferrite or zinc ferrite; in fact, they may be accounted for with a range of spinel ferrite materials not including magnetite. Spinel ferrite compounds adhere to the general chemical formula of $X^{2+}Fe_2O_4$, where X is a divalent cation such as magnesium (forming magnesio-ferrite), copper (forming cuprospinel), manganese (forming jacobsite), or ferrous iron (forming magnetite). In some spinel ferrites, ferric iron can at least partially occupy the tetrahedral sites more commonly occupied by the divalent cation, making an "inverse" spinel (Schwertmann and Cornell, 2008). Other researchers using FDMNES ab initio XANES calculations identified the degree of inversion giving rise to the types of features seen in the MN sample's XANES due to the contribution of tetrahedrally coordinated ferric iron to the spectra (Jutimoosik et al., 2019, 2021).

Spinel ferrite chemical species may be precipitated when a solution containing both the divalent cation and ferric iron is mixed with a highly alkaline solution (Tatarchuk et al., 2017). Generally, researchers synthesizing these minerals in the laboratory include an annealing and/or calcination step (Kumar et al., 1996), to dehydrate and crystallize the material from precursor hydroxide minerals (Ren et al., 2009); others have asserted that the spinel ferrite phase is precipitated at low temperatures, and the annealing step leads to longer-range crystal order (Tang et al., 1991). Iron minerals may also transform into spinel ferrites, such as jacobsite, provided a relatively high ratio of the divalent cation to the iron (Schwertmann and Cornell, 2008). The magnesium and zinc spinel ferrite spectra best fit the MN spectrum, so they are used in the fit. Also plausible as a contributor is maghemite (γ-Fe_2O_3), which possesses the spinel ferrite geometry with some octahedral site vacancies to balance the charge of the mineral; maghemite forms through the oxidation of magnetite (Schwertmann and Cornell, 2008), so magnetite coming from the groundwater's source aquifer also presents a path for the presence of some of these spectral features. Regardless, the features of the MN sample are indicative of an atypical Fe-coordination environment.

b. Mn K-edge. Mn K-edge data for UT and TN are shown in **Figure 33**. These DWTR samples are best reconstructed when manganese(II) carbonate makes up the plurality of the fit. For UT, a small fraction of the fit is allotted to Mn_3O_4 and $MnSiO_3$ (Manceau et al., 2012), which collectively have the effect of slightly muting the features of the $MnCO_3$ spectrum rather than adding particularly distinct features. TN is more clearly different compared to the $MnCO_3$ standard. The fit here uses manganite and $MnSiO_3$ (Manceau et al., 2012), and $MnFe_2O_4$ [(Tanifuji et al., 2019, Masashi et al., 2021); both $MnSiO_3$ and $MnFe_2O_4$ help reconstruct the small feature near 6560 eV in the TN spectrum. Hausmannite, or Mn_3O_4, shows a feature in a similar location, though it does not help with the fit. $MnSiO_3$ would not be expected to easily precipitate, and the TN sample lacks evidence for the presence of $MnFe_2O_4$ in the Fe K-edge spectrum. However, TN shows signs of oxidation over time, as shown in **Figure 34**. This progression shows a clear change towards spectral features consistent with hausmannite. On the other hand, UT has shown no signs of changes in speciation over time (**Figure 35**).

Regardless, these results indicate that manganese is primarily – at least initially – in the reduced +2 oxidation state in these two DWTR samples. This has several implications.

From the perspective of drinking water treatment, this does suggest that Mn^{2+} was not the target for oxidation by $KMnO_4$ at the UT and TN DWTPs. Sulfide is also commonly removed by oxidation at DWTPs; the redox reactions between HS^- and MnO_4^- are shown in equations 11, 12, and 13.

$$\frac{1}{8}SO_4^{=} + e^- + \frac{9}{8}H^+ \rightleftharpoons \frac{1}{2}H_2O + \frac{1}{8}HS^- \qquad Eq.11$$

$$\frac{1}{5}MnO_4^- + e^- + \frac{8}{5}H^+ \rightleftharpoons \frac{1}{5}Mn^{2+} + \frac{4}{5}H_2O \qquad Eq.12$$

$$\frac{1}{8}HS^- + \frac{1}{5}MnO_4^- + \frac{19}{40}H^+ \rightleftharpoons \frac{1}{8}SO_4^{=} + \frac{1}{5}Mn^{2+} + \frac{3}{10}H_2O \qquad Eq.13$$

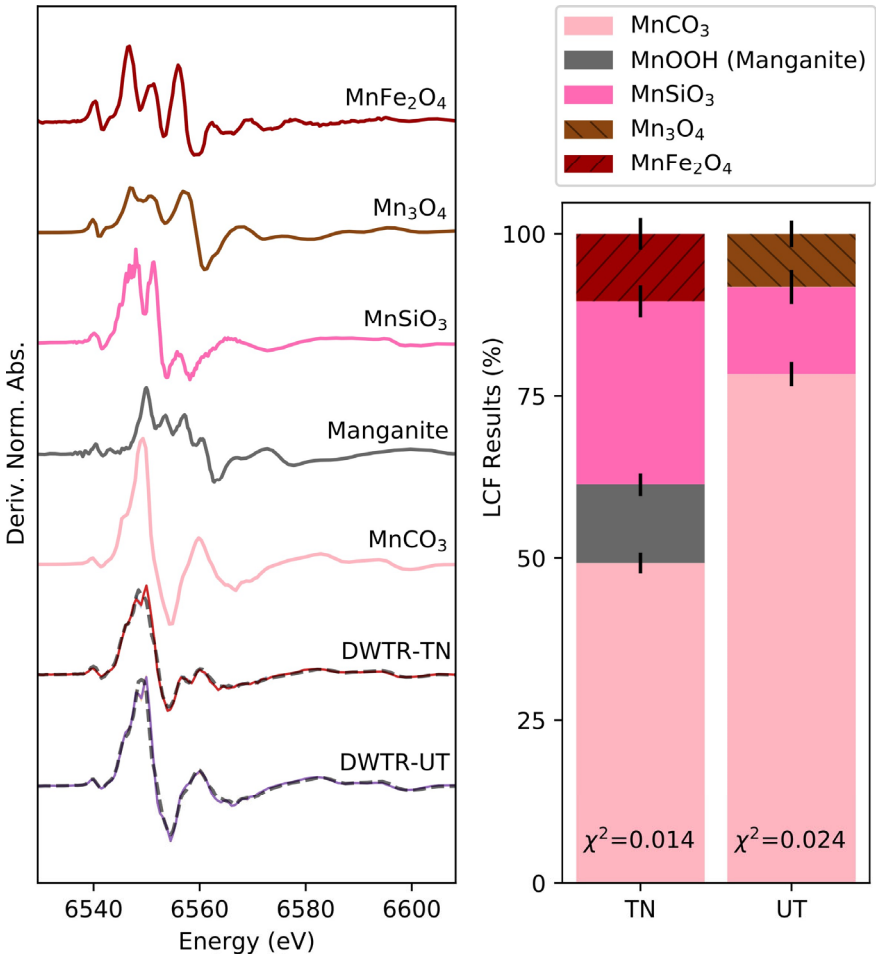


Figure 33. Mn K-edge first-derivative XANES results for DWTRs. On the left, the linear combination fitting (LCF) results are shown with χ^2 goodness-of-fit values at the bottom of each bar. The right subplot shows the spectra for the DWTR samples, and the standards employed in LCF. As in Figure 5.10, the fit results using the standard spectra are shown with the dotted lines.

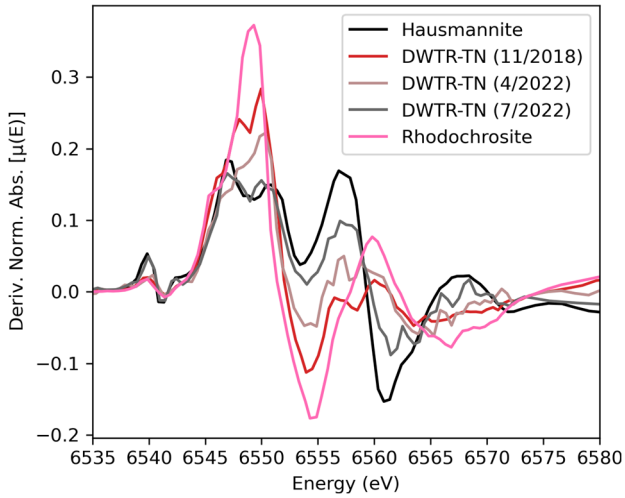


Figure 34. Mn K-edge first-derivative XANES results for DWTR-TN over time. Rhodochrosite ($MnCO_3$) and hausmannite (Mn_3O_4) standards are shown for comparison. Initial scans show that the speciation of manganese in the TN sample is dominated by rhodochrosite. The spectrum increasingly matches that of hausmannite over time, suggesting the manganese in TN has become oxidized.

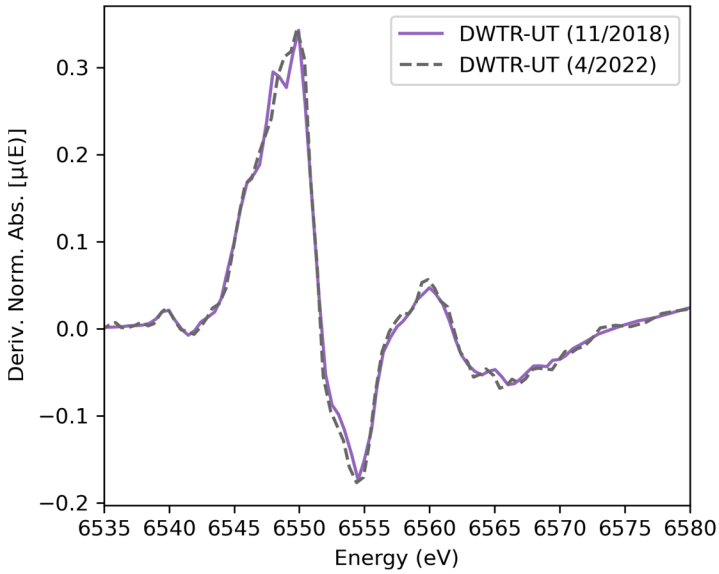


Figure 35. Mn K-edge first-derivative XANES results for DWTR-UT over time. No changes in speciation are apparent.

Moreover, manganous species are more highly soluble than more oxidized forms of manganese, such as manganite (MnOOH) or manganese dioxide. In environmental applications, acidic conditions could dissolve the manganese in these DWTRs. On the other hand, placing these DWTRs in reducing conditions would not result in a sudden release of manganese, and more oxidizing conditions would lead to the transformation of manganese to more stable phases.

4.3 Copper (Cu) and lead (Pb) sorption to DWTRs

4.3.1 Microscopic and Spectroscopic characterization of the association of metals with DWTRs. A two-pronged approach was applied to explore the speciation of Cu and Pb sorbed by 6 different DWTR samples. First, scanning electron microscopy with energy dispersive X-ray spectroscopy (SEM- EDS) was applied to the DWTR samples with Cu or Pb sorbed to them to probe any general elemental associations. Second, the speciation of Cu and Pb were directly probed using X-ray absorption spectroscopy (XAS), with particular emphasis on the extended X-ray absorption fine structure (EXAFS).

For these purposes, we carried experiments in reactors where the water was either buffered using MOPS (pH=6.8) or HEPES (pH=8.4) using as background electrolyte KNO_3 a salt that does not lead to any significant complexation of metals. Typically, batch reactors with DWTRs and either Pb or Cu (from $Pb(NO_3)_2$ or $Cu(NO_3)_2$, respectively) were prepared using 50 mL of solution in metal-free centrifuge tubes (Labcon). Reactors for both elements used 25 mg of DWTR in 50 mL of solution with 10 mM buffer and 10 mM KNO_3. For lead, reactors had an initial concentration of lead of 2.5 ppm in solution, while copper was added to reactors in 7 equivalent spikes for a maximum total concentration of 417 ppb Cu in solution. Reactors were rotated for 1 day, and solids were allowed to subsequently settle for half an hour. The results of these sorption experiments are presented in **Figure 36** that shows various removal across DWTRs for Cu, whereas for Pb removal is more consistent.

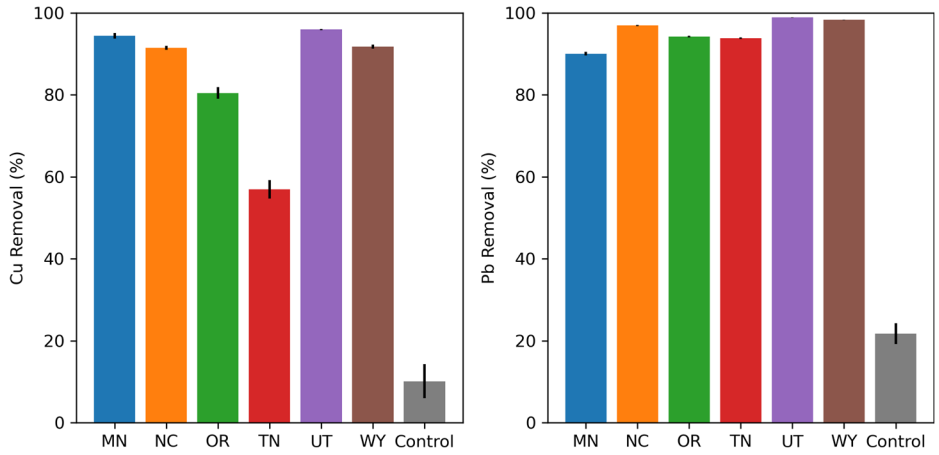


Figure 36. Sorption results for copper and lead to DWTRs in SEM-EDS reactors. The left subplot shows the removal of copper relative to the initial concentration, while the right subplot shows the same for lead. The loss of the metals in control reactors with no DWTRs is also shown.

4.3.2 SEM-EDS results. Selected SEM-EDS data for Cu are shown in Figures **37, 38, and 39.** No well-defined partitioning of Cu is apparent for most of the DWTRs despite the heterogeneity of the materials; for the MN, NC, TN, UT, and WY samples, Cu signals are distributed across the full surface. However, in the OR sample, Cu seems to be concentrated in a small region with elevated carbon content. Since all the samples are mounted on carbon tape, finding the distribution of carbon within the DWTR samples was challenging. However,

the carbon on the OR sample overlaps with the DWTR as seen in the SEM micrograph, and this region is also one of several with elevated Fe content. Since Cu is only concentrated in the region with concentrated carbon and not in the other iron-rich areas, the data indicate that Cu may be associated with organic matter in the OR sample.

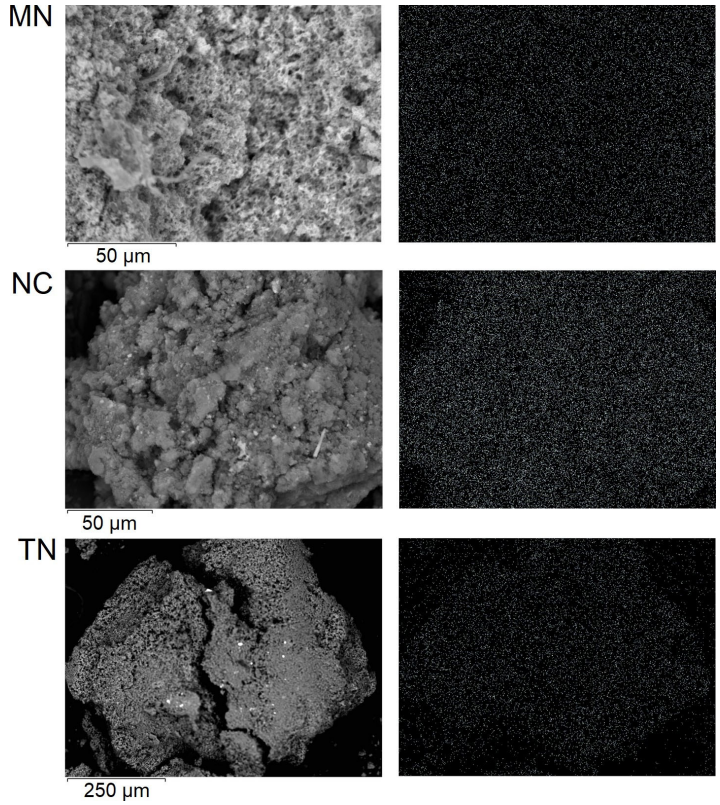


Figure 37. SEM-EDS data for DWTRs with sorbed copper. Here, the DWTRs with a lime additive (MN, NC, and TN) are shown. On the left are the SEM micrographs, taken with backscatter detectors. On the right are copper EDS data; despite heterogeneity in each of these samples, there is no clear distinction in the distribution of copper.

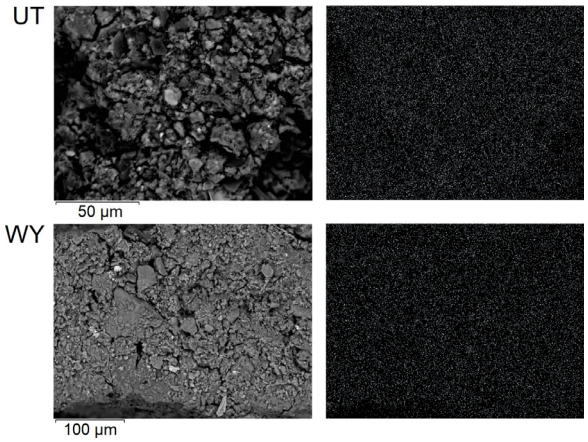


Figure 38. SEM-EDS data for DWTR samples UT and WY with sorbed copper. As in Figure 36, SEM micrographs are on the left and copper EDS data are on the right; as before, copper is broadly distributed.

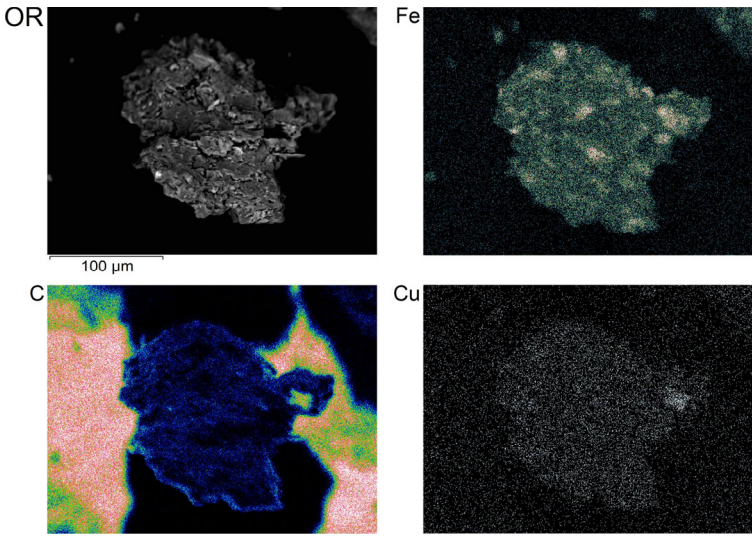


Figure 39. SEM-EDS data for copper sorbed to DWTR-OR. On the top left, the backscatter SEM image of a particle from the sample is shown. EDS data for Fe, C, and Cu are also shown. Since the EDS samples are placed on carbon tape, there is a strong signal for carbon surrounding the particle. However, on the right side of the particle, C is concentrated with Fe; it is also in this location where Cu is most concentrated.

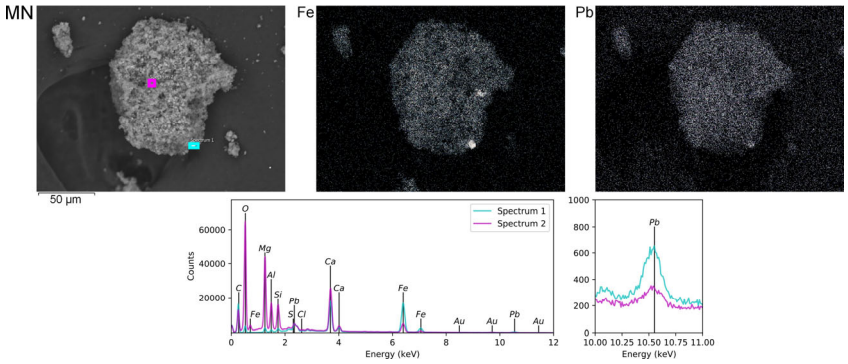


Figure 40. SEM-EDS data for DWTR-MN with sorbed lead. On the left is the micrograph, captured with the backscatter detectors. Areas where EDS spectra were taken are boxed in cyan and magenta and plotted at the bottom of the figure. The center and right subplots show EDS elemental mapping of iron and lead, respectively. Iron shows strong enrichment in two small areas of the sample and lead also seems to slightly concentrate in those areas. The EDS spectra show that the area with higher iron content in cyan also has a stronger Pb signal compared to the other region of the sample.

SEM-EDS results for Pb show its associations with multiple phases on the surface of the DWTR samples. **Figures 40 and 41** show that Fe and Pb have a weak positive correlation in some DWTRs. The TN sample, shown in **Figure 42,** shows a strong connection between

Mn and Pb content; notably, this DWTR includes potassium permanganate as an additive, which plays a role in the sorption potential of this DWTR sample.

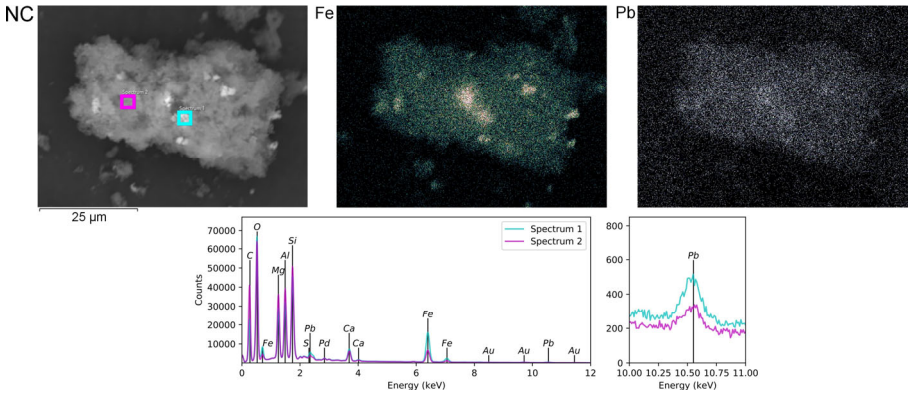


Figure 41. SEM-EDS data for DWTR-NC with sorbed lead. The SEM micrograph is shown on the left, with two areas selected for further EDS analysis shown in the cyan and magenta boxes, which are plotted at the bottom of the figure. Iron and lead elemental maps from EDS are shown in the center and right subplots. Like DWTR-MN, lead seems to concentrate slightly in areas with higher iron content.

DWTR-UT showed no clear enrichment of Pb on any phases; the presence of high concentrations of sulfur interfered with the mapping of Pb, so selected spectra were taken on the surface of the UT sample. The DWTR- WY sample showed lead associating with carbon; no enrichment of lead in areas with concentrated iron is visible, though from a selection of EDS spectra taken from spots on a particle, areas with a stronger peak for carbon also have a stronger peak for lead. Finally, **Figures 45** and **46** show that lead can cluster on multiple parts of a single DWTR; a particularly iron-rich region of the OR sample shows high lead content, while a particularly carbon-rich region shows similar lead enrichment, suggesting that both organic matter and metal oxides contribute to lead sorption.

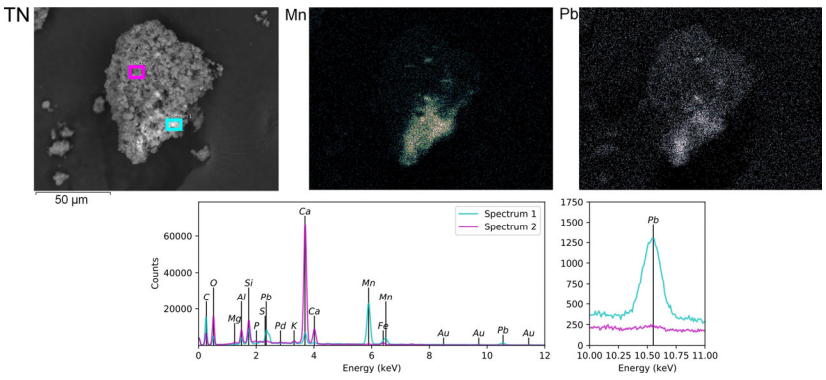


Figure 42. SEM-EDS data for DWTR-TN with sorbed lead. The SEM micrograph is shown on the left, with boxes around the areas used to generate the EDS spectra shown at the bottom. The center and right subplots show manganese and lead elemental maps from EDS, respectively. Here, a rather strong correlation between manganese and lead is apparent.

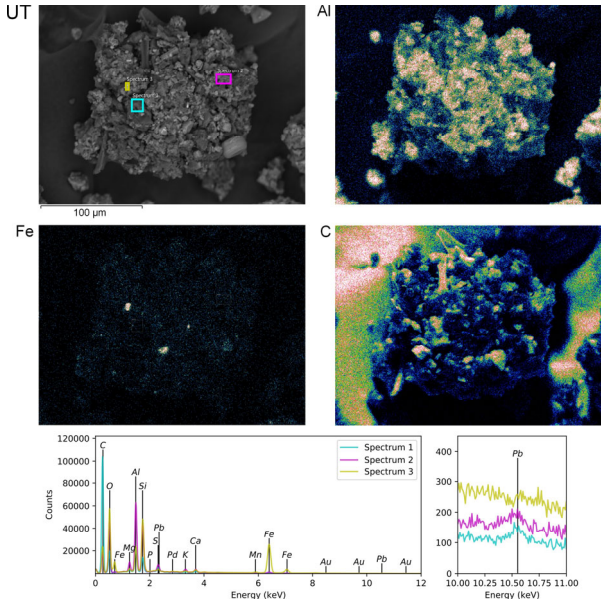


Figure 43. SEM-EDS data for DWTR-UT with sorbed lead. The SEM micrograph is shown at the top left subplot. Al, Fe, and C elemental maps from EDS are shown, and the bottom subplot shows EDS spectra in cyan, magenta, and yellow corresponding with the same-colored boxes overlaid on the SEM micrograph. Due to high enrichment of S in this sample, elemental mapping by EDS for Pb was not feasible. No strong lead associations are observed by targeting areas rich in carbon (spectrum 1), aluminum (spectrum 2), and iron (spectrum 3) on the DWTR.

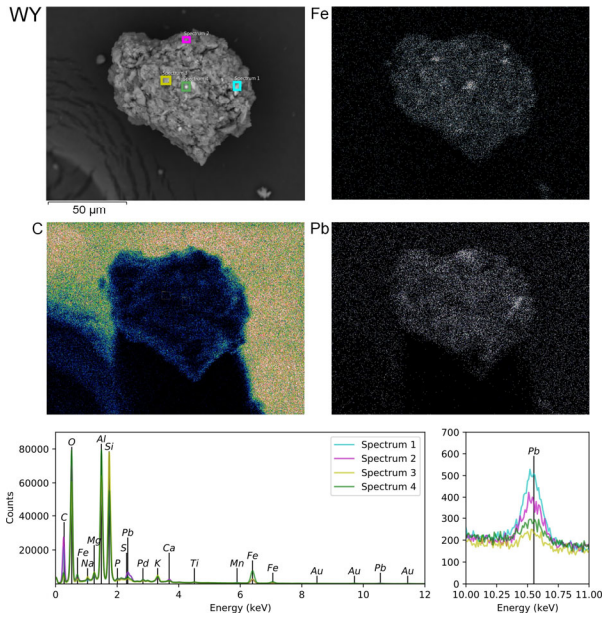


Figure 44. SEM-EDS data for DWTR-WY with sorbed lead. The SEM micrograph is plotted at the top left, and EDS elemental maps for Fe, C, and Pb are shown in the top right, center left, and center right subplots, respectively. The bottom plot shows the EDS spectra for the areas boxed in the SEM micrograph. Here, there is no apparent correlation between iron and lead. In areas of DWTR-WY with elevated carbon content, as in Spectra 1 and 2, elevated lead content is also observed.

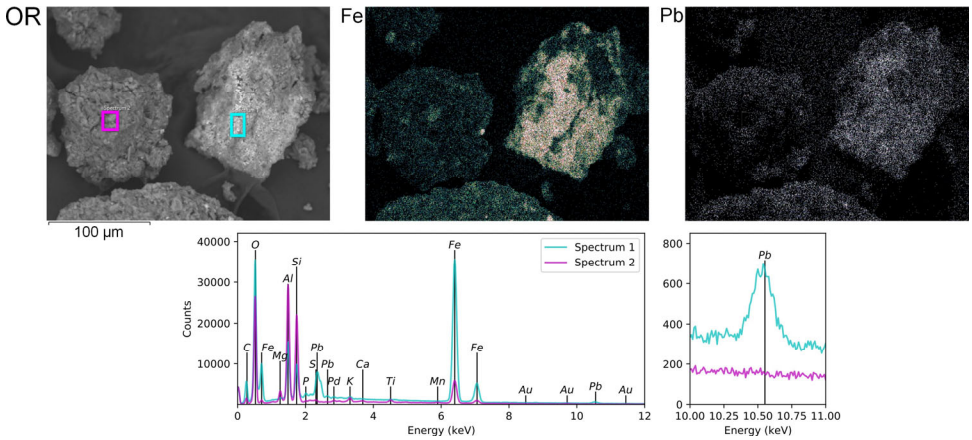


Figure 45. SEM-EDS data for DWTR-OR with sorbed lead. The SEM micrograph is on the left, and EDS elemental maps for iron and lead are plotted in the center and right subplots. An EDS spectrum for a particularly iron-rich region (Spectrum 1) is contrasted with an area low in iron (Spectrum 2). Here, lead content correlates with iron content.

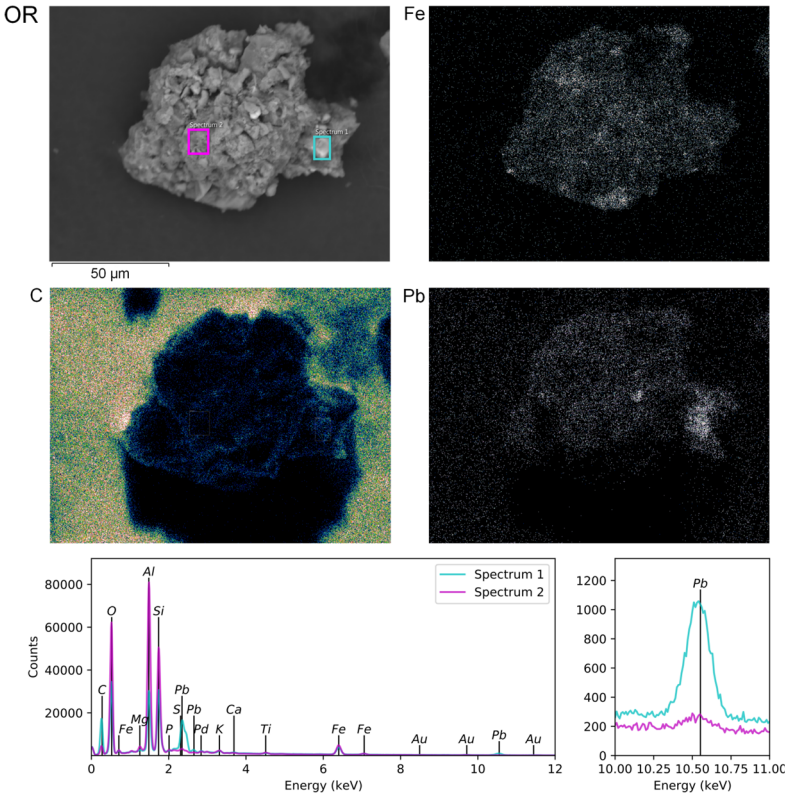


Figure 46. SEM-EDS data for another particle of DWTR-OR with sorbed lead. The SEM micrograph is shown at the top left, and EDS elemental maps for iron, carbon, and lead are also shown. The bottom subplot shows the EDS spectra for the areas of interest boxed in the SEM micrograph. In contrast with the other OR sample (**Figure 45**), lead does not correlate with iron and instead seems to correlate with carbon content.

4.3.3 X-Ray Absorption Spectroscopy.

a. Copper. EXAFS results for copper sorbed to DWTR samples in water samples that were buffered using MOPS are shown in **Figure 48** (to test for another pH buffer, HEPES was used in other reactors are shown in **Figure 49**). The results of the EXAFS fitting are presented in **Tables 7** and **8**. The Fourier transform of the EXAFS highlights a critical difference among the samples: the presence (or absence) of a strong second-shell feature. OR, WY, NC, and MN samples all show similar, sizable peaks between 2 and 3Å in R space. On the other hand, UT and TN samples do not show strong features in this region.

Cluster analysis was applied to the EXAFS data with several standards included for illustrative purposes, as shown in **Figure 47**. Unsurprisingly, the DWTR samples are divided amongst each other based on the presence or absence of the second shell feature.

The results of the PCA analysis of the XANES for Cu are presented in **Figures 50**, **51** and **52**. This information is used to inform about the selection of compounds that can be used to perform linear combination fittings shown in **Figure 53** that provide an estimate of the chemical speciation of Cu when it is sorbed to DWTRs. It suggests that for TN, UT, and WY the sorption of Cu is dominated by the aluminum phase that is formed during these DWTRs formation. In contrast, for DWTRs from MN and NC Cu sorption is controlled predominantly by iron oxides and in the case of OR clays (bentonite used as a proxy) and organic material (humate) explained most of the coordinative environment of sorbed Cu.

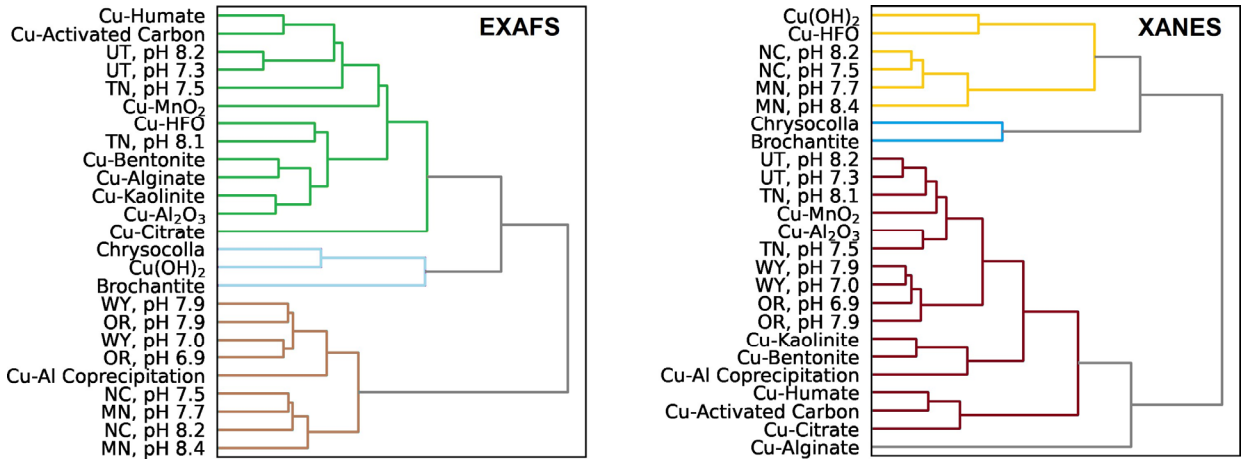


Figure 47. Cluster analysis of selected Cu K-edge XAS data. The left subplot clusters based on the EXAFS data for copper sorbed to DWTRs, with standards for copper sorption or copper minerals included. The right subplot clusters the same samples based on their first-derivative XANES data. DWTR samples are identified by their state of origin and their final measured pH

Table 7. FEFF fitting results for copper sorbed to DWTR samples in MOPS buffer. S_0^2 was fixed at 0.75 for each fit. Scattering paths; their calculated coordination numbers, path distances, σ^2, and ΔE values; and R-factor and reduced-χ^2 goodness-of-fit-metrics are shown.

DWTR	Path	CN	R(Å)	σ^2 (Å^2)	ΔE (eV)	R-factor	χ-red.
MN	Cu-O	5.0 ±0.9	1.962 ±0.012	.006 ±.002	2.97 ±2.26	0.020	21.0
	Cu-O	4.4 ±3.2	3.13 ±0.03	.006 ±.007			
	Cu-O-O	11.6 ±7.6	3.94 ±0.08	.010 (Fixed)			
	Cu-O	4.3 ±0.7	1.962 ±0.011	.005 ±.002	1.89 ±2.03	0.019	19.9
	Cu-Al	1.8 ±1.4	3.02 ±0.03	.005 ±.007			
	Cu-O	4.2 ±2.4	3.68 ±0.06	.010 (Fixed)			
NC	Cu-O	5.0 ±0.6	1.960 ±0.009	.005 ±.001	2.59 ±1.70	0.011	11.5
	Cu-O	2.8 ±2.2	3.13 ±0.03	.005 ±.007			
	Cu-O-O	9.4 ±5.7	3.96 ±0.07	.010 (Fixed)			
	Cu-O	4.3 ±0.4	1.960 ±0.007	.005 ±.001	1.58 ±1.25	0.007	7.0
	Cu-Al	0.8 ±0.6	3.01 ±0.02	.001 ±.005			
	Cu-O	4.2 ±1.6	3.71 ±0.03	.010 (Fixed)			
OR	Cu-O	5.1 ±0.4	1.939 ±0.006	.005 ±.001	−0.35 ±1.19	0.004	4.6
	Cu-O	7.1 ±3.4	3.12 ±0.02	.014 ±.006			
	Cu-O-O	13.4 ±4.2	3.95 ±0.04	.010 (Fixed)			
	Cu-O	4.4 ±0.3	1.938 ±0.005	.004 ±.001	−1.43 ±0.97	0.003	3.6
	Cu-Al	2.4 ±1.0	2.98 ±0.02	.011 ±.004			
	Cu-O	4.9 ±1.2	3.70 ±0.02	.010 (Fixed)			
TN	Cu-O	5.4 ±0.7	1.932 ±0.009	.005 ±.001	−0.43 ±1.73	0.011	7.4
UT	Cu-O	4.9 ±0.5	1.939 ±0.006	.004 ±.001	2.46 ±1.17	0.005	6.9
WY	Cu-O	4.9 ±0.4	1.942 ±0.005	.005 ±.001	0.20 ±1.09	0.004	4.3
	Cu-O	6.6 ±2.3	3.11 ±0.02	.010 ±.004			
	Cu-O-O	15.7 ±3.8	3.97 ±0.03	.010 (Fixed)			
	Cu-O	4.2 ±0.3	1.943 ±0.004	.004 ±.001	−0.49 ±0.80	0.003	2.7
	Cu-Al	2.3 ±0.7	2.99 ±0.01	.008 ±.003			
	Cu-O	6.1 ±1.0	3.72 ±0.02	.010 (Fixed)			

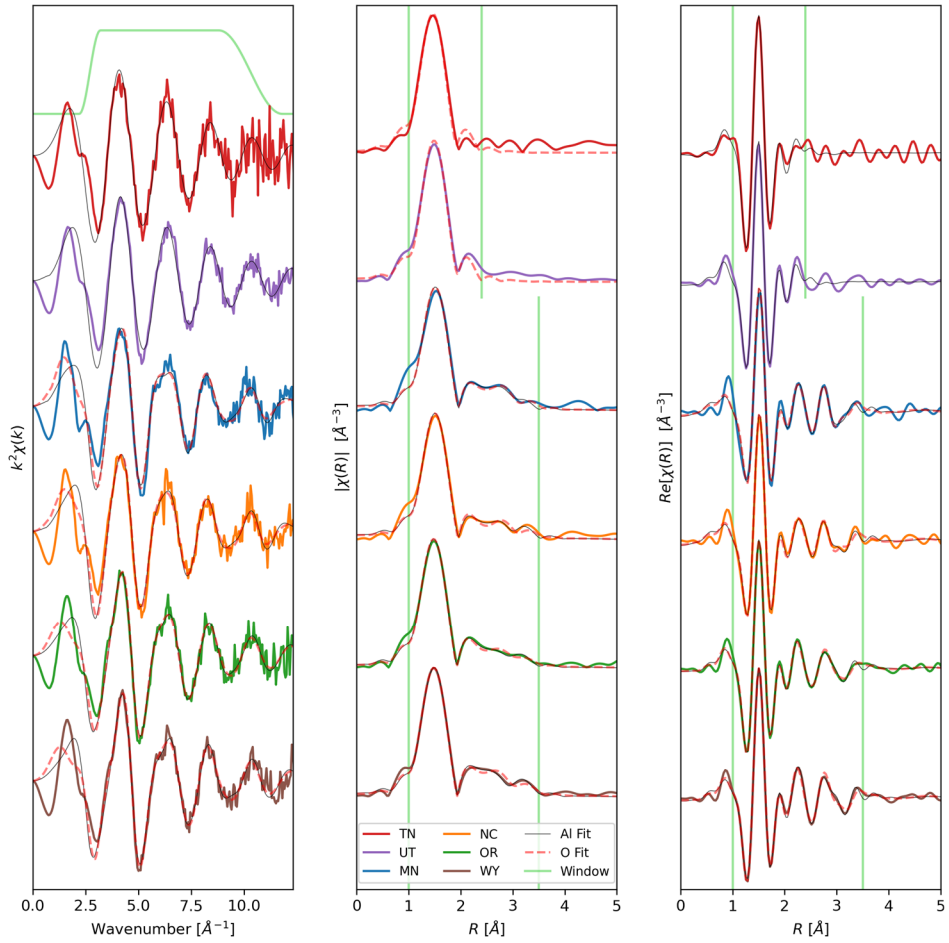


Figure 48. EXAFS fitting results for copper sorbed to DWTRs in MOPS reactors. UT and TN samples are only fit in the first shell; others are fit with both Cu-O and Cu-O-O paths (shown in the red dashed line) or Cu-Al and Cu-O paths (shown in the thin gray line), with parameters shown in Table 7.3. The left subplot shows the EXAFS and fit results in k-space, the center subplot shows the Fourier transform magnitude for each fit and sample, while the right subplot shows the real component of the Fourier transforms of data and fits.

Table 8. DWTR reactor Cu K-edge EXAFS findings for HEPES reactors. S_0^2 was fixed at 0.75, and for samples fit beyond the first shell (MN, NC, OR, and WY), the third scattering path was fixed at a σ^2 value of 0.01. For these reactors, second-shell contributions to EXAFS are modeled separately with Al and O, and the results from both fits are reported here.

Sample	Path	CN	R (Å)	σ^2 (Å^2)	ΔE (eV)	R-factor	χ-red.
MN	Cu-O	5.0 ±0.6	1.956 ±0.008	.005 ±.001	2.46 ±1.52	0.009	17.0
	Cu-O	5.6 ±2.3	3.15 ±0.02	.005 ±.004			
	Cu-O-O	16.9 ±5.8	3.95 ±0.04	.010 (Fixed)			
	Cu-O	4.3 ±0.6	1.957 ±0.010	.004 ±.001	1.72 ±1.79	0.015	27.0
	Cu-Al	2.0 ±1.2	3.04 ±0.02	.004 ±.005			
	Cu-O	6.0 ±2.4	3.69 ±0.04	.010 (Fixed)			
NC	Cu-O	5.1 ±0.5	1.953 ±0.007	.005 ±.001	1.83 ±1.37	0.007	15.3
	Cu-O	2.3 ±1.9	3.13 ±0.03	.005 ±.008			
	Cu-O-O	6.1 ±4.7	3.94 ±0.08	.010 (Fixed)			
	Cu-O	4.5 ±0.5	1.951 ±0.008	.004 ±.001	0.48 ±1.46	0.009	18.9
	Cu-Al	0.9 ±1.0	3.01 ±0.03	.005 ±.010			
	Cu-O	2.3 ±1.8	3.67 ±0.07	.010 (Fixed)			
OR	Cu-O	5.9 ±1.0	1.942 ±0.012	.008 ±.002	−0.62 ±2.26	0.016	17.9
	Cu-O	8.8 ±6.2	3.10 ±0.03	.014 ±.009			
	Cu-O-O	15.9 ±7.4	3.96 ±0.06	.010 (Fixed)			
	Cu-O	4.9 ±0.9	1.943 ±0.013	.007 ±.002	−1.50 ±2.38	0.020	23.1
	Cu-Al	3.4 ±2.8	2.98 ±0.04	.013 ±.009			
	Cu-O	5.5 ±2.8	3.71 ±0.05	.010 (Fixed)			
TN	Cu-O	5.7 ±0.6	1.938 ±0.007	.006 ±.001	1.07 ±1.33	0.007	13.7
UT	Cu-O	5.2 ±0.6	1.940 ±0.007	.005 ±.001	2.21 ±1.39	0.008	8.7
WY	Cu-O	5.5 ±0.6	1.932 ±0.008	.006 ±.002	−1.00 ±1.52	0.007	8.2
	Cu-O	7.5 ±4.2	3.10 ±0.02	.014 ±.007			
	Cu-O-O	13.1 ±5.2	3.94 ±0.05	.010 (Fixed)			
	Cu-O	4.6 ±0.6	1.931 ±0.009	.005 ±.001	−2.01 ±1.68	0.010	11.5
	Cu-Al	3.0 ±2.0	2.97 ±0.03	.012 ±.007			
	Cu-O	4.5 ±2.0	3.70 ±0.04	.010 (Fixed)			

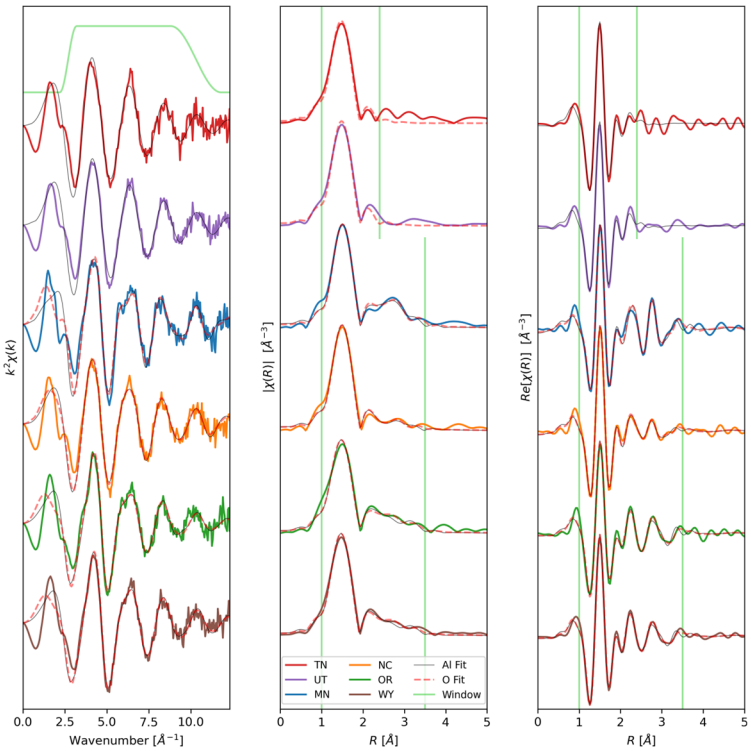


Figure 49. EXAFS fitting results for copper sorbed to DWTRs in HEPES reactors. UT and TN samples are only fit in the first shell; others are fit with both Cu-O and Cu-O-O paths (shown in the red dashed line) or Cu- Al and Cu-O paths (shown in the thin gray line). The left subplot shows the EXAFS and fit results in k-space, the center subplot shows the Fourier transform magnitude for each fit and sample, while the right subplot shows the real component of the Fourier transforms of data and fits.

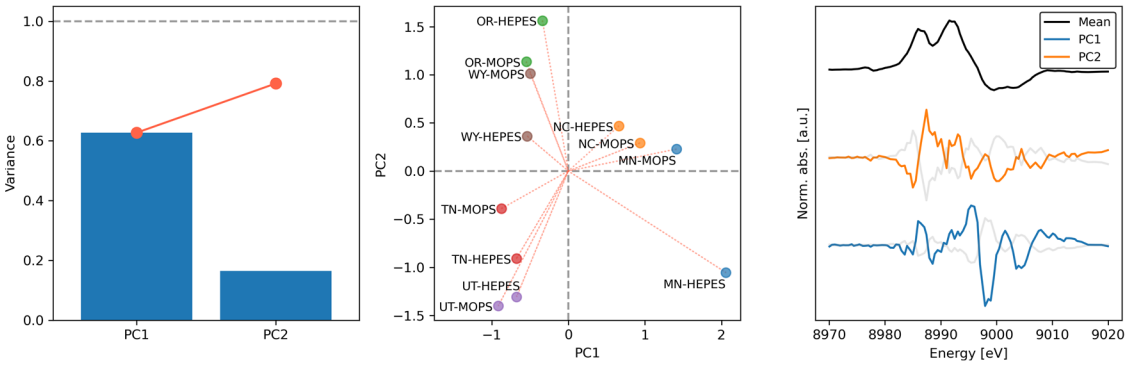


Figure 50. Principal component analysis (PCA) of first-derivative Cu K- edge XANES data for copper sorbed to DWTRs. The left subplot shows the fraction of the variance explained by the principal components. The middle subplot projects the samples onto the two principal components. Finally, the right subplot visualizes the components. The mean of all the spectra is shown in black, and the components are added to or subtracted from the mean.

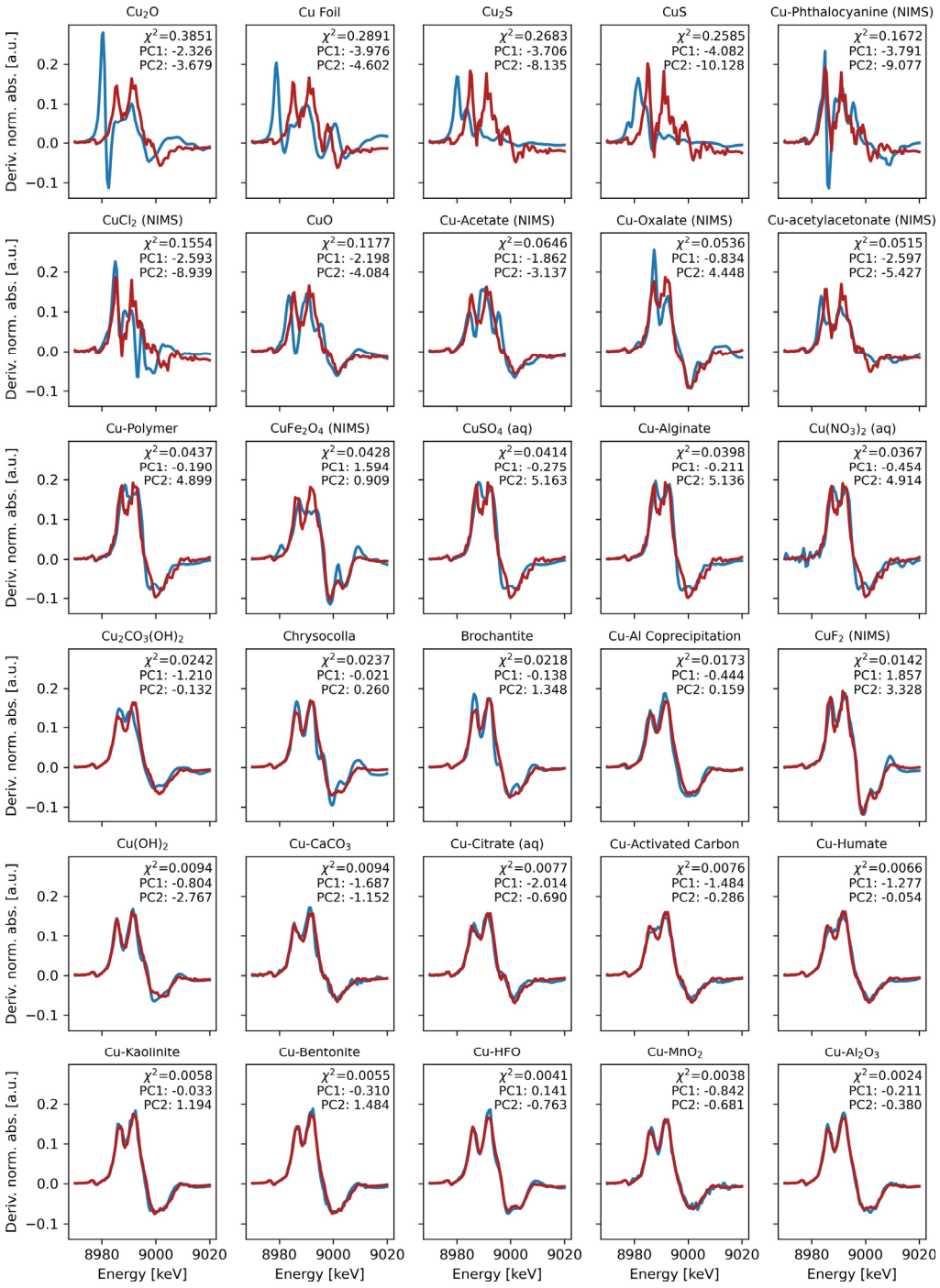


Figure 51. Target transformations of standard materials at the Cu K edge based on PCA of spectra from copper sorbed to DWTRs. "NIMS" standards are sourced from the Materials Data Repository (Masashi et al., 2021).

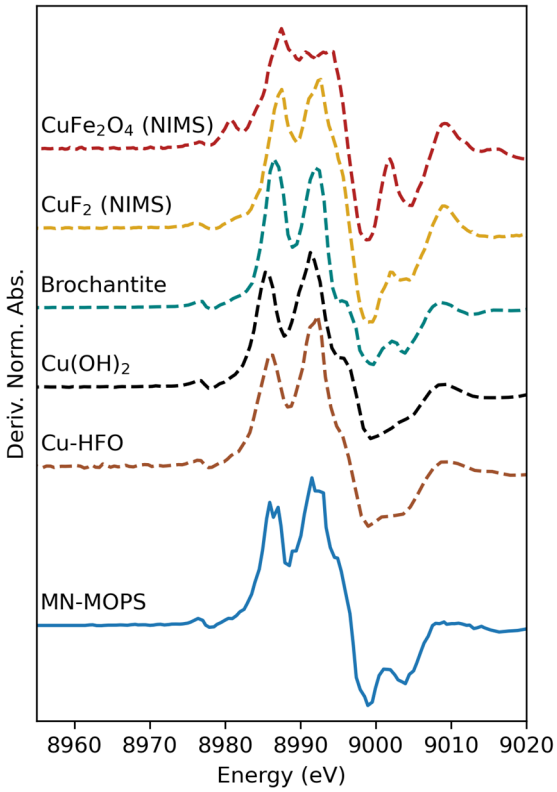


Figure 52. Cu K-edge first-derivative XANES for copper sorbed to DWTR-MN. Selected standards are included for comparison; "NIMS" standards are sourced from the Materials Data Repository (Masashi et al., 2021).

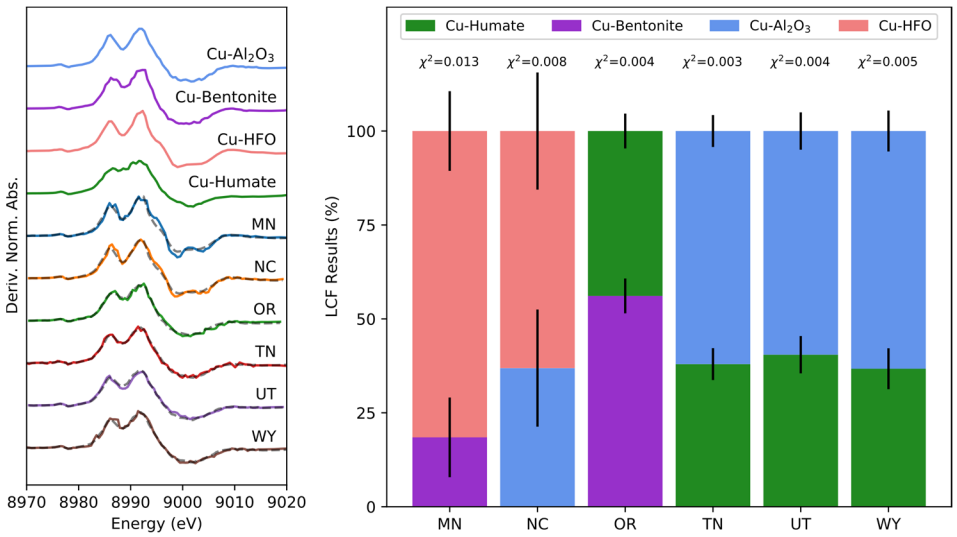


Figure 53. Linear combination fitting of first-derivative XANES data for copper-DWTR reactors in MOPS buffer. Standards selected for fitting are plotted, along with the data and fit for each DWTR sample. The weight of each standard in the fit is shown in the right subplot.

b. Lead. Lead EXAFS results are shown in **Figure 54**. Across the limited range of the EXAFS for all samples, differences are minimal. FEFF modeling results, shown in **Table 9**, indicate that lead is associated with oxygen in the first shell across all atoms, with calculated σ^2 values being high for all samples. However, this finding aligns with previous research in environmental lead speciation, which has emphasized the high disorder of O atoms coordinated with lead (Manceau et al., 2012).

XANES data are shown in **Figure 55**. Like the EXAFS, differences in the results across DWTRs are minimal; there is no strong evidence of divergent speciation in these samples. XANES data are similar to standards for lead sorbed to a range of inorganic materials such as kaolinite, activated carbon, and alumina. Standards for lead associated with organic functional groups, such as carboxyl (as in Pb-Alginate) and/or acryl/amide groups (as in Pb-Polymer) differ modestly from the DWTR spectra.

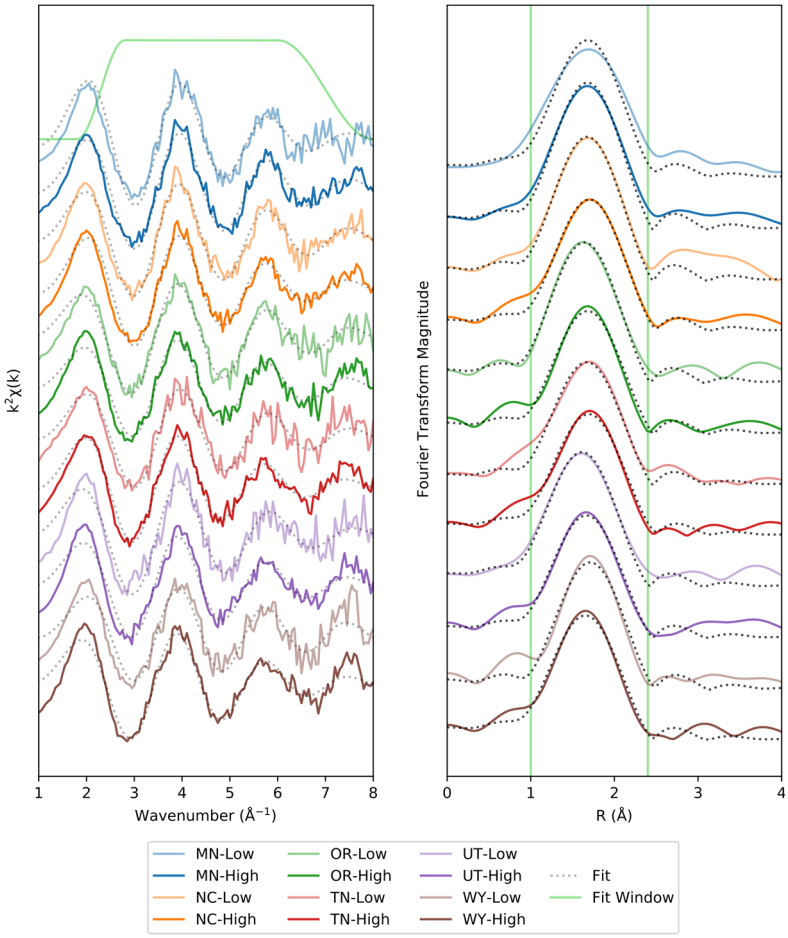


Figure 54. EXAFS for lead sorbed to DWTRs. FEFF fitting results are shown with the dotted lines, and windows for the Fourier transform and the FEFF fit are shown in the plots in k- and R-space, respectively.

Table 9. FEFF fitting results for lead sorbed to DWTR samples at low (1 mg Pb/g DWTR) and high (5 mg Pb/g DWTR) mass loading values. For all fits, the amplitude reduction factor S_0^2 was fixed at 0.90, while all other variables were fit.

Sample	Atom	CN	R (Å)	σ^2 (Å^2)	ΔE (eV)	R-factor	χ-reduced
MN-1	O	5.1 ±2.0	2.33±0.04	.025 ±.008	-3.2 ±3.0	0.016	29.1
MN-5	O	3.8 ±0.7	2.33 ±0.02	.018 ±.003	-3.9 ±1.5	0.004	6.3
NC-1	O	3.7 ±0.6	2.33±0.01	.018 ±.003	-4.2 ±1.4	0.003	6.3
NC-5	O	4.0 ±0.9	2.35 ±0.02	.021 ±.004	-2.8 ±1.7	0.005	4.5
OR-1	O	3.8 ±0.5	2.31±0.01	.018 ±.002	-6.2 ±1.1	0.002	2.9
OR-5	O	3.2 ±0.8	2.34 ±0.02	.018 ±.004	-4.4 ±2.0	0.007	5.0
TN-1	O	3.3 ±1.2	2.32±0.03	.019 ±.006	-4.0 ±2.9	0.014	13.4
TN-5	O	4.3 ±1.1	2.35 ±0.02	.024 ±.005	-3.6 ±2.0	0.007	5.0
UT-1	O	4.3 ±0.6	2.29±0.01	.022 ±.002	-6.8 ±1.1	0.001	1.8
UT-5	O	3.7 ±0.7	2.33 ±0.02	.021 ±.003	-5.1 ±1.6	0.004	2.1
WY-1	O	2.7 ±1.0	2.34±0.03	.014 ±.006	-2.9 ±2.9	0.014	15.6
WY-5	O	4.2 ±0.8	2.33 ±0.02	.022 ±.004	-5.7 ±1.6	0.004	3.3

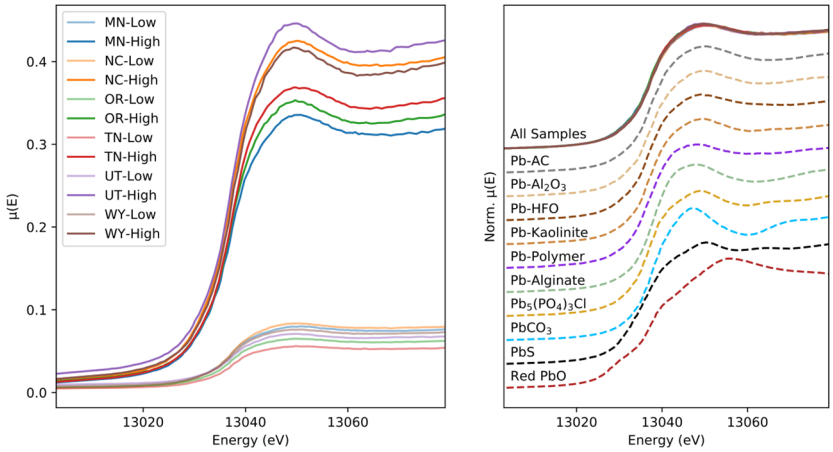


Figure 55. XANES spectra for lead sorbed to DWTRs. The left subplot shows the non-normalized fluorescence μ(E) for the samples. The right subplot shows normalized data; all samples are plotted to overlap in this subplot. Several lead standards are included at the bottom of the right subplot for comparison.

4.3.4. Conclusions for SEM-EDS and XAS analysis of Cu and Pb sorption.

Copper and lead analysis through SEM-EDS shows a broad distribution of both sorbed metals on DWTRs. There is some evidence for copper-organic matter associations in the DWTR-OR sample. No samples show any evidence of a correlation between copper and iron or manganese. On the other hand, lead (Pb) seems to preferentially associate with certain phases on DWTRs, including both transition metal oxides and apparently organic phases.

Despite their diverse compositions, all DWTRs removed lead efficiently. Across all the DWTRs, lead is found to be associated with oxygen in the first shell. These O atoms are approximately 2.3Å from the central Pb atom and highly disordered. Similarly, the XANES are similar across all samples. Despite the diversity of the DWTRs, all are highly effective sorbents, each removing at least 90% of lead from a 2.5 ppm Pb solution at 0.5 g DWTR/L mass loading. Strong differences in lead sorption behavior based on the selection of non-coagulant additives are not apparent. SEM-EDS indicates that lead, though broadly distributed, may preferentially sorb to transition metal oxides in some DWTRs, such as iron oxides or manganese oxides.

Copper sees more variable removal efficiency when exposed to DWTRs, ranging from highly effective sorption to the UT sample to relatively low sorption to DWTR-TN. Cu K-edge EXAFS also suggests diverse sorption processes among different DWTRs. UT and TN samples effectively have one shell in the EXAFS, which aligns well with most sorption processes. For UT, the abundant activated carbon is a likely contributor. In contrast, TN may be more reliant on the limited manganese oxides within the sample.

NC, MN, OR, and WY samples each have distinct second-shell features in the EXAFS. Similar results may be achieved in modeling the EXAFS using either O or Al atoms in the second shell. O (or N or C) atoms would most likely indicate an association with organic matter, while Al would point towards coagulant interactions. OR and WY samples are similar both in the XANES and EXAFS. Given the apparent correlation between Cu and C in the SEM-EDS for the OR sample, organic matter is likely to be a primary contributor for at least both the WY and OR samples.

4.4. Batch sorption studies

4.4.1. A predictive approach for the determination of the ability of DWTR to sorb metals based on their bond-forming properties. For these sorption experiments, strontium (Sr^{2+}), thallium (Tl^{+}), and lead (Pb^{2+}) as nitrate salts were used as sorbates representing type-A, type-B, and borderline metal cations, based on the environmental classification of metals proposed by Nieboer and Richardson (1980). This environmental classification takes into account covalent and ionic bond parameters and defines (i) a covalent index determined as the product of the metal ion electronegativity (X_m^2) and the ionic radius (***r***), reflecting the ability of a given metal to accept electrons from donor ligands; and (ii) an ionic index determined as the ratio z^2/r, where z is the ionic charge and ***r*** is the radius in angstrom and measures the tendency of ionic-bond formation. As sorbents, we selected 4 DWTR samples with different bulk chemical compositions dominated by either Fe (Fe-DWTR), Al (Al-DWTR), a combination of both Fe and Al ((Fe+Al)-DWTR,) or Ca (Ca-DWTR). Therefore, the highly heterogenous DWTRs with potentially several metal binding sites/mechanisms, metals with low covalent index values (Type-A) would be expected to be immobilized onto DWTR primarily by electrostatic forces while metals with high covalent index values (Type-B) will form strong covalent bonds with donor ligand atoms. Therefore, sorbents containing sulfur (S), nitrogen (N) and/or oxygen (O) as electron donor atoms would be ideal for type-B metals, while sorbents with net negative surface charges would efficiently sorb type-A metals. Finally, metals with covalent indices between the above two endmembers will form both ionic and covalent bonds. The relevant physicochemical characteristics of the 4 selected DWTRs are presented in **Table 10**. Two of the selected DWTRs (Fe-DWTR-AR and Al-DWTR-WY) have near-neutral pH values while the (Al+Fe)-DWTR-OR and Ca-DWTR-NC exhibited acidic (5.6) and basic (9.5) pH, respectively. The measured SSA values ranged from 18.4 to 30.3 m^2/g, except for Fe-DWTR-AR, which has a significantly higher SSA of 190 m^2/g. The size distribution analysis gave average particle size values of 436±20, 480±61, 852±147, and 3,829±592 nm for (Al+Fe)-DWTR-OR, Al-DWTR-WY, Ca-DWTR-NC, and Fe-DWTR-AR, respectively. Accordingly, the observed differences in SSA are likely not due to the particle size distribution but probably attributable to the types and abundance of sorption sites on these materials. For instance, the much larger Fe-DWTR-AR particle sizes could be more porous (e.g., micropores ranging from 2 to 10 nm and/or super-micropores <2 nm) providing more sites for N_2 adsorption, whereas the other DWTR samples with smaller particles could have mesopores (100 to 1000 nm) and macropores (>1000 nm).

The organic matter (OM) content estimated as mass loss on ignition (LOI) was quite similar (~36% on average), except for Ca-DWTR-NC with only 6%. Organic compounds tend to be rich in electron donor atoms such as O, N, and S, it could play a significant role in the sorption of metals (Benedetti et al., 1996).

For Al-DWTR-WY, (Al+Fe)-DWTR-OR and Fe-DWTR-AR the calculated ratios of measured total concentrations of Al and Fe are 4.5, 1.2 and 0.6 respectively, corresponding to a decrease in Al content. The Ca-DWTR-NC, a lime-based substrate was overwhelmingly dominated by Ca. As stated earlier, divalent Sr and Pb as well as monovalent Tl cations were selected as sorbates for use in batch sorption studies. Therefore, total concentrations of these metals in the tested DWTRs were determined as well as the fractions leachable in a 0.01M KNO_3 solution. The results show that Sr occurs in relatively high concentrations in all DWTR-samples, but mostly in Ca-DWTR-NC. The analyses for Pb and Tl resulted in rather low values with some below analytical detections.

Table-10. Relevant physicochemical characteristics of the four DWTR used as sorbents in batch sorption studies.

Parameter	**Al-**DWTR-WY	**(Al+Fe)-**DWTR-OR	**Fe-**DWTR-AR	**Ca-**DWTR-NC
pH	7.1	5.6	7.5	9.5
SSA-N_2(BET) (m^2/g)	30	18	190	30
OM as loss on ignition (%)	37	32	39	6
Total Al (mg/kg)	84569 ± 1218	46128 ± 693	61231 ± 673	8601 ± 125
Total Fe (mg/kg)	18747 ± 138	39884 ± 435	94204 ± 542	8978 ± 66
Total Ca (mg/kg)	7045 ± 239	3071 ± 107	2435 ± 29	137935 ± 2329
Total Sr (mg/kg)	97 ± 2.4	43 ± 1.3	17.3 ± 0.8	590 ± 17
Total Pb (mg/kg)	9.8	5.9	4.3	0.5
Total Tl (mg/kg)	0.3	0.1	0.2	<DL
Leachable Sr (mg/kg)	29	5.6	7.8	157
Leachable Pb (mg/kg)	0.1	0.1	0.1	<DL
Leachable Tl (mg/kg)	<DL	<DL	0.1	<DL

<DL = below detection limits. Values are averages of 3 replicates and standard deviation values are shown when different from zero.

The zeta potentials at the natural pH of each DWTR powder were collected using a Malvern Zetasizer Ultra (*https://malvernpanalytical.com*), and the standard ZEN1002 dip cell with automatic control. Initial suspensions were prepared by adding 100 mg of DWTR-powder to 100 mL of DI-water in a wide mouth polyethylene bottle, and then mixed for 60 seconds followed by bath sonication for 10 min. Samples were then aged for about 24h before initial measurements. Changes in the zeta potential of the 4 DWTRs as a function of pH were measured over the pH range of 6 to ~9. Zeta potential titration curves were collected using a DTS1070 folded capillary cell with tubing flowing from and returning to a stirred reservoir in between measurements. For Fe-DWTR-AR, Al-DWTR-WY and (Al+Fe)-DWTR-OR the initial pH was near neutral (6 to 7), and titration was performed by adding 0.01 M NaOH to the suspension reservoir while the zeta potential measurement was proceeding to change the pH by roughly 0.5 pH units. After measurement on the previous pH was completed, peristaltic flow started, pH re-adjusted if necessary, and stabilized before stopping the flow and collecting the next data point. For Ca-DWTR-NC, the native pH was > 9. In this case, 0.01 M HCl was used to adjust the pH of the suspension. During the titration, each pH point was measured three times in succession with a minimum of 10 and a maximum of 50 points. The results are presented in **Figure 56**. At pH 7 and above, Al-DWTR-OR shows a net surface charge of about zero while the other 3 samples exhibit net negative surface charges.

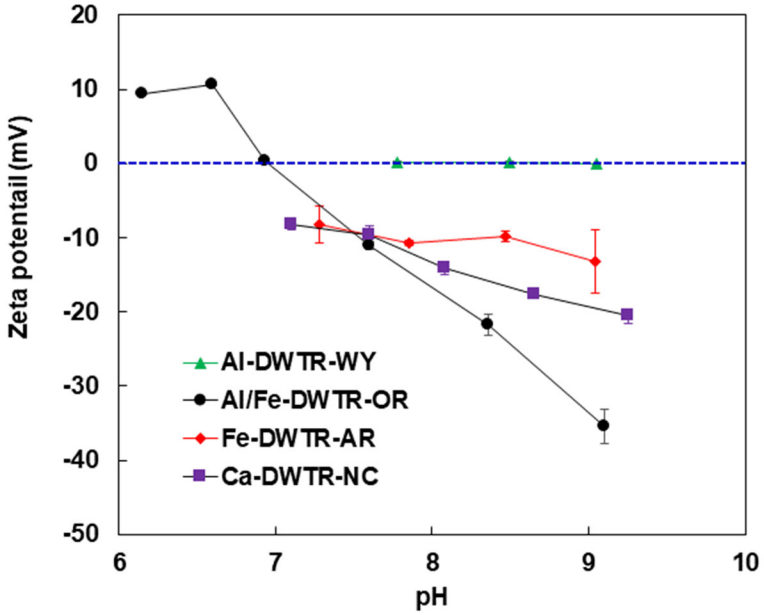


Figure 56. Effect of pH on the zeta potential of the four DWTR samples used in these batch sorption studies. Note the stability of the zeta potential of Al-DWTR-WY with a net surface charge of about zero across the tested range of pH values.

4.4.2 Sorption isotherm studies. Batch sorption experiments were conducted at a fixed pH of 8.0, stabilized with the use of a buffer (HEPES). Solutions of the 3 metal cations were prepared separately using nitrate salts to produce final concentrations of 1000 mg/L for Sr^{2+}, Pb^{2+}, and Tl^{+}. These concentrated solutions were used to prepare solutions with increasing concentrations for the batch sorption studies. The tested initial metal concentrations (C_0) ranged from 1 to 500 mg/L.

Sorption studies were conducted in 50 mL polypropylene (PP) tubes in which DWTRs were mixed with aqueous solutions in a mass to volume ratio of 1g DWTR per liter. Each initial concentration solution was also placed into PP tubes without DWTRs and used as control to account for possible sorption on the walls of the containers. KNO_3 at a final concentration of 0.01M was used as an electrolyte and the pH buffered at 8.0 with HEPES. Sorption studies were conducted at room temperature and the mixtures were continuously shaken at 180 rpm for 72h. After the mixing time, the pH was measured again. The slurries were centrifuged, the supernatant filtered (0.45µm) and analyzed for metals by ICP-MS. All experiments were conducted in triplicates.

The obtained sorption data were fit to Langmuir and Freundlich models described in the "materials and methods" Section. The results are presented in **Figures 57, 58, and 59**. Our experimental data were best fitted by the Langmuir model, except for Sr and Pb sorption by Ca-DWTR-NC, where the experimental data were better fitted by a modified Langmuir (Fig. 57) or a Freundlich (Fig. 58) model, respectively. The model parameters obtained using the experimental data are presented in **Table 10**.

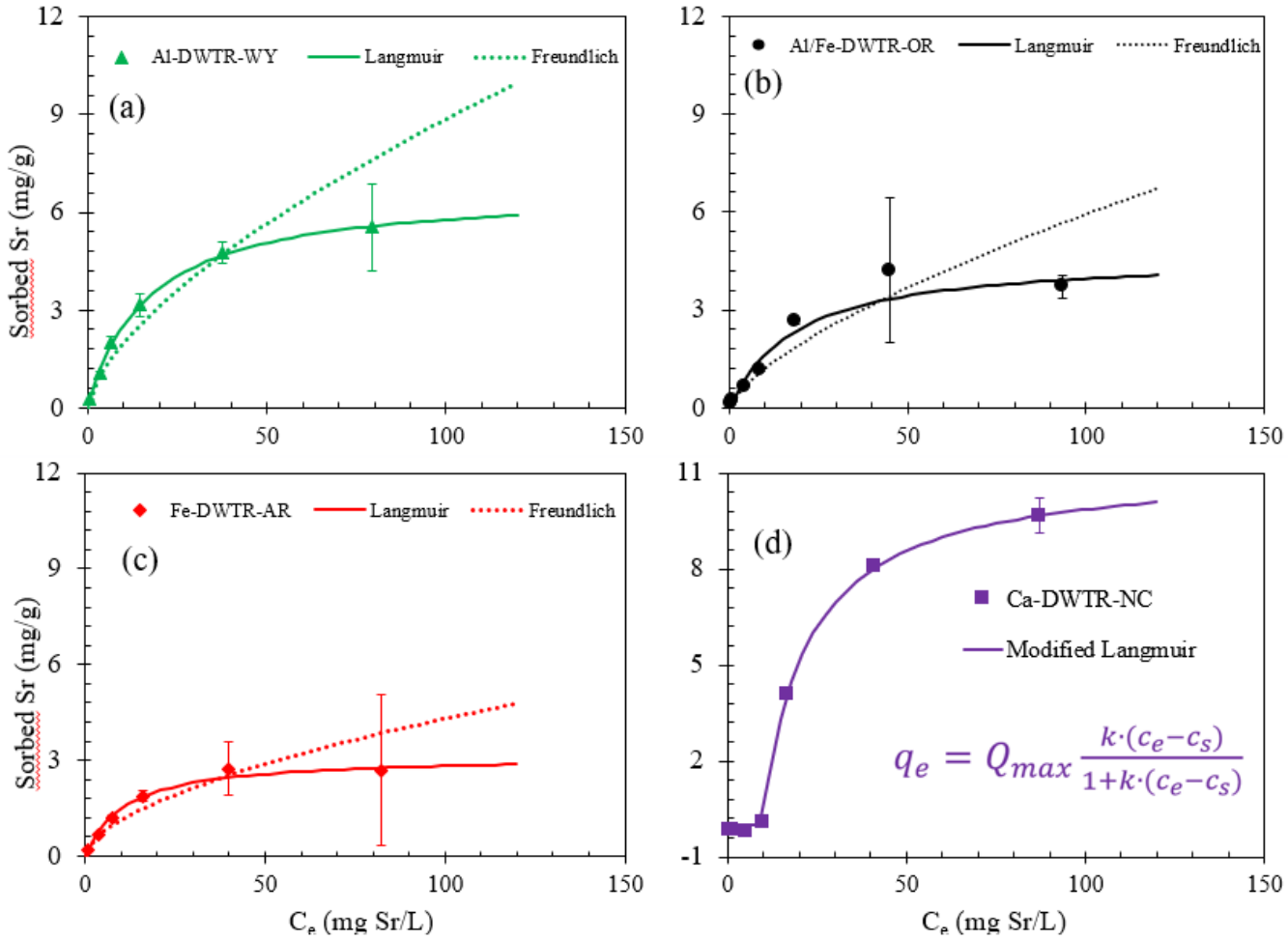


Figure 57: Strontium sorption by the four different DWTR samples at pH 8.0. **(a)** Sorption by Al-DWTR-WY. **(b)** Sorption by (Al+Fe)-DWTR-OR. **(c)** Sorption by Fe-DWTR-AR. **(d)** Sorption on Ca-DWTR-NC. The experimental data were best fit by the Langmuir model for the first 3 DWTR samples. For Ca-DWTR-NC, a modified Langmuir was needed to fit the experimental data.

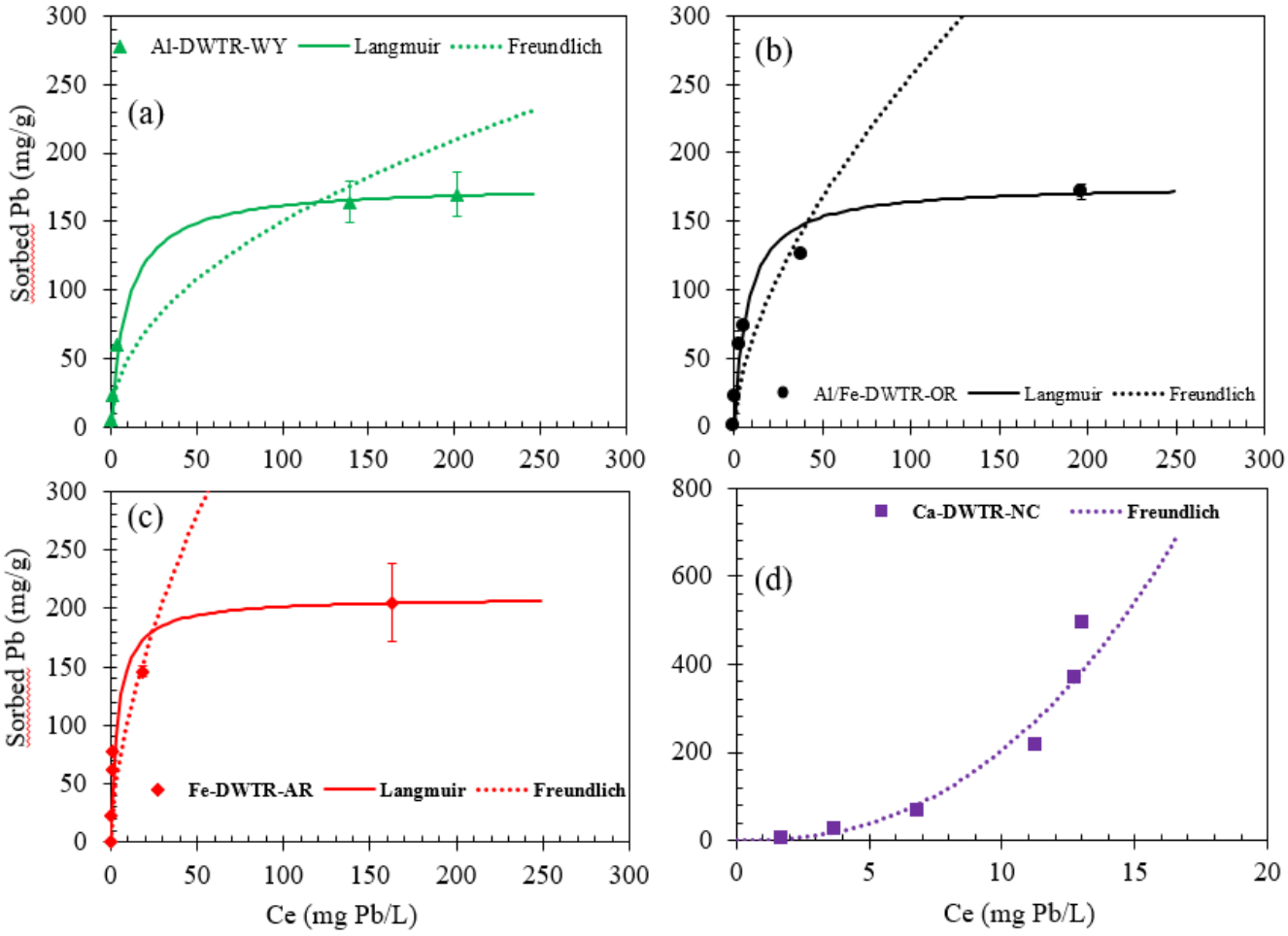


Figure 58: Lead sorption isotherms by four different DWTR samples. **(a)** Sorption by Al-DWTR-WY. **(b)** Sorption by (Al+Fe)-DWTR-OR. **(c)** Sorption by Fe-DWTR-AR. **(d)** Sorption by Ca-DWTR-NC. For the first 3 DWTRs, the experimental data were best fitted by the Langmuir model. For Ca-DWTR, the Freundlich model fitted the experimental better.

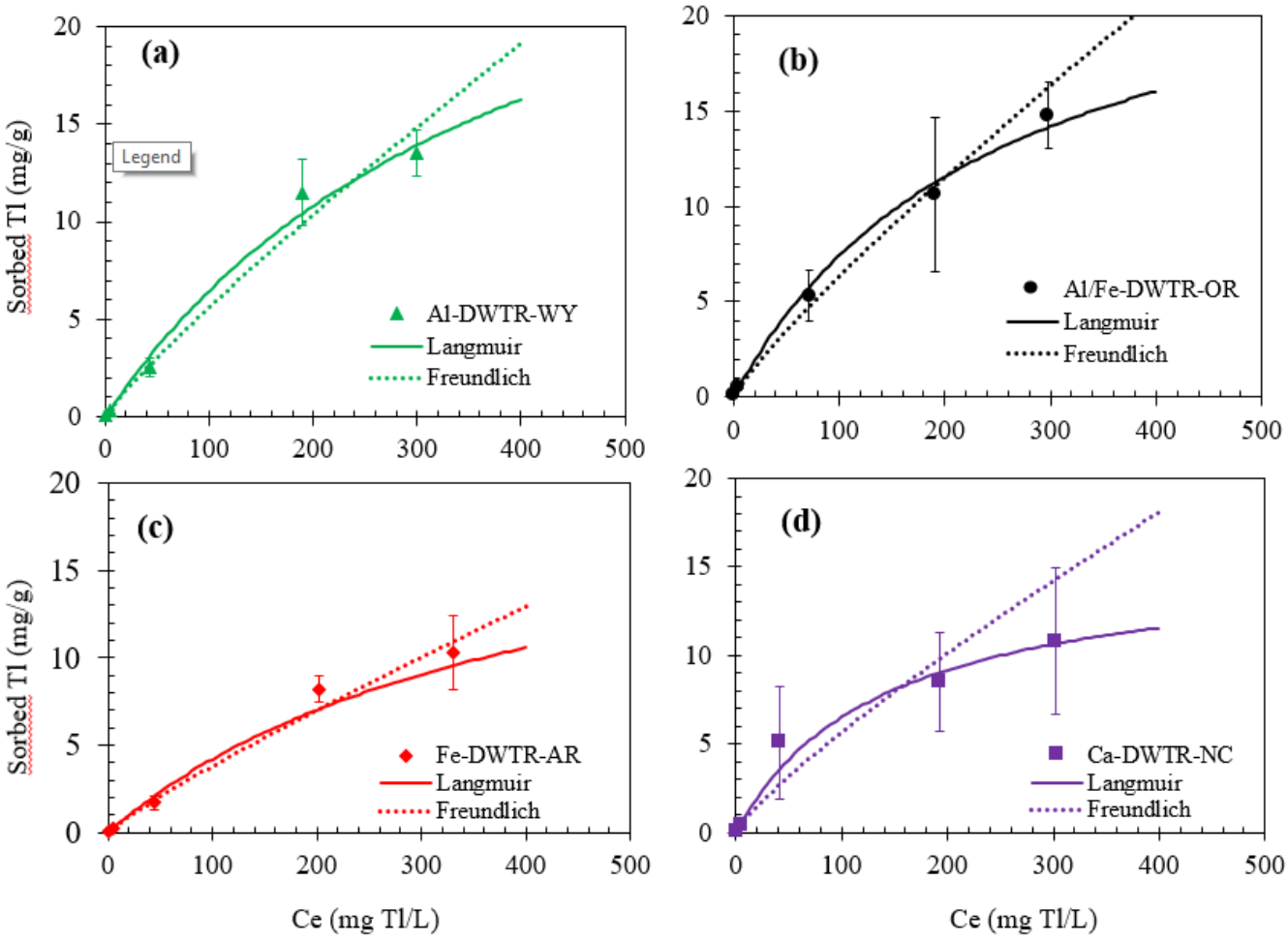


Figure 59: Thallium sorption by the four different DWTR samples. **(a)** Sorption by Al-DWTR-WY. **(b)** Sorption by (Al+Fe)-DWTR-OR. **(c)** Sorption by Fe-DWTR-AR. **(d)** Sorption by Ca-DWTR-NC. Overall, the Langmuir model resulted in the best fit of the experimental data.

Table 11. Parameters for the fitted Langmuir model (***k*** and Q_0) and the modified Langmuir model (*) using experimental data for sorption of Sr, Pb, and Tl by DWTR samples. ***nd: not determined because the removal of Pb from solution by Ca-DWTR-NC involved a combination of sorption and precipitation mechanisms.*

Metals	DWTR samples	***k*** (L/mg)	Q_0 (mg/g)	C_s (mg/g)
Sr	Al-DWTR-WY	0.061	6.73	-
	Al/Fe-DWTR-OR	0.055	4.68	-
	Fe-DWTR-AR	0.090	3.14	-
	Ca-DWTR-NC	0.081	*11.20	*9.83
Pb	Al-DWTR-WY	0.106	176.62	-
	Al/Fe-DWTR-OR	0.123	176.82	-
	Fe-DWTR-AR	0.254	209.54	-
	Ca-DWTR-NC	***nd*	*nd*	-
Tl	Al-DWTR-WY	0.0024	32.91	-
	Al/Fe-DWTR-OR	0.0039	26.20	-
	Fe-DWTR-AR	0.0019	26.85	-
	Ca-DWTR-NC	0.0072	15.54	-

Although one would expect the experimental sorption data obtained in this study to fit better the Freundlich model given the complexity of DWTR matrices, the Langmuir model gave a better prediction, suggesting that metal sorption by DWTR particles would be a monolayer sorption process and that the surface would be covered completely when the initial concentration in solution is high. Finally, because of the significance of the precipitation process as metal removal mechanism on Ca-DWTR, Pb and Sr show sorption behaviors that deviate from the logic discussed above. Further studies are needed in this case to help distinguish between sorption and precipitation. In fact, for Pb sorption onto Ca-DWTR-NC, the plateau was never reached even when the sorbent was in contact with a very high initial Pb concentration. This is likely due to Pb removal through precipitation, giving the impression that Ca-DWTR could still sorb more.

For Sr, when the initial concentration in the solution exceeded 10 mg/L, sorption by Ca-DWTR-NC could still not be simulated using the traditional Langmuir isotherm model. Hence, the modified Langmuir model used to simulate the S- or complex-shaped isotherm was used (Grant et al., 1998). An additional constant representing the concentration value to shift a Langmuir-shaped isotherm was introduced. Then the liquid phase concentration term (C_e) in equation 14 is replaced with (C_e-C_s), and where (C_s) is the shifted concentration as shown in Eq.3 (Grant et al., 1998). In this case, one can manage to get C_s = 10 mg/L, which means that when the initial concentration of Sr is greater than 10 mg/L, Ca-DWTR-NC would sorb strontium.

$$q_e = Q_0 \frac{k \cdot (c_e - c_s)}{1 + k \cdot (c_e - c_s)} \qquad Eq.14$$

From the characterization data of the 4 DWTR samples used, Al-DWTR-WY is the only sorbent with a net charge of nearly zero at the pH of 8 used in these studies, while the other 3 have net negative charges. Therefore, electrostatic adsorption can be excluded as significant sorption mechanism for either Sr, Pb or Tl by Al-DWTR-WY. When focusing on Sr^{+2} (type-A metal cation), the highest maximum sorption capacity is obtained with Ca-DWTR-NC as sorbent, followed by

Al-DWTR-WY, Al/Fe-DWTR-OR, and Fe-DWTR-AR. This observation suggests that Sr sorption is driven by electrostatic forces as the lowest sorption capacity is exhibited by a sorbent with a near-zero zeta potential. On the other end, the highest maximum sorption capacity exhibited by Ca-DWTR-NC can be explained by a combination of sorption and non-sorption (e.g., substitution and precipitation) phenomena. Sr has chemical properties similar to that of Ca and isomorphous substitution in amorphous calcium minerals such as calcite ($CaCO_3$) and gypsum ($CaSO_4 \cdot 2H_2O$) (Dubchak, 2018) could potentially contribute to the reduction of Sr concentrations from the aqueous phase. For Pb^{2+} (a borderline metal), Ca-DWTR-NC seems to have the highest sorption capacity. However, it is clear precipitation plays a significant role in this case. The solubility product (K_{sp}) of $PbCO_{3(s)}$ and $Pb(OH)_{2(s)}$ are ~7.4×10^{-14} and ~1.43×10^{-20} respectively (Stumm and Morgan, 1996). Therefore, if assuming ideal conditions, Pb concentration of 500 ppm corresponding to 2.43×10^{-3} mol/L would result in Pb precipitation as $PbCO_{3(s)}$ and $Pb(OH)_{2(s)}$ if its dissolved concentration exceeds 3.05×10^{-11} mol/L and 2.42×10^{-9} mol/L, respectively. Based on these assumptions, one can conclude that precipitation played a role in the observed removal of Pb from aqueous solutions.

For Tl (type-B metals), Al-DWTR-WY and (Al+Fe)-DWTR-OR show similar sorption capacities, which are higher than those obtained using Fe-DWTR-AR and Ca-DWTR-NC. Tl seems to have a higher affinity for Al-DWTR than Fe-DWTR and Ca-DWTR. However, in our sorption studies, Tl was used as a monovalent ion (Tl^{+}), which can be prone to oxidation to Tl^{3+}. Although these experiments were not conducted under controlled anaerobic conditions, it is believed that the formation of $Tl(OH)_{aq}$ with an association constant of $10^{2.3}$ (Lin and Nriagu, 1998) would be stable in used reactors, which had very limited headspace and maintained at pH 8.0 with HEPES buffer. In conclusion, our results show that the affinity of the tested 3 sorbates for the 4 different DWTR increases in the order $Sr^{2+}<Tl^{+}<Pb^{2+}$. One could therefore assume that the sorption efficiency of DWTR for metals would be in the order *Borderline* > *Type-B* > *Type-A,* based on the environmental classification of metals proposed by Nieboer and Richardson (1980).

Sorption kinetics studies. The results of sorption kinetics for Sr^{2+}, Pb^{2+} and Tl^{+} by each of the four DWTR samples are shown in **Figure 60.** In these studies, equilibrium was attained in ~48h. Using a solid/liquid ratio of 1:1 (*m/v*), the determined mass of sorbed Sr ranged from 0.76 mg/g for Ca-DWTR-NC to 3.26 mg/g for Al-DWTR-WY. The mass of sorbed Pb ranged from 105.58 mg/g for (Al+Fe)-DWTR-OR to 123.59 mg/g for Fe-DWTR-AR, while Tl sorption resulted in much lower values, ranging from only 0.55 mg/g for Ca-DWTR-NC to 0.84 mg/g for (Al+Fe)-DWTR-OR. This trend seems to confirm the highest affinity of the tested borderline metal cation (Pb^{2+}) for the highly heterogenous DWTR matrices, which is likely due to a combination of several immobilization mechanisms. Kinetic models were used to fit the experimental data including the Lagergren's pseudo-first-order model (Moussout et al., 2018), a pseudo-second-order model (Ho and McKay, 1999), and the intra-particle diffusion model. The Lagergren's pseudo-first-order model resulted in rather poor fits of the experimental data (results not shown). In contrast, the pseudo-second-order model using Eq. 15 (Ho and McKay, 1999), and where q_e is the metal concentration at equilibrium per unit mass of DWTRs (mg/g), q_t is the amount of metal adsorbed per unit mass of DWTRs (mg/g) at time (t), and k_2 is the sorption rate constant (in $g.mg^{-1}\cdot min^{-1}$); fitted the experimental data better. The parameters q_e and k_2 shown in **Table 12** were obtained by plotting t/q_t versus time (t) (**Figures 61, 62, and 63**).

$$\frac{t}{q_t} = \frac{1}{k_2 \cdot {q_e}^2} - \frac{t}{q_e} \qquad Eq\ 15.$$

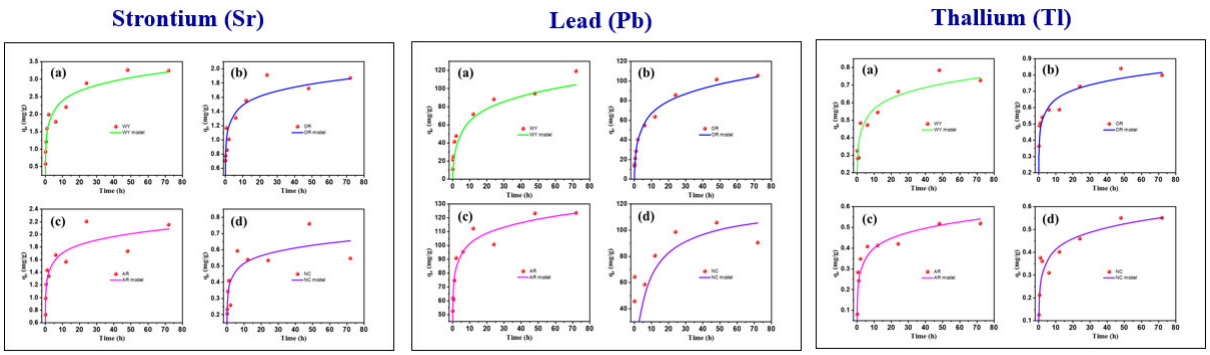


Figure 60. Sorption kinetics of strontium, lead, and thallium by: **(a)** Al-DWTR-WY, **(b)** (Al+Fe)-DWTR-OR, **(c)** Fe-DWTR-AR, and **(d)** Ca-DWTR-NC. Points are experimental data and lines are model predictions. Note the differences in the range of values for sorbed metals on the Y-axes.

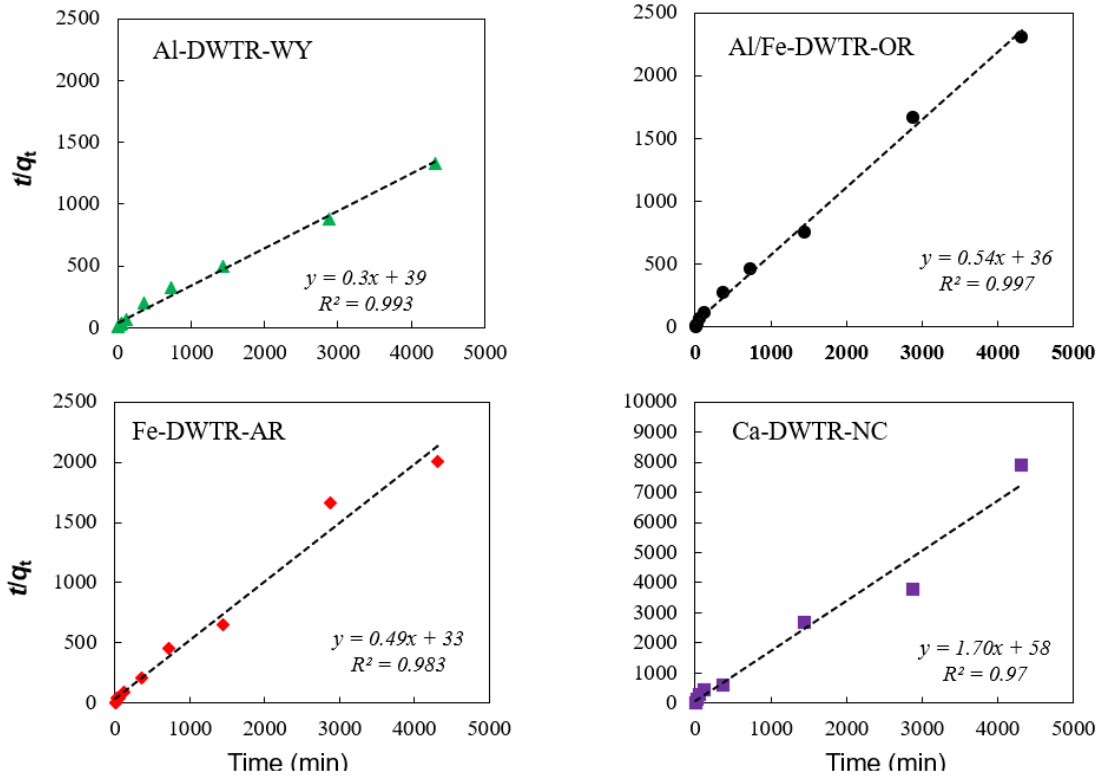


Figure 61. Pseudo-second order kinetics of strontium (Sr) sorption by DWTR samples. Al-DWTR-WY, Al/Fe-DWTR-OR, Fe-DWTR-AR, and Ca-DWTR-NC.

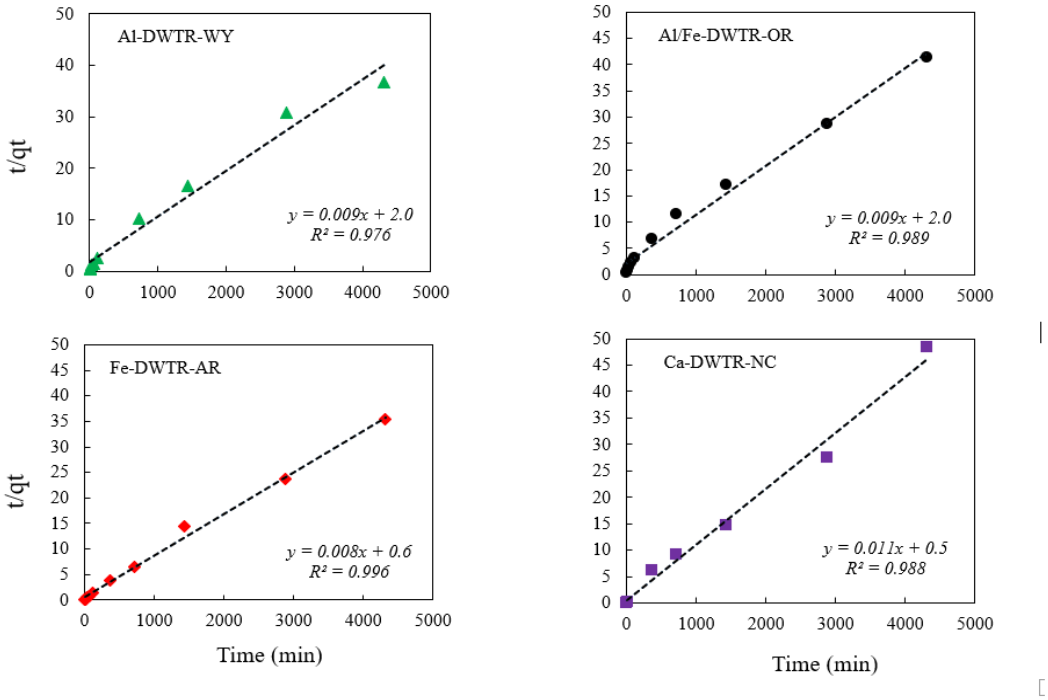


Figure 62. Pseudo-second order kinetics of lead (Pb) sorption by DWTR samples. Al-DWTR-WY, Al/Fe-DWTR-OR, Fe-DWTR-AR, and Ca-DWTR-NC.

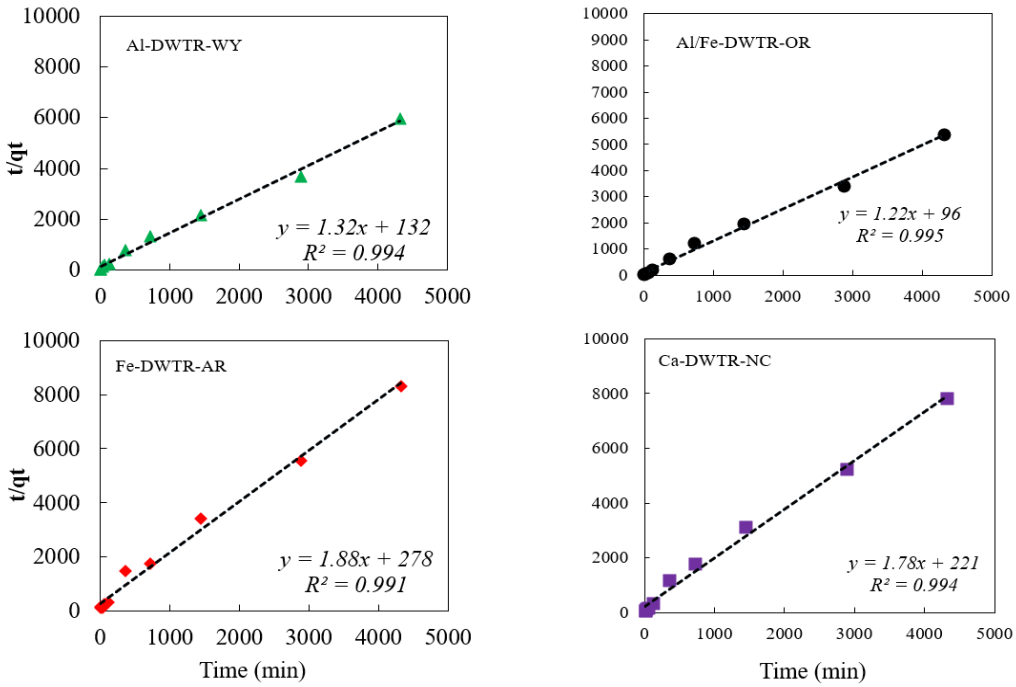


Figure 63. Pseudo-second order kinetics of thallium (Tl) sorption by DWTR samples. Al-DWTR-WY, Al/Fe-DWTR-OR, Fe-DWTR-AR, and Ca-DWTR-NC.

A few studies have shown that when the sorption process is controlled by diffusion, then the sorption kinetics follows a pseudo-first-order model quite well. In such cases, the rate-limiting step is mostly diffusion and less so, the dependence on the concentrations of sorbents and sorbates (Khare et al., 1987; Salim et al., 1992). However, the entire sorption behavior would support the pseudo-second-order model when chemisorption is the rate-controlling step, that is, the rate constant is highly dependent on concentrations and temperature (Ho and McKay, 1998, 1999). Furthermore, pseudo-first order model could fit the experimental data well for an initial period of the first reaction step (20 min - 30 min), whereas the pseudo-second-order model shows a better fit over a much longer period. Given the highly heterogeneous nature of DWTR matrices, it is likely that both chemical reactions and physical processes play significant roles in controlling the sorption of tested metals. Studies on the determination of the coordination environment of the different metals within the DWTR matrices after sorption studies will shed light on both chemisorption and precipitation as metal removal mechanisms from solutions.

Table 12. Fitted pseudo-second-order kinetic parameters for Sr, Pb, and Tl sorption on DWTRs at pH 8.0 and initial concentrations of 20, 100, and 10 mg/L, respectively

DWTR samples	Sr		Pb		Tl	
	k_2 (g.mg^{-1}.min^{-1})	q_e (mg. g^{-1})	k_2 (g.mg^{-1}.min^{-1})	q_e (mg. g^{-1})	k_2 (g.mg^{-1}.min^{-1})	q_e (mg. g^{-1})
Al-DWTR-WY	0.0023	3.32	0.00005	112.80	0.013	0.76
Al+Fe-DWTR-OR	0.0081	1.86	0.00004	107.15	0.016	0.82
Fe-DWTR-AR	0.0072	2.05	0.00816	122.50	0.013	0.53
Ca-DWTR-NC	0.0478	0.60	0.00022	94.56	0.015	0.56

.

Finally, the intra-particle diffusion model (Eq.16), which has been widely used to predict the kinetic sorption process by porous sorbents, and where the rate of sorption is dependent on the speed of diffusion of sorbate towards sorbent (i.e., the sorption process is more inclined to be diffusion-controlled) was used, where, k_i is the rate constant of the intra-particle diffusion model (mg/(g·$\sqrt{t}$)) and C is the intercept that gives information about the thickness of the boundary layer (Weber and Morris, 1963).

$$q_t = k_i \cdot \sqrt{t} + C \qquad Eq.16$$

In general, the larger the value of C, the greater the boundary layer effect would be. It could be concluded that the sorption process is controlled by the intra-particle diffusion if the plot of q_t versus $t^{1/2}$ for the experimental data matches the linear relationships. Otherwise, two or more steps would impact the sorption process if the data show multi-linear segments (Mall et al., 2007). The results of fitting our experimental data to the above-described intra-particle diffusion model are presented in **Figures 64, 65 and 66**.

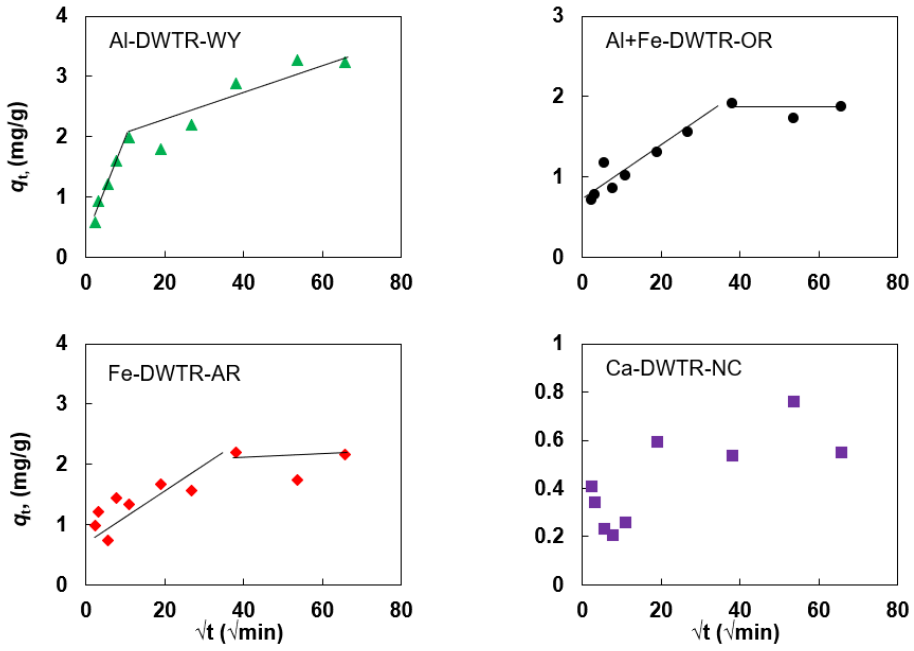


Figure 64. Intra-particle diffusion model for kinetic sorption of Sr by Al-DWTR-WY, Al/Fe-DWTR-OR, Fe-DWTR-AR, and Ca-DWTR-NC.

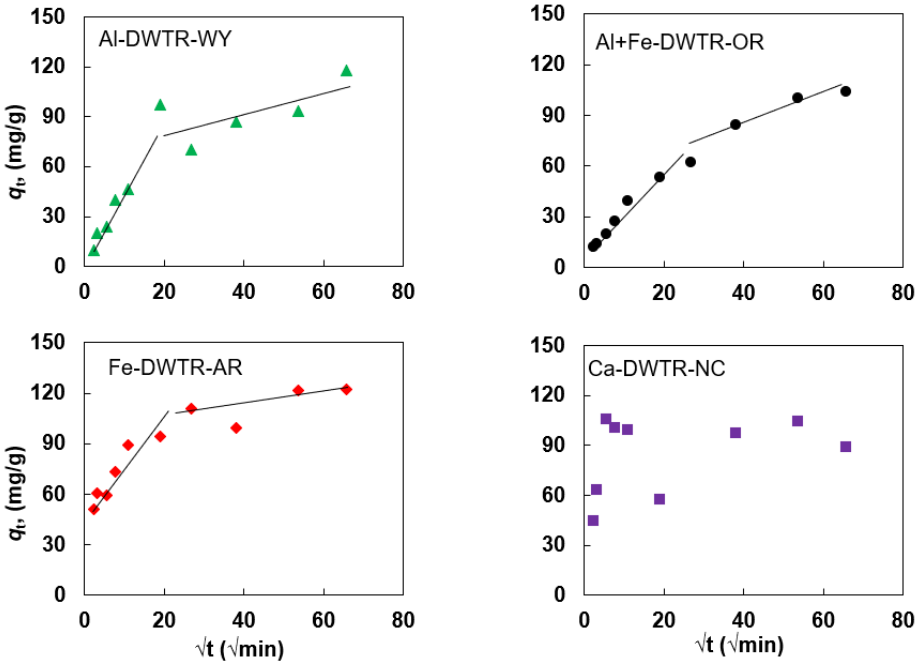


Figure 65. Intra-particle diffusion model for kinetic sorption of Pb by Al-DWTR-WY, Al/Fe-DWTR-OR, Fe-DWTR-AR, and Ca-DWTR-NC.

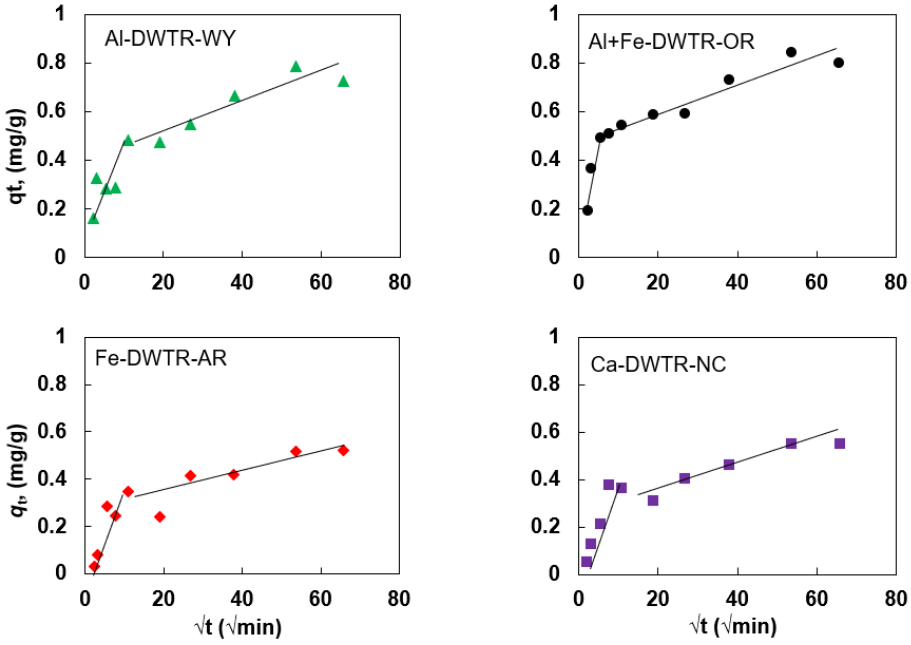


Figure 66. Intra-particle diffusion model for kinetic sorption of Tl by Al-DWTR-WY, Al/Fe-DWTR-OR, Fe-DWTR-AR, and Ca-DWTR-NC.

Except for Sr and Pb data for Ca-DWTR-NC, the observed sorption trends can be divided into two distinct linear segments (**Figures 64, 65 and 66**). The first segment could be attributed to metal diffusion on the boundary layer of DWTR particles or external mass transfer effects, while the second one may result from the gradual intra-particle sorption step on which the intra-particle diffusion plays an important role (Mall et al., 2007). The exceptions are Sr and Pb sorption trends on Ca-DWTR-NC, probably due to the complexity of the physicochemical processes involved. For instance, the tested Ca-DWTR-NC contained ~590 mg/kg Sr and readily released the equivalent of ~156 mg/kg when in contact with water containing KNO_3 as electrolyte at a background concentration of 0.01M. In addition to sorption and desorption processes, precipitation is also possible depending on the concentration of total dissolved inorganic carbon (DIC), which at pH 8.0 will be mostly present as HCO_3^-. For Pb sorption onto Ca-DWTR-NC, precipitation likely plays a role in the removal of Pb from solution. Therefore, depending on the nature of the sorbent, the removal of metals from aqueous solutions may involve mechanisms other than sorption processes.

4.4.3. Batch sorption studies of mercury (Hg) by 6 different DWTR samples.

The six DWTR samples and the results of Hg sorption experiments are presented in **Table 13** and **Figure 67**. The linearized isotherm compares q_e and q_e/C_e values, which results in the data having the slope of $-1/b$ and a y-intercept of Q_0. The linearized Langmuir clearly separates the UT sample from the rest of the DWTRs. Two observations are apparent. First, the q_e/C_e values on the x-axis reach much higher for the UT sample. Since the slope of this plot is taken to be $-1/b$, this indicates a much higher b value for the UT sample compared to the other DWTR samples used as sorbents. However, the UT sample is also poorly linearized,

which suggests at least one of the assumptions underpinning the Langmuir model is not satisfied. For example, this can indicate the presence of multiple sorption processes.

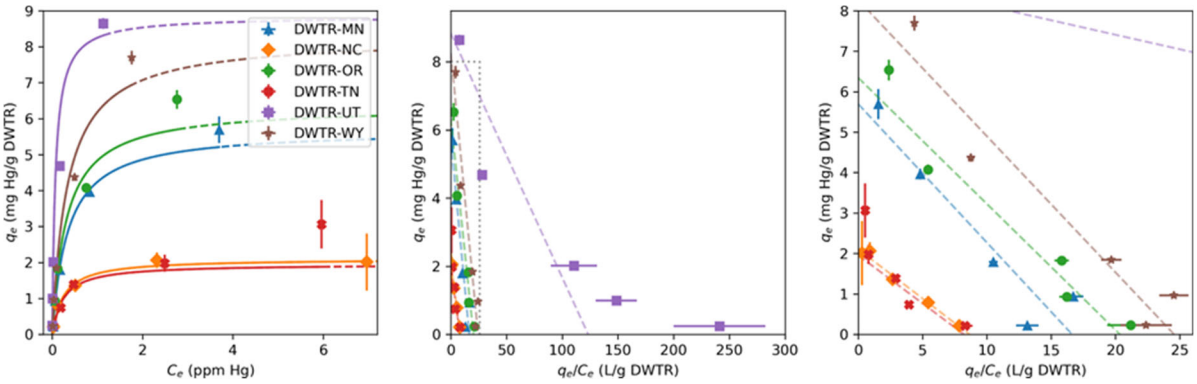


Figure 67. Langmuir sorption model fitting results for DWTR-Hg reactors, presented graphically. The left subplot shows the data in terms of the final concentration of Hg in solution (C_e) against the amount of Hg sorbed per unit mass of the DWTRs (q_e). The center subplot linearizes the model by comparing q_e/C_e with q_e, and the right subplot offers a closer look at the data following the boundaries established by the dotted gray line on the center subplot.

DWTR	Q_0 (mg Hg/g DWTR)	***b***
MN	5.7 ±0.8	2.9 ±0.6
NC	2.1 ±0.1	4.1 ±0.3
OR	6.3 ±0.7	3.2 ±0.6
TN	2.0 ±0.4	4.2 ±1.3
UT	8.8 ±1.2	14 ±6.0
WY	8.3 ±1.0	3.0 ±0.6

Table 13. Langmuir sorption model fitting results. Maximum sorption capacity (Q_0) and sorption affinity (b) are presented.

Generally, the obtained sorption capacity (Q_0) results can be divided into low (NC, TN), intermediate (MN, OR), and high (WY, UT) sorption capacities. NC and TN are lime-based; but another lime-based sample, MN, is in the intermediate tier. Our previous characterization work established MN as having high organic matter content relative to other lime based DWTRs (Zhou et al., 2021a). In fact, a pattern connecting increasing organic matter content with increasing sorption capacity holds across the full range of DWTRs, as shown in **Figure 68.** Q_0 correlates with measures of organic matter in the DWTRs, including non-acid-volatile carbon and particularly thermogravimetric mass loss from 200 to 430^{0}C (Pallasser et al., 2013). Notably, the relationship between the non-acid-volatile carbon content and Q_0 is apparently less linear than the one between thermogravimetric mass loss and Q_0. Non-acid-volatile carbon measurements will include both organic carbon and, in the cases of WY and UT samples, activated carbon, whereas the decomposition of activated carbon during thermogravimetric analysis is minimal under an inert atmosphere. As such, it does not appear that activated carbon drives major differences in the sorption capacity of Hg in DWTRs.

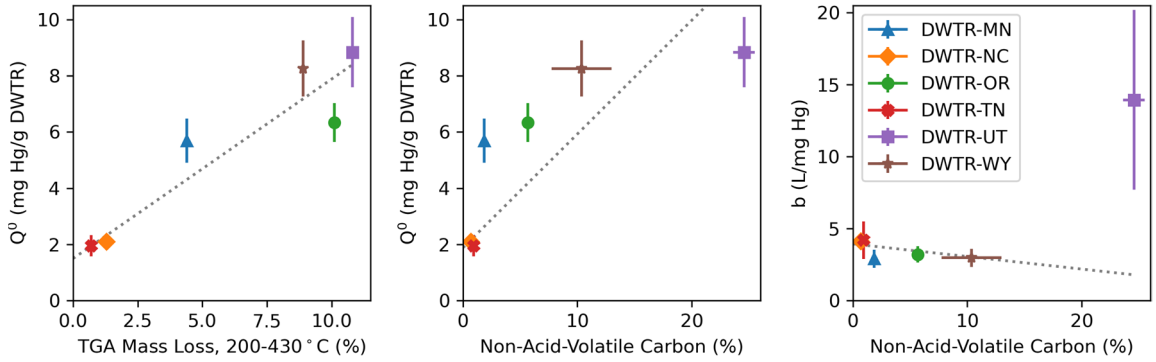


Figure 68. Comparisons of Langmuir sorption model findings against DWTR characteristics. The left subplot compares the mercury sorption capacity (Q_0) against the thermogravimetric mass loss for DWTRs from 200-430°C, an indicator of the amount of organic matter. The center sub- plot compares Q_0 with the non-acid-volatile carbon content of DWTRs, which will consist of organic matter and, for UT and WY samples, activated carbon. Finally, the right subplot compares the non-acid volatile carbon content of DWTRs with the Langmuir sorption affinity (b).

The last subplot of **Figure 68** compares the non-acid-volatile carbon content to the sorption affinity b. Except for the UT sample, all calculated values for b fall in the same general range (**Table 13**). UT is an outlier among these samples both in terms of b and the amount of non-acid-volatile carbon in the DWTR. These findings suggest that the strong binding at lower mass loadings for Hg by the UT sample is due to the abundance of activated carbon. This, in turn, offers a plausible mechanism for multiple sorption processes giving rise to misfit in the Langmuir model for the UT sample.

Based on these findings, the dominant mechanism in DWTRs seems to involve the association of Hg with organic matter. Though non-lime based DWTRs also have higher aluminum content than the non-lime based DWTRs (**Figure 69**), which could account for the elevated sorption capacities of the UT, WY, and OR samples, and connecting sorption to the coagulant alone would be unable to account for the capacity of MN for mercury. Direct characterization of Hg sorption through XAS provides additional clarity.

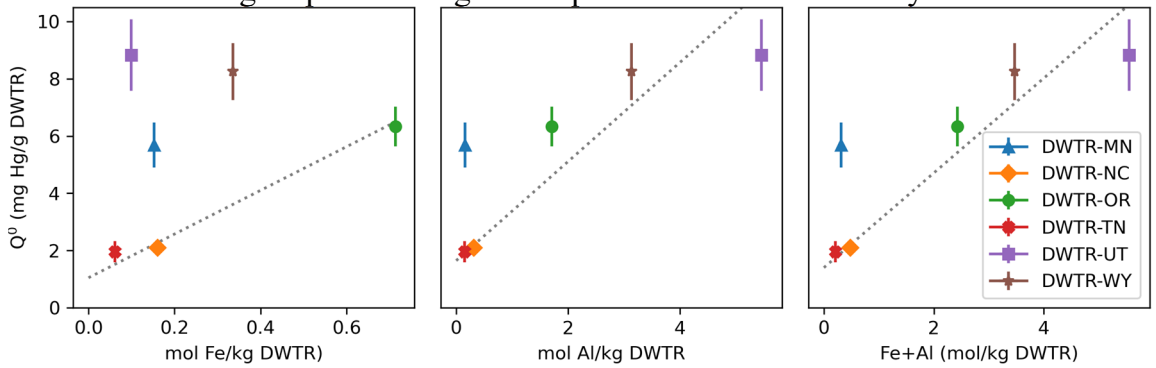


Figure 69. The relationship between the Langmuir sorption capacity for mercury to DWTR samples (Q_0) and the iron and aluminum content of the DWTRs (Zhou et al., 2021a). Iron (the left subplot) does not show a strong relationship with Q_0. The aluminum content (center subplot) and the combined aluminum and iron contend (right subplot) do correlate well with the calculated sorption capacities, but these factors do not account for the high sorption capacity of the MN sample.

a. XAS. The analysis of the XAS data collected was performed by first looking at the insights one might gain from the near-edge structure and further complemented by an interpretation of the extended fine structure (XANES). **Figure 70** shows the principal component analysis (PCA) of Hg L3-edge XANES. Spectra are relatively similar across all conditions, even among different samples and pH values; there is no clear separation of the data. Given the use of conventional XANES, this is not necessarily unexpected. However, two factors do seem to drive some modest differences in the XANES based on how the spectra project on the first two principal components: the mass loading of mercury onto DWTRs and the use of lime as an additive.

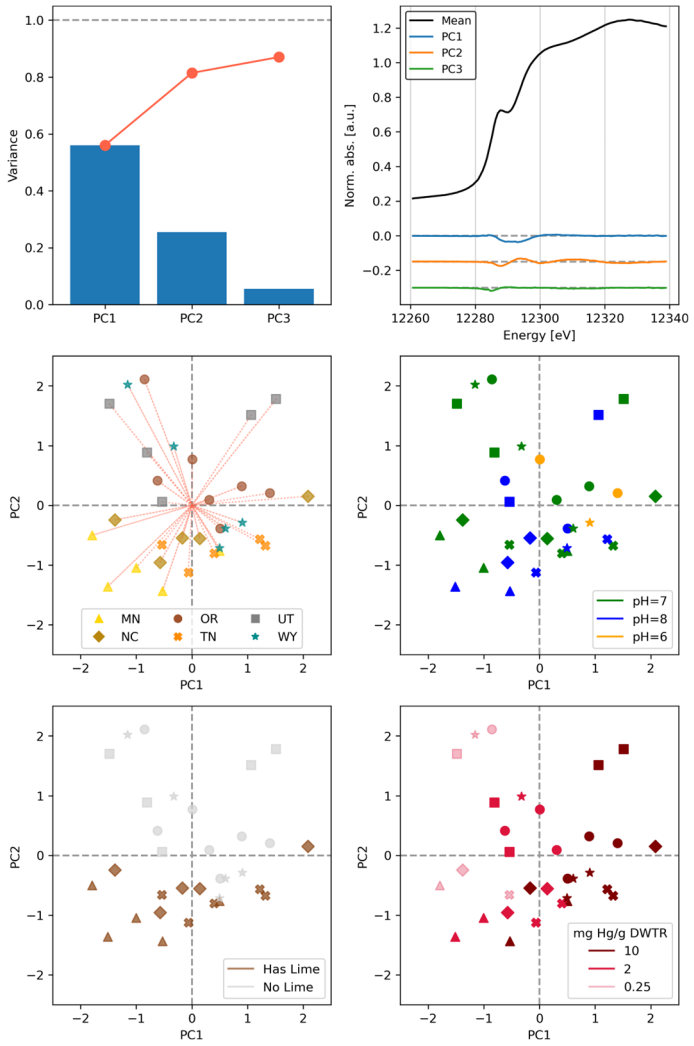


Figure 70. Principal component analysis (PCA) of Hg L3-edge XANES spectra for mercury sorbed to DWTR samples. The top left subplot shows the variance among samples accounted for by the principal components. The top right subplot visualizes the components, which are shown as the difference from the mean spectrum. The remaining subplots project the DWTR samples on the first two principal components, showing the impact of the DWTR sample, the buffer used (MES, MOPS, and HEPES for 6, 7, and 8, respectively), the use of lime as an additive, and the maximum mass loading of mercury to the DWTRs.

XANES provides no evidence for dominant coordination with carboxyl groups in these samples. Target transformations of Hg standards best reconstructed spectra which should be predominated by Hg associated with hydroxyl groups (**Figure 71),** such as Hg sorbed to kaolinite and iron oxide. In contrast, XANES for samples such as Hg(II) acetate, Hg(II) alginate, and Hg-EDTA complexes, which would strongly show Hg associated with carboxyl groups, are relatively poorly reconstructed. Still, the contribution of Hg associated with organic matter to the DWTR spectra cannot be discounted due to the abundance of hydroxyl groups in natural organic matter and the documented affinity of mercury towards phenolic groups (Ge and Hendershot, 2005). Neither can the contribution of inorganic metal (hydr)oxides, such as those precipitated by coagulants used in the drinking water treatment processes, be dismissed at higher mass loading values.

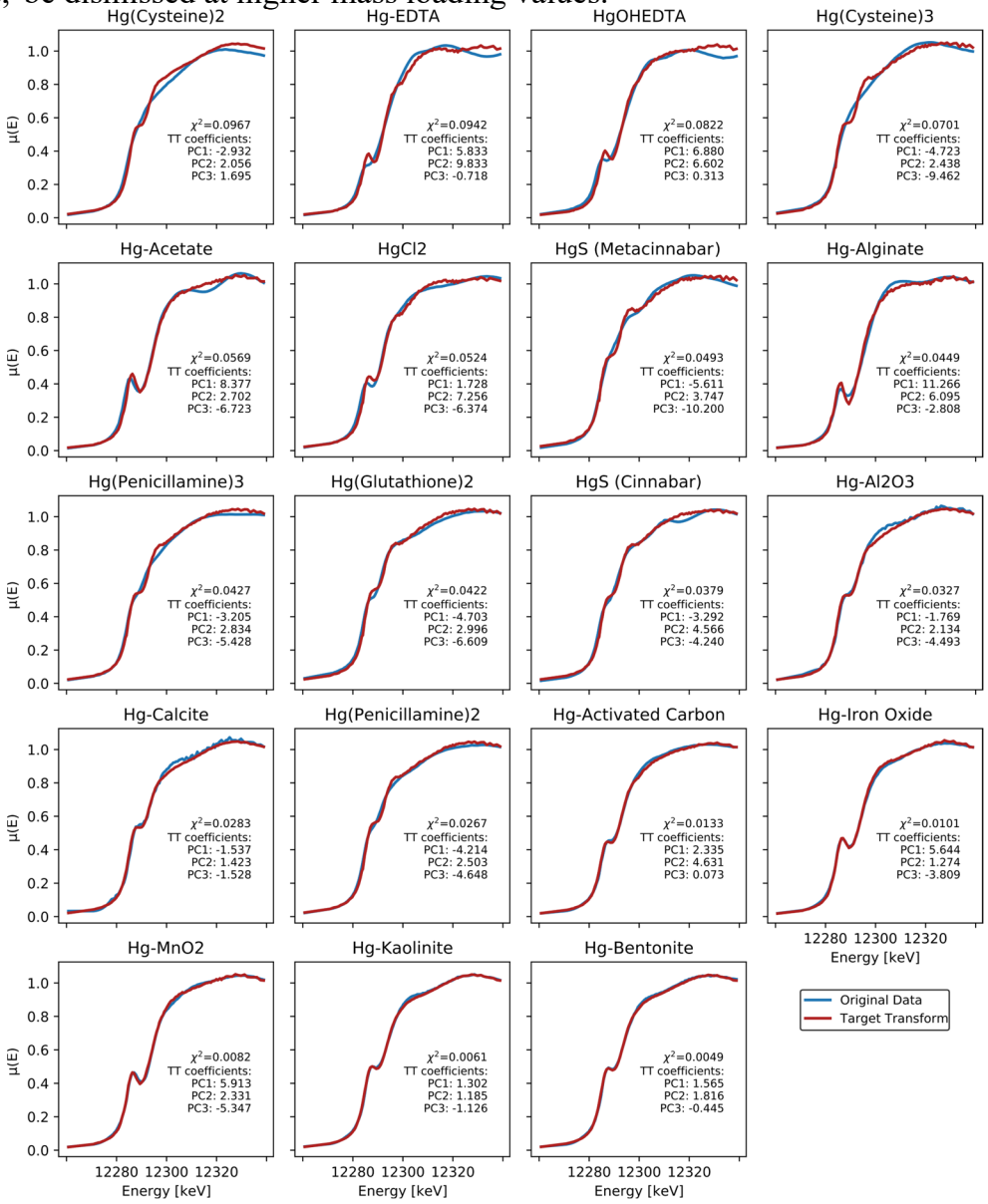


Figure 71. Target transformations of standard spectra based on the PCA of DWTR data. Standards best reconstructed are at the bottom right, while the worst-reconstructed standard spectra are in the top left.

Spectra reconstructed through LCF are shown in **Figure 72.** The standard spectra selected here include one for Hg coordinated with oxygen (Hg sorbed to kaolinite) and a spectrum for Hg in twofold coordination with sulfur (S) (a Hg-penicillamine complex) (Thomas et al., 2014). A general trend emerges where lower mass loading reactors assign a higher weight to the Hg-sulfur spectrum when reconstructed compared to the higher mass loading reactors. This agrees with previous spectroscopic findings for Hg sorbed to biomass, where mercury is expected to associate with high-affinity thiol groups in organic matter first, then oxygen functional groups subsequently (Mishra et al., 2011, Skyllberg et al., 2006).

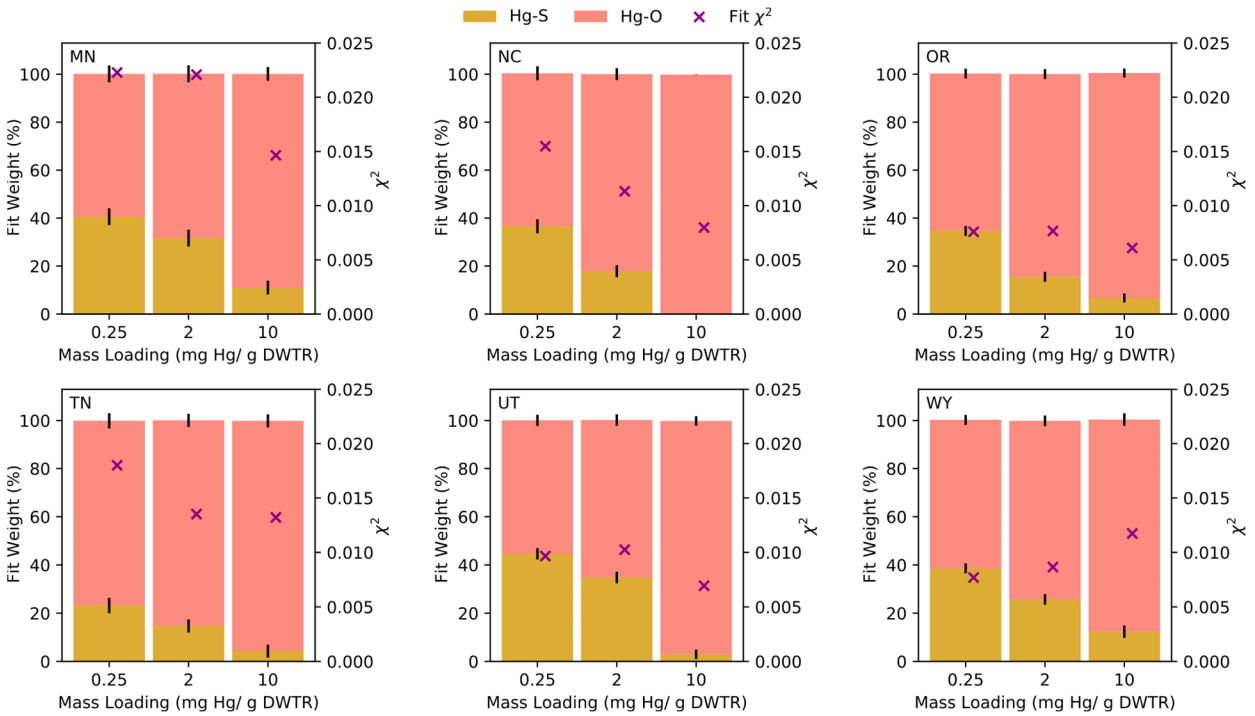


Figure 72. Linear combination fitting (LCF) results of Hg L3-edge XANES data. Data were fit from a range of 20 eV below to 70 eV above the edge energy using flattened, normalized XANES from standards of mercury sorbed to kaolinite (Hg-O) and complexed with penicillamine (Hg-S), forcing the sum to equal 1. The bars correspond with the percent weights on the left y-axis, while the X markers give the value of the χ^2 goodness-of-fit metric shown on the right y-axis.

b. EXAFS. The limitations at the resolution of conventional XANES make strong conclusions based on XANES alone difficult. EXAFS should provide a more precise way of identifying first-shell scattering atoms for these samples (i.e., distinguishing between O and S bonds). EXAFS and FEFF fitting results are presented in **Figures 73** and **74**. Most samples generally align with the EXAFS for the Hg-O single scattering path, and the DWTR-NC and DWTR-TN exhibit consistent features across all conditions. In contrast, the other DWTRs, particularly UT, WY, and OR, show features consistent with sulfur in the first shell for the samples with the lowest mass loading of Hg.

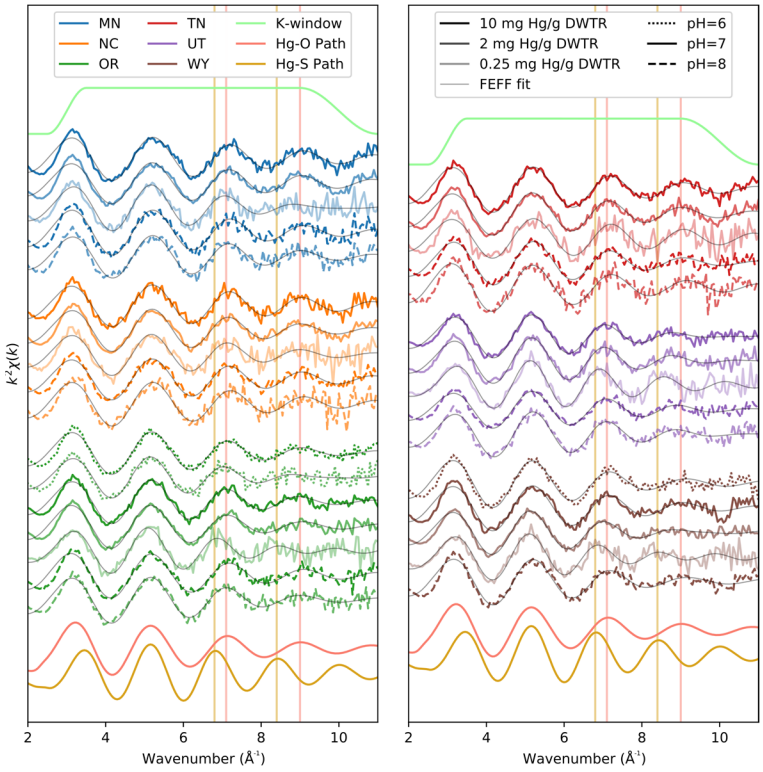


Figure 73. Hg L3-edge EXAFS for all spectra collected for mercury sorbed to DWTRs. The K-window for FEFF fitting is shown in the light green at the top of the plot. Spectra are separated and color-coded based on the DWTR sample used; the pattern of the lines corresponds with the buffer used in the reactor, while the opacity of the lines signifies the maximum mass loading of mercury to the DWTRs. FEFF fitting results, which are listed in Table 13 are shown in the thin gray line overlayed on each of the spectra. Finally, at the bottom of the plot, simulated spectra for Hg-O and Hg-S single-scattering paths are shown.

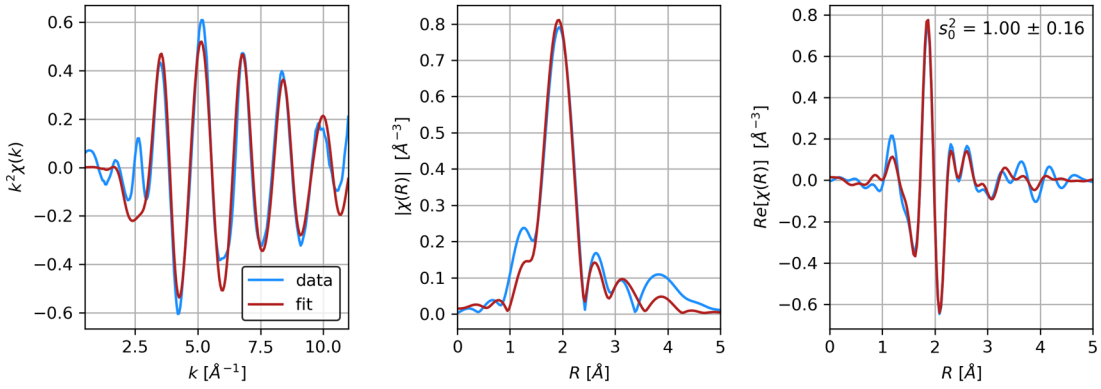


Figure 74. FEFF fitting of α-HgS EXAFS data to extract the S_0^2 value used for the FEFF fits of DWTR samples. Here, an S_0^2 value of 1.00±0.16 is found, so the value is fixed at 1 for all samples.

For FEFF fitting of the EXAFS data, S_0^2 was fixed at 1.0 based on the fit to a cinnabar

standard (**Figure 74**). Fitting was performed using single-scattering paths for both oxygen (O) and sulfur (S), extracted from the crystal structure of HgO and HgS. To ensure the convergence of the fit, the ΔE value was fixed at 0 eV and σ^2 was fixed at 0.006 for both paths. The coordination number N and path length R were fit for both paths.

FEFF fitting results are listed in **Table 14.** Across the samples, Hg is fit to be coordinated with approximately two atoms total. These include oxygen atoms at a distance of ~2Å, and sulfur at a distance of ~2.3 Å.

DWTR	Buffer	mg Hg/g DWTR	Hg-O		Hg-S		R-Factor
			N	*R* (Å)	*N*	*R* (Å)	
MN	HEPES	10	1.6 ±0.2	2.007 ±0.009	0.2 ±0.1	2.25 ±0.05	0.0096
		2	1.4 ±0.2	2.01 ±0.01	0.3 ±0.1	2.26 ±0.03	0.0131
	MOPS	10	1.6 ±0.2	2.02 ±0.02	0.3 ±0.1	2.22 ±0.06	0.0145
		2	1.5 ±0.2	2.02 ±0.02	0.3 ±0.1	2.23 ±0.05	0.0141
		0.25	1.2 ±0.2	2.01 ±0.01	0.5 ±0.2	2.32 ±0.02	0.0183
NC	HEPES	10	1.5 ±0.2	2.02 ±0.01	0.3 ±0.1	2.23 ±0.04	0.0116
		2	1.6 ±0.1	2.010 ±0.007	0.20 ±0.08	2.24 ±0.03	0.0044
	MOPS	10	1.5 ±0.2	2.02 ±0.01	0.3 ±0.1	2.22 ±0.04	0.0087
		2	1.4 ±0.2	2.02 ±0.01	0.3 ±0.1	2.26 ±0.03	0.0135
		0.25	1.4 ±0.2	2.01 ±0.01	0.3 ±0.2	2.29 ±0.04	0.0181
OR	HEPES	10	1.6 ±0.1	2.012 ±0.003	0.14 ±0.05	2.29 ±0.02	0.0016
		2	1.48 ±0.07	2.013 ±0.003	0.33 ±0.05	2.31 ±0.01	0.0018
	MOPS	10	1.4 ±0.2	2.016 ±0.008	0.4 ±0.1	2.29 ±0.02	0.0087
		2	1.5 ±0.1	2.013 ±0.006	0.2 ±0.1	2.32 ±0.03	0.0060
		0.25	0.9 ±0.2	2.02 ±0.02	0.9 ±0.1	2.35 ±0.01	0.0150
	MES	10	1.4 ±0.3	2.011 ±0.007	0.3 ±0.1	2.29 ±0.03	0.0076
		2	1.1 ±0.1	2.011 ±0.009	0.5 ±0.1	2.33 ±0.02	0.0105
TN	HEPES	10	1.4 ±0.1	2.003 ±0.007	0.3 ±0.1	2.28 ±0.03	0.0086
		2	1.81 ±0.08	2.007 ±0.004	0.05 ±0.06	2.26 ±0.09	0.0022
	MOPS	10	1.6 ±0.1	2.010 ±0.007	0.24 ±0.09	2.26 ±0.03	0.0052
		2	1.5 ±0.2	2.02 ±0.01	0.3 ±0.1	2.26 ±0.04	0.0143
		0.25	1.6 ±0.3	2.03 ±0.02	0.4 ±0.2	2.18 ±0.04	0.0107
UT	HEPES	10	1.1 ±0.2	2.02 ±0.01	0.4 ±0.1	2.29 ±0.02	0.0131
		2	1.2 ±0.2	2.01 ±0.01	0.5 ±0.1	2.29 ±0.02	0.0105
	MOPS	10	1.1 ±0.2	2.01 ±0.01	0.6 ±0.1	2.31 ±0.02	0.0136
		2	1.2 ±0.1	2.017 ±0.009	0.6 ±0.1	2.31 ±0.01	0.0073
		0.25	0.7 ±0.1	2.03 ±0.02	1.1 ±0.1	2.320 ±0.006	0.0060
WY	HEPES	10	1.5 ±0.2	1.998 ±0.007	0.3 ±0.1	2.32 ±0.03	0.0095
	MOPS	10	1.5 ±0.1	2.009 ±0.006	0.3 ±0.1	2.29 ±0.02	0.0061
		2	1.2 ±0.1	2.015 ±0.08	0.5 ±0.1	2.34 ±0.01	0.0076
		0.25	0.8 ±0.2	2.00 ±0.02	0.9 ±0.2	2.35 ±0.01	0.0165
	MES	10	1.6 ±0.2	2.00 ±0.01	0.3 ±0.2	2.32 ±0.04	0.0175

Table 14. FEFF fitting results for EXAFS of mercury sorbed to DWTR samples. For each fit, S_0^2 was fixed at 1.0, ΔE_0 was fixed at 0.0, and σ^2 was fixed at 0.006.

The patterns observed in XANES LCF and in the EXAFS oscillations are replicated by the FEFF fitting: samples with lower Hg mass loading are more likely to be coordinated with S atoms. The 0.25 mg Hg/g DWTR-UT sample is fit with the most sulfur: 1.1 ± 0.1

S atoms, with 0.7±0.1 O atoms completing the fit. In contrast, neither DWTR-NC nor DWTR-TN have any samples fit with more than 0.4 S atoms or less than 1.4 O atoms. These EXAFS results are again in agreement with previous work exploring the sorption of Hg to biomass, mercury was found to be coordinated with two atoms in the first shell: at low mass loading of mercury to biomass, those atoms were sulfur associated with thiol groups, while at high mass loading, the fit was dominated by oxygen associated with carboxyl groups (Mishra et al., 2011). Other work in natural systems has repeatedly found that organic matter strongly impacts the speciation of mercury (Haitzer et al., 2002; Ravichandra et al., 1998 and 2004; Skyllberg and Drott, 2010).

Alone, the oxygen association shown in the EXAFS along with the high weight given to the Hg-Kaolinite spectrum in XANES LCF would perhaps reinforce the importance of inorganic phases, potentially from coagulants, in driving Hg sorption to DWTRs. Indeed, at high concentrations of mercury and in DWTRs with limited organic matter, this may well be the case. However, at the high range of concentrations used in these experiments, environmental conditions are not reflected as mercury concentrations reach up to 10 ppm in solution and nearly 1% mass loading to DWTRs. These figures are approximately four orders of magnitude above environmental guidelines (based on a 0.77 ppb criterion continuous concentration in freshwater (USEPA, 2022), and a probable effect concentration of 1.06 mg Hg/kg dry freshwater sediments (MacDonald et al., 2003). These high-concentration reactors allow for the collection of quality conventional XAS data and for the separation of DWTRs in sorption "isotherm" experiments. However, through EXAFS and direct Hg analysis, this research was able to reach into much lower mercury concentrations than previous research seeking mechanistic explanations for the sorption of Hg to DWTRs (Quinones et al., 2016). First, at low mass loading values for mercury, in samples with high organic matter content, Hg-S bonds are distinctly visible in the EXAFS. Meanwhile, there exists no evidence in the XANES of the precipitation of inorganic mercury sulfide, suggesting mercury association with organic thiol groups. Second, given the correlation between organic matter content and mercury sorption capacity, organic matter in DWTRs is likely to play a critical role in the mercury sorption processes. Metal hydroxides from coagulant salts alone will not sufficiently explain the overall Hg immobilization properties that DWTRs exhibit for mercury.

4.5. Fixed bed flow-through column studies.

Fixed-bed flow-through columns were used to comparatively evaluate the dynamic performance of DWTR and apatite as an example specialized substrate (USEPA, 2005). Metal-contaminated water influents contained 3 different metals (Pb, Cd, and Cu), each at a final concentration of 2 mg/L. The Yan's model was used to fit the breakthrough experimental data. The results are presented in **Figures 75 and 76, and Table 15**.

The aqueous solutions of metals used as influents in these experiments had acidic pH values ranging from 5.0 to 5.6 in the presence and absence of DOM, respectively. However, and except for the sand packed columns which had no buffering capacity, the pH of the effluents coming from DTWR of apatite packed columns increased to values ranging from 7 to 8.

First, for influents without DOM, the results (**Figure 75**) show that the 3 evaluated reactive substrates do significantly delay the breakthrough of the tested metals when compared to either the tracer or the blank columns packed with sand only. Overall, the breakthrough delay follows the order ***WY*** > ***apatite*** >***OR*** for the 3 metal cations. However, while the model used fitted quite well the experimental data for Cd and Cu, Pb data were mostly scattered.

Accordingly, except for the sorption of Cd and Cu by DWTR-OR and Cd by DWTR-WY for which adsorption seems to play a significant role in metal immobilization ($R^2 \geq 0.93$), the results suggest the co-occurrence of other metal immobilization mechanisms other than adsorption.

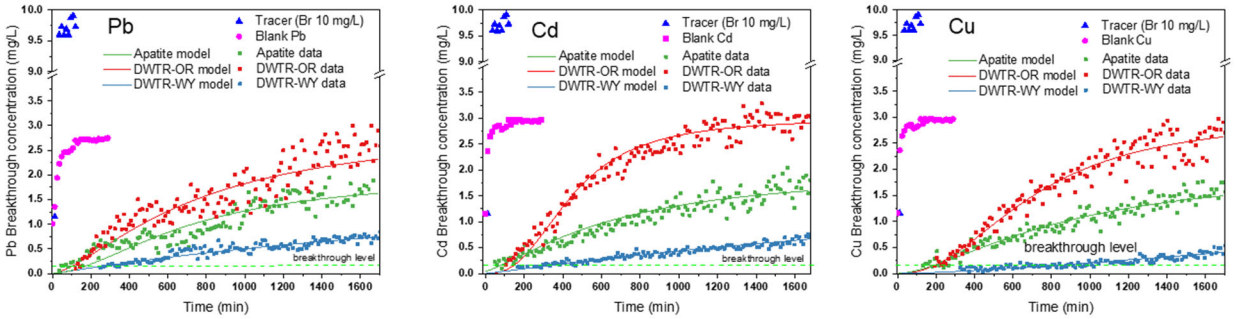


Figure 75. Breakthrough profiles from influents containing Pb, Cd, Cu in columns packed with either a non-reactive (sand referred to as blank) or reactive (i.e., DWTR-OR, DWTR-WY, apatite) substrates, and compared to the breakthrough of bromide used as tracer (blue triangles). Experimental data (points) were fitted by the Yan's adsorption model (lines).

The calculated maximum sorption capacities (Q_0) for the studied metals by each of the three evaluated substrates are presented in **Table 15**. The highest values were obtained with DWTR-WY, followed by DWTR-OR, and then apatite.

Chemically reactive substrates, such as apatite (Knox et al., 2012, 2014), and DWTR (Hovsepyan and Bonzongo, 2009; Quinones and Bonzongo, 2023; Wallace et al., 2023 and 2024), can be used as amendments/caps for metal-contaminated sediments and soils. The trends of the breakthrough curves obtained using such substrates (e.g., **Figure 75**) are likely influenced by a combination of the physicochemical properties of each of the tested substrates and the aqueous chemistry of the tested metal cations.

First, considering metal immobilization through electrostatic forces, *i.e.,* the formation of outer-sphere surface complex, the zeta potential data presented earlier in **Figure 56** indicate that DWTR-OR particles carry a net positive charge in aqueous solutions with pH<7. Since the pH of the influents used in these column studies was 5.6, it is reasonable to assume that metal immobilization through electrostatic forces would be negligible. Moreover, considering the pH of the effluents (pH ~7), which aligns with the isoelectric point charge of DWTR-OR, immobilization by electrostatic forces would be negligible as well. Therefore, a fast breakthrough as observed should be expected, unless other metal immobilization mechanisms were prevalent. Regarding apatite, while changes in its zeta potential were not measured in this study, this substrate has been extensively studied, and data in peer-reviewed literature suggest that the isoelectric point value of apatite tends to vary with changes in the chemical composition of tested waters. This variability arises from the different mechanisms of charge development at the surface of apatite particles (Simukanga and Lombe, 1995). In laboratory-prepared synthetic waters such as those used in this study, the isoelectric point of apatite varied from pH 4 to 6 over time (Somasundaran, 1968). Based on the pH (5.6) of influent used in our column studies, metal immobilization by electrostatic forces should be negligible. When considering the effluent's pH (between 7 and 8), which was up to 2 pH units above the highest value of the aforementioned range of isoelectric point values, it would be reasonable to assume the development of net negatively charged surfaces, and therefore, a potential for retention of metal cations. Therefore, based on electrostatic attraction and metal

immobilization, apatite should perform better than DWTR-OR. Finally, unlike DWTR-OR and apatite, DWTR-WY particles appear to be mostly neutrally charged over a wide range of pH (**Figure 56**), particularly for pH values overlapping with those of the effluent, suggesting that immobilization by electrostatic forces might not be significant, and the observed delay in breakthrough curves is likely related to other specific characteristics of this substrate.

Second, a closer examination of the physicochemical characteristics of DWTR-OR and DWTR-WY reveals their substantial similarity, except for the presence of activated carbon (AC) as an additive in DWTR-WY. This additive impacts the substrates' ability to immobilize metal cations from aqueous solutions. Our sorption studies using Pb, Cu, and Hg, along with the SEM-EDS data collected from the resulting metal-spiked substrates, consistently showed higher sorption by DWTR-WY compared to DWTR-OR. Sorbed metals were primarily associated with C and Al-mineral phases in DWTR-WY, and with C, Fe-mineral phases, and clay in DWTR-OR. Therefore, the distinct separation of the breakthrough curves depicted in **Figure 75** can be attributed to differences in sorption mechanisms involved in the mobilization of metal cations by these two substrates.

Table 15. Dynamic maximum sorption capacities (Q_0) derived from the Yan's model for Apatite, DWTR-OR, and DWTR-WY used as sorbents for Pb, Cd, and Cu.

Sorbents	**Lead (Pb)**		**Cadmium (Cd)**		**Copper (Cu)**	
	Q_0 (mg/kg)	*R^2*	*Q_0 (mg/kg)*	*R^2*	*Q_0 (mg/kg)*	*R^2*
Apatite	181.9	0.87	168.7	0.85	217.1	0.89
DWTR-**OR**	202.8	0.86	180.8	**0.93**	246.4	**0.95**
DWTR-**WY**	699.2	0.85	788.1	**0.94**	1076	0.84

When influents containing dissolved organic matter (DOM) were pumped through the columns, the results were counterintuitive: DOM addition resulted in retardation instead of a speeding up of metal breakthroughs (**Figure 76**). The Yan model was employed, yet the poor fit of the experimental data suggested that adsorption was not the dominant immobilization mechanism in the presence of DOM. Indeed, DOM comprises a complex array of chemical components that are intertwined with numerous environmental processes. This includes carboxyl-rich alicyclic molecules, heteropolysaccharides, aromatic compounds, and materials derived from linear terpenoids (Lam et al., 2007). Consequently, DOM frequently impacts metal speciation, alters the surface charge of particles, sorbs to mineral surfaces, interferes with mineral dissolution/precipitation reactions, and drives redox reactions (Aiken et al., 2011).

For the influents utilized in this study (pH 5.6), the tested metals would primarily exist as hydrated divalent cations ($e.g., Me(H_2O)_n^{2+}$, where ***Me*** represents the metal and ***n*** denotes the coordination number) (Sheha, 2012; Oyatade et al., 2018; Niu et al., 2019). Consequently, these metals would interact with the negatively charged functional groups of the DOM, behaving as ligands and thus controlling the fate of these metals. Upon entering the column and coming into contact with solid substrates, the aforementioned impacts of DOM on the surface charge of particles, their sorption onto mineral surfaces, and their interferences with reactions involving mineral dissolution and precipitation would influence the transport of metals through the column,

and in this case, resulting in significant breakthrough delays. For example, the breakthrough of Pb is substantially delayed in a column packed with apatite, suggesting that DOM enhances the release of phosphate from the apatite and consequently leading to precipitation of Pb as hydroxyl-pyromorphite – $Pb_5(PO_4)_3OH_{(s)}$ - or chloropyropmorphite – $Pb_5(PO_4)_3Cl_{(s)}$ - (**Figure 76**). In contrast, Cu, for instance, elutes much more rapidly as the solubility of a copper phosphate phase is larger in contrast to Pb. Upon examining DWTR-OR and DWTR-WY, the retention behavior differs significantly, with the separation being more pronounced for Cd and Cu, and DWTR-WY outperforming DWTR-OR. As discussed earlier, we believe this difference is attributed to the presence of activated carbon, which would exhibit a strong sorption for DOM and DOM-bound metals in DWTR-WY packed columns.

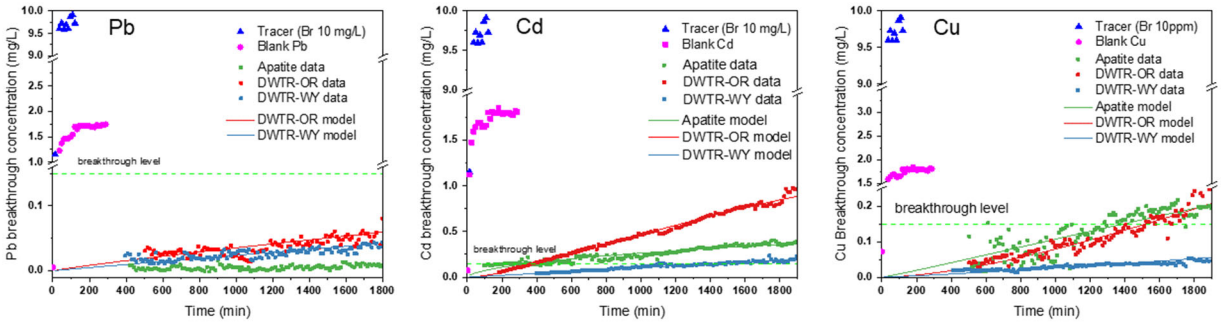


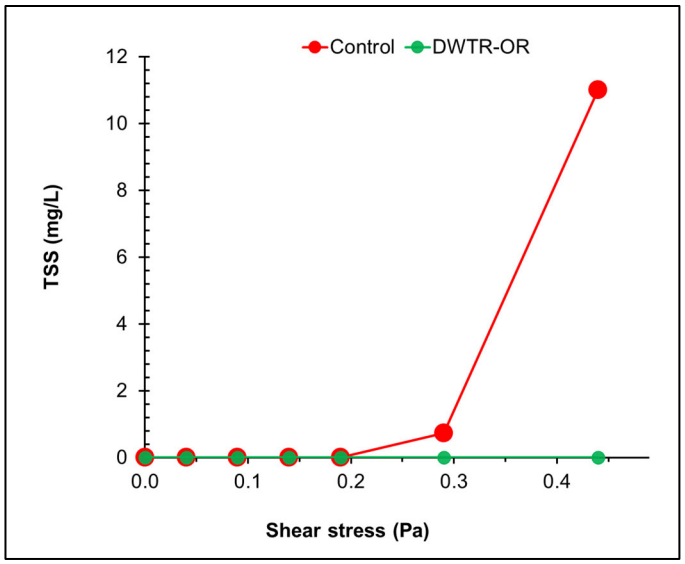
Figure 76. Breakthrough profiles from influents containing Pb, Cd, Cu in columns packed with either a non-reactive (sand referred to as blank) or reactive (i.e., DWTR-OR, DWTR-WY, apatite) substrates, and compared to the breakthrough of bromide used as tracer (blue triangles). Experimental data (points) were fitted by the Yan's model (lines).

The overall efflux of dissolved metals at sediment-water interfaces depends on various parameters, including metal concentrations in sediments and pore waters, sediment porosity, the physicochemical composition of the sediments, and relevant pore water chemistry parameters. However, the chemical speciation of metals present in the treated aquatic system is particularly crucial, as only the fraction of metals available for biological uptake has the potential to cause toxicity (Knox et al., 2014). A closer look at the results presented in Figure 76 show that DWTR-WY does either slightly better (e.g., Pb) or simply better (e.g., Cd and Cu) than DWTR-OR. These overall trends are similar to those observed in the absence of DOM. Based on the physicochemical characteristics of these two substrates, it seems like activated carbon present in DWTR-WY is responsible for most of the observed differences. Activated carbon has a high affinity for dissolved organic compounds (Schriber et al., 2005), which in turn behave as complexing ligands for metals. Accordingly, the retention of metals by DWTR-WY particles could be from the sorption of previously formed metal-DOM complexes in the influent, rather than a direct AC–metal interactions.

In aquatic systems, reactive materials used in active caps are also able to immobilize contaminants in sediments beneath that layer in addition to preventing contaminant migration into the water column (Knox et al., 2012). The flow rate of 0.5 mL/min used in our column studies is relatively high and would be relevant for sediment sites affected by groundwater and/or hyporheic flow. However, under conditions where metals released to pore waters by contaminated sediments simply diffuse towards the overlying water, this tested flow rate would be several orders of magnitude higher. As a result, breakthroughs under such conditions would take much longer.

4.6. Using DWTR as cap layer at the interface of metal-contaminated sediments and overlying water: Effects on metal fluxes and vertical concentration profiles in pore waters.

4.6.1. DWTR cap and particles resuspension from sediment as a function of increasing hydrodynamic shear stress. For the determination of the increasing hydrodynamic shear stress (τ) on the resuspension of sediment particles, a quasi-uniform shear stress was applied at the water-sediment interface using forces generated by a spinning disk and central suction of the erosion head of the Gust Chamber (Green Eyes, 2015; Xie et al., 2015). After ~20 minutes, an equilibrium was achieved based on turbidity readings, that is, the observed turbidity became constant at the applied shear stress.



Sediment characteristics

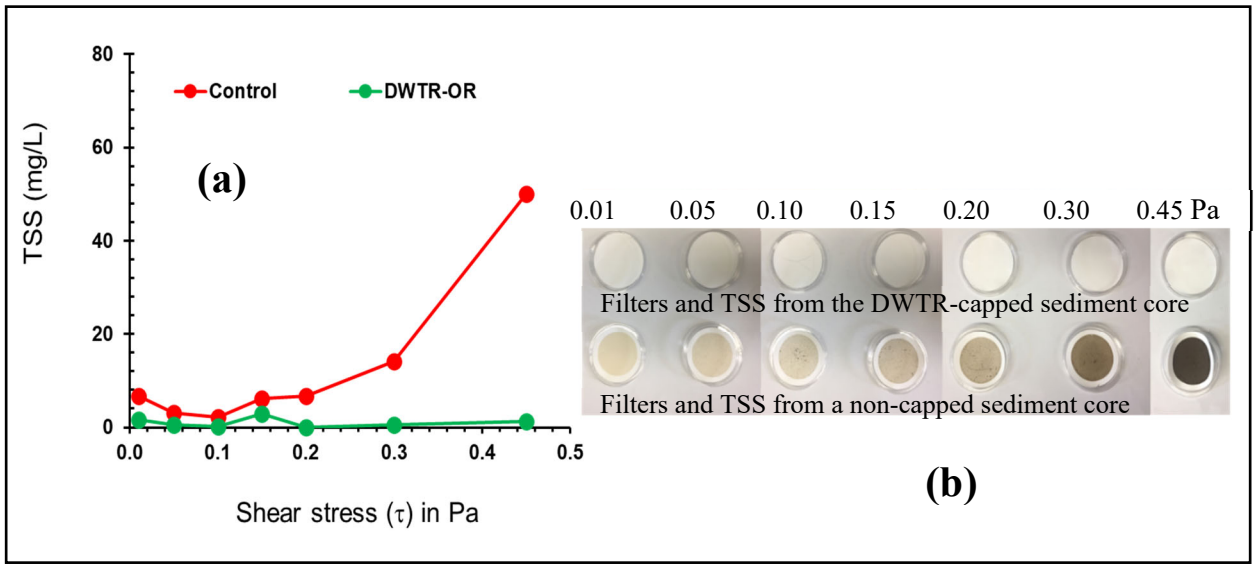
pH	5.6
% Organic matter (LOI)	0.8
% Sand (2 to 0.05 mm)	95
% Silt (0.05 to 0.002 mm)	4.0
% Clay (<0.002 mm)	1.0

Figure 77. Resuspension of particles to the overlying waters from sandy metal-contaminated sediments as a function of increasing hydrodynamic shear stress (τ) for sediment cores without (red) and with (green) a DWTR cap layer. The major characteristics of this sediment show the prevalence of sand particles which require very strong disturbance to be suspended in the overlying water. The presence of the cap layer stops the resuspension of sediment particles even at a shear stress of 0.45 Pa. *TSS*: Total suspended solids.

In this study, the emphasis was on the actual measurement of total suspended solids (TSS) as the use of readings from the turbidity meter is not advised as reliable parameter by the

manufacturer. Water samples (500 mL) for TSS measurements were collected once the plateau in turbidity was reached. Tested τ values ranged from 0, 0.05, 0.10, 0.15, 0.20, 0.30, and 0.45 Pa, each applied for at least 20 minutes. In this process of investigating the effect of increasing hydrodynamic shear stress in the gust chambers on sediment resuspension, a critical shear stress value, defined as the lowest value that causes measurable sediment erosion (Xie et al., 2015; Work and Schoellhamer, 2018) was determined.

Using data obtained with DWTR-OR as example for illustration (similar trends were obtained with DWTR-WY), the determined TSS concentrations are plotted as a function of increasing power of water disturbance over the 2 types of metal-contaminated sediments used (**Figures 77 and 78**).



Sediment characteristics

pH	5.7
% Organic matter (LOI)	8.6
% Sand (2 to 0.05 mm)	15
% Silt (0.05 to 0.002 mm)	79
% Clay (<0.002 mm)	3.0

Figure 78. **(a)** - Resuspension of particles to the overlying waters from metal-contaminated sediments collected from NAS near Pensacola Florida, plotted as a function of increasing hydrodynamic shear stress (τ) for sediment cores without (control) and with (treatment) a DWTR cap layer. TSS: Total suspended solids. **(b)** – Pictures of filters resulting from the filtration of water samples collected as a function of increasing τ values ranging from 0.01 to 0.45 Pa. This sediment is dominated by fine particles and well resuspended with increasing hydrologic shear stress (red line). However, capping with DWTR reduced the resuspension of metal-contaminated particles across the full range of applied shear stress (green line).

For metal-contaminated sediment containing 95% of sand, the coarse characteristics of the particles resulted in nearly no resuspension, except when the disturbance was very high (τ>0.2 Pa), and only for non-capped sediment (**Figure 77**).

For sediment dominated by finer particles (79% silt and 3% clay), the results (**Figure 78a**) show that a DWTR cap layer at the water-sediment interface reduces the resuspension of sediment particles and the difference in measured TSS concentrations between non-capped and DWTR-capped sediments increases with increasing τ values. This can also be seen visually (**Figure 78b**) as the mass of TSS retained on filters (0.45μm) increases with increasing τ.

Overall, when dewatered and used not as a slurry but solid particles (2mm), DWTR could reduce the resuspension of metal-contaminated sediment particles, acting as a protective layer for the water column.

4.6.2. Gust chamber studies of metals release from non-capped and capped sediment as a function of changing hydrodynamic shear stress (τ). Two types of experiments were conducted to investigate the ability of DWTR to control the upward flux of metals from sediments to the overlying water. In the first set of experiments, the impact of hydrologic disturbances on metal concentrations in the overlying waters was assessed by testing different τ values (0.05, 0.10, 0.15, 0.20, 0.30, and 0.45 Pa), each applied for a period of 12 hours on uncapped or capped sediment cores. Unlike the TSS study, in the experiments on metal release, water samples (5 mL) were collected at pre-defined times for the determination of total metal concentrations as described earlier. The second set of experiments looked at the kinetics of metal release to the overlying waters as a function of time and at a fixed shear stress value of 0.05 Pa.

a. Effect of increasing hydrologic shear stress (τ) on metal release by uncapped and capped metal contaminated sediments. For metal-contaminated sediments collected from NAS near Pensacola Florida, with high concentrations of Cu, Cd, Cr, Pb and Zn, **Figure 79** shows the results obtained using DWTR-OR as capping substrate in comparison to uncapped sediments. The results show that the presence of DWTR as capping agent reduces the release of tested metals to the overlying water with metal concentrations in the aqueous phase ranging 0.3 to 37.9 μg/L (ppb). In the absence of DWTR, metal concentrations increased with increasing τ, reaching values in hundreds of ppb for Cu, Cr, Pb, and Zn. The rather low levels of metals transferred to the aqueous phase (ppb range) in the absence of a DWTR cap is explained by the small percentage of water extractable and exchangeable metal fractions in the intertidal sediment.

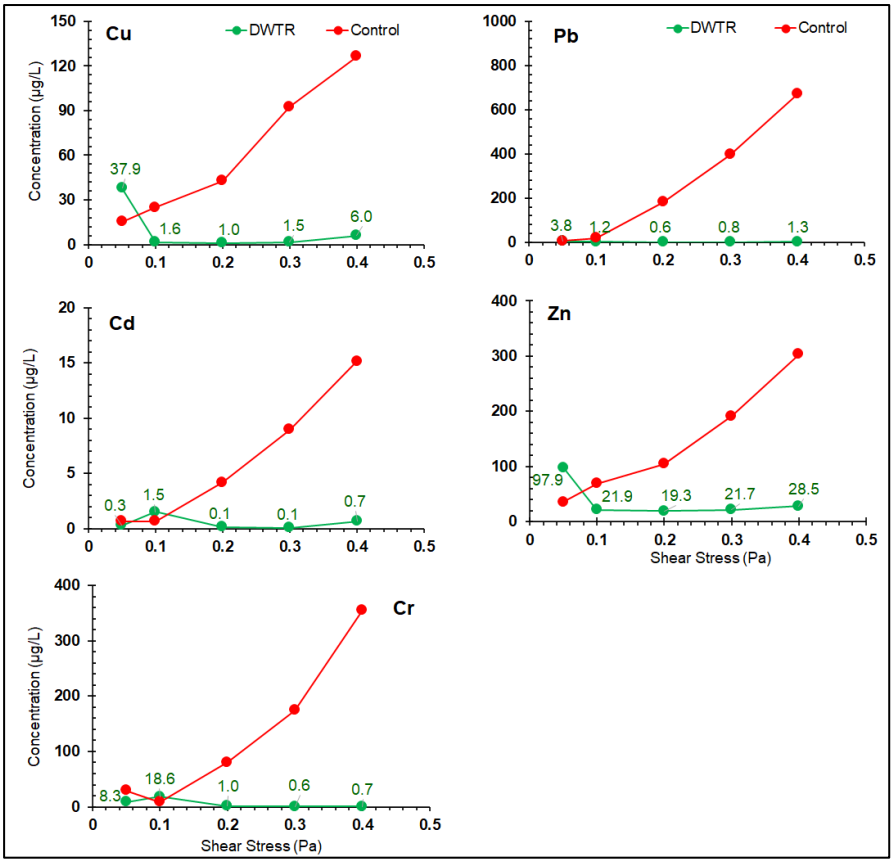


Figure 79. Concentrations of metals (Cu, Cd, Cr, Pb, and Zn) in the aqueous phase of the gust chambers containing site-sediments without (control) or with a DWTR cap layer and as a function of increasing hydrologic shear stress. In contrast to the metal-spiked sediments, all measured total metal concentrations in water in contact with site-sediments were in the ppb range and the actual values shown on the graph. Note the differences in the range of Y-axis values.

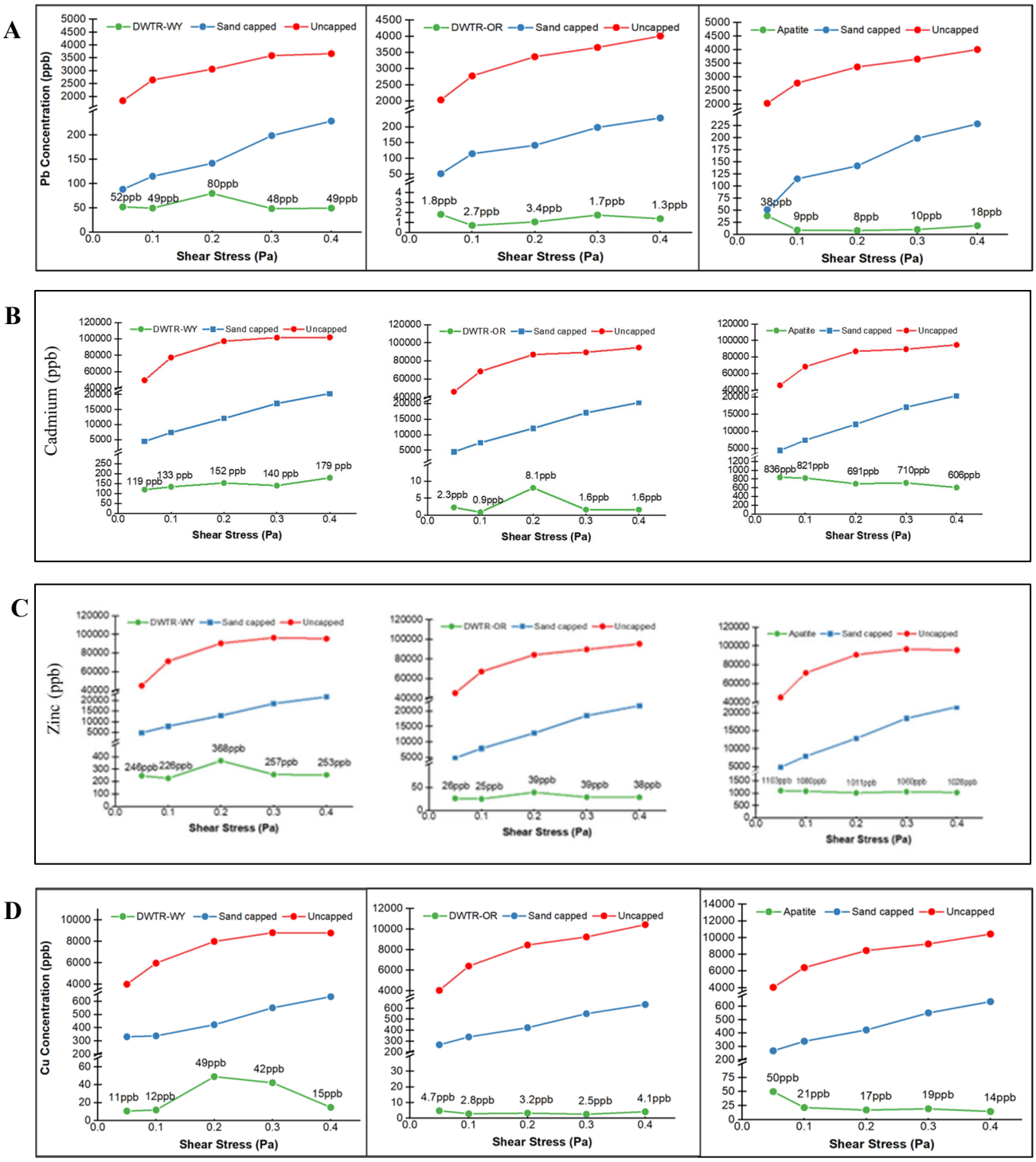


Figure 80. Trends of total lead (A), cadmium (B), zinc (Zn), and copper (Cu) concentrations in sediment cores overlying waters as a function of increasing hydrologic shear stress (τ). Red lines represent metal concentrations in water overlying non-capped sediments. The blue lines correspond to metal concentrations in waters overlying sediment cores capped with sand, and the green lines are for metal concentrations in waters overlying sediments capped with an active substrate, either DWTR (WY or OR) or apatite.

For the sandy sediment with much higher percentage of water soluble and exchangeable metal fractions (**Table 4**) and higher porosity, the expected high release of metals was observed in the absence of capping substrates, with metal aqueous concentrations in ppm range (from 2 to ~11 ppm) as shown for each of the metals in Figure 79. In addition to the uncapped sediments, 4 different substrates were used as capping agent. First, clean sand was used as inert capping substrate to help differentiate between a simple physical barrier effect and metal immobilization through specific mechanisms such as sorption. Apatite was also used, but as one of reactive sorbents proposed by the USEPA for capping of metal-contaminated sediments (USEPA, 2005). Finally, we tested two of the DWTR retained from the screening method developed earlier (WY and OR). The results are shown in Figure 79. Overall, the total metal concentrations measured in waters overlying the uncapped sediments increased with increasing $\boldsymbol{\tau}$ (red lines). The use of sand as capping substrate did reduce the transfer of metals from contaminated sediments to the overlying water (blue lines). For instance, the total concentrations of Pb and Cu increased with increasing $\boldsymbol{\tau}$ from 0.05 to ~0.2 ppm and 0.2 to ~0.6 ppm, respectively. These values are at least one order of magnitude lower than those measured in the absence of a capping substrate (e.g., the total concentrations of Pb and Cu increased with increasing $\boldsymbol{\tau}$ from 1 to 4 ppm and 2 to 11ppm, respectively). Based on the non-reactive character of sand, the observed reduction is attributed to a simple physical barrier effect. When the hydrologic shear stress was increased incrementally from 0.05 to 0.4 Pa, the sand cap became less and less efficient, resulting in a near linear response.

Regarding the 3 reactive capping substrates (DWTR-OR, DWTR-WY, and apatite), the total concentrations of all metals in the aqueous phase were the lowest (**Figure 80**, green bottom lines). It is apparent that in addition to behaving as physical barriers, these substrates do retain metals through a combination of mechanisms that could include sorption as well as precipitation. For example, Pb could be removed through a combination of binding and precipitation mechanisms, and the latter would be due to the presence of anionic ligands such as carbonates in DWTRs (Eq. 14 and 15), and phosphates (Eq.16) in apatite ($Ca_5(PO_4)_3OH$).

$$3Pb^{2+}_{(aq)} + 2HCO^{-}_{3(aq)} + 2H_2O_{(l)} = \boldsymbol{Pb_3(OH)_2(CO_3)_{2(s)}} + 4H^{+}_{(aq)} \qquad Eq.14.$$

$$Pb^{2+}_{(aq)} + CO^{2-}_{3(aq)} = \boldsymbol{PbCO_{3(s)}} \qquad Eq.15.$$

$$5Pb^{2+}_{(aq)} + 3PO^{2-}_{4(aq)} + Cl^{-}_{(aq)} = \boldsymbol{Pb_5(PO_4)_3Cl_{(s)}} \qquad Eq.16.$$

The complex chemical composition of DWTRs does likely favor the immobilization of metals through sorption mechanisms (e.g., chemisorption through binding to electron donor atoms and electrostatic attraction depending on the net charge at the surface of the particles), and precipitation favored by the presence anionic ligands (carbonates and phosphates).

b. Kinetics of metal release to the overlying water by uncapped and capped metal-contaminated sediments using DWTR-OR as case study. The results of the kinetics of metal release at a fixed hydrologic shear stress (τ=0.05 Pa) show that for the intertidal sediments characterized by very low fractions of water soluble and exchangeable metals, the impact of the presence of a DWTR cap varies from non-existent to negligible as total metal concentrations in the aqueous phase of the gust chambers with (capped sediments) or without (uncapped sediments) DWTR were similar and in low ppb range (**Figure 81**).

In contrast, for the sandy sediments with much higher fractions of water-soluble and exchangeable metals, the presence of a DWTR cap at the water-sediment interface maintained the concentrations of metals in the aqueous phase in low ppb (µg/L) range, while control samples exhibited total metal concentrations in ppm (**Figure 82**).

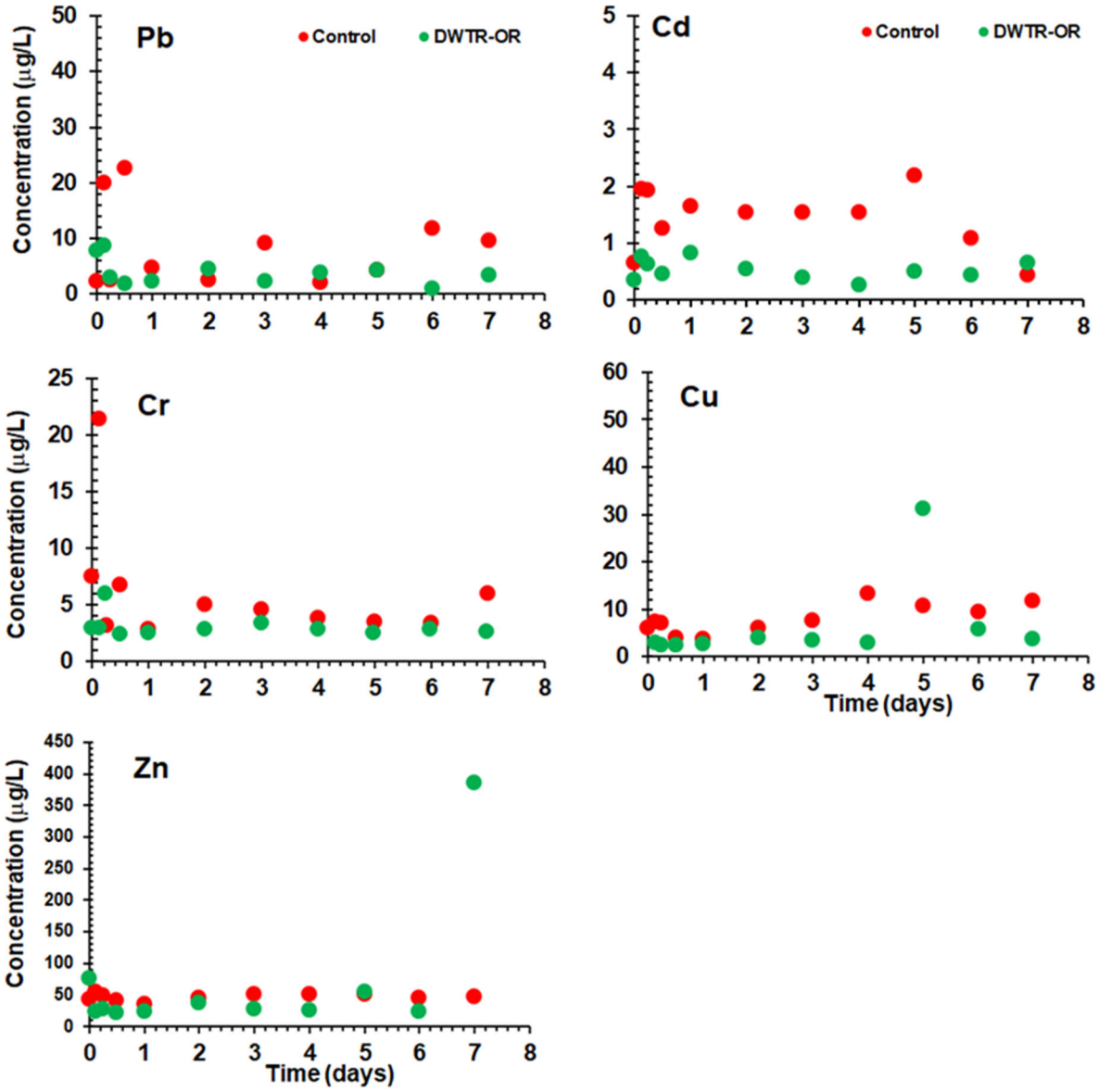


Figure 81. Kinetics of metal release from intertidal sediments as a function time at a fixed shear stress of 0.05 Pa over 7 days. Sediments capped with DWTR are represented by green circles (treatment), and the non-capped sediments by red circles.

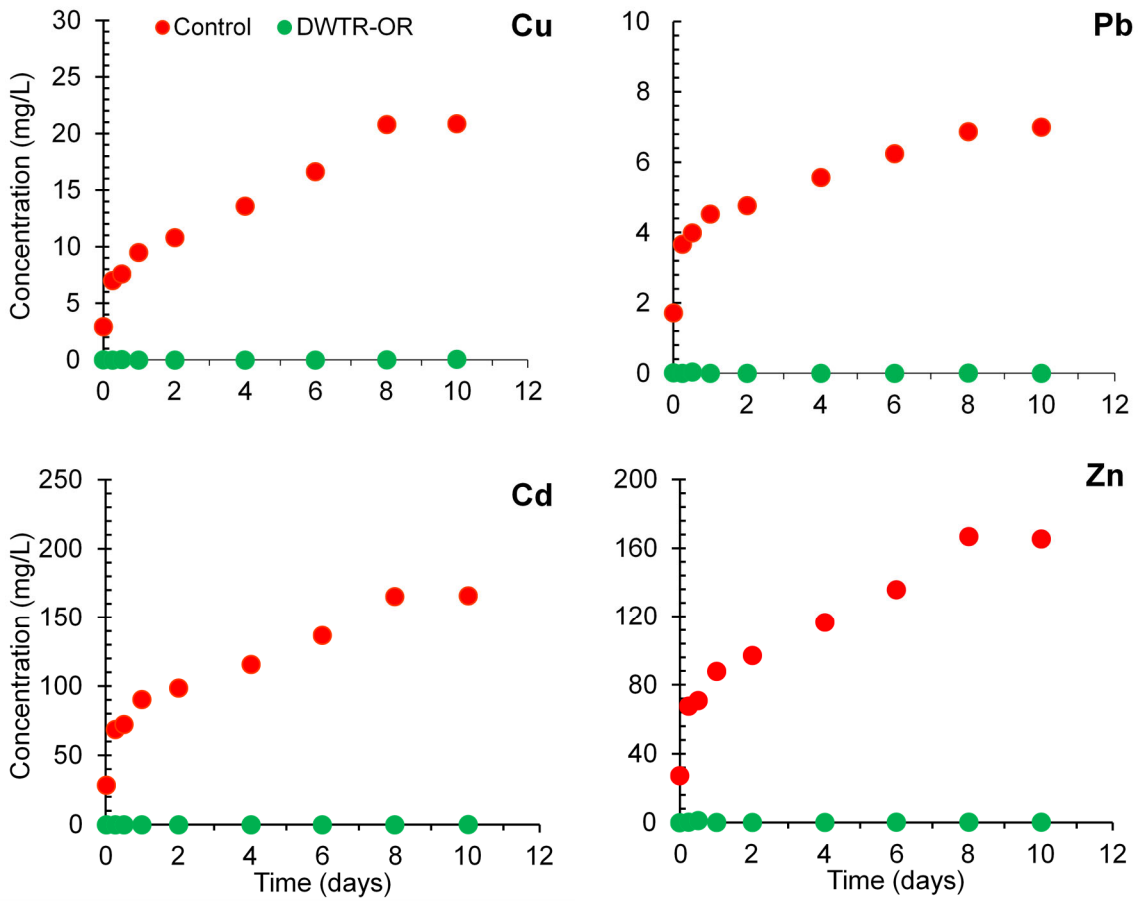


Figure 82. Kinetics of metal release from the freshwater sandy sediments as a function time at a fixed shear stress of 0.05 Pa over 10 days. Sediments capped with DWTR are represented by green circles (treatment), and the non-capped sediments by red circles. Metal concentrations measured in the aqueous phase of the DWTR-capped sediment core (green circles) ranged from 2.3 to 59 ppb for Cu and Cd, and from 2.1 to 59 ppb and 51 to 1,1196 ppb for Pb and Zn, respectively.

4.6.3. Effect of capping with DWTR on vertical profiles of dissolved metals in sediment pore and overlying waters using DGT samplers. The technique of DGT (diffusive gradients in thin films) was used here to obtain vertical profiles of trace metals in metal-contaminated sediments, capped or uncapped, to gain insights in the mobility of sediment bound metals when capped by different types of substrates. Although a good number of papers have been published in peer reviewed literature on vertical profiles of trace metals in sediment pore waters using DGT (e.g., Wu et al., 2015, Xu et al., 2017, Zhou et al., 2020, Valero et al., 2020, and Liu et al., 2022), we couldn't find published studies on the combined use of gust chambers and DGT samplers. Briefly, the results presented here were obtained from sediment cores, after equilibration of water and sediment in a gust chamber for 7 days at the pre-determined critical shear stress value of 0.05 Pa. Tested sediment cores were either capped (sand, apatite, DWTR-WY, DWTR-OR) or uncapped (control). At the end of the 7 days, the DGT samplers were gently inserted into the sediments and retrieved after a contact period of 24 hours. Because of the high water extractable and

exchangeable metal fractions in the metal-contaminated sandy sediment, the sorbent gel was sliced every 0.3 cm to obtain a high-resolution vertical profiles of targeted trace metals

For the non-capped sediments, the concentrations of each of the 4 metals analyzed were in ppm range, and in general, with an increasing trend from top to bottom. Of interest are the concentrations of metals in the overlying water, which ranged from a low of ~1.3 mg/L for lead to >10 mg/L for zinc (**Figure 83**). This was expected given the high concentrations of the mobile metal fractions in these sediments, and the dissolution of metals would be limited only when saturation levels are reached. The concentrations of iron and manganese, two indicators of redox changes, were very low and in ppb range. Iron concentrations started to pick up around a depth of 5 cm from values <0.1 mg/L to 0.3 mg/L. Manganese appeared to be in equilibrium between pore and overlying waters.

For sediments capped with sand (**Figure 84**), which is assumed to behave as an inert substrate with regard to the active sorption of metals, vertical profiles of dissolved metals similar to those observed in the absence of a cap would be expected, but with much lower concentrations in the overlying water as the sand cap would still act as a physical barrier. However, the observed trends were quite different, mostly for lead and copper as they exhibited very low concentrations (<1ppm) along the entire depth profiles. In contrast, cadmium and zinc showed vertical profiles that were quite similar to those obtained in the absence of a cap, but with much lower concentrations in the pore water. As an inert physical barrier, sand would restrict not only the flux of metals, but also the diffusion of oxygen. This would then result in the development of a reducing environment. Unfortunately, and except for the non-capped and DWTR-WY capped sediments, Fe and Mn were not analyzed. However, it can be said that the low levels of Pb and Cu in both pore and overlying waters are due mostly to precipitation reactions.

The use of apatite as capping substrate gave low concentration profiles for Pb and Cu, but the concentrations of Cd and Zn were highly variable with very high values (**Figure 85**). Since Pb forms insoluble species with phophaste under appropriate conditions, it is logical to see low dissolved Pb concentrations and it is possible that the Pb concentrations peaks (up to ~2.8 mg/L) within the apatite layer could be due to analytical error (e.g., contamination), since Pb concentrations did not exceed 3 mg/L in waters from non-capped sediments.

Finally, the use of DWTR (OR and WY) as capping substrates resulted in dissolved metal vertical profiles which are typical for most aquatic sediments, and attributable primarily to redox gradients (**Figures 86 and 87**). The trends of Fe and Mn obtained from sediments capped with DWTR-WY seem to confirm the above observations. Although the particle size of all used capping substrates were < 2mm, the porosity of the layers were different as both the sand and apatite were granular and the DWTR samples more powdery. The vertical profiles of the concentrations of the analyzed metals in the presence of apatite-cap were clearly different from those obtained when the DWTR were used as capping substrates. From the column studies we know that sorption is not the only metal immobilization mechanism with these substrates, and that metal precipitation is likely a significant process for metals such as Pb and Cu. One can conclude that the very low concentrations of metals in waters overlying the DWTR layers are due to the sorption capacity of these substrates while within the actual DWTR layers, both sorption and precipitation do occur. The lower porosity of DWTR as compared to the granular apartite and sand did drove the development of a redox gradient, which explains the higher concentrations of dissolved metals observed in the bottom layers of the sediment cores.

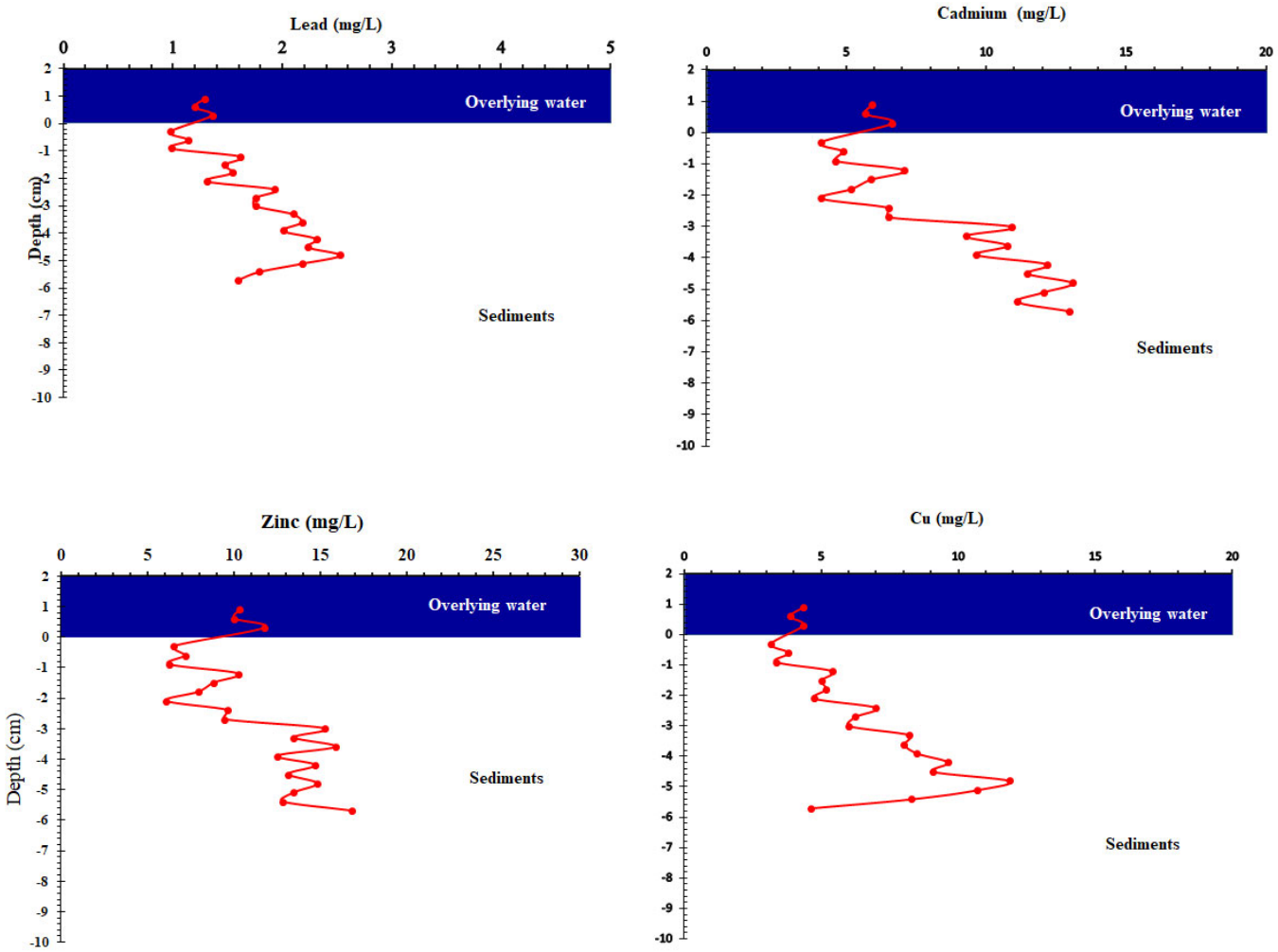


Figure 83. DGT depth profiles of lead (Pb), cadmium (Cd), Zinc (Zn), copper (Cu), iron (Fe), and manganese (Mn) in a **non-capped sediment core** after an initial equilibration in a gust chamber for 7 days. After seven days, the DGT sampler was inserted into the sediments and left in place for 24 hours. The determined total dissolved metal concentrations (X-axis) are plotted as a function of depth (Y-axis), including values from the overlying water.

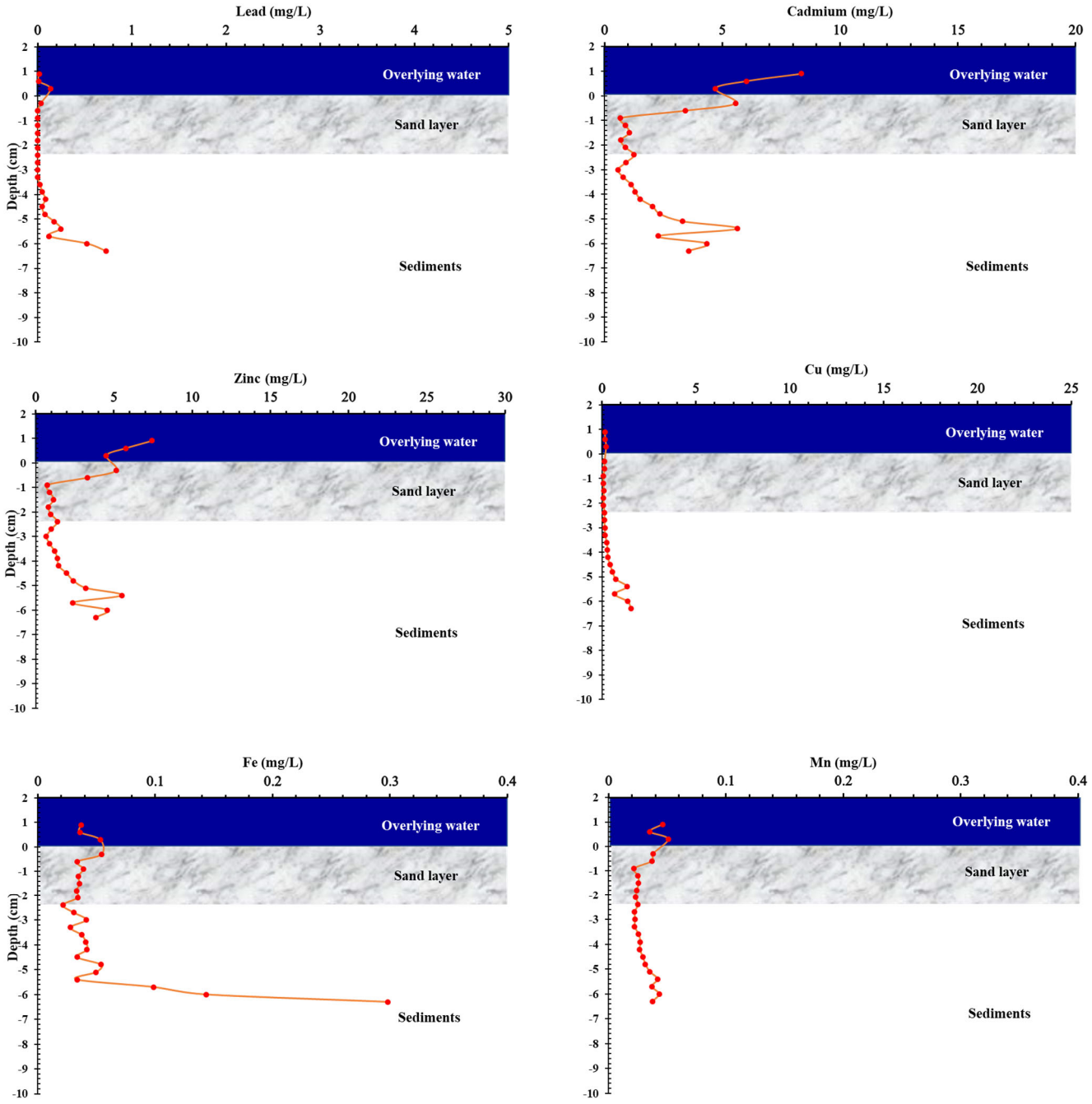


Figure 84. DGT depth profiles of lead (Pb), cadmium (Cd), Zinc (Zn), and copper (Cu) in **sand** capped sediment core after an initial equilibration in a gust chamber for 7 days. After seven days, the DGT sampler was inserted into the sediments and left in place for 24 hours. The determined total dissolved metal concentrations (X-axis) are plotted as a function of depth (Y-axis), including values from the overlying water.

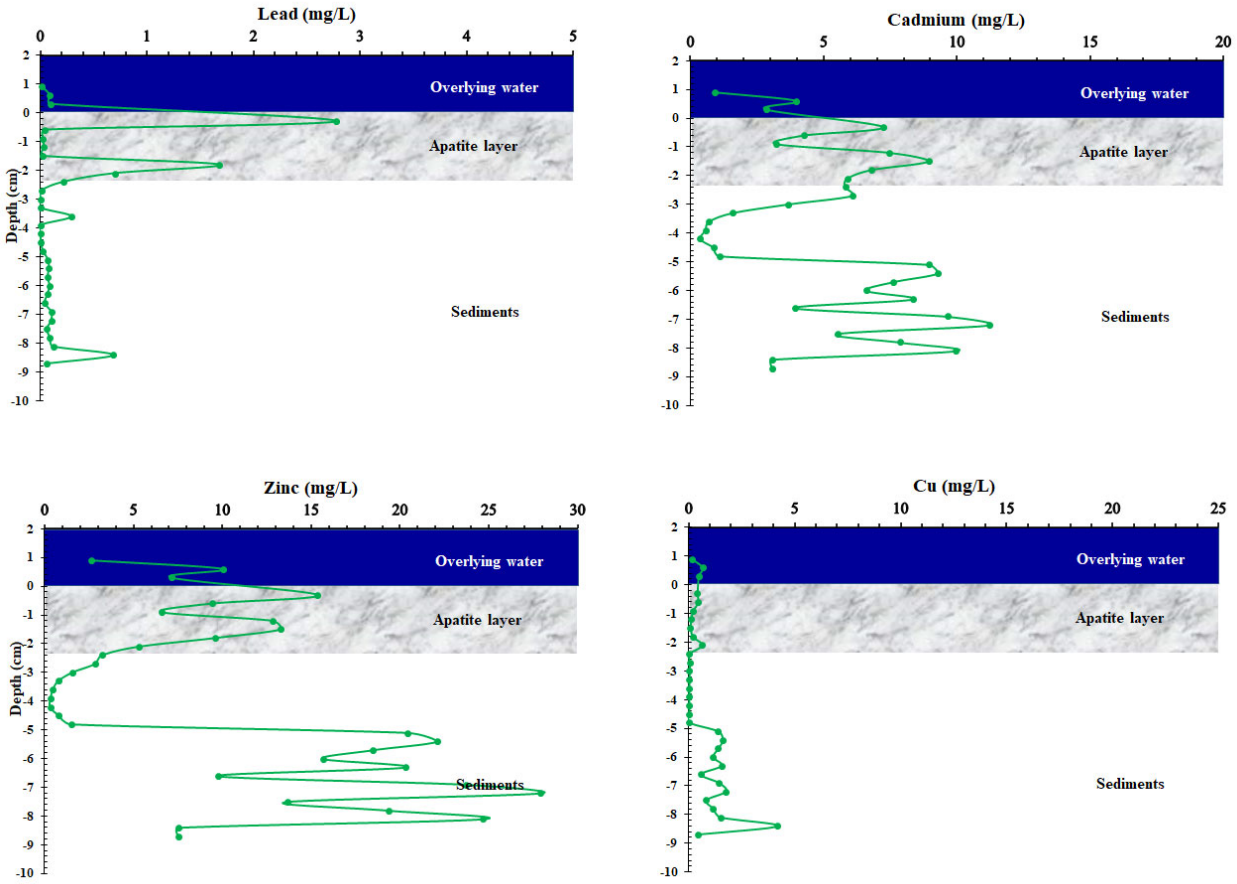


Figure 85. DGT depth profiles of lead (Pb), cadmium (Cd), Zinc (Zn), and copper (Cu) in **apatite** capped sediment core after an initial equilibration in a gust chamber for 7 days. After seven days, the DGT sampler was inserted into the sediments and left in place for 24 hours. The determined total dissolved metal concentrations (X-axis) are plotted as a function of depth (Y-axis), including values from the overlying water.

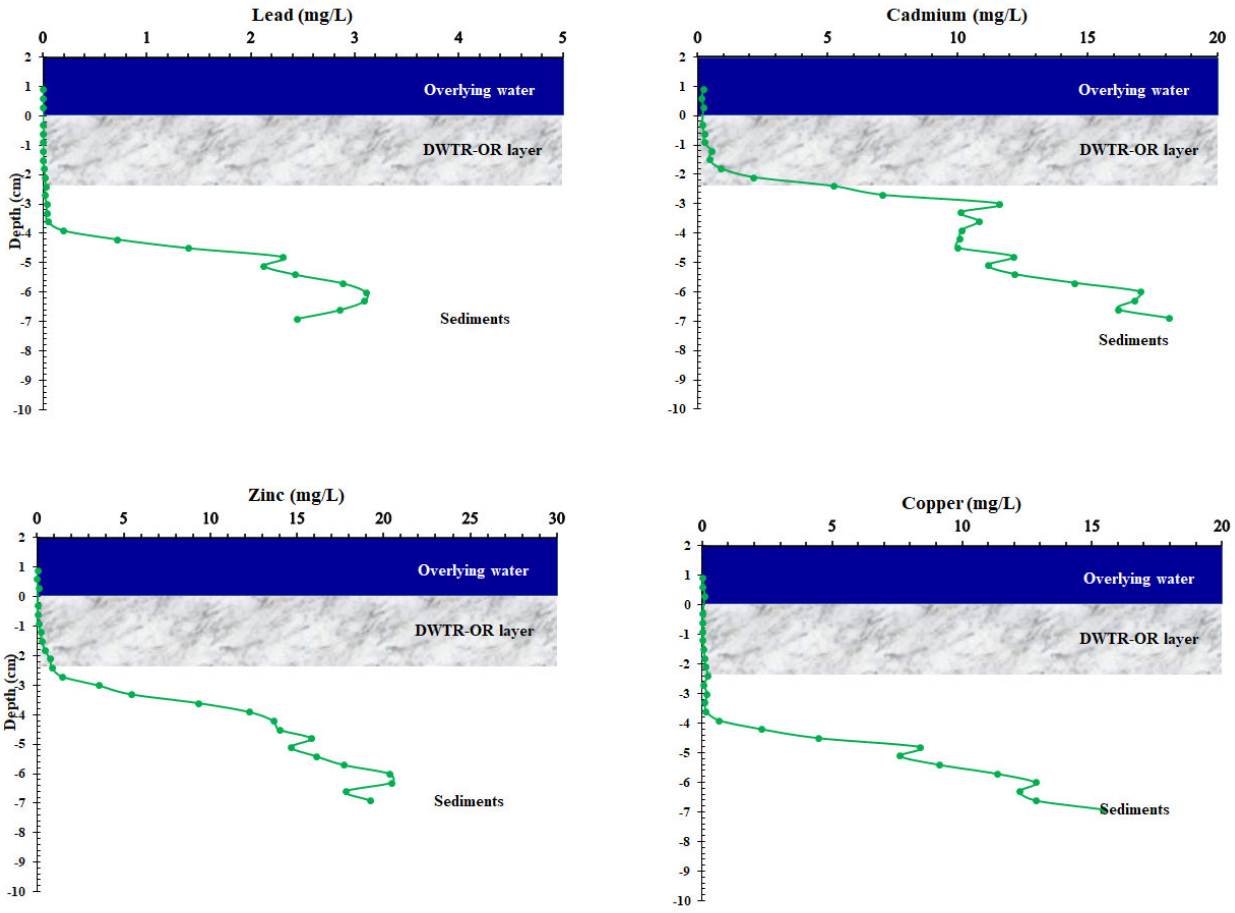


Figure 86. DGT depth profiles of lead (Pb), cadmium (Cd), Zinc (Zn), and copper (Cu) in **DWTR-OR** capped sediment core after an initial equilibration in a gust chamber for 7 days. After seven days, the DGT sampler was inserted into the sediments and left in place for 24 hours. The determined total dissolved metal concentrations (X-axis) are plotted as a function of depth (Y-axis), including values from the overlying water.

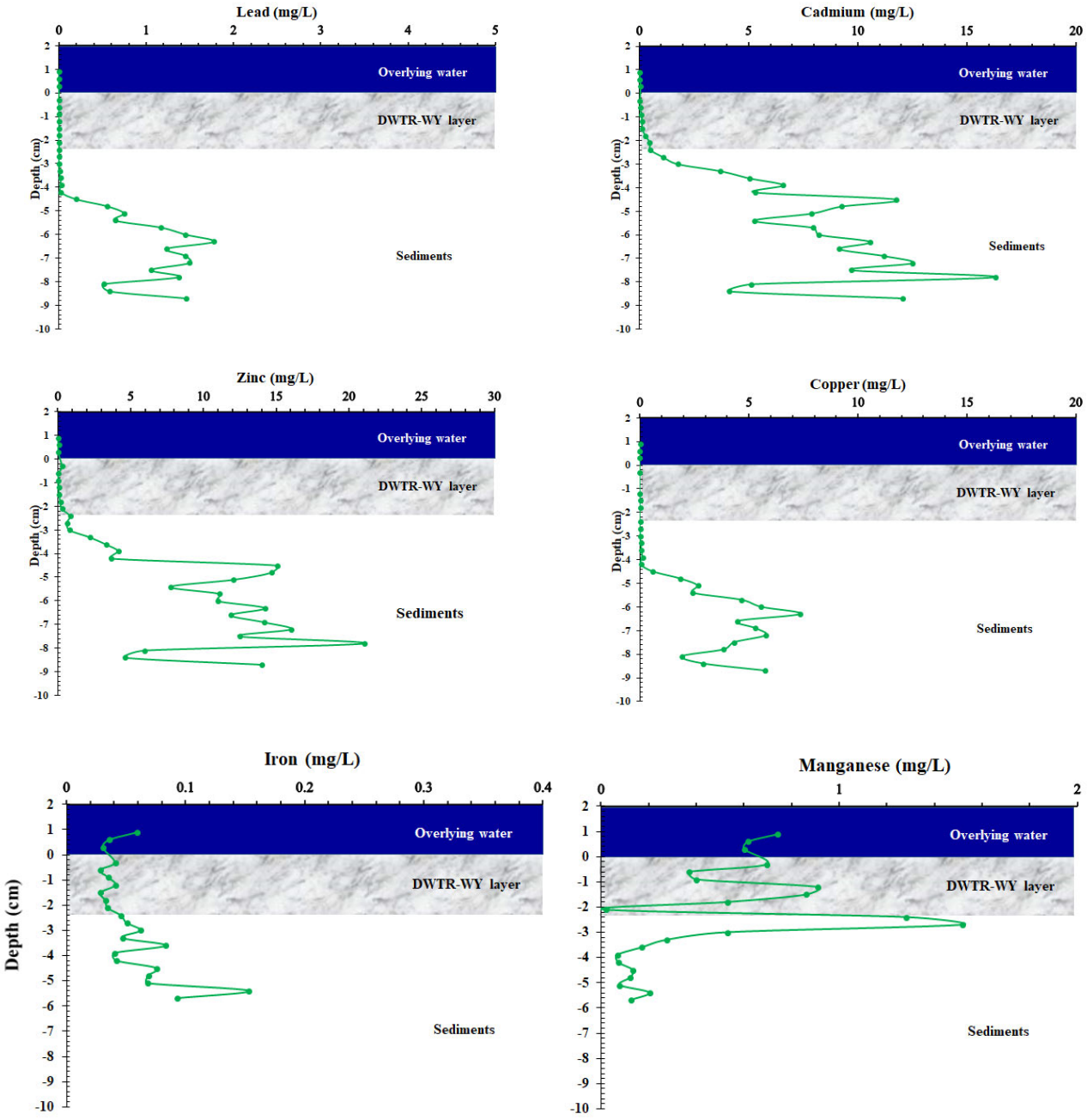


Figure 87. DGT depth profiles of lead (Pb), cadmium (Cd), Zinc (Zn), copper (Cu), iron (Fe), and manganese (Mn) in **DWTR-WY-capped** sediment core after an initial equilibration in a gust chamber for 7 days. After seven days, the DGT sampler was inserted into the sediments and left in place for 24 hours. The determined total dissolved metal concentrations (X-axis) are plotted as a function of depth (Y-axis), including values from the overlying water

.

Unlike the metal-contaminated sandy sediments characterized by a large mobile metal fraction, the intertidal sediment had a very small easily leachable metal fraction. Accordingly, the retrieved DGT gel was sliced into much larger sections (0.5 cm) to have metal (Cd, Cu, Cr, Pb, and Zn) concentrations above the detection limits of used analytical equipment. Using DWTR-OR for illustration (**Figure 88**), all measured metal concentrations were in low ppb range and none did exceed 30 ppb. Similar trends were obtained when DWTR-WY was used, and in this case, **Figure A2** in the appendix section shows an illustration of metal fluxes at the water-solid interface, and how capping sediments with DWTRs-WY affected such metal fluxes (**Figure A3**). Overall, the presented vertical profiles of metal concentrations suggested the following:

- Depth profiles of Cd and Zn exhibit the highest concentrations in the overlying water, suggesting a downward flux for these metals. Therefore, in both the control and DWTR-treated systems, Cd and Zn could be moving downward.
- Depth profiles of Cu show a near-equilibrium between sediments and overlying waters in both control and DWTR-capped sediments.
- Trends of Cr and Pb near the sediment-water interface appear to be in favor of downward fluxes for cores with DWTR-capped sediments, and upward fluxes for control sediments.
- Overall, the results showed that in metal-contaminated sediments with very low levels of water-soluble and easily-exchangeable metal fractions, the use of a DWTR cap may not be necessary based on these short-term experiments.

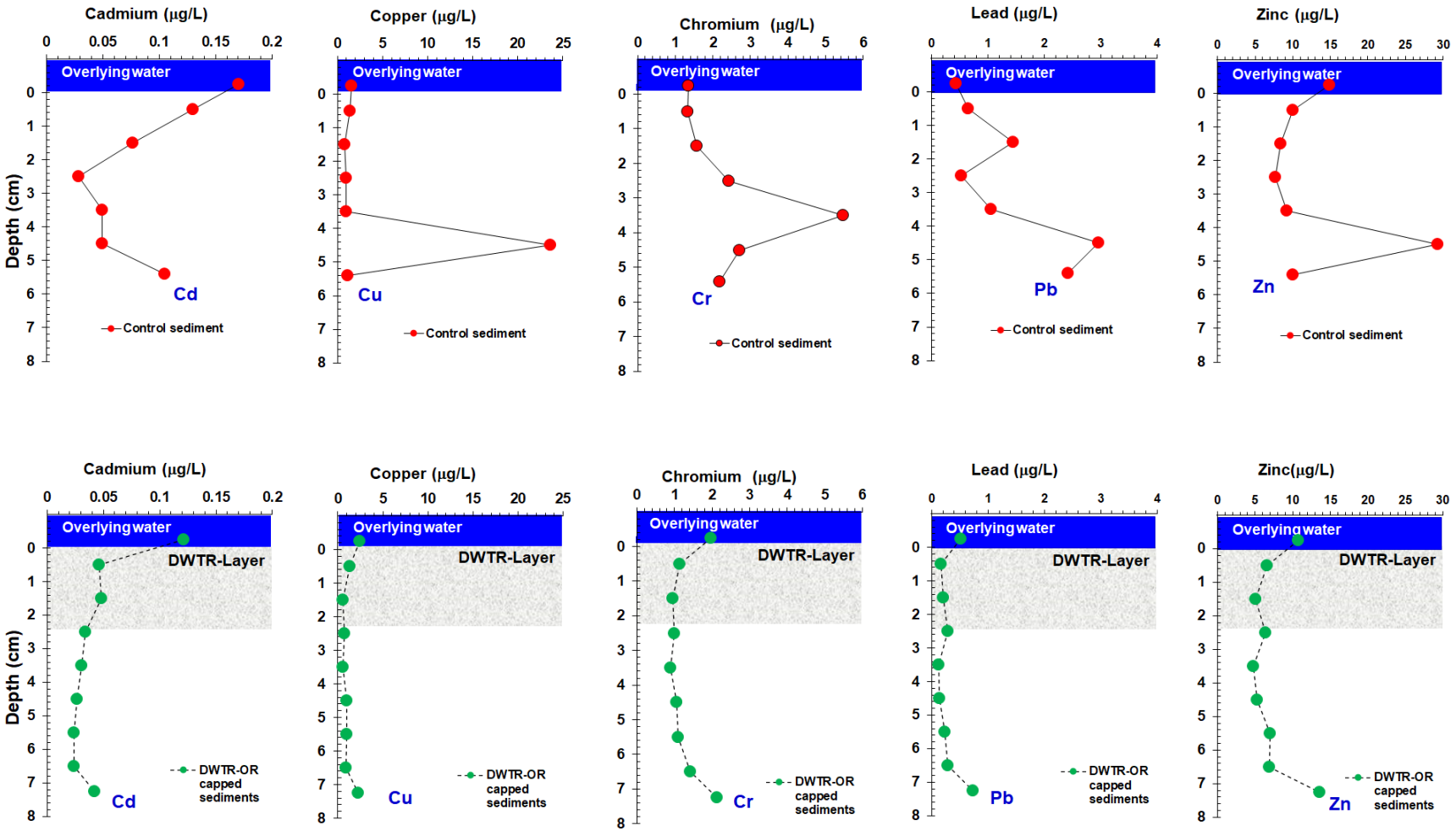


Figure 88. DGT profiles of dissolved concentrations of Cd, Cu, Cr, Pb, and Zn in the pore and overlying waters of non-capped (top panel) and DWTR-OR capped intertidal sediment (bottom panel). DGT samplers were inserted into the sediment after a water-sediment equilibration period of 7 days at a fixed hydrologic shear stress of 0.05 Pa. The DGT samplers were retrieved after a 24h contact period and sectioned every 0.5 cm and processed for metal analysis.

4.6.4. Toxicity of water overlying uncapped and capped sandy sediments on FHM juveniles. The toxicity results presented earlier focused on benthic organisms. Here we assessed the effects of the presence of a capping layer at the interface of water and metal-contaminated sediments on pelagic organisms. As described in the *method section*, cores of metal-contaminated sediments non-capped or capped with either sand, apatite, DWTR-OR or DWTR-WY were first equilibrated with facility water at a constant and critical hydrologic shear stress of 0.05 Pa, and the overlying waters used in fish exposure studies. The results of the survival of exposed FHM juveniles monitored over 96h are presented in **Figure 89**. First, fish exposed to facility water which had no contact with metal-contaminated sediments showed no mortality for duration of the study. Second, for water overlying non-capped and sand-capped sediments, all exposed organisms died within an hour. Third, when apatite was used as capping substrate, all exposed organisms died within 24h. However, when DWTR samples were used, fish mortality was delayed and reduced. For DWTR-OR, fish mortality started after 48h, and at the end of the exposure period, 70% of exposed organisms survived. A much higher mortality was recorded in the case of DWTR-WY, where fish mortality started to occur after 24h of exposure and increased over time to reach a survival rate of ~30% after 96h.

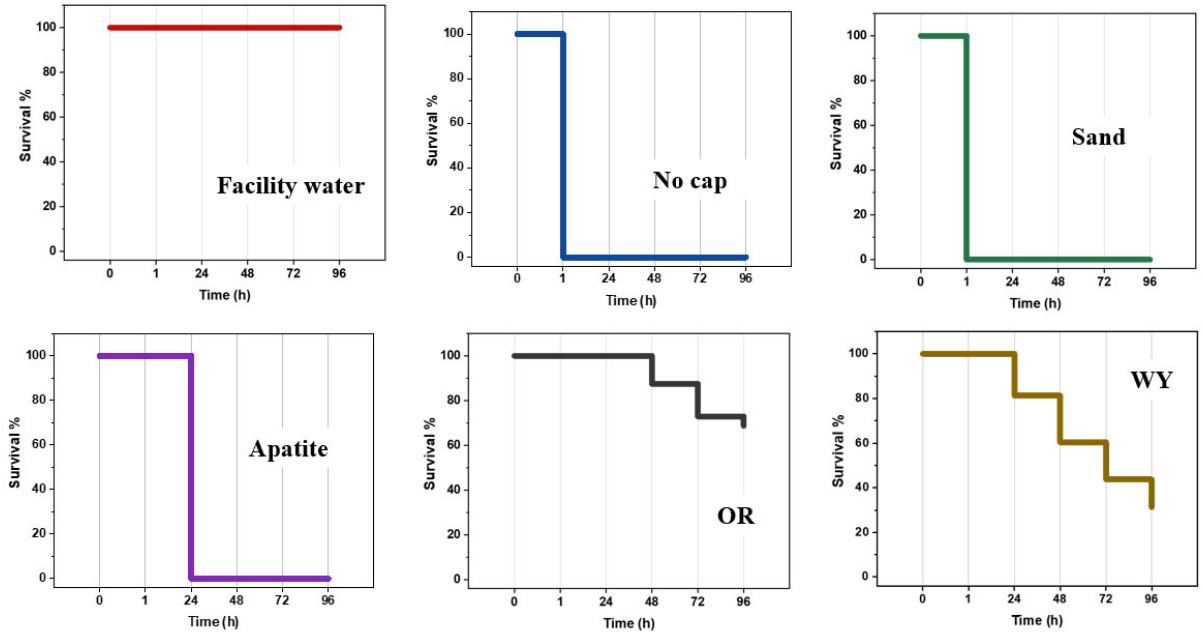


Figure 89. Survival of Fathead minnow juveniles in a 96h bioassay using water overlying metal-contaminated sediments in the absence and presence of capping substrates. Sand is used as inert substrate while apatite, DWTR-OR and DWTR-WY are reactive substrates.

While the use of sand as a sediment-capping layer resulted in toxicity trends similar to those of non-capped sediments due to the lack of or very limited sorption capacity for dissolved metals, the other three substrates delayed the onset of toxic effects by 24 to 48 hours. Of particular significance is the discrepancy in the survival rate trends observed in the presence of the two tested DWTR samples. Based on the metal sorption results obtained from column studies presented earlier, one would expect DWTR-WY to attenuate toxicity to FHM better than DWTR-OR, owing to its higher metal sorption capacity. However, the opposite was observed. This difference is likely attributed to the significance of the bioavailable metal fractions not immobilized by the cap layers. The presence of activated carbon in DWTR-WY could facilitate the immobilization of metals already complexed by dissolved organic matter (DOM), with the metal fraction reaching the overlying water likely in the form of bioavailable hydrated metal

cations. In contrast, the presence of DWTR-OR would allow DOM-complexed metals to pass through the cap. These DOM-complexed metals are likely less bioavailable and therefore less toxic, at least for the duration of our exposure studies. With the exception of sand-capped sediments, the analysis of total dissolved concentrations of Cd, Cu, Pb, and Zn in waters from either apatite or DWTR capped sediment cores, which were used in fish exposure studies exhibited low concentrations for Pb and Cu (low ppb range). However, the concentrations of Cd and Zn were much higher only in waters that were in contact with apatite-capped sediments (high ppb range), which is likely the reason for the observed total fish mortality when apatite was used as cap layer. **Figure 1A** in the Appendix Section shows additional examples of significant toxicity reduction or elimination by different DWTR samples.

Overall, these bioassays confirmed the potential protective role of DWTR, and although the complete elimination of toxicity was not always attained, the DWTRs outperformed both the sand and apatite in the attenuation of the toxicity of aqueous solutions containing a mixture of Cd, Cu, Pb, and Zn to FHM juveniles.

5. TECHNOLOGY TRANSITION

5.1. Batch to batch variability of DWTR substrates from either a single or multiple sources and potential effects on their short- and long-term metal immobilization performances.

Since DWTR-OR and DWTR-WY were selected as potential adequate substrates for introduction to US waterways, and although the corresponding DWTPs agreed to supply us with DWTR samples every year for the duration of the project, we ended receiving only two batches sent to us before the pandemic. Accordingly, we lack a solid data set for this specific assessment, which we would classify as an avenue for further research. Meanwhile, tracking the metal content of these DWTR over a period of two years gave the results presented in **Figure 90**. Overall, for DWTR-WY, Cu and Zn had noticeable increases from year 1 to year 2, while only Cu increased in DWTR-OR. From the second-year metal concentrations and based on the SQG presented earlier; DWTR-OR would still pass the screening based on metal content. DWTR-WY, with Cu concentration >150 mg/kg would fail the metal screening test. Unfortunately, bioassays were not conducted with the second batch. The results obtained based on this limited set of samples suggest that long-term monitoring should be conducted from pre-screened multiple DWTP to gain insights into the physicochemical changes of these materials with seasons and over a few years. Groundwater sources would probably be more stable in terms of chemical composition. However, most tend to fail the screening criteria because of high metal content (e.g., As, Cu, and Zn).

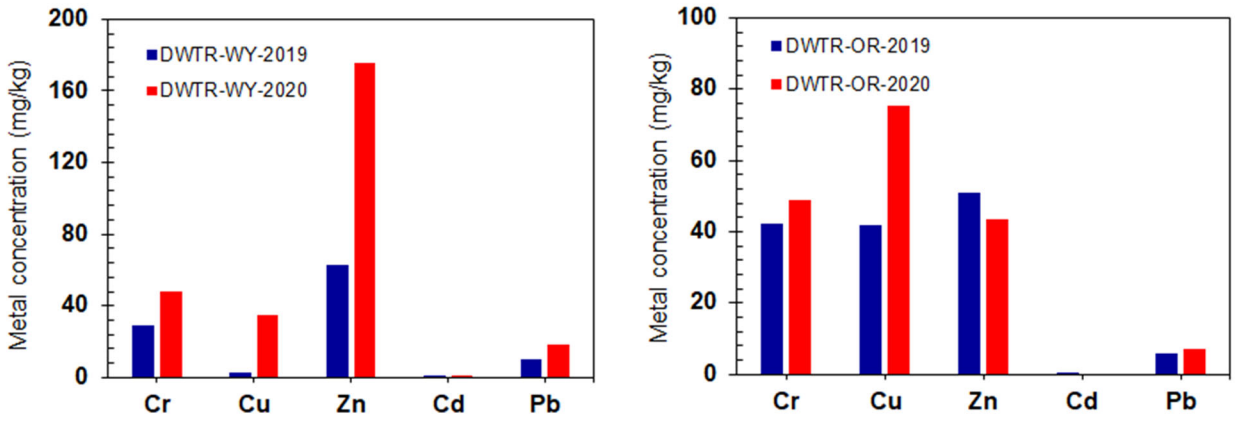


Figure 90. Total metal concentrations in DWTR samples obtained from Oregon and Wyoming over a period of two years, 2019 and 2020.

5.2. Parametric sensitivity analysis linking key compositional characteristics to DWTRs for potential applications.

Like the monitoring aspect discussed above, a solid parametric sensitivity analysis linking the composition of DWTR to their efficiency as metal-contaminated sediment capping substrates would require more than just two samples. Here, we feel that the robustness of this approach would depend on the size of the data set, which was not met in this effort. This is obviously an important step, which could result in the development of a predictive tool. Based on data available to us at this point, we consider the development of a predictive tool as a necessary future research avenue.

5.3. Cost and availability of DWTR from various sources to support commercial scale sediment capping projects.

From our conversations with several DWTPs, the following answers were given to us regarding the accessibility and cost of DWTR.

- Most DWTPs have relatively stable production rates of DWTR, with an increasing trend from year to year as they try to keep up with population growth whenever applicable. We received the following annual production rates from 5 of the facilities we contacted (**Table 16**), including WY and OR

Table 16. Annual production rates of DWTR obtained from 5 DWTP

	DWTR production rates (tons/year)
MN	~20,000
TN	~8,400
WY	~345
OR	~ 2,352
UT	~940

- Regarding cost, most DWTP have not thought of charging for their waste materials. They would gladly give the waste materials away free of charge and save money on disposal cost as the landfilling cost of non-hazardous DWTR is ~ $50/metric ton, which can substantially increase the cost of treated drinking water. For the in-situ remediation of metal-contaminated sediments, dewatered DWTR are preferred. Therefore, DWTPs might consider charging a fee to defray the cost of dewatering if not already part of their existing waste management program.

- The obvious cost would however be associated with hauling/transportation of DWTR from the point of production/accumulation to the site to be remediated. Several parameters are considered in this cost including the quantity, the distance, types of point of collection and discharge, etc. By calling a few hauling companies we got rough estimates based on hypothetical distances, and prices ranged from as low as $2 to $25/ton/mile, with the hauling of non-dewatered DWTR being the most expensive.

- Finally, one could explore the possibility of using just the additives or combinations of additives utilized during drinking water treatments as capping substrates for metal-contaminated sediments. While the cost for this option up to production of the residuals would be quite similar to that of DWTR production, the use of readily available DWTR would likely be less. Additionally, employing *"virgin"* drinking water treatment compounds can be justified only after laboratory testing to assess their toxicity characteristics and abilities to immobilize metals, as tested for DWTR in this study. This is because our findings suggest that substances present in treated raw waters (e.g., organic matter, clay minerals) play a significant role in metal immobilization by DWTR, and not solely the additives. Therefore, a comparative study evaluating the efficacy of DWTR, as demonstrated in this study, against laboratory-generated residuals based on synthetic waters rather than raw natural waters, would be necessary before considering this option.

5.4. Short Course / Community meeting

- In our initial proposal, a short course was included as a vehicle for the dissemination of the findings of this research. However, due to plan changes imposed upon us by the COVID-19 pandemic, we reconsidered our options and decided to hold a community meeting instead. Therefore, we ended up organizing a virtual **"*community meeting*" on 3/09/2023. The topic of the meeting was *"Evaluation of Drinking Water Treatment Residuals as Substrate for in situ Capping of Metal-Contaminated Sediments"***. For this meeting we targeted the DWTP managers, primarily those who supplied us with the DWTR samples used in the study, as well as researchers from different academic institutions, working on the remediation of contaminated soils and sediments. We had a total of nineteen participants. *Unfortunately, the recorded presentation and the Q&A session that followed were stored on Cloud and deleted after 180 days. We contacted Zoom in our effort to recover the recording but was told that the deletion became permanent after 30 days and could no longer be recovered. Therefore, the URL provided in the initial draft of the final report is no longer working.*

5.5. High quality video summary

A high-quality video summarizing this research was produced and was submitted through SEMS. The video is available through YouTube (***https://youtu.be/Qp5oOTtJ73g***), and accessible through the project's webpage at the University of Florida (*https://faculty.eng.ufl.edu/jean-claude-bonzongo/dod-serdp-project/*).

5.6. Publication List

5.6.1 Peer-reviewed and conference publications.

Wallace, S. M., Zhou, L., Ma, Q., Denslow, N. D., Bonzongo, J. C. J., & Gaillard, J. F. (2024). An XAS study of Hg (II) sorption to Al-based drinking water treatment residuals. ***Chemosphere***, *349*, 140922.

Wallace, SM., Zhang Y, Zhou L, Ma Q, Guise WE, Denslow ND, Bonzongo JC, and Gaillard JF. (2023). The diversity of aluminum-based drinking water treatment residuals for use in environmental remediation. ***Environmental Science: Water Research & Technology***, *9*(3), 935-947.

Quiñones, KYD., & Bonzongo, JC. (2023). Effects of simulated acid rain and carbon rich water on mercury mobilization in soils amended with aluminum-based drinking water treatment residuals. ***Soil & Environmental Health***, 100020.

Wallace S.M., Alsina, M.A., Gaillard J.-F. (2021) An algorithm for the automatic deglitching of x-ray absorption spectroscopy data. ***Journal of Synchrotron Radiation***, 28-4 1178–1183.

Zhou, L., Wallace, SM., Denslow, ND., Gaillard, JF., Meyer, P., & Bonzongo, JC. (2021). A screening approach for the selection of drinking water treatment residuals for their introduction to marine systems. ***Environmental Toxicology and Chemistry***, *40*(4), 1194-1203.

Zhou, L., Wallace, SM., Kroll, KJ., Denslow, ND., Gaillard, JF., Meyer, P., & Bonzongo, JC. (2021). Acute and chronic toxicity testing of drinking water treatment residuals in freshwater systems. ***Environmental Toxicology and Chemistry***, *40*(7), 2003-2012.

Wallace SM, Zhou L, Gaillard JF, Denslow ND, & Bonzongo JC (2021). Probing Cu sorption to drinking water treatment residuals (DWTRs) by XAS. ***American Chemical Society Spring meeting****, April 2021.*

Zhou L, Wallace SM, Denslow ND, Gaillard JF, & Bonzongo JC (2021). Total and leachable concentrations of toxic metals in drinking water treatment residuals (DWTRs) and toxicity implications in marine and freshwater systems. ***American Chemical Society Spring meeting****, April 2021.*

Bonzongo JC, Gaillard JF and Denslow ND. 2021. Evaluation of Drinking Water Treatment Residuals for Use as Capping Sorbent in Metal Contaminated Sediments. *SERDP & ESTCP Annual Symposium*. Washington, DC, 11/2022.

Zhou L., Wallace SM, Chen T, Kevin KJ, Denslow ND, Gaillard, JF. and Bonzongo, JC. **2019**: Evaluation of Drinking Water Treatment Residuals for Use as Capping Sorbent in Metal Contaminated Sediments. *SERDP & ESTCP Annual Symposium*. Washington, DC, 12/2019.

Bonzongo, JC, Gaillard, JF, Denslow Nd, Zhou L, Wallace SM, Gendusa W, & Kroll KJ. (2018). Drinking Water Treatment Residuals as Material for in situ Capping of Metal-Contaminated Sediments. *SERDP & ESTCP Symposium Sediment Meeting*. Washington, DC, 11/2018.

Wallace, S. M., Zhou, L., Gaillard, J. F., Kroll, K., Denslow, N. D., & Bonzongo, J. C. (2021, November 29-December 3). Drinking Water Treatment Residuals (DWTRs) as Material for in situ Capping of Metal-Contaminated Sediments: Metal Sorption Studies. *Virtual Poser Session, SERDP-ESTCP Symposium*.

Zhou, L., Wallace, S. M., Denslow, N. D., Gaillard, J. F., & Bonzongo, J. C. (2021, April 5-16). Total and Leachable Concentrations of Toxic Metals in Drinking Water Treatment Residuals (DWTRs) and Toxicity Implications in Marine and Freshwater Systems. *Virtual Poster session, American Chemical Society Spring 2021.*

Zhou, L., Wallace, S. M., Chen, T., Zhang, Y., Kroll, K., Denslow, N. D., Gaillard, J. F., & Bonzongo, J. C. (2019, December 3-5). Evaluation of Drinking Water Treatment Residuals for Use as Capping Sorbent in Metal Contaminated Sediments. *Poster session, SERDP- ESTCP Symposium, Washington, D.C.*

Bonzongo, J. C., Gaillard, J. F., Denslow, N. D., Hill, A., Wallace, S. M., Chen, T., Zhou, L., Gendusa, W., & Kroll, K. (2018, November 27-29). Can drinking water treatment residuals be used as material for in-situ capping of metal contaminated sediments? *Poster session, SERDP-ESTCP Symposium, Washington, D.C.*

5.6.2 Manuscripts in preparation

Oyamada GK, Kroll K, Zhou L, Wallace SM, Bonzongo J-C, Gaillard J-F, and Denslow ND. (2024). Drinking water treatment residuals minimize the effect of metals on fish exposed to metal contaminated sediments. *In prep*.

Zhou L, Zheng Y, Wallace SM, Denslow ND, Gaillard J-F, and Bonzongo J-C. (2024). Predicting the sorption affinity of metals for drinking water treatment residuals of different chemical compositions based on the environmental classification of metals. *In prep.*

Wei J, Zheng Y, Zhou L, Wallace SM, Denslow ND, Gaillard J-F, and Bonzongo J-C. (2024). Assessing the effectiveness of drinking water treatment residuals as in-situ capping substrates for metal-contaminated sediments. *In prep.*

Wallace, S. M., Alsina M.A., Shindel B., Zhou, L., Ma, Q., Denslow, N. D., Bonzongo, J. C., and Gaillard, J.-F. (2024). A spectroscopic examination of copper and lead sorption to aluminum-based drinking water treatment residuals. (*In prep)*

6. FUTURE RESEARCH AVENUES

This research program consisted of laboratory studies conducted primarily to determine if DWTRs could be used as in-situ capping substrates for metal-contaminated sediments.

First, based on the results of the screening component of this study, some DWTRs can qualify for introduction to U.S. waters. However, this initial research is more of a snapshot. This is because the DWTR samples were collected only once in 2019 from 13 of the contacted DWTPs, and twice, in 2019 and 2020, for DWTR-OR and DWTR-WY. Therefore, after establishing the criteria for the screening of DWTRs, the logical follow up step should be a monitoring program to

determine the temporal stability or variability of the physicochemical and ecotoxicological characteristics of DWTRs as these parameters would affect the availability of DWTRs for field applications. Ideally, a few DWTPs should be selected based on the quality and quantity of DWTRs they produce, and then monitored as a function of seasons over periods of months to years.

Second, the advanced characterization of DWTRs can be costly (e.g., use of synchrotron source radiation for solid phase analysis and bioassays). Given the high variability of the physicochemical characteristics of these waste materials, the ideal approach would be to generate a relatively large dataset by taking advantage of the analytical methods and protocols we have described herein. Such data could then be used to develop a predictive tool, and ideally with internet interface, which one can use when routine and easy to determine parameters are known (e.g., total metal concentrations, particle size, types of additives used during water treatment, etc.), to determine the suitability of DWTRs for introduction to U.S. waterways.

Third, our gust chamber studies showed that DWTRs can act as both physical barrier and active sorbents for metal contaminants. As a result, DWTRs reduce an in some cases eliminate the toxicity of metals to pelagic organisms. However, the use of sediment cores in gust chambers lasted only 1 to 2 weeks. Since it is rather difficult to predict the long-term effects of using DWTRs as capping substrates based solely on the results of short-term experiments, long-term studies are needed.

Overall, additional work is needed for the development of a robust approach that reduces the probability of failure when contemplating real world applications.

7. CITED REFERENCES

Aiken, G. R., Hsu-Kim, H., & Ryan, J. N. (2011). Influence of dissolved organic matter on the environmental fate of metals, nanoparticles, and colloids. *Environ. Sci. Technol.* 2011, 45, 8, 3196–3201. *https://doi.org/10.1021/es103992s*

Akcil, A., et al. (2015). A review of approaches and techniques used in aquatic contaminated sediments: metal removal and stabilization by chemical and biotechnological processes. *Journal of Cleaner Production*, 86: 24-36.

Alsina, M. A. et al. (2021). Araucaria: A Python library to process x-ray absorption data. (*https://marcoalsina.github.io/araucaria/build/html/index.html*).

Ahrland, S., Chatt, J., & Davies, N. R. (1958). The relative affinities of ligand atoms for acceptor molecules and ions. *Quarterly Reviews, Chemical Society*, *12*(3), 265–276.

Babatunde, A. and Y. Zhao (2007). Constructive approaches toward water treatment works sludge management: an international review of beneficial reuses. Critical Reviews in *Environmental Science and Technology*, 37(2): 129-164.

Benedetti, M. F., Van Riemsdijk, W. H., Koopal, L. K., Kinniburgh, D. G., Gooddy, D. C., & Milne, C. J. (1996). Metal ion binding by natural organic matter: From the model to the field. *Geochimica et Cosmochimica Acta*, 60(14), 2503–2513.

Bertin, EP (1975). *Principles and Practice of X-Ray Spectrometric Analysis*. Plenum Press, New York, NY, 2 Edition.

Castaldi, P., et al. (2015). Copper(II) and lead(II) removal from aqueous solution by water treatment residues. *Journal of Hazardous materials*, 283: 140-147.

Davison, W., & Zhang, H. (1994). In situ speciation measurements of trace components in natural waters using thin-film gels. *Nature*, 367(6463), 546-548.

Davison, W., Fones, G. R., & Grime, G. W. (1997). Dissolved metals in surface sediment and a microbial mat at 100-μm resolution. *Nature*, 387(6636), 885-888.

Degnan, JR, Lindsey BD, Levitt JP, and Szabo Z. (2020). The relation of geogenic contaminants to groundwater age, aquifer hydrologic position, water type, and redox conditions in atlantic and gulf coastal plain aquifers, eastern and south-central USA. *Science of the Total Environment*, 723. 137835

Downs, R. T.; Hall-Wallace, M.(2003). The American mineralogist crystal structure database. *American Mineralogist,* 88 (1), 247-250.

Dubchak, S. (2018). Distribution of Strontium in Soil: Interception, Weathering, Speciation, and Translocation to Plants. In *Behaviour of Strontium in Plants and the Environment* (pp. 33–43). https://doi.org/10.1007/978-3-319-66574-0_3

Fakra, S., XAS Databases. Lawrence Berkeley National Laboratory: 2010.

Freundlich, H. (1907). Über die adsorption in lösungen. *Zeitschrift Für Physikalische Chemie*, 57(1), 385–470.

Gates-Rector, S.; Blanton, T. (2019). The Powder Diffraction File: a quality materials characterization database. *Powder Diffraction,* 34 (4), 352-360.

Ge, Y., & Hendershot, W. (2005). Modeling sorption of Cd, Hg and Pb in soils by the NICA-Donnan model. *Soil & Sediment Contamination*, 14(1), 53-69.

Ghorbel-Abid, I., et al., Effect of cadmium and chromium adsorption on the zeta potential of clays. *Desalination and Water Treatment*, 2016. 57(36): p. 17128-17138.

Gibbons, M.K. and G.A. Gagnon (2011). Understanding removal of phosphate or arsenate onto water treatment residual solids. *Journal of Hazardous materials*, 186(2–3): p. 1916-1923.

Grant, P. G., Lemke, S. L., Dwyer, M. R., & Phillips, T. D. (1998). Modified Langmuir equation for S-shaped and multisite isotherm plots. *Langmuir*, 14(15), 4292-4299.

Green Eyes. (2015). *U-GEMS Manual-Version 3.0*. Green Eyes LLC, Easton, MD. http://gescience.com/wp-content/uploads/2017/02/UGEMS-manual-v3.0-GE-version.pdf

Gust, G., & Müller, V. (1997). Interfacial hydrodynamics and entrainment functions of currently used erosion devices. In N. Burt (Ed.), *Cohesive Sediments: 4th Nearshore and Estuarine Cohesive Sediment Transport Conference, INTERCOH 94.*

Haitzer, M., Aiken, G. R., & Ryan, J. N. (2002). Binding of mercury (II) to dissolved organic matter: the role of the mercury-to-DOM concentration ratio. *Environmental science & technology*, 36(16), 3564-3570.

Hardy R.G. and Tucker M. (1988). *Techniques in Sedimentology*, chapter X-ray pow- der diffraction of sediments, p. 191–228. *Blackwell Scientific Publications*.

Harper, M. P., Davison, W., Zhang, H., & Tych, W. (1998). Kinetics of metal exchange between solids and solutions in sediments and soils interpreted from DGT measured fluxes. *Geochimica et Cosmochimica Acta*, 62(16), 2757–2770.

Ho, Y. S., & McKay, G. (1999). Pseudo-second order model for sorption processes. *Process Biochemistry*, 34(5), 451–465. https://doi.org/10.1016/S0032-9592(98)00112-5

Ho, Y. S., & McKay, G. (1998). A Comparison of Chemisorption Kinetic Models Applied to Pollutant Removal on Various Sorbents. *Process Safety and Environmental Protection*, 76(4), 332–340. https://doi.org/10.1205/095758298529696

Hu, K., Pang, Y., Wang, H., Wang, X., Wu, X., Bao, K., & Liu, Q. (2011). Simulation study on water quality based on sediment release flume experiment in Lake Taihu, China. *Ecological Engineering*, 37(4), 607–615.

Huang, J., Xu, Q., Xi, B., Wang, X., Li, W., Gao, G., Huo, S., Xia, X., Jiang, T., & Ji, D. (2015). Impacts of hydrodynamic disturbance on sediment resuspension, phosphorus and phosphatase release, and cyanobacterial growth in Lake Tai. *Environmental Earth Sciences*, 74(5), 3945–3954.

Ippolito, J.A., K.A. Barbarick, and H.A. Elliott (2011). Drinking Water Treatment Residuals: A Review of Recent Uses All rights reserved. No part of this periodical may be reproduced or transmitted in any form or by any means, electronic or mechanical, including photocopying, recording, or any information storage and retrieval system, without permission in writing from the publisher. *Journal of Environmental Quality*, 40(1): 1-12.

Jutimoosik J, P. Kidkhunthod, T. Bongkarn, and R. Yimnirun. Influence of calci- nation temperature on phase formation and local structure of co0.6zn0.4fe1.6cr0.4o4 nanoparticles. *Ferroelectrics*, 552(1):177–185, 2019.

Jutimoosik J, P. Kidkhunthod, T. Bongkarn, and R. Yimnirun (2021). Local structure and cation distribution analysis of mn1-xznxfe2o4 powders by x-ray absorption near edge structure spectroscopy. *Radiation Physics and Chemistry*, 188, 2021.

Kalnejais, L., Martin, W., Signall, R., & Bothner, M. (2007). Role of sediment resuspension in the remobilization of particulate-phase metals from coastal sediments. *Environmental Science & Technology*, 41(7), 2282–2288. https://doi.org/10.1021/es061770z

Kelderman, P., Ang'weya, R., De Rozari, P., & Vijverberg, T. (2012). Sediment characteristics and wind-induced sediment dynamics in shallow Lake Markermeer, the Netherlands. *Aquatic Sciences*, 74(2), 301–313. https://doi.org/10.1007/s00027-011-0222-7

Khare, S. K., Panday, K. K., Srivastava, R. M., & Singh, V. N. (1987). Removal of victoria blue from aqueous solution by fly ash. *Journal of Chemical Technology & Biotechnology*, 38(2), 99–104.

Kim, C.S., G.E. Brown, and J.J. Rytuba (2000). Characterization and speciation of mercury-bearing mine wastes using X-ray absorption spectroscopy. *Science of the Total Environment*, **261**(1): 157-168.

Kumar PSA, J. J. Shrotri, S. D. Kulkarni, C. E. Deshpande, and Date SK. (1996) Low temperature synthesis of ni0.8zn0.2fe2o4 powder and its characterization. *Materials Letters*, 27(6):293–296.

Laima, M. H. C., Matthiesen, H., Lund-Hansen, L. C., & Christiansen, C. (1998). Resuspension studies in cylindrical microcosms: Effects of stirring velocity on the dynamics of redox sensitive elements in a coastal sediment. *Biogeochemistry*, 43(3), 293–309.

Lam, B., Baer, A., Alaee, M., Lefebvre, B., Moser, A., Williams, A., & Simpson, A. J. (2007). Major structural components in freshwater dissolved organic matter. *Environmental Science & Technology*, 41(24), 8240-8247.

Langmuir, I. (1918). The adsorption of gases on plane surfaces of glass, mica and platinum. *Journal of the American Chemical Society*, 40(9), 1361–1403.

Lin, T.-S., & Nriagu, J. (1998). Revised hydrolysis constants for thallium (I) and thallium (III) and the environmental implications. *Journal of the Air & Waste Management Association*, 48(2), 151–156.

Liu, W., Lu, G., & Wang, W. X. (2022). In situ high-resolution two-dimensional profiles of redox sensitive metal mobility in sediment-water interface and porewater from estuarine sediments. *Science of the Total Environment*, 820, 153034.

Luettich Jr, R. A., Harleman, D. R. F., & Somlyody, L. (1990). Dynamic behavior of suspended sediment concentrations in a shallow lake perturbed by episodic wind events. *Limnology and Oceanography*, 35(5), 1050–1067.

Mall, I., Srivastava, V., & Agarwal, N. (2007). Adsorptive removal of Auramine-O: Kinetic and equilibrium study. *Journal of Hazardous Materials*, 143(1–2), 386–395. https://doi.org/10.1016/j.jhazmat.2006.09.059

Makavipour, F. and R. Pashley (2015). A study of ion adsorption onto surface functionalized silica particles. *Chemical Engineering Journal*, 262: 119-124.

MDI-JADE (2023). Materials Data: Livermore, CA - https://www.materialsdata.com/prodjd.html. *Accessed on 7/01/2023*

Mishra, B., O'Loughlin, E. J., Boyanov, M. I., & Kemner, K. M. (2011). Binding of HgII to high-affinity sites on bacteria inhibits reduction to Hg0 by mixed FeII/III phases. *Environmental science & technology*, *45*(22), 9597-9603.

Moussout, H., Ahlafi, H., Aazza, M., & Maghat, H. (2018). Critical of linear and nonlinear equations of pseudo-first order and pseudo-second order kinetic models. *Karbala International Journal of Modern Science*, 4(2), 244–254. https://doi.org/10.1016/j.kijoms.2018.04.001

Mu, T., & Sun, H.-N. (2019). Sweet Potato Leaf Polyphenols: Preparation, Individual Phenolic Compound Composition and Antioxidant Activity. *Polyphenols in Plants*, 365-380. Academic Press.

Nieboer, E., & Richardson, D. H. S. (1980). The replacement of the nondescript term 'heavy metals' by a biologically and chemically significant classification of metal ions. *Environmental Pollution Series B, Chemical and Physical*, 1(1), 3–26.

Knox, A. S., Paller, M. H., & Roberts, J. (2012). Active capping technology—new approaches for in situ remediation of contaminated sediments. *Remediation Journal*, 22(2), 93-117.

Knox, A. S., Paller, M. H., & Dixon, K. L. (2014). Evaluation of active cap materials for metal retention in sediments. *Remediation Journal*, 24(3), 49-69.

Niu, Z., Zhang, S., Ma, M., Wang, Z., Zhao, H., & Wang, Y. (2019). Synthesis of novel waste batteries-sawdust-based adsorbent via a two-stage activation method for Pb 2+ removal. *Environmental Science and Pollution Research*, 26, 4730-4745.

Ociński, D., et al. (2016). Water treatment residuals containing iron and manganese oxides for arsenic removal from water–Characterization of physicochemical properties and adsorption studies. *Chemical Engineering Journal*, 294, 210-221.

Oyetade, O. A., Nyamori, V. O., Jonnalagadda, S. B., & Martincigh, B. S. (2018). Removal of Cd^{2+} and Hg^{2+} from aqueous solutions by adsorption onto nitrogen-functionalized carbon nanotubes. *Desalin. Water Treat*, 108, 253-267.

Pallasser, R.; Minasny, B.; McBratney, A. B. (2013). Soil carbon determination by thermogravimetrics. *Peerj* **,** *1, e6*.

Parker, R., Bolam, T., Barry, J., Mason, C., Kroger, S., Warford, L., Silburn, B., Sivyer, D., Birchenough, S., Mayes, A., & Fones, G. (2017). The application of diffusive gradients in thin films (DGT) for improved understanding of metal behaviour at marine disposal sites. *Science of the Total Environment*, 575, 1074–1086.

Perret, D, Gaillard JF, Dominik, J, and Atteia O. (2000). The diversity of natural hydrous iron oxides. *Environmental Science & Technology*, 34(17):3540–3546.

Phillips, S. C.; Johnson, J. E.; Miranda, E.; Disenhof, C. (2011). Improving CHN measurements in carbonate-rich marine sediments. *Limnology and Oceanography-Methods*, 9, 194-203.

Punamiya, P., et al. (2015). Effect of solution properties, competing ligands, and complexing metal on sorption of tetracyclines on Al-based drinking water treatment residuals. *Environmental Science and Pollution Research*, 22(10): 7508-7518.

Quiñones, K. Y. D., & Bonzongo, J. C. J. (2023). Effects of simulated acid rain and carbon-rich water on mercury mobilization in soils amended with aluminum-based drinking water treatment residuals. *Soil & Environmental Health*, 1(2), 100020.

Quinones, J. L., & Carpi, A. (2011). An Investigation of the kinetic processes influencing mercury emissions from sand and soil samples of varying thickness. *Journal of environmental quality*, *40*(2), 647-652.

Quiñones, K.D., et al. (2016). Insights into the mechanisms of mercury sorption onto aluminum-based drinking water treatment residuals. *Journal of Hazardous materials*, 307: 184-192.

Ravichandran, Mahalingam. (2004). Interactions between mercury and dissolved organic matter—a review. *Chemosphere* 55.3: 319-331.

Ravichandran, M., Aiken, G. R., Reddy, M. M., & Ryan, J. N. (1998). Enhanced dissolution of cinnabar (mercuric sulfide) by dissolved organic matter isolated from the Florida Everglades. *Environmental Science & Technology*, 32(21), 3305-3311.

Ren P, Zhang JX, and Deng HY. (2009). Preparation and microstructure of spinel zinc ferrite znfe2o4 by co-precipitation method. *Journal of Wuhan University of Technology-Materials Science Edition*, 24(6):927–930.

Salim, R., Al-Subu, M. M., & Sahrhage, E. (1992). Uptake of cadmium from water by beech leaves. *Journal of Environmental Science and Health. Part A: Environmental Science and Engineering and Toxicology*, 27(3), 603–627. https://doi.org/10.1080/10934529209375751

Schreiber, B., Brinkmann, T., Schmalz, V., & Worch, E. (2005). Adsorption of dissolved organic matter onto activated carbon—the influence of temperature, absorption wavelength, and molecular size. *Water Research*, 39(15), 3449-3456.

Sheha, R. R. (2012). Preparation and performance of a novel composite as a reactive resin for copper retention. *Chemical engineering journal*, 213, 163-174.

Silvetti, M., et al. (2015). Sorption of Cadmium (II) and Zinc (II) from Aqueous Solution by Water Treatment Residuals at Different pH Values. *Water, Air, & Soil Pollution*, **226**(9): 1-13.

Simukanga, S., & Lombe, W.C. (1995). Electrochemical properties of apatite and other minerals of Zambian phosphate ores in aqueous solution. *Fertilizer research*, *41*, 159-166.

Schwertmann U. and Cornell R.M. (2008). *Iron Oxides in the Laboratory: Prepa- ration and Characterization*. John Wiley & Sons

Skyllberg, U., & Drott, A. (2010). Competition between disordered iron sulfide and natural organic matter associated thiols for mercury (II): An EXAFS study. *Environmental Science & Technology*, *44*(4), 1254-1259.

Skyllberg, U., Bloom, P. R., Qian, J., Lin, C. M., & Bleam, W. F. (2006). Complexation of mercury (II) in soil organic matter: EXAFS evidence for linear two-coordination with reduced sulfur groups. *Environmental science & technology*, *40*(13), 4174-4180.

Simpson, S., Apte, S., & Batley, G. (1998). Effect of short-term resuspension events on trace metal speciation in polluted anoxic sediments. *Environmental Science & Technology*, *32*(5), 620–625. https://doi.org/10.1021/es970568g

Soleimanifar, H., et al., Water treatment residual (WTR)-coated wood mulch for alleviation of toxic metals and phosphorus from polluted urban stormwater runoff. *Chemosphere*, 2016. 154: 289-292.

Somasundaran, P. (1968). Zeta potential of apatite in aqueous solutions and its change during equilibration. *Journal of Colloid and Interface Science*, 27(4), 659-666).

Stumm W. and Morgan J.J. (1996). Aquatic Chemistry: Chemical Equilibria and Rates in Natural Waters, Wiley, 1022p.

Tanifuji, M.; Matsuda, A.; Yoshikawa, H. (2019) In *Materials data platform-a FAIR system for data-driven materials science*, 8th International Congress on Advanced Applied Informatics (IIAI-AAI), IEEE: pp 1021-1022.

Tang ZX, Sorensen CM, Klabunde KJ, and Hadjipanayis GC. (1991). Preparation of manganese ferrite fine particles from aqueous solution. *Journal of Colloid and Interface Science*, 146(1):38–52.

Tatarchuk T, Bououdina M, Vijaya JJ, and Kennedy LJ. (2017). Spinel ferrite nanopar- ticles: Synthesis, crystal structure, properties, and perspective applications. In *4th International Research and Practice Conference on Nanotechnology and Nanoma- terials (NANO)*, volume 195 of *Springer Proceedings in Physics*, pp. 305–325.

Tessier, A., Campbell, P. G. C., & Bisson, M. (1979). Sequential extraction procedure for the speciation of particulate trace metals. *Analytical Chemistry*, 51(7), 844–851.

Thomas, H. C. (1948). Chromatography: a problem in kinetics. *Annals of the New York Academy of Sciences*, *49*(2), 161-182.

Thomas, S. A., Tong, T., & Gaillard, J. F. (2014). Hg (II) bacterial biouptake: the role of anthropogenic and biogenic ligands present in solution and spectroscopic evidence of ligand exchange reactions at the cell surface. *Metallomics*, 6(12), 2213-2222.

Turiel, E., Perez-Conde, C., & Martin-Esteban, A. (2003). Assessment of the cross-reactivity and binding sites characterisation of a propazine-imprinted polymer using the Langmuir-Freundlich isotherm. *Analyst*, 128(2), 137–141.

U.S. Environmental Protection Agency (1991). Evaluation of dredged material proposed for ocean disposal. EPA 503/8-91/001, February 1991. 214 p.

U.S. Environmental Protection Agency (2022). National recommended water quality criteria – aquatic life criteria table. Webpage link: *National Recommended Water Quality Criteria - Aquatic Life Criteria Table, US EPA* (*Accessed in December 2022*)

Valero, A., Umbría-Salinas, K., Wallner-Kersanach, M., de Andrade, C. F., Yabe, M. J. S., Contreira-Pereira, L., ... & Zhang, H. (2020). Potential availability of trace metals in sediments in southeastern and southern Brazilian shipyard areas using the DGT technique and chemical extraction methods. *Science of the Total Environment*, *710*, 136216.

Wallace, S. M., Zhou, L., Ma, Q., Denslow, N. D., Bonzongo, J. C. J., & Gaillard, J. F. (2024). An XAS study of Hg (II) sorption to Al-based drinking water treatment residuals. *Chemosphere*, 349, 140922.

Wallace, S. M., Zhang, Y., Zhou, L., Ma, Q., Guise, W. E., Denslow, N. D., ... & Gaillard, J. F. (2023). The diversity of aluminum-based drinking water treatment residuals for use in environmental remediation. *Environmental Science: Water Research & Technology*, *9*(3), 935-947.

Wang, C., et al. (2016). Tuning the adsorptive properties of drinking water treatment residue via oxygen-limited heat treatment for environmental recycle. *Chemical Engineering Journal*, 2016. 284: 571-581.

Wang, J. and C. Chen (2009). Biosorbents for heavy metals removal and their future. *Biotechnology advances*, 27(2): 195-226.

Wang, P.-F., Rivera, I., Richter, K., Liao, Q., Farley, K., Chen, H.-C., Germano, J., Markillie, K., & Gailani, J. (2016). Evaluation of resuspension from propeller wash in DoD Harbors (Technical Report 3049). SSC Pacific.

Weber Jr, W. J., & Morris, J. C. (1963). Kinetics of adsorption on carbon from solution. *Journal of the sanitary engineering division*, 89(2), 31-59.

Work, P. A., and Schoellhamer, D. H. (2018). *Measurements of erosion potential using Gust chamber in Yolo Bypass near Sacramento, California* (Report No. 2018–1062; Open-File Report). USGS Publications Warehouse. https://doi.org/10.3133/ofr20181062

Wu, Z. H., Wang, S. R., He, M. C., & Wu, F. C. (2015). The measurement of metals by diffusive gradients in thin films (DGT) at sediment/water interface (SWI) of bay and remobilization assessment. *Environmental Earth Sciences*, 73(10), 6283–6295.

Xie, M., Jarrett, B., Da Silva-Cadoux, C., Fetters, K., Burton, G., Gaillard, J., & Packman, A. (2015). Coupled Effects of Hydrodynamics and Biogeochemistry on Zn Mobility and Speciation in Highly Contaminated Sediments. *Environmental Science & Technology*, *49*(9), 5346–5353. https://doi.org/10.1021/acs.est.5b00416.

Xu, J., Zhang, J., Huo, S., Xi, B., He, Z., & Xu, Y. (2017). High-resolution profiles of trace metals assessed by DGT techniques in lake sediment porewaters. *Environmental Earth Sciences*, 76, 1-10.

Xu, X., et al. (2015). Use of drinking water treatment solids for arsenate removal from desalination concentrate. *Journal of colloid and interface science*, 445: 252-261.

Yan JS, Sharma N, Flynn ED, Giammar DE, Schwartz GE, Brooks SC, Weisenhorn P, Kemner KM, O'Loughlin EJ, Kaplan DI, and Catalano JG. (2002). Consistent controls on trace metal micronutrient speciation in wetland soils and stream sediments. *Geochimica Et Cosmochimica Acta*, 317: 234–254.

Yan, G., Viraraghavan, T., & Chen, M. (2001). A new model for heavy metal removal in a biosorption column. *Adsorption Science & Technology*, 19(1), 25-43.

Zhang, L., et al. (2016). Zeta potential-assisted sorption of uranyl tricarbonate complex from aqueous solution by polyamidoxime-functionalized colloidal particles. *Physical Chemistry Chemical Physics*, 18(18): 13026-13032.

Zhang, C., Zhu, M., Zeng, G., Yu, Z., Cui, F., Yang, Z., & Shen, L. (2016). Active capping technology: A new environmental remediation of contaminated sediment. *Environmental Science and Pollution Research*, 23(5), 4370–4386.

Zhang, C. S., Ding, S. M., Xu, D., Tang, Y., & Wong, M. H. (2014). Bioavailability assessment of phosphorus and metals in soils and sediments: A review of diffusive gradients in thin films (DGT). *Environmental Monitoring and Assessment*, 186(11), 7367–7378.

Zhang, H., Davison, W., Miller, S., & Tych, W. (1995). In situ high resolution measurements of fluxes of Ni, Cu, Fe, and Mn and concentrations of Zn and Cd in porewaters by DGT. *Geochimica et Cosmochimica Acta*, 59(20), 4181-4192.

Zhang, H., & Davison, W. (1995). Performance characteristics of diffusion gradients in thin-films for the in-situ measurement of trace-metals in aqueous-solution. *Analytical Chemistry*, 67(19), 3391–3400.

Zhang, H., Davison, W., Miller, S., & Tych, W. (1995). In situ high resolution measurements of fluxes of Ni, Cu, Fe, and Mn and concentrations of Zn and Cd in porewaters by DGT. *Geochimica Et Cosmochimica Acta*, 59(20), 4181–4192.

Zhao, J., Qin, Y., Shen, J., Zhou, B., Li, C., & Li, G. (2019). Effects of pore structures of different maceral compositions on methane adsorption and diffusion in anthracite. *Applied Sciences*, 9(23), 5130.

Zhou, L., Wallace, S. M., Denslow, N. D., Gaillard, J., Meyer, P., & Bonzongo, J. J. (2021a). A screening approach for the selection of drinking water treatment residuals for their introduction to marine systems. *Environmental Toxicology and Chemistry*, 40(4), 1194–1203.

Zhou, L., Wallace, S. M., Kroll, K. J., Denslow, N. D., Gaillard, J., Meyer, P., & Bonzongo, J. J. (2021b). Acute and Chronic Toxicity Testing of Drinking Water Treatment Residuals in Freshwater Systems. *Environmental Toxicology and Chemistry*, 40(7), 10.

Zhou, C. Y., Guan, D. X., Williams, P. N., Luo, J., & Ma, L. Q. (2016). Novel DGT method with tri-metal oxide adsorbent for in situ spatiotemporal flux measurement of fluoride in waters and sediments. *Water Research*, 99, 200–208.

Zhou, C., Gao, Y., Gaulier, C., Luo, M., Zhang, X., Bratkic, A., ... & Baeyens, W. (2020). Advances in understanding mobilization processes of trace metals in marine sediments. *Environmental Science & Technology*, 54(23), 15151-15161.

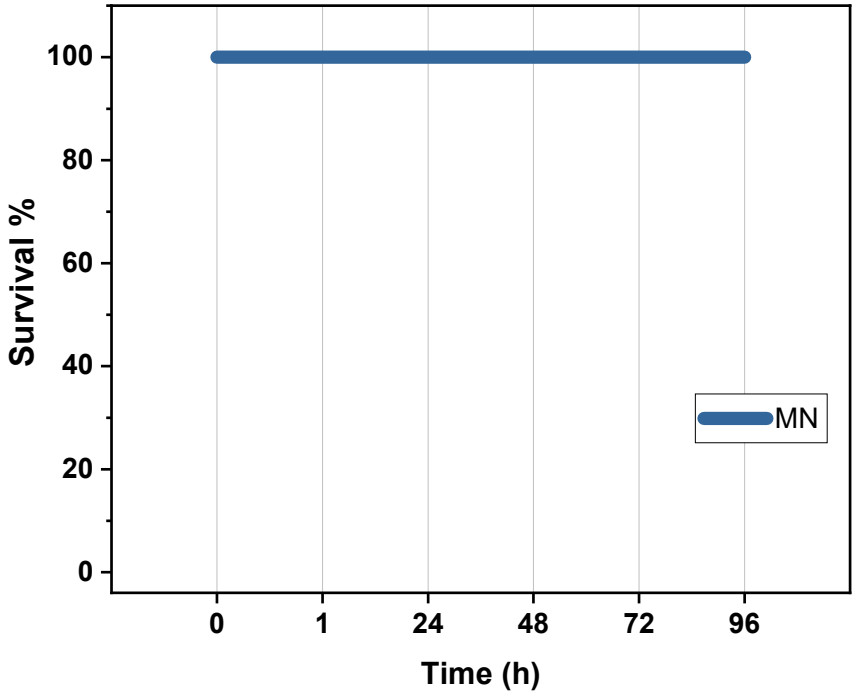
APPENDIX A

	ID	TCLP	TEC	PEC
DWTRs with Minimal toxic effects	IL	Passed	Passed	Passed
	NC	Passed	Passed	Passed
	TN	Passed	Passed	Passed
	WY	Passed	Passed	Passed
DWTRs with Possible toxic effects	OR	Passed	Failed (Cu)	Passed
	FL	Passed	Failed (Cu)	Passed
	KS	Passed	Failed (As)	Passed
	MN	Passed	Failed (Cu)	Passed
	UT	Passed	Failed (As)	Passed
DWTRs with Probable toxic effects	AZ-1	Passed	Failed (Ni)	Failed (Ni, Cr)
	AZ-2	Passed	Failed (As)	Failed (As)
	AR	Passed	Failed (Cd, Cu)	Failed (As)
	PA	Passed	Failed (Zn)	Failed (Cu)
	ME	Passed	Failed (As)	Failed (As)
	TX	Passed	Failed (As, Cu, Ni)	Failed (Cr)

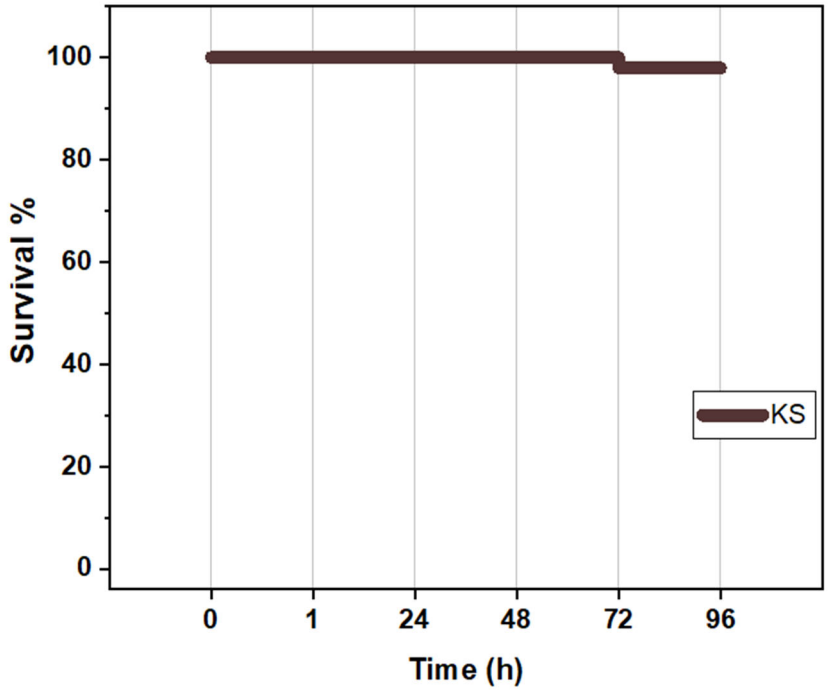
Table A1: Summary of the results of DWTR screening based on the combination of the results of the toxicity characteristics leaching procedure (TCLP), and qualification based on metal contents and sediment quality guidelines (SQGs).

Figure A1. Survival of fathead minnow (FHM) juveniles in a 96-h bioassay using water overlying metal-contaminated sediments in the presence of DWTRs as capping substrates. Examples of toxicity elimination or significant reduction.

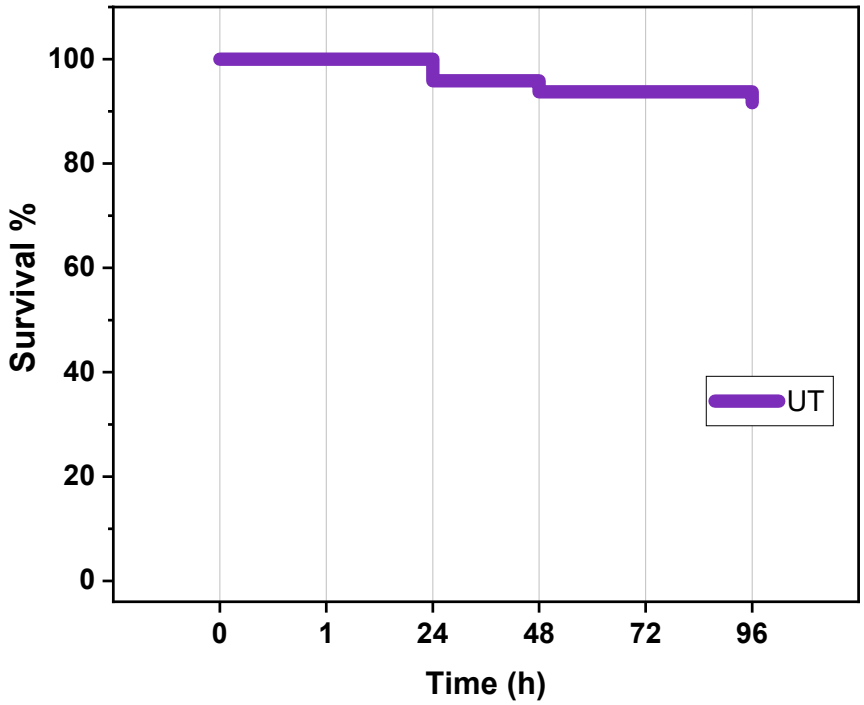
a. DWTR-MN: Toxicity to FHM completely eliminated



b. DWTR-KS: Near complete elimination of toxicity



c. DWTR-UT: Survival >90% after 96 hours



d. DWTR-AZ1: Survival >90%

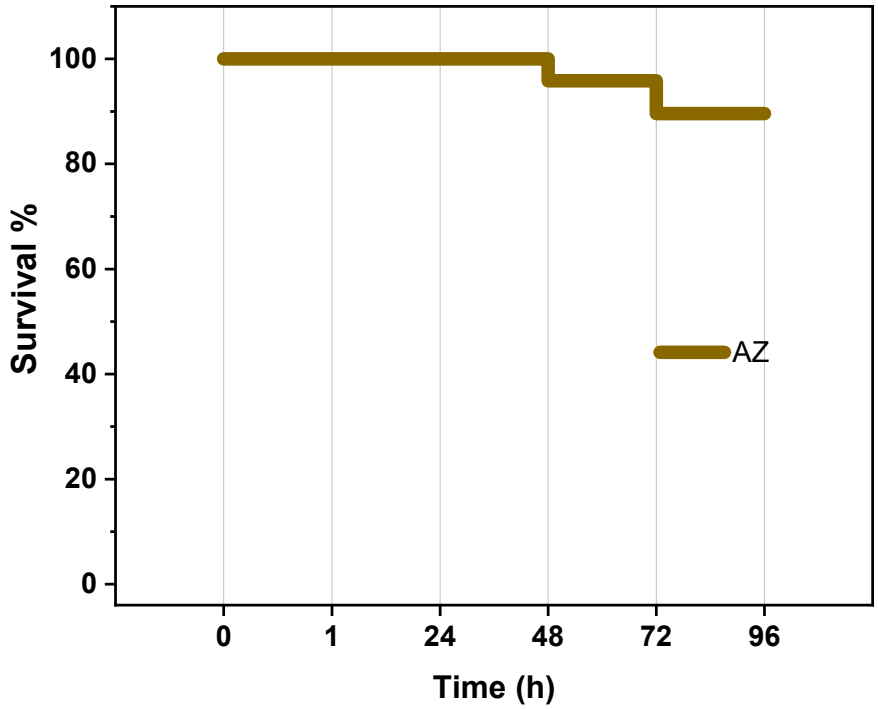


Figure A2. Example depth profiles of dissolved concentrations ($C_i = \frac{F \times \Delta g}{D}$) of lead (Pb), cadmium (Cd), Zinc (Zn), and copper (Cu) in pore and overlying waters of (a) non-capped and (b) DWTR-WY-capped sediment cores after an initial equilibration in a gust chamber for 7 days at τ = 0.05 Pa, followed by the insertion of the DGT samplers which were left in place for 24 hours. These concentrations profiles were used to calculate the diffusive fluxes illustrated in Figure A3.

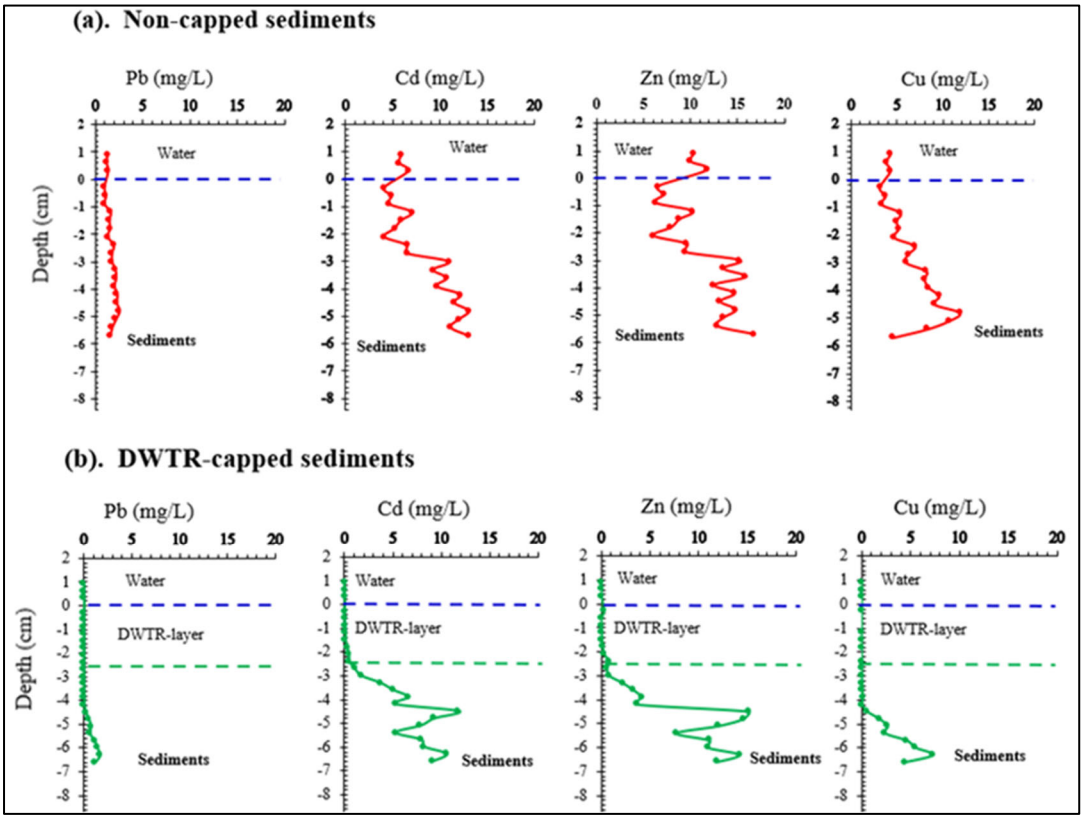
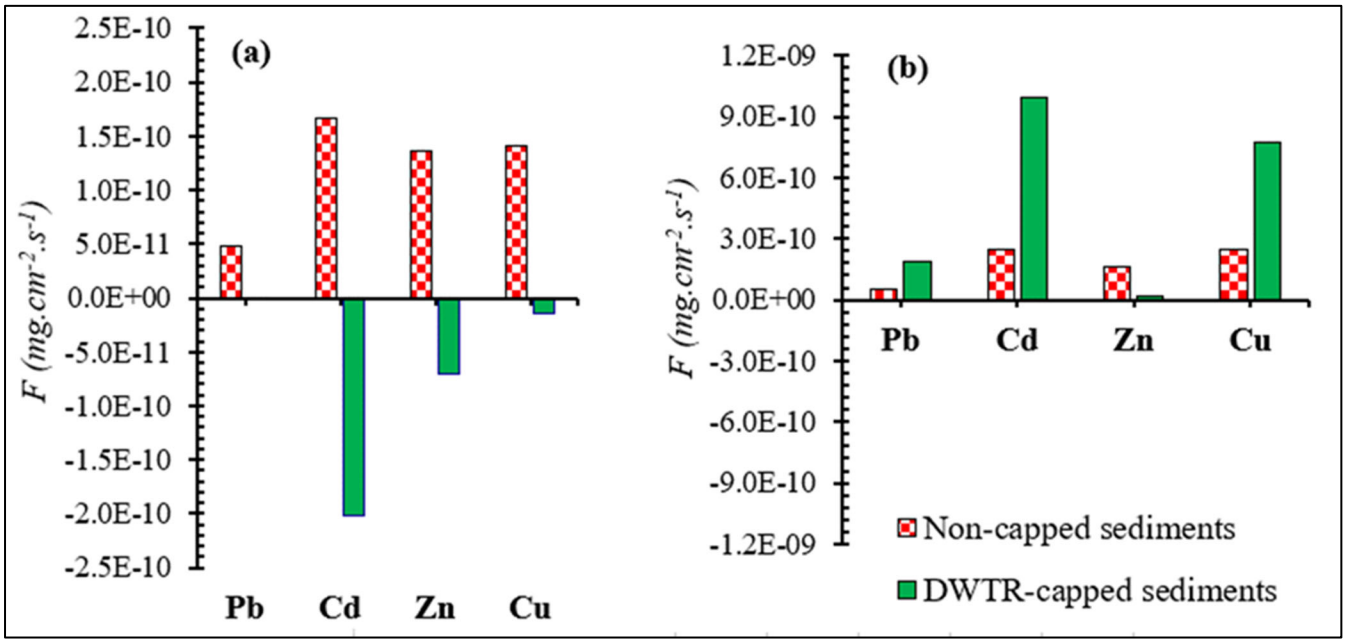


Figure A3. Diffusion fluxes ($\boldsymbol{F = -\emptyset D_s \frac{dC_{DGT}}{dz}}$) of Pb, Cd, Zn, and Cu calculated for two different solid phase layers in non-capped and DWTR-capped sediments, and where $\emptyset$ is the sediment porosity, $\boldsymbol{D_s}$ is the sediment diffusion coefficient, $\boldsymbol{C_{DGT}}$ is the porewater concentration, and $\boldsymbol{z}$ is the depth below the sediment–water interface.

(a). Metal fluxes ($\boldsymbol{F}$) at the solid-water interface (top 1 cm).

(b). Metal fluxes ($\boldsymbol{F}$) within the sediments ~4 cm below the solid-water interface. Negative bars indicate downward fluxes.



The results depicted in **Figure A3** indicate that in the absence of a capping layer (red bars), positive F values were observed both near the surface and 4 cm below the surface, suggesting that sediments act as sources of metals to the overlying water, with higher F-values near the sediment-water interface. When DWTR-WY was used as a capping substrate (green bars), the overall trend of F-values remained positive at a depth of 4 cm (**Figure A3b**). However, in the top 1 cm (**Figure A3a**), except for Pb which showed no measurable flux, negative F values were observed, highlighting the influence of DWTR on the fluxes of the analyzed metals.

Berner, R. A. (1980). Early diagenesis: a theoretical approach (No. 1). Princeton University Press.